Sol-Gel Matrix-Mediated Synthesis of Superparamagnetic Iron Oxide Clusters And Supported Iron Porphyrin Oxidation Catalysts

by

Lei Zhang

B. S. in Chemical Engineering
Tsinghua University, Beijing, P. R. China, 1992

Submitted to the Department of Chemical Engineering in Partial Fulfillment
of the Requirements for the Degree of

Doctor of Philosophy in Chemical Engineering

at the

MASSACHUSETTS INSTITUTE OF TECHNOLOGY

June 1998

Author ....
Department of Chemical Engineering
April 10, 1998

Certified by..
Professor Jackie Y. Ying
Raymond A. and Helen E. St. Laurent Associate Professor of Chemical Engineering
Thesis Supervisor

Accepted by ....
Professor Robert E. Cohen
St. Laurent Professor of Chemical Engineering
Chairman, Departmental Committee on Graduate Studies

Sol-Gel Matrix-Mediated Synthesis of Superparamagnetic Iron Oxide Clusters And Supported Iron Porphyrin Oxidation Catalysts

by

Lei Zhang

Submitted to the Department of Chemical Engineering
on April 10, 1998 in Partial Fulfillment of the Requirements
for the Degree of Doctor of Philosophy in Chemical Engineering

ABSTRACT

This thesis examined the matrix-mediated approach as a means to derive unique superparamagnetic nanoclusters and active supported metalloporphyrin catalysts. Nanoporous silicate-based matrices generated by modified sol-gel processing were used to stably host clusters and complexes through designed guest-host interactions. The matrix microstructure and surface chemistry were further tailored to control the size, morphology, dispersion and interfacial characteristics of guest species such as iron oxide and iron porphyrins. Iron oxide nanoclusters are of interest for both fundamental understanding of nanoscopic magnetism and advanced magnetic applications. In this thesis, we have successfully synthesized and stabilized iron oxide nanoclusters via three matrix-mediation routes. The first approach involved the derivation of a sulfonated silica via modified sol-gel processing of a unique SO_3^--functionalized organoalkoxysilane precursor. Metal cations attracted to this inorganic ion-exchange material could be oxidized to form oxide clusters that assumed the pore dimension and morphology of the matrix. γ-Fe_2O_3 nanoclusters thus generated were elongated (4 nm x 20 nm) in nature. Non-agglomerated γ-Fe_2O_3 has also been processed by encapsulation of precipitated iron oxide nanoparticles within a silica coating. This method produced spherical magnetic particles with diameters of ~4 nm. Thirdly, γ-Fe_2O_3 nanoclusters were synthesized within the hexagonally-packed mesopores of MCM-41 matrices via an evaporation-condensation approach. The well-defined cylindrical pore structure of MCM-41 aluminosilicates led to the synthesis of clusters of spherical and elongated morphologies. Magnetization studies and Mössbauer spectroscopy indicated that the three types of γ-Fe_2O_3/SiO_2 nanocomposites exhibited interesting superparamagnetic behavior. The surface magnetic structure of these clusters and the strain effects imposed by the host played a critical role in determining the overall magnetic and optical behavior of these nanocomposites. The coercivities and superparamagnetic barrier energies can be manipulated through modification of the host microstructure and the cluster/matrix interface. Tailoring of the magnetic properties of these novel systems was possible through the control of matrix structure and cluster synthesis conditions.

Matrix-mediated synthesis can also be used for deriving novel supported catalysts of organometallic complexes, such as metalloporphyrins, which offer unique chemoselectivity and excellent catalytic oxidation activity under mild reaction conditions. The development of an effective heterogeneous system for supporting these complexes would prevent self-oxidation of the active centers and allow for facile recovery of the catalyst. A design strategy was developed in this thesis to encapsulate the large metalloporphyrin complexes in mesoporous MCM-41 material. To ensure fixation of the catalyst within the support's pore structure, mesoporous silicate was doped with Al or Nb. In the former, Al doping provided more surface hydroxyl groups for interactions between the matrix and the Fe center of phthalocyanine complexes. In the latter, covalent bonding was possible between the Nb dopants on the support pore walls and the amine terminal groups of iron(III) meso-(tetra-aminophenyl)porphyrin bromide. This second approach was particularly effective at immobilizing metalloporphyrins within the porous matrix, preventing catalyst leaching during the oxidation reactions. The supported metalloporphyrin catalysts demonstrated excellent catalytic activity and selectivity for alkene epoxidation and alkane hydroxylation at ambient conditions. By controlling the structural characteristics of the mesoporous matrix materials, such as nature of dopant, dopant concentration, pore size and surface area, the local catalytic environment for hosting metalloporphyrins and the diffusion characteristics of reactants and products were successfully tailored to optimize the catalyst performance.

Thesis Advisor: Jackie Y. Ying
Title: Raymond A. and Helen E. St. Laurent Associate Professor

ACKNOWLEGMENTS

Towards the end of my five years of graduate studies, I feel I have matured in both my professional and personal lives. There are so many people I met at MIT who have been tremendously helpful, I greatly appreciate them from the bottom of my heart and will always be indebted to them. First of all, I would like to acknowledge my thesis advisor, Prof. Jackie Y. Ying, for her guidance and support during my entire thesis work. Her dedication to the group and hard work were always a good example for my own research. I would also like to thank my thesis committee members: Prof. Karen Gleason, Prof. Klavs Jensen, and Prof. Edward Merrill for their many thoughtful comments during the course of my thesis. I would like to thank Dr. Georgia Papaefthymiou for sharing her knowledge on Mössbauer spectroscopy and Dr. Ronald Ziolo for his helpful suggestions for the superparamagnetic nanocluster project.

It is my great pleasure to work with many talented, bright colleagues in the Nanostructure Materials Research Laboratory. They all gave me a great deal of help in both the scientific arena and my daily-life experience in this country. Thanks go to Dr. Andreas Tschöpe, Dr. Atsushi Nakahira, Dr. David Antonelli, Dr. Tao Sun, Dr. Christian Mehnert, Dr. Kenneth Bryden, Dr. Darren Castro, Dr. Doron Levin, Larry Panchula, Mark Fokema, Chen-Chi Wang, Micheal Wong, Andrey Zarur, Ron Kuse, Edward Ahn, Ruma Chakravorty, John Lettow, Duane Myers, Neeraj Sangar, Justin McCue, and Jason Sweeney. I would especially like to thank Dr. Tao Sun for many useful discussions on my research project. I would also like to acknowledge UROP students Tom Gubiotti and Chris Liu for their assistance in the supported metalloporphyrin catalyst project. CMSE staff has also been a great resource for my thesis. I would like to thank Mike Frongillo, Zhibo Zhang, and Tony Garratt-Reed for their assistance in the TEM and STEM studies, Tim McCllure and Fang-cheng Chou for teaching me how to use the SQUID facility.

I would like to acknowledge the great job that Linda Mousseeau and Ellen Weene did in the day-to-day administrative tasks of the group. I feel very fortunate to have Ellen's advice with life experience in the States. I would also like to thank Elaine Aufiero and Janet Fischer of the Students Office for their great efforts in making my stay at MIT as smooth as possible. Financial support of the National Science Foundation (CTS-9257223 and CTS-9411901) and the Packard Foundation for my research is also greatly appreciated.

I would like to thank all my friends around the campus and across the miles who were always cheering me on and made my life more colorful outside the lab in the past five years. They are Jane Pei-cheng Chang, Tani Chen, Xin Chen, Sherry Gu, Wei Guo, Lily Lee, Gene Lin, Jianfeng Luo, Bing Zhang, Bing Zhu, Qian Zhu. I will miss you all and look forward to continue sharing my friendship with you.

Last but not least, I would like to express my deepest thanks and appreciation to my family. My parents and brother who live thousands of miles away in China were always providing me tremendous encouragement and unconditional love. My sister in New York City lives much closer by and made me feel not homesick in this country. Her first lovely baby, Allan, has just entered the world and gives me so much joy during my thesis writing. I would

like to express my heartfelt thanks to my boyfriend, Liezhong Gong, he has always been so patient and supportive whenever I experienced any difficulties. All I have accomplished has everything to do with him. Without his love, this thesis would not have been possible. Finally, I wish to dedicate this thesis to my grandmother, my first teacher. She was an elementary school principal for 30 years. I learned not only knowledge from her but also an optimistic attitude for life. She passed away during my second year at MIT. I would like to dedicate this work in memory of her.

TABLE OF CONTENTS

1. INTRODUCTION

LIST OF FIGURES

LIST OF TABLES

Chapter 1

INTRODUCTION

1.1 Background

Nanocrystalline materials consist of nanometer-sized crystallites, which are unique because of their high surface-to-volume ratio and size-dependent properties. Techniques such as conventional melt-quenching, inert-gas condensation, spray pyrolysis and chemical precipitation have been developed to synthesize nanocrystalline materials.[1,2,3,4] Recently, the synthesis of nanocrystallites within a porous matrix has attracted a great deal of research attention for potential catalytic, magnetic, electronic, and optical applications.[5,6,7,8] Such matrix-mediated approach offers an effective means of tailoring the size, morphology and interfacial characteristics of the nanoclusters. The matrix pore structure and the cluster-matrix interaction play an important role in tailoring the properties and stability of the resulting nanocomposites.

Sol-gel processing and surfactant templating of inorganic materials can produce nanoporous materials with well-defined surface chemistry. Porous oxide matrices derived from the sol-gel route offer (i) a fairly narrow pore size distribution in the nanometer range that can be controlled by the wet chemical processing parameters, and (ii) a high thermal stability associated with the inorganic network structure. Although substantial progress has been made in the design of porous materials via sol-gel process, several challenges remain in the engineering of desirable matrix features for hosting guest molecules or clusters. Advances in this area could lead to the generation of novel stable nanocomposites with high dispersion of guest species. The objectives of this thesis are (i) to synthesize silica-based mesoporous supports using novel wet-chemical approaches, and (ii) to utilize silica matrices for hosting/encapsulating Fe-based compounds in magnetic and catalytic applications.

1.2 Sol-Gel Processing

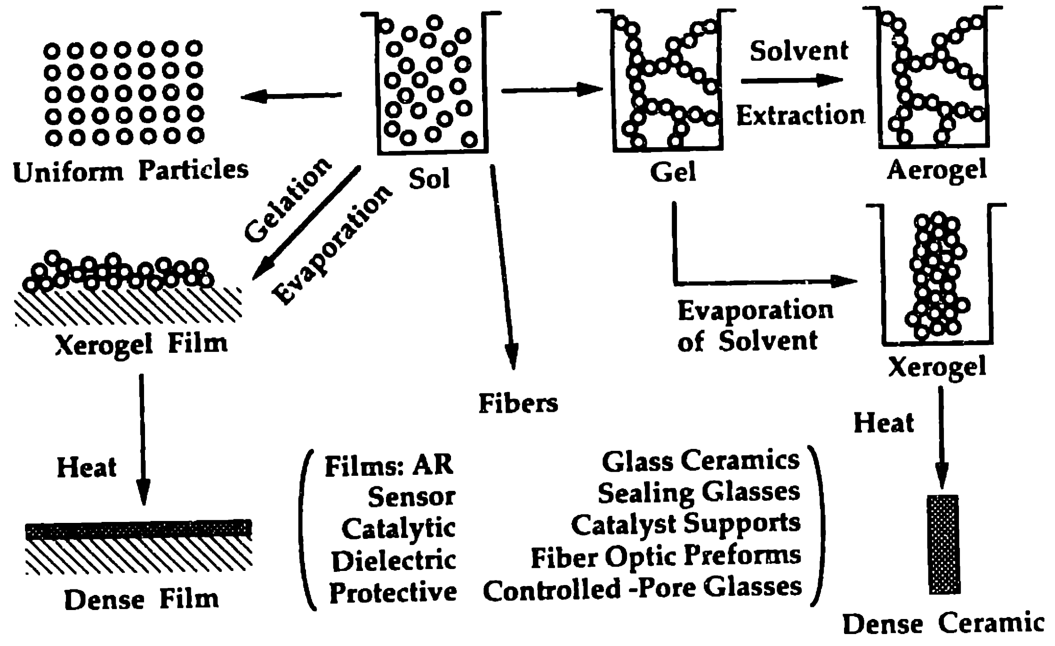

Figure 1.1. The overview of sol-gel process for various applications.[9]

Sol-gel processing is a useful low-temperature approach for preparing high-purity ceramics, glasses, thin films, fibers, oxide powders, and porous materials.[10] The various applications of sol-gel technique are presented schematically in Figure 1.1.[9] A porous oxide gel network can grow from an array of discrete colloidal particles, or be obtained from the hydrolysis and polycondensation reactions of a metal alkoxide precursor, M-$(OR)_x$, where R is an alkyl group (C_nH_{2n+1}). The alkoxide sol-gel processing of silica can be represented by the following reactions:

Hydrolysis:

$$\equiv \mathrm{Si}-\mathrm{OR} + \mathrm{H_2O} \underset{\text{esterification}}{\overset{\text{hydrolysis}}{\rightleftharpoons}} \equiv \mathrm{Si}-\mathrm{OH} + \mathrm{ROH} \tag{1.1}$$

Polycondensation:

$$\equiv\mathrm{Si{-}OR} + \mathrm{HO{-}Si}\equiv \;\underset{\text{alcoholysis}}{\overset{\substack{\text{alcohol}\\ \text{condensation}}}{\rightleftarrows}}\; \equiv\mathrm{Si{-}O{-}Si}\equiv + \mathrm{ROH} \tag{1.2}$$

$$\equiv\mathrm{Si{-}OH} + \mathrm{HO{-}Si}\equiv \;\underset{\text{hydrolysis}}{\overset{\substack{\text{water}\\ \text{condensation}}}{\rightleftarrows}}\; \equiv\mathrm{Si{-}O{-}Si}\equiv + \mathrm{H_2O} \tag{1.3}$$

During polycondensation, the formation of three-dimensional silicate network alters the rheological behavior of the system, and is affected by the sol composition , pH and reaction temperature. The structure of the material continues to change after gelation in a process called aging, which includes polycondensation, syneresis, coarsening, and phase transformation. Polycondensation increases the connectivity of the network and its fractal dimension. Syneresis involves the spontaneous shrinkage of the gel and the resulting liquid expulsion from the pores. Coarsening is a dissolution-reprecipitation process that results in an irreversible decrease in the surface area of the material. Time, temperature, and pH of the mother liquor are parameters that can substantially influence the aging process.

After aging, liquid is removed from the pore network in the drying step. Drying under the ambient condition will give rise to a xerogel. The shrinkage of the gel during aging and drying results from the ongoing condensation reaction between M-OH groups, and forces on the liquid-solid interface. Significant capillary stresses develop during solvent evaporation when the pore size is less than 20 nm. The resulting cracking problem can be alleviated by the use of either drying control chemical additives (DCCA) or supercritical drying. Gels prepared with DCCA such as oxalic acid, glycerol and formamide have a higher surface area than those processed without DCCA.[11] In supercritical drying, the pore liquid is extracted as a supercritical fluid so that the porous framework will be maintained without cracking during volatile removal, yielding a low-density aerogel.[12,13]

After drying, heat treatment is used to burn out volatile and organic species from a gel, and to initiate the densification process if desired. For the synthesis of porous matrices, pore collapse from sintering is to be avoided. In sol-gel processing, the microstructure of the final product can be tailored with controlled pore size distribution, pore volume and surface area for a variety of applications.

1.2.1 Advances in Sol-Gel Derived Materials as a Host Matrix

Sol-gel derived materials with high surface areas and controlled pore sizes are attractive as host matrices for applications in catalysis, chromatography, optics, biosensors and composites. Taking advantage of the low reaction temperature and the porous structure associated with sol-gel processing, inorganic dopants, organometallics, and salts of organic acids can be either introduced into the gel matrix during gelation, or anchored onto the gel surface through surface modification. Careful selection of modifying agents and reaction conditions can be used to control the dispersion and the morphology of guest clusters. Systems such as Fe_3O_4/SiO_2,[14] NiO/SiO_2, and NiO/Al_2O_3[15] have been prepared as supported catalysts by introducing Fe or Ni precursor to Si alkoxide prior to gelation. Silica gels containing copper or cobalt complexes have been examined for their interesting catalytic properties.[16,17] Attaching organometallic complexes of Ti, Ni, Zr, Nb, Hf, V, Cr, Mo, and W to the silica surface followed by oxidation-reduction have resulted in efficient catalysts for olefin polymerization.[18] The oxide gel surface can also be modified with certain organic polydentate ligands to change the interaction between the matrix and the guest species. Mizukami *et al.* reported using tartaric acid to produce a SiO_2 gel with a modified surface suitable for dispersion of Pt particles with controlled sizes.[19]

1.3 Surfactant-Templated Mesoporous Materials

By IUPAC definition, porous materials can be classified as microporous (pore diameter < 20 Å), mesoporous (20 Å < pore diameter < 500 Å), or macroporous (pore diameter > 500 Å).[20] Mesoporous materials are of interest for size-selective catalysis, gas separation, and electronic/optical applications. They may be synthesized by sol-gel processing, extraction, or pillaring of layered structures. Sol-gel derived materials usually undergo substantial pore shrinkage and collapse during drying. It is therefore a challenge to attain a precisely controlled pore structure in the mesoporous range via conventional sol-gel processing. A major breakthrough in the synthesis of mesoporous materials came about in 1992, when Mobil scientists announced the discovery of a novel silicate-based family of molecular sieves, termed M41S. These new mesoporous materials were derived via a surfactant templating approach. They possessed well-defined pore structures with uniform pore diameters of 2-10 nm, and surface areas > 1000 m^2/g.[21,22]

1.3.1 Pure Mesoporous Silica

Mesoporous silica can be derived from alkoxysilanes, fumed silica, sodium silicate solutions, tetramethylammonium silicates, and layered silicate kanemite.[23] Surfactants with different sizes, shapes, charges and functionalities have been used as templating agents. They are typically categorized as cationic, anionic or neutral surfactants. The synthesis condition can be varied from room temperature to 180 °C. Different mesostructure formation mechanisms have been proposed for M41S synthesis.[24-33]

1.3.1.1 Liquid-Crystal Templating Mechanism

The M41S materials were first produced under basic conditions via the charge interaction between a silica precursor and a cationic alkyltrimethylammonium surfactant

$(C_nH_{2n+1}(CH_3)_3NBr)$.[21] The resulting gel was heat treated for condensation of the silicate framework before it was washed and recovered by filtration. The surfactant was removed by calcination at 540 °C under N_2 or air. The pore size of the mesostructure could be controlled between 2 nm and 10 nm by varying the surfactant chain length (from C12 to C20) and by adding a swelling agent such as mesitylene. Three different mesostructures could be obtained by altering the surfactant-to-silica ratio: (i) a hexagonal array of cylindrical pores (space group P6m), (ii) a bicontinuous network of pores with cubic symmetry (Ia3d), and (iii) a lamellar phase with alternating sheets of silicate and surfactant (L) (see Figure 1.2).[24]

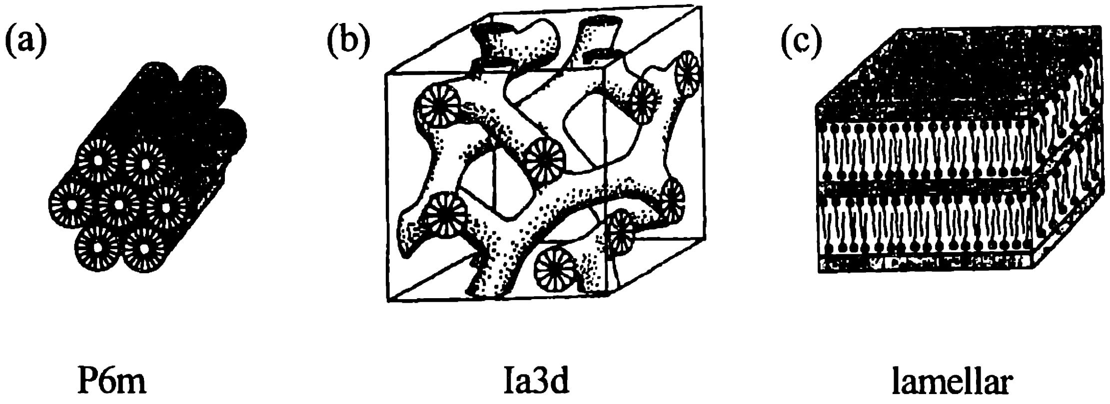

Figure 1.2. Mesostructures of M41S materials: (a) hexagonal phase, (b) cubic phase, and (c) lamellar phase.[25]

A liquid-crystal templating mechanism with two possible pathways was proposed for the formation of the hexagonal mesostructure termed MCM-41 (Figure 1.3).[26] In the first route, a hexagonal phase was initially formed from the self-assembly of surfactant molecules. A critical micelle concentration (CMC) was required to produce this liquid crystalline phase. The negatively charged silicate species were then polymerized around the preformed micellar rods by electrostatic interaction. This pathway might not be unique since mesoporous silica could be synthesized with surfactant concentrations well below CMC. In the second pathway, the silicate anions first interacted with the cationic surfactant head groups in the aqueous solution via charge balance. This silicate-surfactant charge interaction then directed the formation of the hexagonally-packed mesostructure. Chen *et al.* have provided evidence for MCM-41 formation via the second route with in-situ ^{14}N NMR studies.[27]

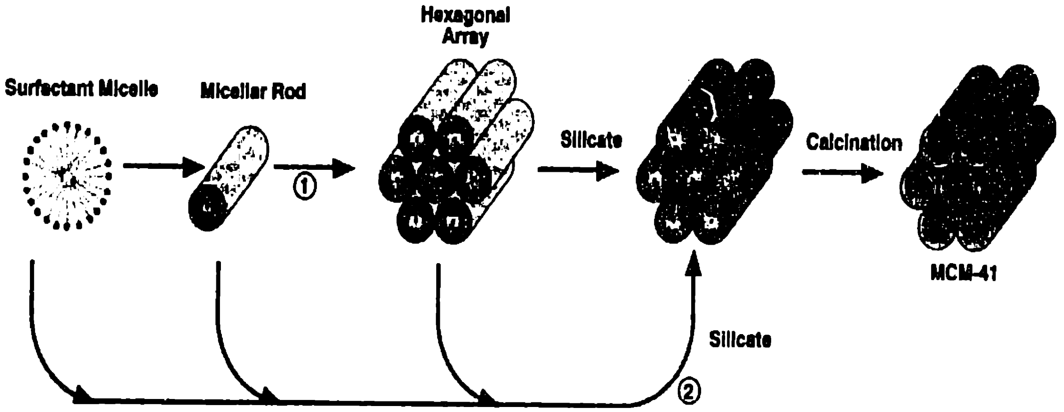

Figure 1.3. The proposed liquid-crystal templating mechanism for MCM-41 formation.[26]

1.3.1.2 Cooperative Assembly Mechanism

Mobil's liquid-crystal templating mechanism involved a strong electrostatic interaction between quaternary ammonium cationic surfactants (S^+) and anionic silicate species (I^-). The concept was further extended by Huo *et al.*[28,29] to cooperative organization pathways, which emphasized the interaction of species at the inorganic/organic interface without the existence of preformed surfactant arrays (see Figure 1.4). In the cooperative assembly mechanism, the multidentate inorganic species preferentially interacted with the hydrophilic head groups of the surfactants based on charge-density matching. During the cooperative nucleation, inorganic/organic arrays were formed depending on the ion-pair charge, geometry and Van der Waals forces. The condensation of silica then occurred between the neighboring inorganic species. In addition to charge balance of S^+I^-, charge matching of S^-I^+ could also be applied to direct the self-assembly of mesostructures, such as hexagonally-packed iron or lead oxides, and lamellar-structured lead and aluminum oxides.[28] Similarly charged inorganic species and surfactants could also self-assemble through mediating counterions ($S^+X^-I^+$ or $S^-X^+I^-$). Novel silicate mesostructures were achieved with cooperative assembly of cationic surfactants (S^+), halogen anions (X^-) and cationic silicate species (I^+) under acidic conditions (pH < 2). In contrast to synthesis under basic conditions, acidic synthesis could be conducted at room temperature in short durations with low surfactant concentrations. After the mesostructure was formed under acidic conditions, the surfactant could be easily removed by ethanol washing. The resulting mesoporous silica has thicker pore walls and a slightly positively-charged framework. By varying the surfactant concentration under acidic conditions, new mesostructured cubic phase (Pm3n) and 3-D hexagonal phase ($P6_3/mmc$) were obtained.[30]

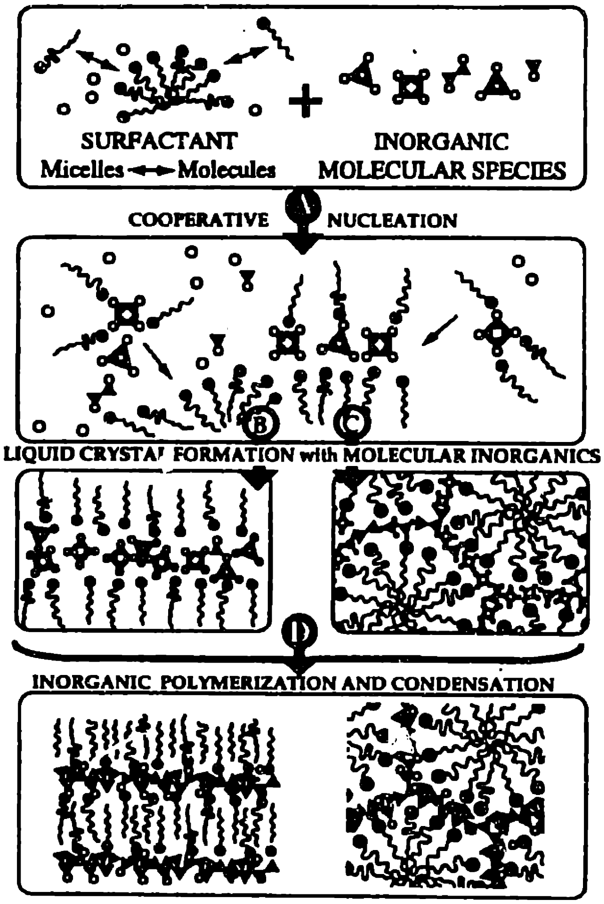

Figure 1.4. The charge-matching cooperative assembly mechanism.[28]

1.3.1.3 Neutral Templating Mechanism

A neutral surfactant templating route (S^oI^o) has been developed by Pinnavaia and coworkers for mesoporous materials synthesis.[31] This pathway was based on hydrogen-bonding interaction between neutral primary amine surfactants (S^o) and neutral

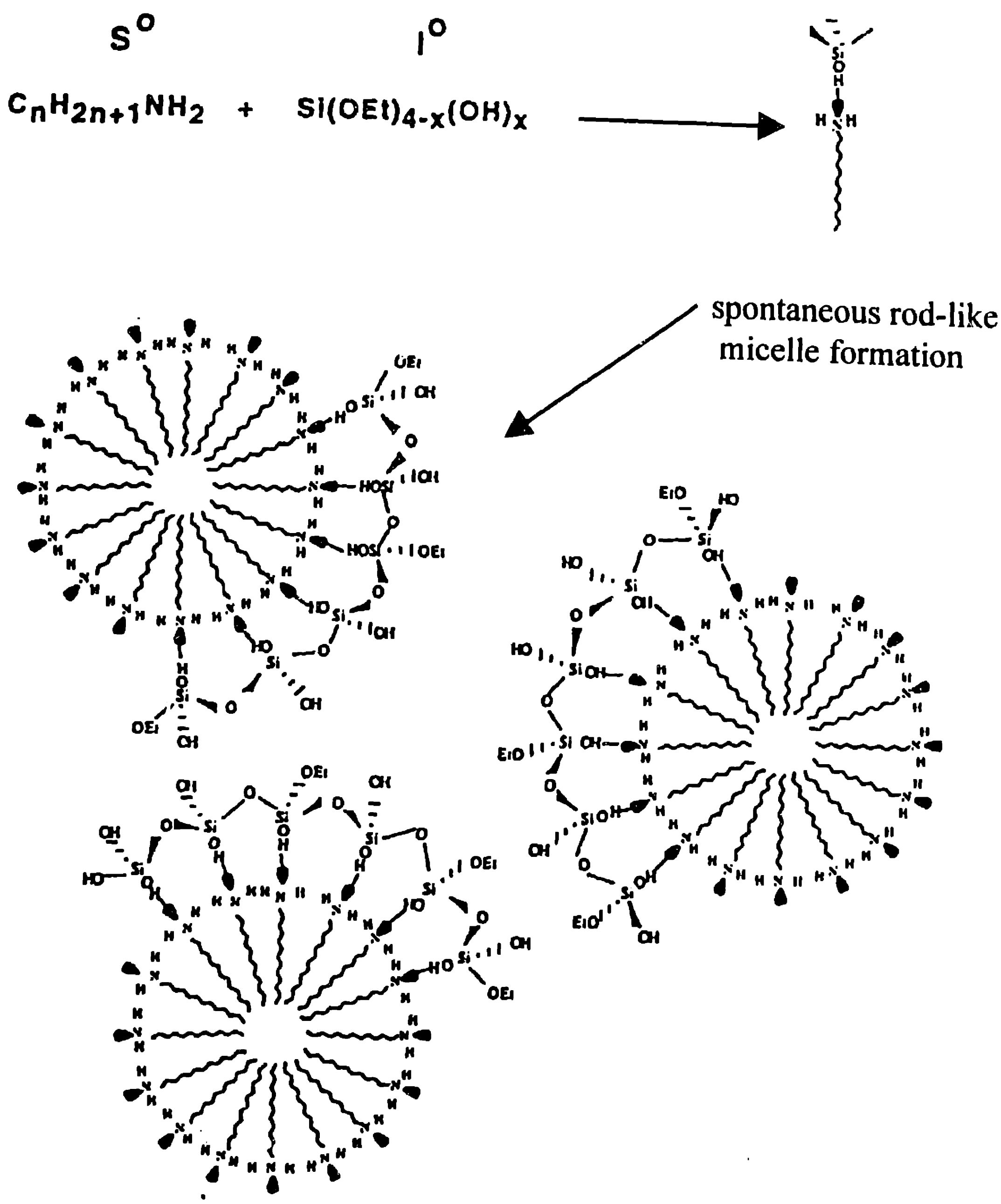

Figure 1.5. The neutral (S°I°) templating mechanism for mesoporous silica formation.[32]

hydrolyzed silicate precursors (I°). Rod-like micelles were spontaneously formed, and the silicate precursors were further hydrolyzed and condensed between the bulky surfactant head groups to induce the short-range hexagonal packing (see Figure 1.5).[32] This synthesis route produced mesoporous silica with thicker walls, smaller X-ray scattering domains and improved textural mesoporosity, compared to the mesoporous silicates prepared through electrostatic interactions. The lack of long-range packing order of pores could be attributed to the absence of charge interplay. A lamellar phase could also be produced using α,ω-dialkylamine surfactants.[33] It has further been demonstrated that non-ionic polyethylene oxide surfactants could act as effective hydrogen-bonding templating agents to produce mesostructures with worm-like pores.[34] This neutral templating pathway enabled low-temperature synthesis and surfactants removal by solvent extraction, which would be useful towards large-scale production of mesoporous materials.

1.3.1.4 Other Templating Routes

Polymeric surfactants have been successfully employed for the synthesis of hexagonally-packed mesoporous silica with large pore sizes of 7-15 nm.[35] Using a lyotropic polystyrene-polyethylene oxide solution, this templating approach involves the formation of a liquid crystalline phase that was responsible for directing the assembly of mesostructures.

Recently, a new 3-dimentional L_3 phase was obtained in lyotropic cetylpyridinium bromide solutions.[36] The pore size of this interconnected bilayer mesostructure could be controlled systematically between 6 nm and 35 nm by changing the solvent volume fraction. In addition, the pores of the resulting mesostructured silica were accessible without surfactant washes.

1.3.2 Mesoporous Doped Silica

Many applications can benefit from increased compositional flexibility of the well-defined mesoporous systems. For example, isomorphous substitution of silica with other metal dopants is an excellent strategy for creating (i) catalytically active sites and (ii) anchoring sites for catalytically active molecules in the design of new heterogeneous catalysts.

The amorphous framework of mesoporous MCM-41 silicates has a greater flexibility and capacity for incorporating dopants than the crystalline zeolitic framework. Mesoporous aluminosilicates could be easily synthesized.[21,22] Compared to aluminosilicate zeolites, the mesoporous systems offer size selectivity towards larger molecules and improved hydrothermal stability. Various synthetic efforts have been devoted to obtaining a high Al dopant concentration within the MCM-41 silica framework using a variety of aluminum precursors and synthesis conditions.[37,38,39]

Mesoporous Ti-substituted silicates were studied quite extensively due to their high activity in selective oxidation. Titanium alkoxide was used as a dopant source, and the synthesis could be achieved through both S^+I^- and S^oI^o routes.[40,41] Other heteroatoms incorporated in mesoporous silicates include B,[42] Ga,[43] V,[44,45] Cr,[46] Mn,[47] Fe,[48] Co,[49] Sn,[50] Zr,[51] Cs,[52] etc. Various techniques, such as Fourier-transform infrared (FTIR), ultraviolet-visible (UV-Vis), nuclear magnetic resonance (NMR) and electron paramagnetic resonance (EPR) spectroscopies, have been used to characterize the nature and the local environment of the dopants in the silicate framework.

1.3.3 Non-silicate Mesoporous Materials

The variable oxidation states associated with transition metal oxides are highly desirable for catalytic, electronic and magnetic applications. Earlier attempts to prepare mesoporous transition metal oxides through an electrostatic interaction between inorganic precursors and cationic surfactants have led to the formation of hexagonally-packed WO_3, PbO_2 and Fe_2O_3 mesostructures.[28,29,53] However, these mesostructures would collapse upon the removal of surfactants so that no stable porous structures could be obtained. The collapse of mesostructure might be attributed to the incomplete condensation of the transition metal precursors in these cases.

Two novel synthesis approaches were developed by Antonelli and Ying to achieve thermally stable hexagonally-packed mesoporous transition metal oxides. In the first method, a mesoporous hexagonally-packed titania was prepared with titanium isopropoxide bis-acetylacetonate and alkylphosphate surfactant.[54] The acetylacetone chelating agent helped to slow down the hydrolysis of titanium alkoxide, allowing for proper self-assembly to occur prior to gel formation. The calcined material, Ti-TMS1, has a surface area of ~200 m^2/g with residual phosphate species on the titania pore walls.

The second approach operated through a ligand-assisted templating (LAT) mechanism, which involved the covalent bonding of the surfactant head group to the metal alkoxide precursor prior to the addition of water. Mesoporous niobium oxide (Nb-TMS1) and tantalum oxide (Ta-TMS1) have been successfully prepared with the formation of N-metal bonds between amine surfactants and alkoxide precursors.[55,56,57] A surfactant-free mesoporous material could be obtained by acidic alcohol washes. A high surface area Zr-TMS1 (560 m^2/g) was also synthesized through the LAT mechanism with zirconia n-propoxide and phosphate surfactant for acid catalysis.[58]

The high surface area, well-defined pore structure, and flexible composition make mesoporous materials ideally suited for a variety of catalytic applications. Compared to zeolitic materials that have pore sizes less than 2 nm, the mesoporous systems with 2-10 nm pore sizes facilitate diffusion of bulky molecules. They can be used as catalysts or catalytic supports, and have been examined for acid and base catalysis, selective oxidation, polymerization, fine chemical synthesis and environment catalysis.

1.4 Matrix-Mediated Synthesis of Magnetic Nanoclusters

Well-dispersed, mono-sized nanoclusters can serve as model systems for studying the electronic, magnetic and optical properties of quantum-confined materials. Below a critical size, magnetic particles form single domains in zero applied field, and demonstrate superparamagnetism and quantum tunneling of magnetization.[59,60,61] Compared to semiconducting clusters, quantum-size effects in magnetic clusters are further complicated by the internal magnetic order of the electronic spins and sharp magnetic discontinuities at the surface. The manipulation of quantum-size effects in magnetic nanoclusters, and the means to control and stabilize different spin configurations would be important to the integration of micromagnetics with microelectronics. An effective synthesis strategy would enable us to achieve a fundamental understanding of magnetic nanoclusters, and lead to significant advances in the application of nanoclusters towards biomineralization processes, information storage, magnetic refrigeration, and magnetic resonance imaging enhancement.[62,63,64]

Most nanocrystalline magnetic materials involve metallic iron, iron oxide, iron nitride or iron alloy. They have been produced via physical routes, such as inert gas condensation, microwave plasma deposition, and melt-quench technique. The major challenges in the production of high-quality nanocrystalline materials include reduction of grain size and control of morphology. Recent studies have exploited chemical routes to prepare and isolate nanoclusters using an inert matrix. These processes have been referred to as matrix-mediated synthesis.[65] Examples of such approach include deposition of semiconducting clusters in zeolite cages,[66] self-assembly and cluster encapsulation by terminal ligation,[67,68] and growth of magnetic nanophases within protein cages.[69] The magnetic properties of nanoclusters embedded in a matrix are dependent on the host structure, as well as the volume fraction and crystallite size of the magnetic clusters.

The key to matrix-mediated synthesis is to control the interactions between the host material and the guest species so that a high cluster dispersion is achieved uniformly within the matrix. The pore structure of the matrix and the host-guest interaction can be used to control the size, morphology, and stability of the nanoclusters. The matrix can be an organic polymer or inorganic membrane, a porous gel, or a zeolitic material. Nanometer-sized γ-Fe_2O_3 particles have been synthesized in a network of cross-linked sulfonated polystyrene/divinylbenzene polymer via ion-exchange and a precipitation reaction.[65] The iron oxide nanocrystals exhibited unique superparamagnetic properties and were optically transparent. An electrically conducting polymer, polypyrrole, has been used as a host matrix for the preparation of magnetic nanoparticles with the following reaction scheme:[70,71]

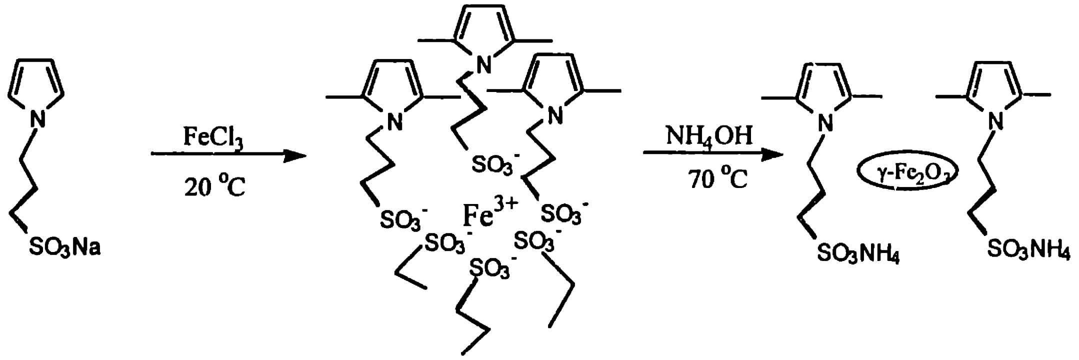

(1.4)

The polymer network's interaction with the Fe^{3+} precursor was based on charge balance. Magnetic oxide particles in conducting matrices could be used in batteries, electrochromic devices, and electromagnetic interference shielding.

Zeolites are crystalline aluminosilicate molecular sieves with uniform pore structures. The channel opening, which ranges from 0.3 nm to 2.0 nm, depends on the type of zeolite, the cations present, and the nature of the treatment that the material has received (e.g. calcination and leaching). Composites of metal clusters and zeolites have been used as catalysts for Fischer-Tropsch synthesis of hydrocarbons from CO and H_2.[72] The guest metal or metallic complex, such as $Fe(CO)_5$, was introduced into the cavities of the zeolite and reduced to a zero-valent oxidation state to form active catalytic species. HY-zeolites have been successfully used as supports for highly dispersed iron particles.[73] The analogous cobalt and nickel clusters in zeolites have also been reported.[74,75] Small metallic clusters in zeolite matrices have demonstrated superparamagnetic behavior.

Although polymers and zeolites were used first as hosts in matrix-mediated synthesis of nanocrystals, a number of drawbacks exist in both types of matrix structures. Polymer matrices suffer from low thermal stability, high elasticity, and a broad pore size distribution due to random cross-linking. The channel diameters of zeolites are well under 20 Å, so that mass transfer is governed by configurational diffusion. The micropores of this type of matrix may not be accessible to bulky reactant molecules.

Sol-gel derived matrices were recently used to prepare nanocrystalline magnetic materials. Sol-gel derived systems present a thermally stable mesoporous structure. Among the different oxides, silica has been the most widely studied. Roy and Chakravorty have prepared nanometer-sized iron particles in a silica glass by hot pressing a suitably reduced precursor gel powder.[76] In their synthesis, $Fe(NO_3)_3{\cdot}9H_2O$ and tetraethoxysilane were used as precursors, the resultant iron particles have diameters in the range of 3.8-10.2 nm. The electrical resistivity of the samples might be changed by four orders of magnitude depending on the particle size. The variation in electrical resistivity could be explained by electron tunneling between metal islands. Shull *et al.* found that Fe-silica nanocomposites underwent a change in magnetic states when the gels were subjected to different thermal histories.[77] This gave rise to a way of converting the magnetic particles from the superparamagnetic state at room temperature to the ferromagnetic state by chemical treatment of as-prepared samples at elevated temperatures.

Mobil's development of mesoporous silicate-based MCM-41 presents a new host material for the matrix-mediated synthesis of nanoclusters. The regular array of cylindrical channels with controlled wall thickness is ideal for the modification of electronic and magnetic behavior on the nanometer scale. By varying the pore size as well as the composition and thickness of the pore wall, a tunable quantum well can be fabricated. In addition to synthesis of magnetic nanoclusters, one-dimensional continuous growth of clusters along the channels can lead to formation of quantum wires. Conducting polyaniline filaments have been formed inside the channels of copper- or iron-exchanged MCM-41 by an in-situ oxidative adsorption and polymerization of monomeric aniline.[78] The DC conductivity of the encapsulated molecular wires was more than 7 orders of magnitude lower than that of bulk polyaniline. A significant low-field conductivity indicated that the confined polymer still supported mobile charge carriers. Germanium wires have also been obtained by vapor phase epitaxial deposition onto the pore walls of MCM-41 matrix.[79] However, TEM studies showed that the hexagonally-packed mesopores were only partially filled with germanium semiconducting wires via such approach.

In this thesis, porous matrices were developed via modified sol-gel processing and surfactant templating routes to exploit the flexibility in the synthetic chemistry of these approaches for tailoring microstructure, surface chemistry and thermal stability. The goal was to design and derive silica-based host materials that could provide a greater control in the size, morphology, and dispersion of Fe-based nanoclusters and complexes for magnetic and catalytic applications.

1.5 Alkene Epoxidation and Alkane Hydroxylation with Supported Metalloporphyrin Catalysts

Catalysts are used in over 90% of the processes in fine chemical and petroleum refining industries. Of particular interest to this thesis is the development of novel supported catalysts for the epoxidation of alkenes and the hydroxylation of alkanes. Products of these reactions are highly demanded chemicals. For example, products of lower alkenes epoxidation are the raw materials or intermediates for the synthesis of polyurethanes, polyesters, and alkanoamines.[80] Certain catalytic epoxidation and hydroxylation processes are also convenient model reactions for the study of enzymatic oxidation reactions that play a key role in various biological functions.[81]

Catalytic epoxidation and hydroxylation can be carried out at ambient conditions with high activity and chemoselectivity using transition metal complexes. Examples of conventional catalysts include homogeneous metalloporphyrins, cationic manganese complexes of bis-Schiff base, and metal-macrocyclic polyamine complexes.[82] All of these catalysts require a mono-oxygen source such as hydrogen peroxide, tert-butyl hydroperoxide, sodium hypochlorite, or iodosobenzene. Investigations of these catalyst systems have been focused on the mechanism of oxidation, the nature of active oxidant, and the controlling factors for selectivity.[83] The main challenges in producing such catalysts in large-scale synthesis have not been addressed. These expensive catalysts undergo auto-oxidation easily, losing their active sites over time. The recovery and re-use of such homogeneous systems are further hampered by costly separation processes.

Recent trends in improving metalloporphyrin-based catalysts included developing supported systems that would effectively avoid auto-oxidation through a physical separation of active sites, and provide an easy means of catalysts recovery. Metalloporphyrins could be anchored onto a support by covalent binding, coordinative bonding, ionic interactions, and intercalation. The support materials examined varied from insoluble polymers to inorganic substrates such as silica or zeolites.

Surface-modified polystyrene ion-exchange resin has been used as a support for iron (III) tetraarylporphyrins.[84] These supported catalysts demonstrated significantly different behavior from the homogeneous catalysts in cyclohexene oxidation. Epoxidation selectivity was improved by increasing the cross-linking of the resin support. Allylic oxidation resulting from the radical auto-oxidation could be suppressed by carrying out the reaction under nitrogen. A cationic ion-exchange resin, poly(vinylpyridinium), has been employed for supporting sulfonated manganese and iron porphyrins for alkene epoxidation.[85] The coordination between the metalloporphyrins and the support provided a proximal effect, which involved a strong coordination of a basic ligand to the metal center of the porphyrin that enhanced both the metal-oxo formation and oxygen transfer steps. The interaction between the sulfonated metalloporphyrins and the polymer matrix immobilized the active complexes to a greater extent than the simple electrostatic interaction between metalloporphyrins and amberlite-type resins. The supported sulfonated metalloporphyrins gave an activity similar to the corresponding homogeneous metalloporphyrin complexes.

In contrast to the polymer supports, inorganic supports have the added benefits of thermal stability and controlled microstructure. Imidazole-modified silica (Si-Im) has been employed as a support for various metalloporphyrin catalysts.[86,87] All complexes were mono-ligated on Si-Im, but the slow diffusion of reactants and products to and from the complexes in the pores of silica resulted in low reaction rates. Encapsulation of the metal complexes in the supercage of zeolites X and Y based on ship-in-a-bottle synthesis has led to catalytic epoxidation of cyclohexene without the undesired auto-oxidation effects.[88] A new catalytic composite system, which mimicked cytochrome P-450, involved iron phthalocyanine complexes encapsulated in zeolite Y crystals that were embedded in a polydimethysiloxane membrane.[89] This catalyst showed a 300-fold increase in activity for cyclohexane oxidation with tert-butyl hydroperoxide compared to the regular zeolite-supported catalysts.

Catalytic organometallic complexes can also be anchored onto the internal surface of mesoporous materials. The large pore diameter of the mesostructure provides sufficient space to host the large catalytic complexes, and facilitates diffusion of reactants and products. Liu *et al.* first reported the immobilization of iron phenanthroline chloride on Al-MCM-41 for hydroxylation of phenol using H_2O_2 as an oxidant.[90,91] A higher conversion was obtained with the Al-MCM-41 supported system than the homogeneous counterpart. Kim *et al.* reported the incorporation of manganese (II) bipyridine complex in Al-MCM-41 for the oxidation of styrene.[92] The product selectivity greatly depended on the size of the oxidant due to steric restrictions. Because of the weak electrostatic interaction between the catalyst and the support in this case, significant amounts of catalyst leaching occurred during the reaction. In order to improve the fixation of catalysts, ruthenium porphyrins were covalently bonded to the surface of MCM-41 by modifying the support surface with 3-aminopropyltriethoxysilane.[93] The resulting heterogeneous catalyst showed high activity and selectivity in epoxidation of various alkenes, such as cyclohexene, styrene, cyclooctene, norbornene, cis-stilbene, and trans-stilbene. Surface modification approach was also used to prepare two supported Mn complex catalysts.[94,95] Sutra and Brunel first modified the MCM-41 surface with 3-chloropropylsilane that can react with a Schiff-base ligand (3-[N,N''-Bis-3-(3,5-di-tert-butylsalicylidenaminopropyl]amine). The Mn(II)$(acac)_2$ was then introduced into the channels of the support, and oxidized. The second catalyst was prepared by the immobilization of manganese trizacyclononane on a glycidylated MCM-41 support. Both catalysts presented a good activity in the epoxidation of cyclohexene and styrene.

From the above review of catalysts development for alkene epoxidation and alkane hydroxylation, we see that the design of heterogeneous catalysts has been focused on controlling the interaction between active metal complexes and their supports. This thesis describes the design of metal-doped mesoporous matrices for this purpose. The mesoporous support can provide a unique interaction with the metal complexes through its surface dopants. The local catalytic environment and diffusion characteristics can also be modified by fine tuning the pore size of the matrix material.

1.6 Research Motivation

The overall objective of this thesis was to gain a fundamental understanding of the processing chemistry, structure and properties of novel nanocomposites derived via matrix-mediated synthesis. Specifically, we have developed Fe-based nanoclusters and complexes within silica-based matrices for magnetic and catalytic applications.

For magnetic studies, our research has focused on devising various matrix-mediated synthesis strategies to create and stabilize superparamagnetic γ-Fe_2O_3 nanoclusters. One of the goals was to gain an understanding of the size-dependent surface and strain effects that influence the overall magnetic behavior and optical properties of the single-domain particles. Cluster size, shape and morphology were systematically manipulated via the matrix microstructure, cluster synthesis conditions and heat treatment.

The thesis has also examined the encapsulation of iron porphyrin catalysts in hexagonally-packed mesoporous metal-doped silicate matrices for epoxidation and hydroxylation reactions. The synthetic chemistry in these matrix-mediated synthesis routes, which was governed by precursor reactivity, sol composition, catalyst/pH, and reaction temperature, was investigated and optimized to correlate the structure of the support with the catalytic properties of the heterogenized systems.

1.7 References

[1] D. Chakravorty, A. K. Bandyopadhyay, and V. K. Nagesh, J. Phys. D: Appl. Phys., **10**, (1977) 2077.

[2] M. R. Zachariah, M. J. Aquino, R. D. Shull, and E. B. Steel, Nanostr. Mater., **5**, (1995) 383.

[3] A. Gurav, T. Kodas, T. Pluym, and Y. Xiong, Aerosol Sci. Technol., **19**, (1993) 411.

[4] E. Tronc and J. P. Jolivet, in *Nanophase Materials: Synthesis-Properties-Applications*, edited by G. C. Hadjipanayis and R. W. Siegel, Kluwer, Boston, (1994) 21.

[5] H. Gleiter, Prog. Mater. Sci., **33**, (1989) 223.

[6] R. P. Andres, R. S. Averback, W. L. Brown, L. E. Brus, W. A. Goddard, III, A. Kaldor, S. G. Louie, M. Moscovits, P. S. Peercy, S. J. Riley, R. W. Siegel, F. Spaepen, and Y. Wang, J. Mater. Res., **4**, (1989) 704.

[7] R. W. Siegel, in *Physics of New Materials*, edited by F. E. Fujita, Springer, Berlin, (1994) 65.

[8] C. Suryanarayana, Inter. Mater. Rev., **40**, (1995) 41.

[9] C. J. Brinker and G. W. Scherer, *Sol-Gel Science: The Physics and Chemistry of Sol-Gel Processing*, Academic Press, New York, (1989).

[10] L. L. Hench and J. K. West, Chem. Rev., **90**, (1990) 33.

[11] J. Y. Ying, Ph.D. Thesis, Princeton University, Princeton, (1991).

[12] L. C. Klein, Rev. Mater. Sci., **15**, (1985) 227.

[13] D. W. Schaefer, MRS Bulletin, **Apr.**, (1994) 49.

[14] F. Blanchard, B. Pommierm, J. P. Reymond, and S. J. Teichner, in *Preparation of Catalysts III: Scientific Bases for the Preparation of Heterogeneous Catalysts*, edited by G. Poncelet, P. Grange, and P. A. Jacobs, Elsevier, Amsterdam, (1983) 395.

[15] A. Sayari, A. Ghorbel, G. M. Pajonk, and S. J. Teichner, Bull. Soc. Chim. Fr., (1981) I-2, I-7, I-16.

[16] J. P. Carpenter, C. M. Lukehart, H. R. Stock, and J. E. Witting, Chem. Mater., **7**, (1995) 201.

[17] J. Yan, A. M. Buckley, and M. Greenblatt, J. Non-Cryst. Solids, **180**, (1995) 180.

[18] Y. I. Yermakov, B. N. Kuznetsov, and V. A. Zakharov, *Catalysis by Supported Complexes*, Elsevier, Amsterdam, (1981) 13.

[19] F. Mizukami, F. Taniguchi, Y. Kiyozumi, and A. Kobayashi, Adv. Mater., **6**, (1994) 858.

[20] K. S. W. Sing, D. H. Everett, R. A. W. Haul, L. Moscou, R. A. Pierotti, J. Rouquerol, and T. Siemieniewska, Pure Appl. Chem., **57**, (1985), 603.

[21] C. T. Kresge, M. E. Leonowicz, W. J. Roth, J. C. Vartuli, and J. S. Beck, Nature, **359**, (1992) 710.

[22] C. T. Kresge, M. E. Leonowicz, W. J. Roth, J. C. Vartuli, and J. S. Beck, US Patent No. 5,098,684, (1992).

[23] T. Yanagisawa, T. Schumizu, K. Kiroda, and C. Kato, Bull. Chem. Soc. Jpn., **63**, (1990) 988.

[24] J. C. Vartuli, K. D. Schmitt, C. T. Kresge, W. J. Roth, M. E. Leonowicz, S. B. McCullen, S. D. Hellring, J. S. Beck, J. L. Schlenker, D. H. Olsen, and E. W. Sheppard, Chem. Mater., **6**, (1994) 2317.

[25] N. K. Raman, M. T. Anderson, and C. J. Brinker, Chem. Mater., **8**, (1996) 1682.

[26] J. S. Beck, J. C. Vartuli, W. J. Roth, M. E. Leonowicz, C. T. Kresge, K. D. Schmitt, C. T.-W. Chu, D. H. Olsen, E. W. Sheppard, S. B. McCullen, J. B. Higgins, and J. L. Schlenker, J. Am. Chem. Soc., **114**, (1992) 10834.

[27] C.-Y. Chen, S. L. Burkett, H.-X. Li, and M. E. Davis, Microporous Mater., **2**, (1993) 27.

[28] Q. Huo, D. I. Margolese, U. Ciesla, D. G. Demuth, P. Feng, T. E. Gier, P. Sieger, A. Firouzi, B. F. Chmelka, F. Schüth, and G. D. Stucky, Chem. Mater., **6**, (1994) 1176.

[29] Q. Huo, D. I. Margolese, U. Ciesla, P. Feng, T. E. Gier, P. Sieger, R. Leon, P. M. Petroff, F. Schüth, and G. D. Stucky, Nature, **368**, (1994) 317.

[30] Q. Huo, D. I. Margolese, and G. D. Stucky, Chem. Mater., **8**, (1996) 1147.

[31] P. T. Tanev and T. J. Pinnavaia, Science, **267**, (1995) 865.

[32] P. T. Tanev and T. J. Pinnavaia, in *Access in Nanoporous Materials*, edited by T. J. Pinnavaia and M. F. Thorpe, Plenum Press, New York, (1995) 13.

[33] P. T. Tanev and T. J. Pinnavaia, Science, **271**, (1996) 1267.

[34] S. A. Bagshaw, E. Prouzet, and T. J. Pinnavaia, Science, **269**, (1995) 1242.

[35] C. G. Göltner and M. Antonietti, Adv. Mater., **9**, (1997) 431.

[36] K. M. McGrath, D. M. Dabbs, N. Yao, I. A. Aksay, and S. M. Gruner, Science, **277**, (1997) 552.

[37] Z. Luan, C.-F. Cheng, W. Zhou, and J. Klinowski, J. Phys. Chem., **99**, (1995) 1018.

[38] G. Fu, C. A. Fyfe, W. Schwieger, and G. T. Kokotailo, Angew. Chem. Int. Ed. Engl., **34**, (1995) 1499.

[39] R. Ryoo, C. H. Ko, and R. F. Howe, Chem. Mater., **9**, (1997) 1607.

[40] A. Corma, M. T. Navarro, and J. Perez Pariente, J. Chem. Soc., Chem. Commun., (1994) 147.

[41] P. T. Tanev, M. Chibwe, and T. J. Pinnavaia, Nature, **368**, (1994) 321.

[42] A. Sayari, C. Danumah, I. L. Moudrakouski, A. I. Ratcliffe, J. A. Ripmeester, and K. F. Preston, J. Phys. Chem., **99**, (1995) 16373.

[43] C. F. Cheng, H. He, W. Zhou, J. Klinowski, J. A. Sousa Gonçalves, and L. F. Gladden, J. Phys. Chem., **100**, (1996) 390.

[44] K. M. Reddy, I. L. Moudrakouski, and A. Sayari, J. Chem. Soc., Chem. Commun., (1994) 1059.

[45] J. S. Reddy and A. Sayari, J. Chem. Soc., Chem. Commun., (1995) 2231.

[46] W. Zhang, J. Wang, P. T. Tanev, and T. J. Pinnavaia, Chem. Commun., (1996) 979.

[47] D. Zhao and D. Goldfarb, J. Chem. Soc., Chem. Commun., (1995) 875.

[48] Z. Y. Yuan, S. Q. Liu, T. H. Chen, Z. J. Wang, H. X. Li, J. Chem. Soc., Chem. Commun., (1995) 973.

[49] W. A. Carvaiho, P. B. Varaldo, M. Wallau, and U. Schuchardt, Zeolites, **18**, (1997), 408.

[50] T. K. R. Das, K. Chaudhari, A. J. Chandwadkar, and A. Sivasanker, J. Chem. Soc., Chem. Commun., (1995).

[51] S. Gontier and A. Tuel, Appl. Catal., **143**, (1996) 125.

[52] R. K. Kloetstra and H. Van Bekkum, J. Chem. Soc., Chem. Commun., (1995) 1005.

[53] U. Ciesla, D. Demuth, R. Leon, P. Petroff, G. D. Stucky, K. Unger, and F. Schüth, J. Chem. Soc., Chem. Commun., (1994) 1387.

[54] D. M. Antonelli and J. Y. Ying, Angew. Chem. Int. Ed. Engl., **34**, (1995) 2014.

[55] D. M. Antonelli and J. Y. Ying, Angew. Chem. Int. Ed. Engl., **35**, (1995) 426.

[56] D. M. Antonelli, A. Nakahira, and J. Y. Ying, Inorg. Chem., **35**, (1996) 3126.

[57] D. M. Antonelli and J. Y. Ying, Chem. Mater., **8**, (1996) 874.

[58] M. S. Wong, D. M. Antonelli, and J. Y. Ying, Nanostr. Mater., **9**, (1997) 165.

[59] S. Chikazumi, *Physics of Magnetism*, Wiley, New York, (1964).

[60] C. G. Granqvist and O. Humderi, Phys. Rev. B, **16**, (1977) 3513.

[61] L. Gunther, in *Magnetic Properties of Fine Particles*, edited by J. L. Dormann and D. Fiorani, Elsevier, North-Holland, (1991) 213.

[62] S. Mann, Nature, **365**, (1993) 499.

[63] J. C. Parker and R. W. Siegel, Nanostr. Mater., **1**, (1992) 53.

[64] R. D. Shull and L. E. Bennett, Nanostr. Mater., **1**, (1992) 83.

[65] R. F. Ziolo, E. P. Giannelis, B. A. Weinstein, M. P. O'Horo, B. N. Ganguly, V. Mehrotra, M. W. Russell, and D. R. Huffman, Science, **257**, (1992) 219.

[66] G. D. Stucky and J. E. MacDougall, Science, **247**, (1990) 669.

[67] J. F. You, B. S. Snyder, G. C. Papaefthymiou and R. H. Holm, J. Am. Chem. Soc., **112**, (1990) 1064.

[68] G. D. Stucky, Naval Res. Rev., **43**, (1991) 28.

[69] F. C. Meldrum, B. R. Heywood, and S. Mann, Science, **257**, (1992) 522.

[70] M. T. Nguyen and A. F. Diaz, Adv. Mater., **6**, (1994) 858.

[71] G. Bidan, O. Jarjayes, J. M. Fruchart, and E. Hannecart, Adv. Mater., **6**, (1994) 152.

[72] T. Bein, G. Schmiester, and P. A. Jacobs, J. Phys. Chem., **90**, (1986) 4851.

[73] J. B. Nagy, M. V. Eenoo, and E. G. Derouane, J. Catal., **58**, (1979) 230.

[74] R. L. Schneider, R. F. Howe, and K. L. Watter, Inorg. Chem., **23**, (1984) 4600.

[75] E. G. Derouane, J. B. Nagy, and J. C. Vedrine, J. Catal., **61**, (1980) 39.

[76] S. Roy and D. Chakravorty, J. Mater. Res., **9**, (1994) 2314.

[77] R. D. Shull, J. J. Ritter, and L.J. Swartzendruber, J. Appl. Phys., **69**, (1991) 5144.

[78] C.-G Wu and T. Bein, Chem. Mater., **6**, (1994) 1109.

[79] R. Leon, D. Margolese, G. D. Stucky, and P. M. Petroff, Phys. Rev. B, **52**, (1995) 2285.

[80] E. J. Mistrik, Chem. Tech. (Leipzig), **27**, (1975) 23.

[81] S. M. May, R. D. Schwartz, B. J. Abbott, and O. R. Zaborsky, Biochim. Biophys. Acta, **403**, (1975) 245.

[82] C. L. Hill, *Activation and Functionalization of Alkanes,* Wiley, New York, (1989).

[83] B. Meunier, *Chem. Rev.*, **92**, (1992) 1411.

[84] D. R. Leanord and J. R. L. Smith, J. Chem. Soc., Perkin Trans., **2**, (1990) 1917.

[85] S. Campestrini and B. Meunier, Inorg. Chem., **31**, (1992) 1999.

[86] P. R. Coke and J. R. L. Smith, J. Chem. Soc. Perkin Trans., **1**, (1994) 1913.

[87] P. R. Coke and J. R. L. Smith, Tetrahedron Lett., **33**, (1992) 2737.

[88] P. P. Knops-Gerrits, D. D. Vos, F. Thibault-Starzyk, and P. A. Jacobs, Nature, **369**, (1994) 543.

[89] R. F. Parton, I. F. J. Vankelecom, M. J. A. Casselman, C. P. Bezoukhanova, J. B. Uytterhoeven, and P. A. Jacobs, Nature, **370**, (1994) 541.

[90] C. Liu, X. Ye, and Y. Wu, Catal. Lett., **36**, (1996) 263.

[91] C. Liu, Y. Shan, X. Yang, X. Ye, and Y. Wu, J. Catal., **168**, (1997) 35.

[92] S.-S. Kim, W.-Z. Zhang, and T. J. Pinnavaia, Catal. Lett., **43**, (1997) 149.

[93] C.-J. Liu, S.-G. Li, W.-Q. Pang, and C.-M. Che, Chem. Commun., (1997) 65.

[94] P. Sutra and D. Brunel, Chem. Commun., (1996) 2485.

[95] Y. V. S. Rao, D. E. De Vos, T. Bein, and P. A. Jacobs, Chem. Commun., (1997) 355.

Chapter 2

SYNTHESIS AND MAGNETIC PROPERTIES OF γ-Fe_2O_3 NANOCLUSTERS IN SOL-GEL DERIVED SULFONATED-SILICA MATRIX

2.1 Introduction

Surface functionalization of a porous matrix, such as silica gel, provides a wide range of synthesis possibilities in the design of nanocrystalline materials and mesostructured catalysts. Silica gels are commonly synthesized from silicon alkoxides or colloidal silica by sol-gel method. To introduce surface functionalization in silica sol-gel processing, organotrialkoxysilanes (R'Si(OR)$_3$) can be used as precursors, where R' represents a non-hydrolyzable organic substituent. Such precursor molecules react through the alkoxy groups (-OR) to form the silica gel network, and the uncondensed R' group can be modified separately for further functionalization.

Sulfonated polymer networks, such as polystyrene ion-exchange resin, have been used to host iron oxide nanoclusters, but they suffer from low thermal stability.[1] In this chapter, we have synthesized a porous silicate matrix functionalized with surface sulfite (SO_3^-) groups by a modified sol-gel process for use as an inorganic host material for iron oxide nanoclusters.[2] The unique interaction between the functionalized inorganic gel matrix and highly dispersed nanoclusters generates a thermally stable Fe_2O_3/sulfonated-SiO_2 nanocomposite. To elucidate the relationship between processing, microstructure and properties of Fe_2O_3/sulfonated-SiO_2 nanocomposite, we have studied the magnetic characteristics of this system with superconducting quantum interference device (SQUID) magnetometry and Mössbauer spectroscopy.

2.2 Synthesis and Characterization of Sulfonated-Silica Gel

2.2.1 Preparation of Sulfonated-Silica Gel

The target matrix material is a SiO_2-based gel containing organo-SO_3^- groups that provides an ion-exchange capability. There are a number ways to attach the SO_3^- group onto the silica network. However, the choice of sulfonation method is limited by the compatibility of the sulfonate precursor with the organotrialkoxysilane, and to reaction conditions that would not disrupt subsequent silica gel formation. We have utilized a nucleophilic displacement reaction of alkyl halide with sodium sulfite (Na_2SO_3) or sodium bisulfite ($NaHSO_3$), which produced a high yield of sulfonic acid salts in aqueous ethanol solution under refluxing condition.[3] This method has mild reaction conditions and great compatibility with sol-gel precursors.

To synthesize such an organically modified silica, alkylation of alkali sulfites or bisulfite was employed. Typically, 3-bromopropyltrimethoxysilane [$(MeO)_3SiCH_2CH_2CH_2Br$] (United Chemical) was used as the precursor. The bromide group in this precursor allows for sulfonation with $NaHSO_3$ or Na_2SO_3 (Aldrich), and the methoxy groups can undergo hydrolysis and polycondensation in the sol-gel reaction to form an inorganic polymer gel. $(MeO)_3SiCH_2CH_2CH_2Br$ was dissolved in methanol (MeOH) and added dropwise to the vigorously-stirred aqueous $NaHSO_3$ or Na_2SO_3 solution. A molar ratio of $(MeO)_3SiCH_2CH_2CH_2Br$: MeOH : $NaHSO_3$ or Na_2SO_3 : H_2O of 1:4:1.5:8 was used. The reactants were kept at 75 °C for 3 hours, after which 0.01 M HCl was added until pH = 1.5 to catalyze hydrolysis for 1.5 hr. Condensation was subsequently catalyzed by the addition of 0.01 M NH_4OH solution until pH = 8.5. The gel obtained was aged at room temperature for 3-7 days and dried at ambient conditions. It was washed with ethanol and deionized water to remove the excess $NaHSO_3$ and Na_2SO_3. The overall sulfonated silica synthesis can be represented as follows:

(i) Sulfonation by Na_2SO_3 or $NaHSO_3$

$$(MeO)_3Si(CH_2)_3Br + Na_2SO_3 \xrightarrow[H_2O]{MeOH} (MeO)_3Si(CH_2)_3SO_3^-Na^+ + NaBr \qquad (2.1)$$

$$(MeO)_3Si(CH_2)_3Br + NaHSO_3 \xrightarrow[H_2O]{MeOH} (MeO)_3Si(CH_2)_3SO_3^-Na^+ + HBr \qquad (2.2)$$

(ii) Hydrolysis

$$(MeO)_3Si(CH_2)_3SO_3^-Na^+ + 3H_2O \underset{MeOH\ @75^oC}{\overset{HCl}{\rightleftharpoons}} (HO)_3Si(CH_2)_3SO_3^-Na^+ + 3\ MeOH \qquad (2.3)$$

(iii) Polycondensation

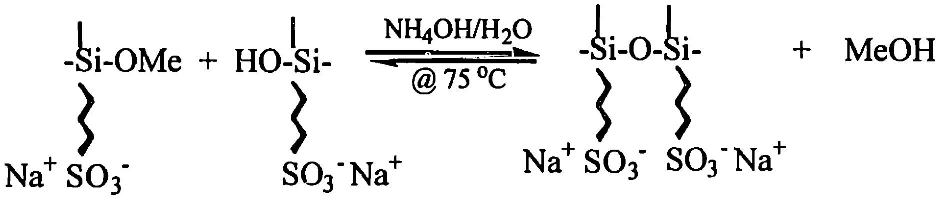

$$\text{-Si-OMe} + \text{HO-Si-} \underset{@\,75\ ^oC}{\overset{NH_4OH/H_2O}{\rightleftharpoons}} \text{-Si-O-Si-} + MeOH \qquad (2.4)$$

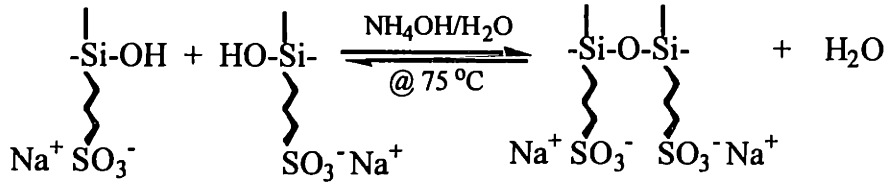

$$\text{-Si-OH} + \text{HO-Si-} \underset{@\,75\ ^oC}{\overset{NH_4OH/H_2O}{\rightleftharpoons}} \text{-Si-O-Si-} + H_2O \qquad (2.5)$$

The key sol-gel synthesis parameters included precursor reactivity, catalyst/pH, reaction temperature, and drying condition. The nature of alkoxy group has a great effect on the hydrolysis and condensation rates due to steric considerations. The alkoxysilane with non-bulky methoxy groups could promote the reaction rates. Catalyst/pH was an important parameter for controlling the gel microstructure. Besides pH adjustments, increasing reaction temperature could accelerate the sol-gel reaction. However, non-homogeneous gel composition and structure could result if temperatures were too high. An optimal gel structure was obtained at a temperature range of 60-80 °C. The preservation of gel porosity could be affected by the drying method. The as-prepared gel was dried either in its as-prepared form or after water had been exchanged out of its mother liquor with ethanol. Supercritical drying is a widely used method for solvent removal without causing pore collapse in gels, but it is not applicable to this case due to the ease of decomposition of organic moieties in our functionalized silica gel.

2.2.2 Structural Characterization of Sulfonated-Silica Gel

Photoacoustic Fourier-transform infrared (PA-FTIR) spectroscopy was used to obtain information on the molecular structure and surface chemistry of the sulfonated-SiO_2 gel. Spectra were collected in a 2.5 kHz rapid-scan mode at 4 cm^{-1} resolution in a Bio-Rad FTS-60A spectrometer using a MTEC Model 200 photoacoustic cell. Figure 2.1 shows the PA-FTIR spectrum of sulfonated-silica gel. The characteristic Si-O-Si backbone phonon vibrations (960-1280 cm^{-1})[4] as well as the unique SO_3^- asymmetric (1120-1260 cm^{-1}) and symmetric (1010-1080 cm^{-1}) stretchings indicated the presence of SO_3^- groups in the silica gel. The chemical composition of the as-prepared gel obtained with $NaHSO_3$ sulfonation under two-step catalysis was 15.8 wt% C, 4.22 wt% H, 36.6 wt% Si, and 2.43 wt% S (S : Si atomic ratio = 1 : 17).

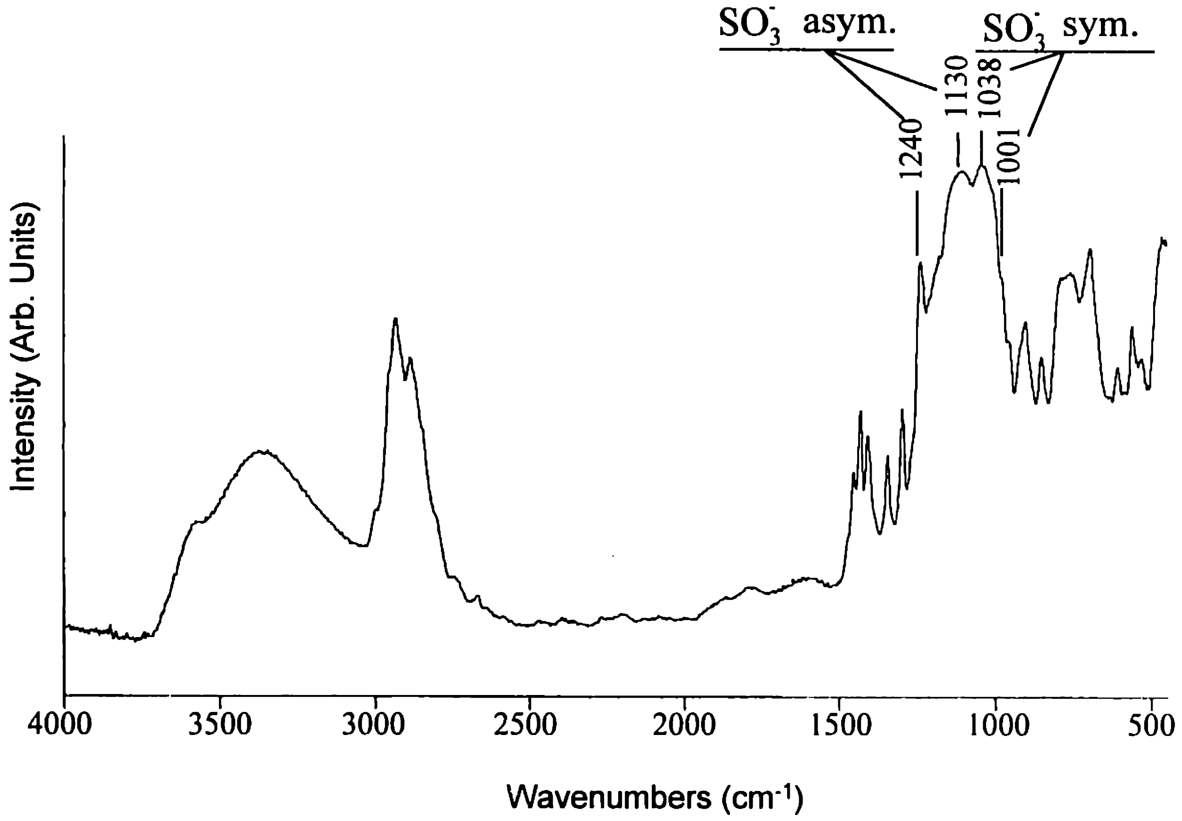

Figure 2.1. PA-FTIR spectrum of sulfonated-silica gel.

The thermal stability of the sulfonated gel was characterized by thermogravimetric analysis (TGA) using Perkin Elmer TGA7. There were two stages of weight loss during the heat treatment from 25 °C to 1200 °C under O_2 atmosphere (see Figure 2.2). The first stage weight loss at ~100-150 °C corresponded to the removal of water. Significant weight loss was found between 200 °C and 300 °C, associated with the combustion of organic species.

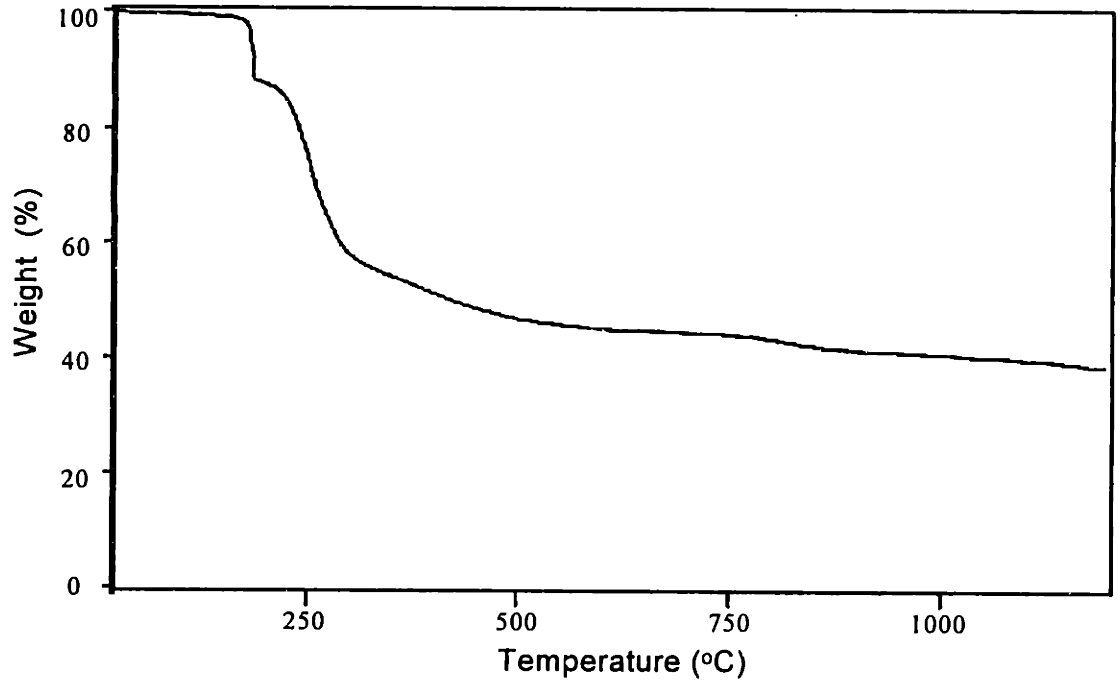

Figure 2.2. Thermogravimetric analysis of as-prepared sulfonated-SiO_2 gel under O_2.

X-ray diffraction (XRD) studies of the samples were conducted with Siemens D5000 θ-θ diffractometer operated at 45 kV and 40 mA using CuKα radiation (1.541 Å). For the as-prepared gel, only a broad amorphous band at $2\theta \sim 22°$ was detected (see Figure 2.3). After calcination in O_2 at 900 °C for 3 hours, distinct peaks associated with a SiO_2 cristobalite phase were noted. It was unusual for an amorphous silica gel to transform to cristobalite at such a low temperature. This might be due to the unique chemical structure of the sulfonated gel. The presence of alkali cations (Na^+) might have promoted the crystallization of the silica gel.[4,5]

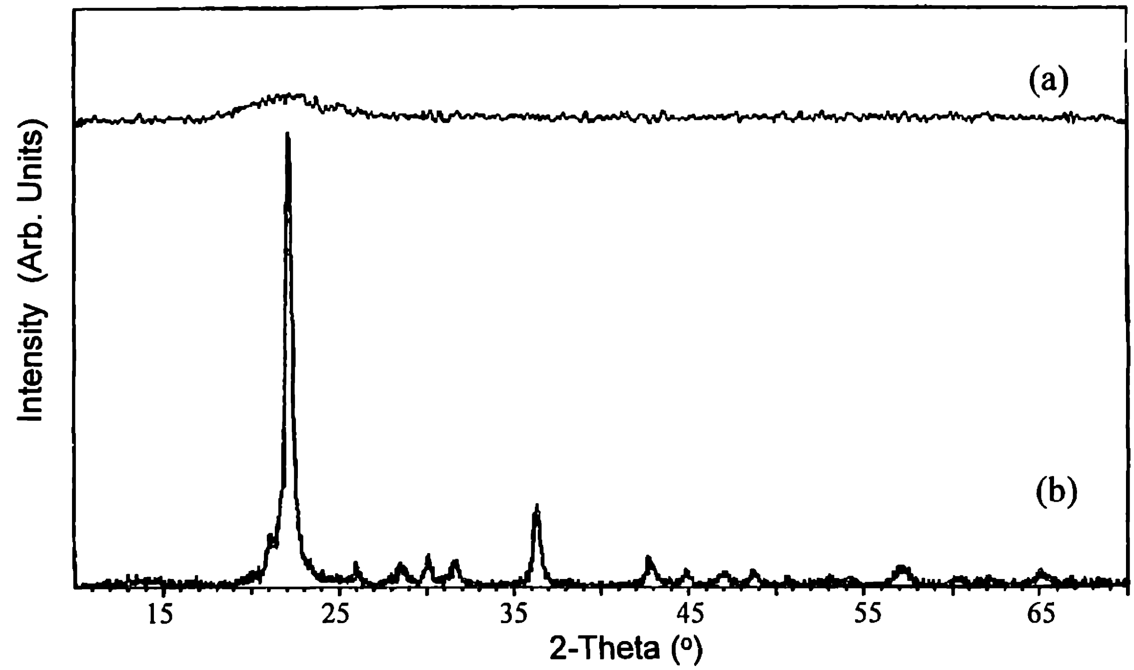

Figure 2.3. XRD patterns of (a) as-prepared sulfonated-SiO_2 gel and (b) sulfoanted-SiO_2 gel calcined at 900 °C.

2.3 Synthesis and Properties of γ-Fe_2O_3/Sulfonated-SiO_2 Nanocomposites

2.3.1 Synthesis of Fe_2O_3 Nanoclusters Within Sulfonated-Silica Matrix

The Na^+-sulfonated silica gel was subjected to ion-exchange with Fe^{2+} in an aqueous $FeCl_2$ solution. The Fe^{2+} cations in the gel matrix were converted to $Fe(OH)_2$ clusters with the addition of 0.625 M NaOH. The clusters were then oxidized to Fe_2O_3 with the dropwise introduction of a diluted aqueous H_2O_2 solution to the gel suspension at 60 °C. The Fe_2O_3-loaded nanocomposite was then washed until the pH of the filtrate became neutral. The schematic of the synthesis process is shown in Figure 2.4.

The Fe^{2+} exchange level could be controlled by the concentration of iron salt, the solution pH and the availability of SO_3^- sites. Different pH values resulted in various cationic species in the aqueous solution. High concentrations of Fe^{2+} would lead to Fe ion-exchange with the SO_3^-, and also the precipitation of excess iron on the matrix surface. Iron deposits on the external surface of the porous matrix would result in a broad cluster size distribution and should be avoided. The optimal nanocrystalline Fe_2O_3 loading within the pores of sulfonated-silica matrix was found to be ~ 1-5 wt%.

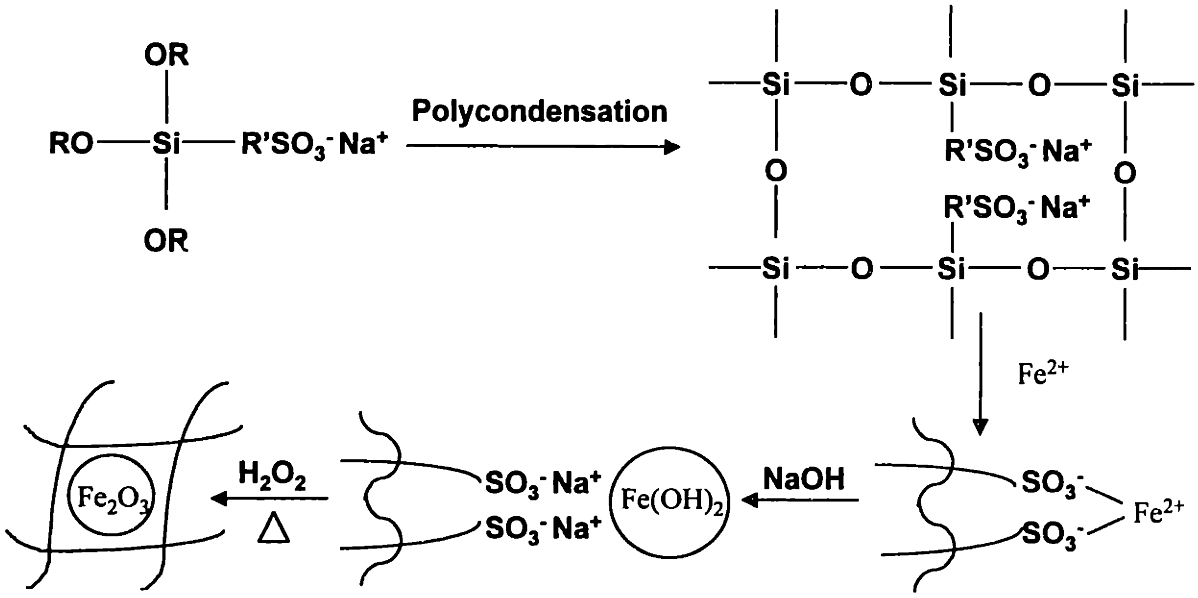

Figure 2.4. Schematic of Fe_2O_3 formation in sulfonated-silica matrix.

2.3.2 Structural Characterization of Fe_2O_3/Sulfonated-SiO_2 Nanocomposites

The Fe_2O_3/sulfonated-SiO_2 nanocomposite was characterized to examine the interaction between the porous host and the nanocrystalline guests. The incorporation of Fe_2O_3 clusters into sol-gel derived matrix was reflected by PA-FTIR spectroscopy through the change in the local chemical environment of the SO_3^- sites. Upon the introduction of Fe_2O_3 clusters, a slight shift in the SO_3^- stretching bands was observed due to a local confinement effect. Similar results were also obtained with Fe_2O_3 nanoclusters embedded in polymer ion-exchange resin.[6] The total iron loading in the as-prepared nanocomposites was determined as 2.6 wt% by atomic absorption spectroscopy. The atomic ratio of S and Fe was calculated to be 1.63 (theoretical ratio = 2 for a stoichiometric loading), indicating the effective ion-exchange capability of the sulfonated-SiO_2 gel.

The size, shape and distribution of Fe_2O_3 nanoclusters in the sulfonated-SiO_2 matrix could be observed with transmission electron microscopy (TEM). High-resolution TEM of the as-prepared Fe_2O_3/sulfonated-SiO_2 nanocomposite could also elucidate the crystallinity of the iron oxide clusters. Electron diffraction patterns of selected area were used to estimate the lattice spacings in the nanocrystals, thus identifying their crystalline phase. XRD data were collected to determine the phase and cluster size using Scherrer's line broadening method.[7]

A challenge in nanocomposite engineering lies in the thermal stability of the nanometer-sized particles since the morphology and interaction between the nanoclusters and the matrix may change during heat treatment. The thermal evolution of the nanocomposite was followed by XRD, which could illustrate phase transformation in both the sulfonated silica matrix and the iron oxide nanoclusters. Fe_2O_3 nanoclusters might migrate out of the matrix upon heat treatment and cause bulk phase segregation and substantial grain growth. This could be monitored by TEM and scanning transmission electron microscopy (STEM) with the elemental mapping capability.

TEM micrograph of the as-prepared Fe_2O_3/sulfonated-SiO_2 nanocomposite indicated the presence of crystalline elongated clusters with a diameter of ~ 4 nm and a length of 10-20 nm in the amorphous gel matrix (Figure 2.5). The diffuse rings of the electron diffraction pattern on a selected area suggested that the clusters in the sample were very small. The Fe and O elemental mappings of the nanocomposite by STEM confirmed the uniform dispersion of elongated iron oxide clusters (Figure 2.6). After calcination in O_2 at 500 °C for 3 hours, the clusters took on a more spherical morphology with a wider size distribution (Figure 2.7). However, no significant aggregation or grain coarsening occurred during this heat treatment. The d-spacing calculated from the corresponding electron diffraction pattern was 2.53 Å, which corresponded to the (110) plane of α-Fe_2O_3. This suggested that the clusters transformed to nanometer-sized α-Fe_2O_3 crystals upon calcination of the Fe_2O_3/sulfonated-SiO_2 nanocomposite at 500 °C.

Figure 2.5. TEM micrograph of as-prepared Fe_2O_3/sulfonated-SiO_2 nanocomposite.

The as-prepared nanocomposite was a X-ray amorphous material that gave only one broad peak centered at $2\theta \sim 22^\circ$ (Figure 2.8), similar to the as-prepared sulfonated silica gel. Upon calcination to 300 °C for 3 hours with a heating rate of 1 °C/min, small XRD peaks that corresponded to the α-Fe_2O_3 phase were noted. By 900 °C, two major crystal phases were observed in the nanocomposite: cristobalite (SiO_2) and hematite (α-Fe_2O_3). Their average crystal sizes were calculated by Scherrer's formula to be 41 nm and 60 nm, respectively, indicating that the size of the crystallites still remained in the nanometer range even after the heat treatment to 900 °C.

The Fe_2O_3/sulfonated-SiO_2 nanocomposites were examined with N_2 adsorption-desorption (Table 2.1). The Brunauer-Emmett-Teller (BET) surface area of the as-prepared Fe_2O_3/sulfonated-SiO_2 nanocomposite was determined to be 52 m^2/g. This low value might be due to (i) the presence of adsorbed water, which was confirmed by a large weight loss between 100-200 °C in TGA, and (ii) the presence of long-chained organic SO_3^- groups associated with the matrix material. The hysteresis in the adsorption-desorption isotherms (Figure 2.9) suggested that the nanocomposite consisted of ink-bottle type pores with pore diameters in the mesoporous range. Barrett-Joyner-Halenda (BJH) pore size distribution

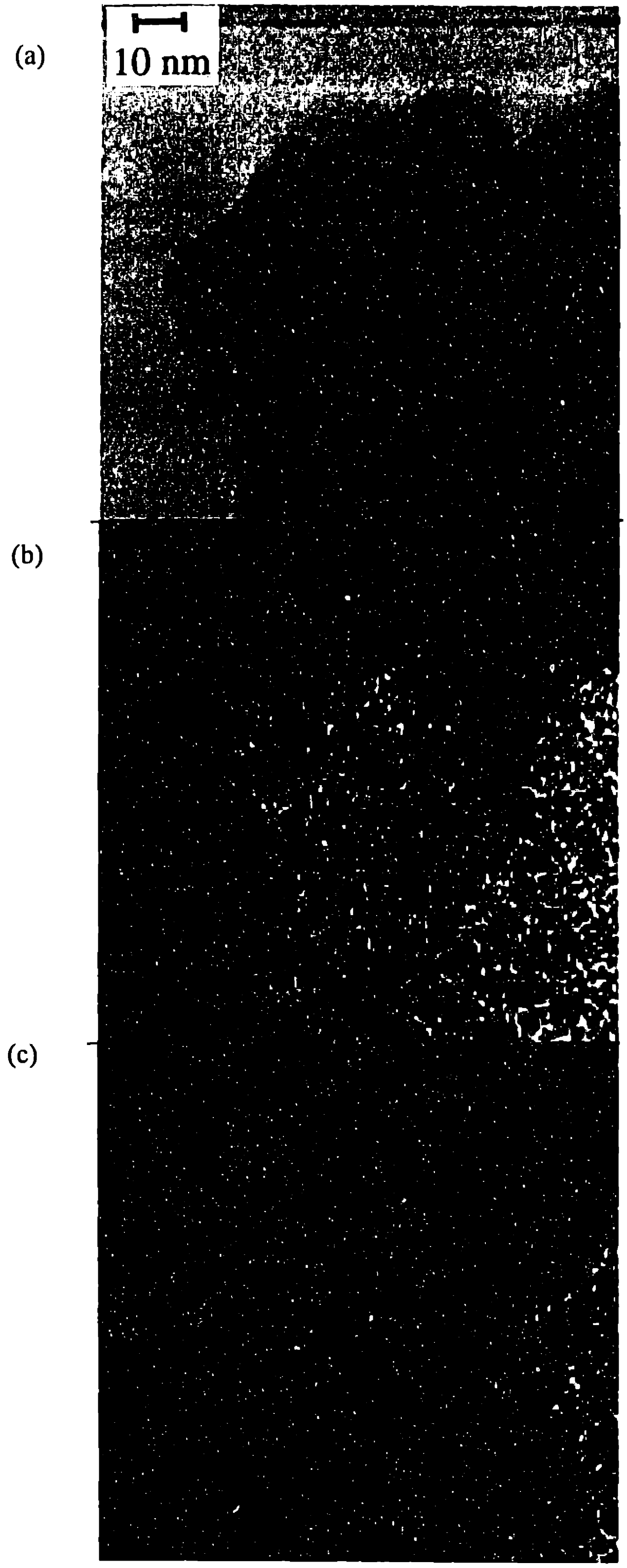

Figure 2.6. STEM study of as-prepared Fe_2O_3/sulfonated-SiO_2 nanocomposite: (a) image, (b) O map, and (c) Fe map.

Figure 2.7. TEM micrograph of Fe_2O_3/sulfonated-SiO_2 nanocomposite calcined at 500 °C under O_2.

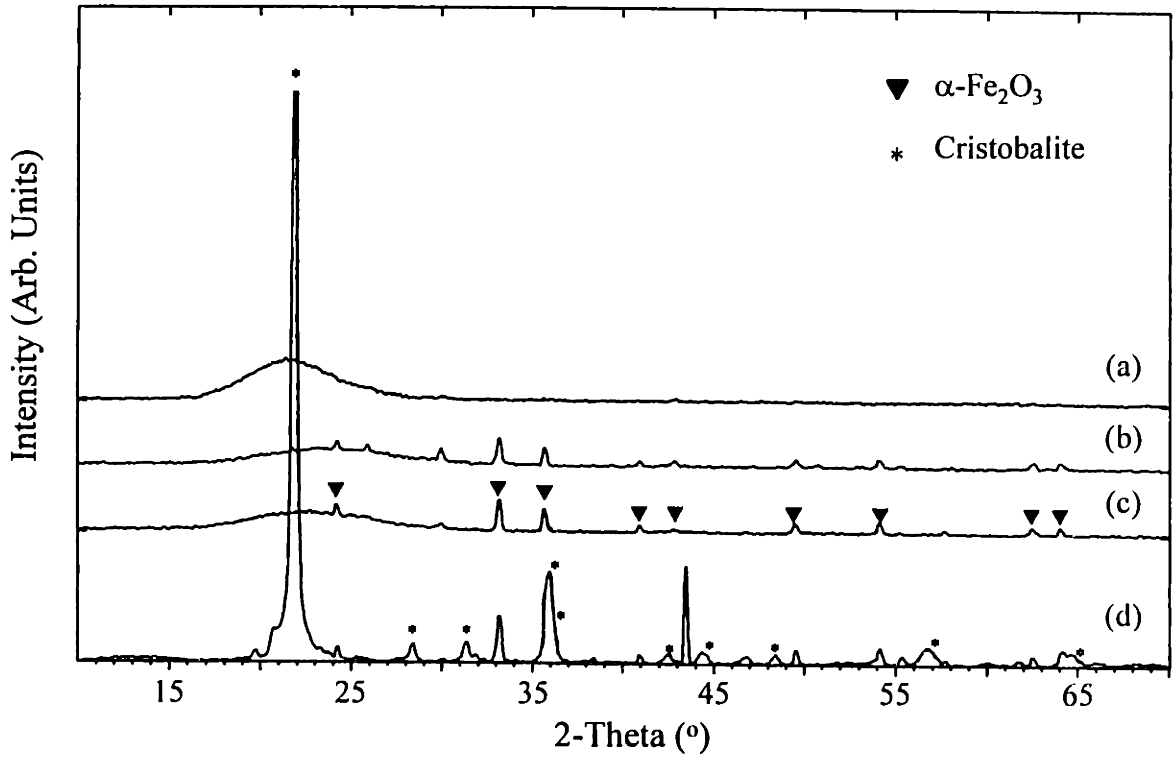

Figure 2.8. XRD patterns of Fe_2O_3/sulfonated-SiO_2 nanocomposites: (a) as-prepared, (b) calcined at 300 °C, (c) calcined at 500 °C, and (d) calcined at 900 °C.

calculated from the desorption isotherm illustrated that the pore sizes were narrowly distributed at ~ 40 Å (Figure 2.10). The nanocluster diameter (~ 4 nm) illustrated by TEM corresponded to the average pore diameter of the matrix, demonstrating that the formation of nanoclusters was confined to the pores in the functionalized silica matrix. The surface area of the nanocomposite increased from 52 m^2/g for the as-prepared sample to 205 m^2/g and 210 m^2/g upon calcination at 300 °C and 500 °C, respectively, due to the removal of the organic side chains. FTIR spectrum of sample calcined at 300 °C confirmed the elimination of H_2O and organics. Further calcination to 700 °C reduced the surface area of the nanocomposite due to pore collapse. The nanocomposite sintered significantly by 900 °C, at which temperature the silica matrix also crystallized to cristobalite phase.

Table 2.1. Surface area and average pore size of Fe_2O_3/sulfonated-SiO_2 nanocomposites

	B.E.T. Surface Area (m^2/g)	Average Pore Size (Å)
As-prepared nanocomposite	52	35
Sample calcined at 300 °C	205	35
Sample calcined at 500 °C	210	39
Sample calcined at 900 °C	~1	--

2.3.3 Magnetic and Optical Properties of Fe_2O_3/Sulfonated-SiO_2 Nanocomposites

Highly dispersed magnetic nanoclusters have been shown to possess unique characteristics associated with quantum confinement effects. In bulk ferromagnetic or ferrimagnetic crystals, magnetic domains are spontaneously formed with different magnetization directions to minimize the demagnetizing energy. In contrast, a paramagnetic material is consisted of individual atomic spins that are independent and randomly oriented. For nanometer-sized clusters, the magnetic behavior is basically related to the energy barrier of a single domain, which is proportional to the volume of the clusters and the magnetic anisotropy constants (K_{eff}).[8] At a temperature higher than

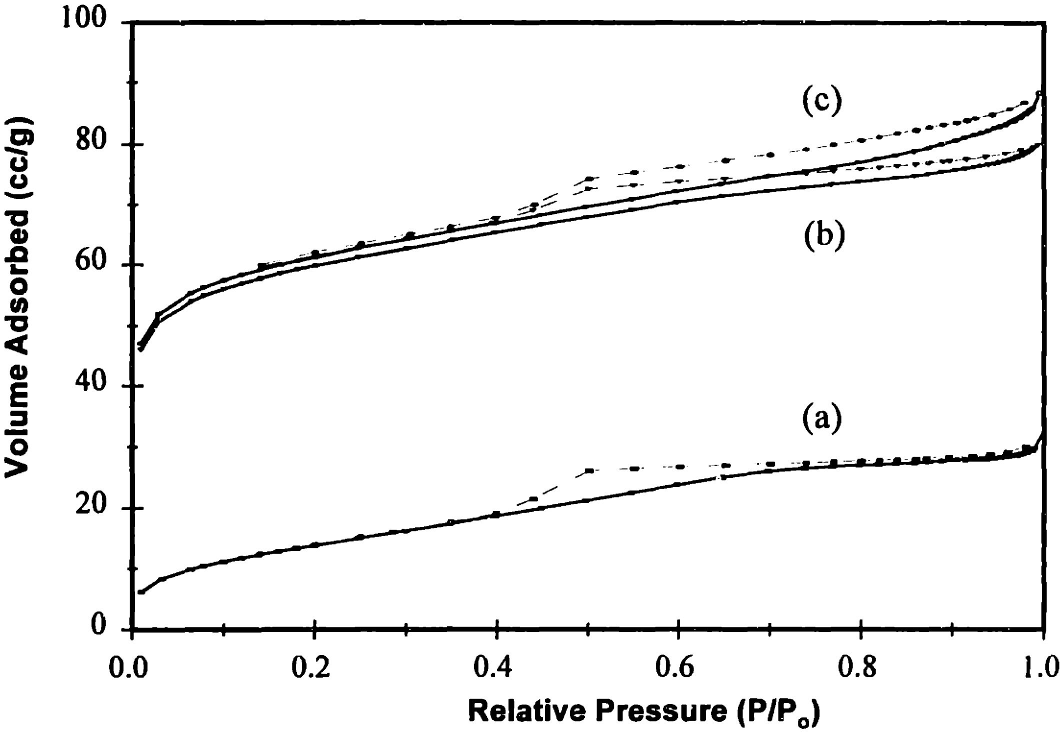

Figure 2.9. N_2 adsorption-desorption isotherms of Fe_2O_3/sulfonated-SiO_2 nanocomposites: (a) as-prepared, (b) calcined at 300 °C, and (c) calcined at 500 °C.

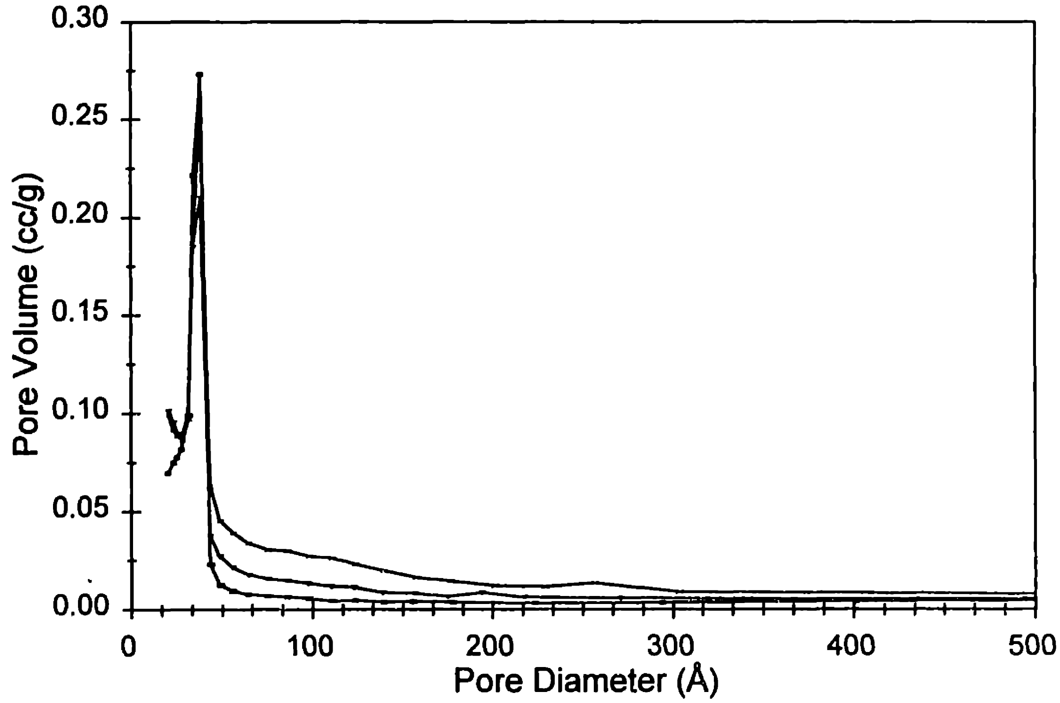

Figure 2.10. BJH pore size distributions of Fe_2O_3/sulfonated-SiO_2 nanocomposites: (a) as-prepared, (b) calcined at 300 °C, and (c) calcined at 500 °C.

the critical magnetic blocking temperature (T_b), the thermal energy (kT) is comparable to the magnetic energy barrier. The spins in the magnetic domain will then fluctuate between the easy directions of the magnetic moment. The change in the magnetization of these clusters under an applied field will therefore be analogous to a paramagnetic system, except with a larger magnetic moment. This phenomenon is known as superparamagnetism, and can be observed when the superparamagnetic relaxation is rapid compared to the characteristic measurement time of the instrument.

In the case of single-domain particles with uniaxial anisotropy, the superparamagnetic relaxation time τ for the reorientation of the magnetization can be calculated by the expression:[9]

$$\tau = \frac{M\pi^{\frac{1}{2}}}{K_{eff}\gamma_0}\sqrt{\frac{kT}{K_{eff}V}}\exp\{\frac{K_{eff}V}{kT}\} \approx \tau_0 \exp\{\frac{K_{eff}V}{kT}\} \qquad (2.6)$$

where M is the magnetization, γ_0 is the gyromagnetic ratio, K_{eff} is the uniaxial magnetic anisotropy constant, V is the volume of the particle, k is Boltzmann's constant, T is the absolute temperature, and τ_0 is a simplified time constant on the order of 10^{-10}-10^{-12} s. Thermal energies surpassing the superparamagnetic energy barrier (E) given by,

$$E(\theta) = K_{eff}V \sin^2\theta \qquad (2.7)$$

can induce spontaneous reversals of the particle magnetization with a relaxation time τ, with θ as the angle between the magnetization direction and the easy axis of the particle.[10]

Superparamagnetic clusters are of interest for a number of applications. For example, they can provide magnetic refrigerants with large magnetocaloric effects with operability at a higher temperature or a smaller applied magnetic field than conventional paramagnetic materials.[11] We are interested in the size control and dispersion of the metallic clusters in our nanocomposite system so as to achieve optimal magnetic properties. The samples were characterized for superparamagnetism using superconducting quantum interference device (SQUID) magnetometry and Mössbauer spectroscopy.

One test for superparamagnetism is to measure the coercivity of a system as a function of temperature. The particle size distribution will have a significant effect on the measurement. As the temperature decreases, the coercivity increases in a manner dependent on the portion of particles that are superparamagnetic. Another test is to measure the magnetization curve at different temperatures. The magnetization of superparamagnetic particles is given by the Langevin equation:[12]

$$M = M_s(\coth\alpha - \frac{1}{\alpha}) \tag{2.8}$$

where M_S is the saturation magnetization, and $\alpha = \mu H/kT$, where μ is the magnetic moment of the particle and H is the applied field. When $T < T_b$, the moments of the clusters are frozen along their anisotropy axes, and the thermodynamic equilibrium is blocked. The magnetic behavior of the system is then determined by the bulk magnetic properties of the material. When magnetization is plotted as a function of H/T, the curves at the different temperatures are superimposed. Deviation from the Langevin equation results when the assumption that all particles share the same magnetic moment is not valid.

The blocking temperature T_b, is defined as the temperature at which the superparamagnetic relaxation time (τ) of Eq. (2.6) equals the measurement time (τ_m). Since τ depends critically on the magnitude of the energy barrier, $K_{eff}V$, which separates the two easy directions of magnetization of the particle, Mössbauer studies at the vicinity of T_b will provide information about the energy barrier. The 10^{-8} sec characteristic measuring time for Mössbauer spectroscopy yields information on blocking temperatures, below which spin relaxation is slowed down. This allows for investigation of dynamic and static magnetic properties over a convenient temperature range, and provides the capability of zero external field magnetic study. In addition, Mössbauer spectroscopy detects the internal or local magnetization at Fe sites and, therefore, is amenable to investigations of the magnetic microstructure of the particle and its surface. For very small particles, where a large fraction of the atoms is surface bound, Mössbauer spectroscopy can be used to probe the interfacial characteristics of the nanocomposite.

The as-prepared Fe_2O_3/sulfonated-SiO_2 nanocomposite displayed a quadrupole splitting between 30 K and 300 K. This was consistent with ferric ion (Fe^{3+}) in a paramagnetic or superparamagnetic state. As measurement temperature decreased, the intensity of the doublet was reduced. An isomer shift (δ) of 0.44 mm/s and a quadrupole splitting (ΔE_0) of 0.78 mm/s were obtained at 150 K (Figure 2.11). These values were in agreement with the values for SiO_2-coated γ-Fe_2O_3 (see Chapter 3) at the same temperature,[13] indicating the presence of nanocrystalline γ-Fe_2O_3 in the nanocomposite. Below 25 K, the quadrupole doublet was magnetically split. A single-site fitting to the experimental data gave an internal hyperfine field (H_{hf}) of 480 kOe at 4.2 K. These low-temperature magnetic transformations confirmed the presence of ultrafine γ-Fe_2O_3 particles. A detailed temperature-dependence study was hindered by (i) the rather weak Mössbauer signal associated with the low Fe loading in the Fe_2O_3/sulfonated-SiO_2 nanocomposite, and (ii) the competing non-resonant absorption of the 14.4 keV Mössbauer γ-rays by the SiO_2 matrix, which resulted in a poor signal-to-noise ratio. The synthesis of a sample enriched in ^{57}Fe could enhance the Mössbauer signal in future studies.

The SQUID magnetization measurement has an instrument measurement time on the order of 10^2 sec. The Fe_2O_3/sulfonated-SiO_2 nanocomposite displayed superparamagnetic behavior at room temperature (Figure 2.12(a)), whereby no hysteresis was obtained under the applied field. The onset of hysteresis occurred at about 10 K (Figure 2.12(b)). The magnetic measurement at 5 K (Figure 2.12(c)) gave a lower

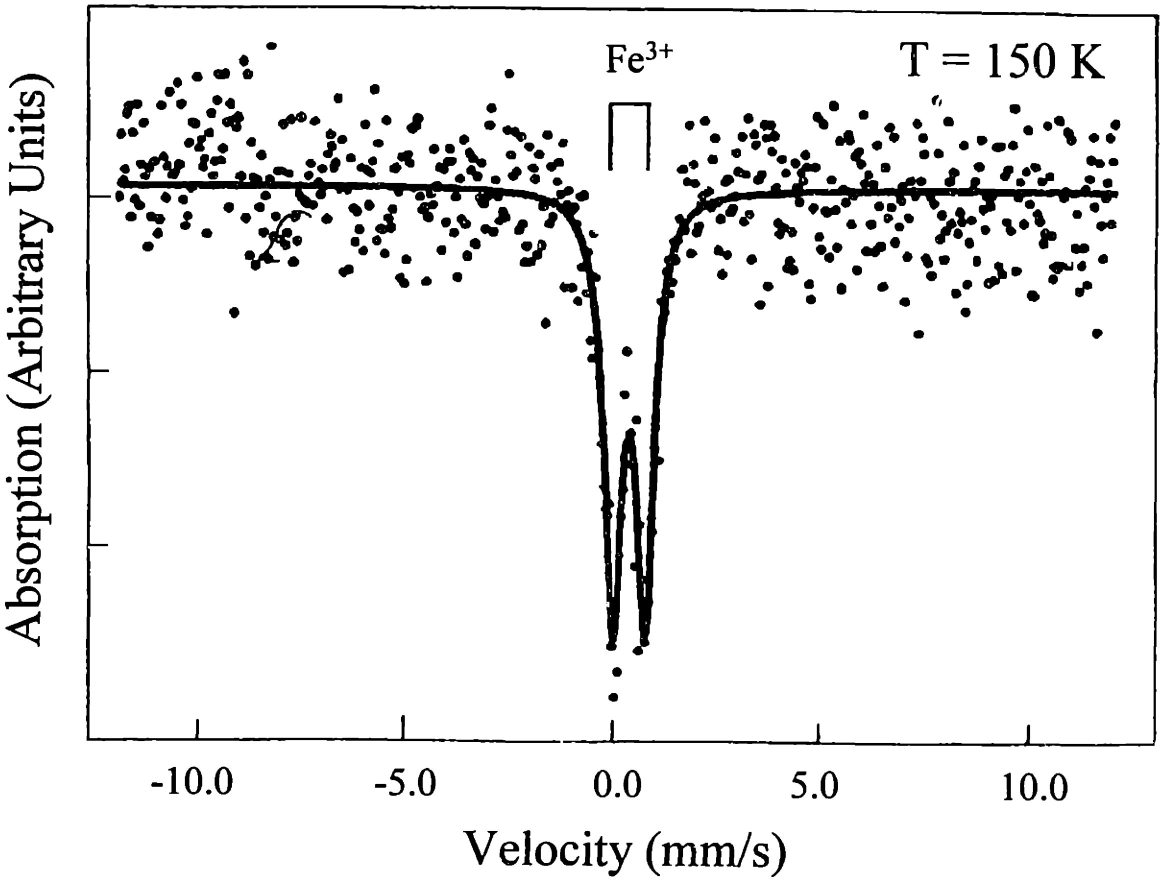

Figure 2.11. Mössbauer spectrum of as-prepared Fe_2O_3/sulfonated-SiO_2 nanocomposite.

remanence (M_r) of 1.4 emu/g Fe_2O_3 and a smaller coercivity (H_c) of 270 G compared to the γ-Fe_2O_3/SiO_2-coated system (Chapter 3).[2,13] According to the Stoner and Wohlfarth model,[14] shape anisotropy alone for these acicular particles could yield a coercive field on the order of 900 G, assuming an ellipsoid with uniform magnetization and a ratio of major to minor axis of 5:1, as observed for the larger particles in Figure 2.5. The low coercivity value measured implied that (i) the internal spin structure of the particles substantially deviated from the uniform magnetization assumed in the Stoner and Wohlfarth model, and/or (ii) the anisotropy was dominated by strain exerted by the matrix on the nanoclusters.

A magnetization peak at T_{max} = 10 K was noted under zero field cooling (ZFC) upon decreasing the temperature (Figure 2.13). The splitting or the irreversibility

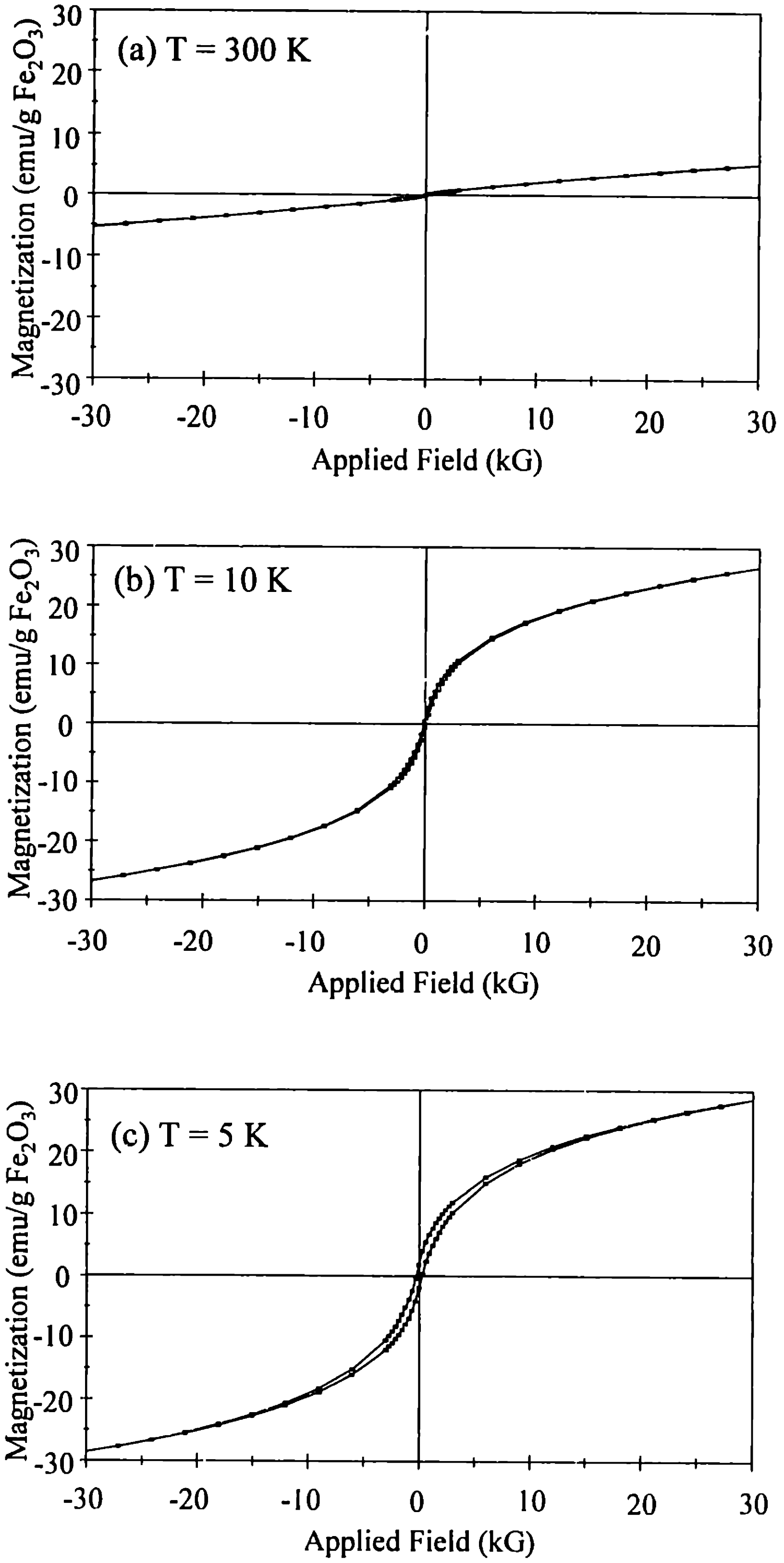

Figure 2.12. Plots of magnetization vs. applied field for as-prepared Fe_2O_3/sulfonated-SiO_2 nanocomposite obtained at (a) 300 K, (b) 10 K, and (c) 5 K.

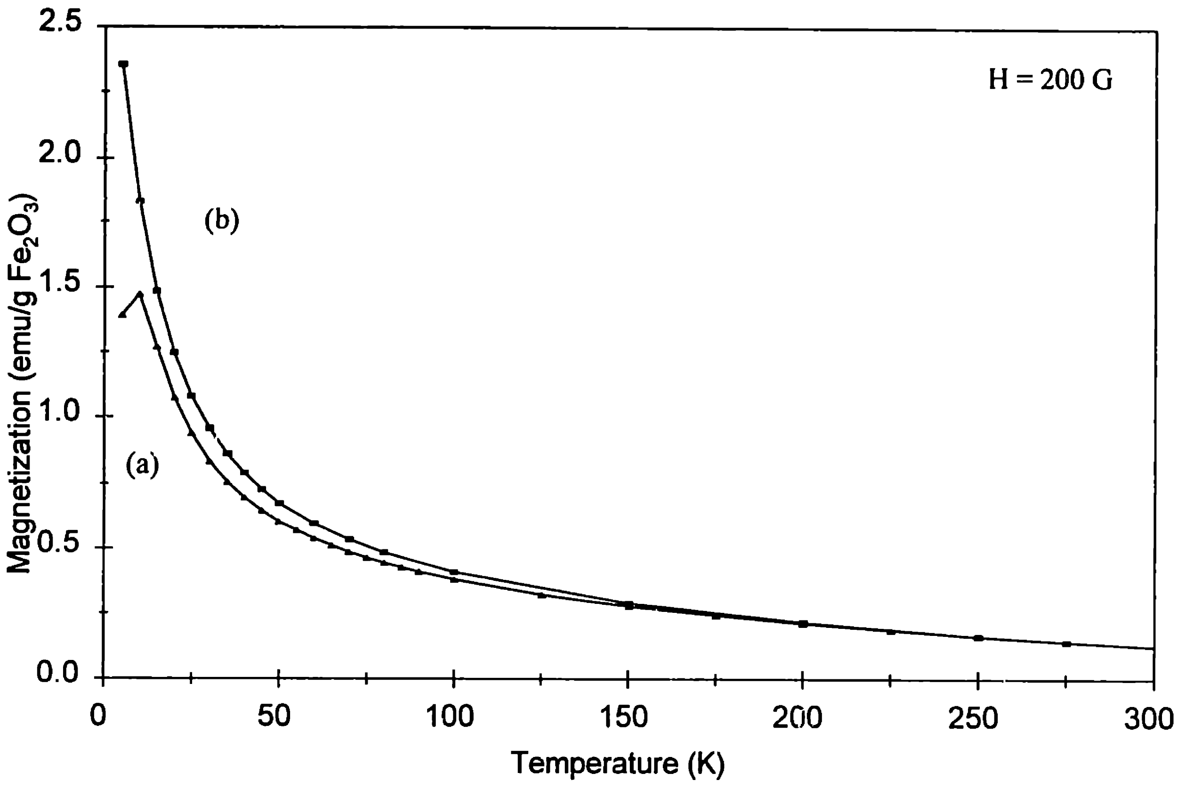

Figure 2.13. Temperature dependence of the magnetization curves under (a) zero field cooling and (b) field cooling for as-prepared Fe_2O_3/sulfonated-SiO_2 nanocomposite.

between the ZFC and field cooling (FC) magnetization curves occurred at $T >> T_{max}$, consistent with the broad size distribution of the iron oxide particles in the sulfonated-silica system. The complexity might also be due to the electronic interaction between the nanoclusters and the functionalized matrix.

Diffuse reflectance ultraviolet-visible (UV-Vis) spectrum of the nanocomposite was obtained on a Cary 5E spectrometer (Figure 2.14). The acicular iron oxide nanoparticles in sulfonated-silica matrix exhibited a strong blue shift of 110 nm relative to the bulk iron oxide. A similarly strong blue shift in the diffuse reflectance UV-Vis spectrum was recently observed for Fe_2O_3 particles impregnated within the channels of hexagonally-packed MCM-41 matrix.[15] This widening of the bandgap is consistent with quantum confinement effects.

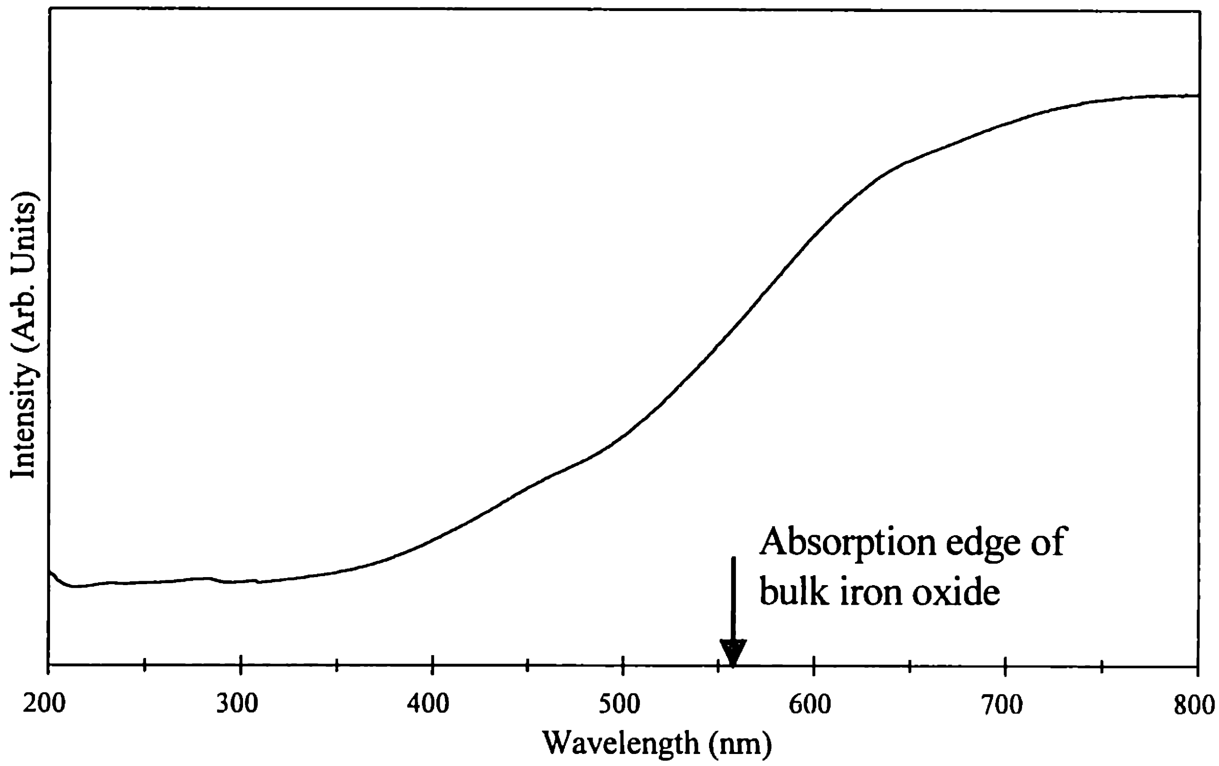

Figure 2.14. Diffuse reflectance UV-Vis spectrum of Fe_2O_3/sulfonated-SiO_2 nanocomposite.

The effect of thermal treatment on the magnetic properties of the nanocomposites was investigated by Mössbauer spectroscopy. Calcination of the Fe_2O_3/sulfonated-SiO_2 sample under O_2 at 250 °C led to an increase in the quadrupole splitting in the Mössbauer spectrum (Figure 2.15(b)), suggesting an increase in γ-Fe_2O_3 cluster size. Mössbauer absorption corresponding to α-Fe_2O_3 was also resolved in Figure 2.15(b), indicating that the phase transformation to α-Fe_2O_3 was initiated with calcination at 250 °C. Calcination at 500 °C induced significant γ-$Fe_2O_3 \rightarrow \alpha$-$Fe_2O_3$ transformation (Figure 2.15(c)). These results agreed with the XRD patterns, which illustrated the presence of α-Fe_2O_3 upon calcinaton to 300 °C. We noted that γ-Fe_2O_3 peaks could not be detected in the XRD patterns, possibly because the crystallite sizes of γ-Fe_2O_3 clusters were less than the detection limit of 5 nm.

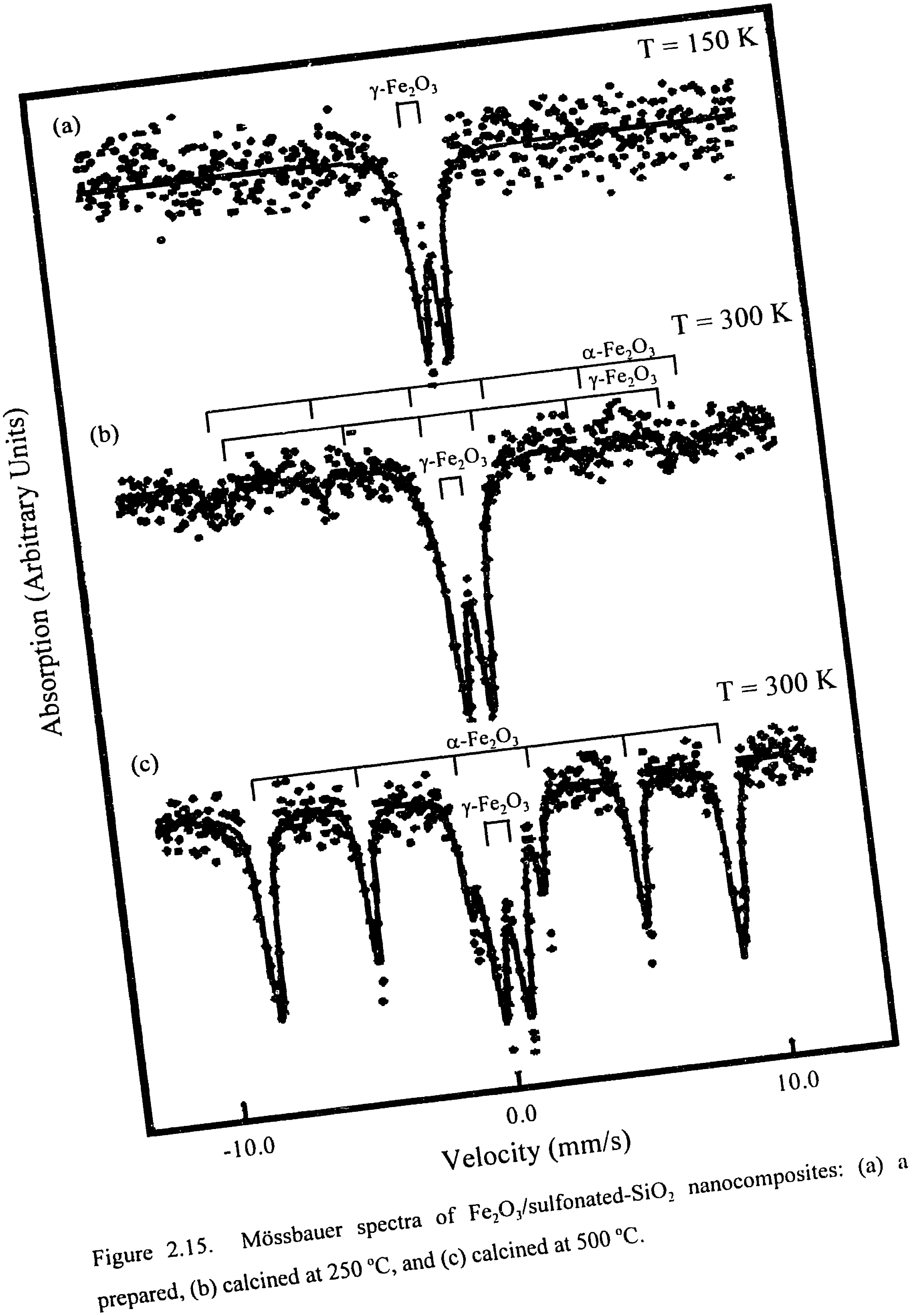

Figure 2.15. Mössbauer spectra of Fe_2O_3/sulfonated-SiO_2 nanocomposites: (a) as-prepared, (b) calcined at 250 °C, and (c) calcined at 500 °C.

2.4 Summary

Starting with an organoalkoxysilane precursor modified with sulfite (SO_3^-) groups, a porous sulfonated-silica gel with ion-exchange capability was successfully synthesized for hosting iron oxide nanoclusters. The chemistry of this functionalized sol-gel synthesis was governed by the precursor reactivity, catalyst/pH, and reaction temperature. Fe_2O_3 nanoclusters introduced via ion-exchange and post-oxidation were elongated (4 nm x 20 nm) and uniformly dispersed within the porous sulfonated-silica gel. The resulting γ-Fe_2O_3/sulfonated-SiO_2 nanocomposite demonstrated superparamagnetism, and exhibited a strong blue shift in optical spectroscopy associated with size-dependent quantum confinement.

2.5 References

[1] R. F. Ziolo, E. P. Giannelis, B. A. Weinstein, M. P. O'Horo, B. N. Ganguly, V. Mehrotra, M. W. Russell, and D. R. Huffman, Science, **257**, (1992) 219.

[2] L. Zhang, G. C. Papaethymiou, R. F. Ziolo, and J. Y. Ying, Nanostr. Mater., **9**, (1997) 185.

[3] R. M. Reed and H. V. Tarter, J. Am. Chem. Soc., **57**, (1935) 571.

[4] J. Y. Ying, J. B. Benziger, and A. Navrotsky, J. Am. Ceram. Soc., **76**, (1993) 2571.

[5] I. Schwart, P. Anderson, H. deLambilly, and L. C. Klein, J. Non-Cryst. Solids, **83**, (1986) 391.

[6] R. F. Ziolo, Xerox Corporation, private communication.

[7] H. P. Klug and L. E. Alexander, *X-ray Diffraction Procedures for Polycrystalline and Amorphous Materials*, Wiley, New York, (1974), Chapter 9.

[8] B. D. Cullity, *Introduction to Magnetic Materials*, Addison-Wesley, Reading, MA, (1972), Chapters 9 and 11.

[9] A. Aharoni, Phys. Rev. A, **135**, (1964) 447.

[10] S. Mørup, Appl. Phys., **11**, (1976) 63.

[11] R. D. McMichael, R. D. Shull, L. J. Swartzendruber, and L. H. Bennett, J. Magn. Magn. Mater., **111**, (1992) 29.

[12] A. H. Morrish, *The Physical Principles of Magnetism*, Wiley, New York, (1966) 362.

[13] L. Zhang, G. C. Papaefthymiou, and J. Y. Ying, J. Appl. Phys., **81**, (1997) 6892.

[14] E. C. Stoner and E. P. Wohlfarth, Phil. Trans. Roy. Soc. A, **240**, (1948) 599.

[15] T. Abe, Y. Tachibana, T. Vematsu, and M. Iwamoto, J. Chem. Soc., Chem. Commun., (1995) 1617.

Chapter 3

SIZE QUANTIZATION AND INTERFACIAL EFFECTS IN γ-Fe_2O_3/SiO_2-COATED NANOCOMPOSITES

3.1 Introduction

The main challenge in the synthesis of nanoclusters is the attainment of well-defined particle size and morphology. As demonstrated in Chapter 2, the use of an inorganic matrix as host for nanocrystalline particles can provide an effective way for tailoring uniform particle size and for controlling homogeneous dispersion of ultrafine metal oxide clusters. This chapter describes another approach for the synthesis of nanocrystalline superparamagnetic Fe_2O_3 clusters that makes use of an inert silica coating.[1,2] Comparing to the matrix-mediated synthesis discussed in Chapter 2, this second approach offers a higher loading of γ-Fe_2O_3. The magnetic and optical properties of the resulting γ-Fe_2O_3/SiO_2-coated nanocomposites derived were investigated to illustrate the importance of particle shape and size control, and the particle/matrix interfacial chemistry.

3.2 Synthesis of γ-Fe_2O_3/SiO_2-Coated Nanocomposites

A computer-controlled constant-pH apparatus was used in the $FeCl_2$-$FeCl_3$ coprecipitation experiments (Figure 3.1). The iron salt solution was prepared by mixing 10 ml of 2 M $FeCl_2$ (Aldrich) and 40 ml of 1 M $FeCl_3$ (Aldrich), such that $Fe^{2+}/Fe^{3+} = 0.5$. The reason for using both ferrous and ferric cations in the precipitation is to promote the formation of γ-Fe_2O_3 that has the cation-deficient spinel (AB_2O_4) structure. In a spinel, the cations on A and B sites have tetrahedral and octahedral coordination with oxygen, respectively. Since Fe^{3+} cations do not fill all A and B sites, vacancies are present in the B sub-lattice for charge balance. Precipitation of pure Fe^{3+} ions typically produces an amorphous hydrated oxyhydroxide that will be easily converted to α-Fe_2O_3 with all Fe^{3+} having octahedral coordination.[3] To form the spinel structure, some of the Fe^{3+} ions should occupy tetrahedral sites. By introducing Fe^{2+} cations, which have a stronger preference for octahedral site than Fe^{3+} cations, the spinel structure is favored during crystallization.[4]

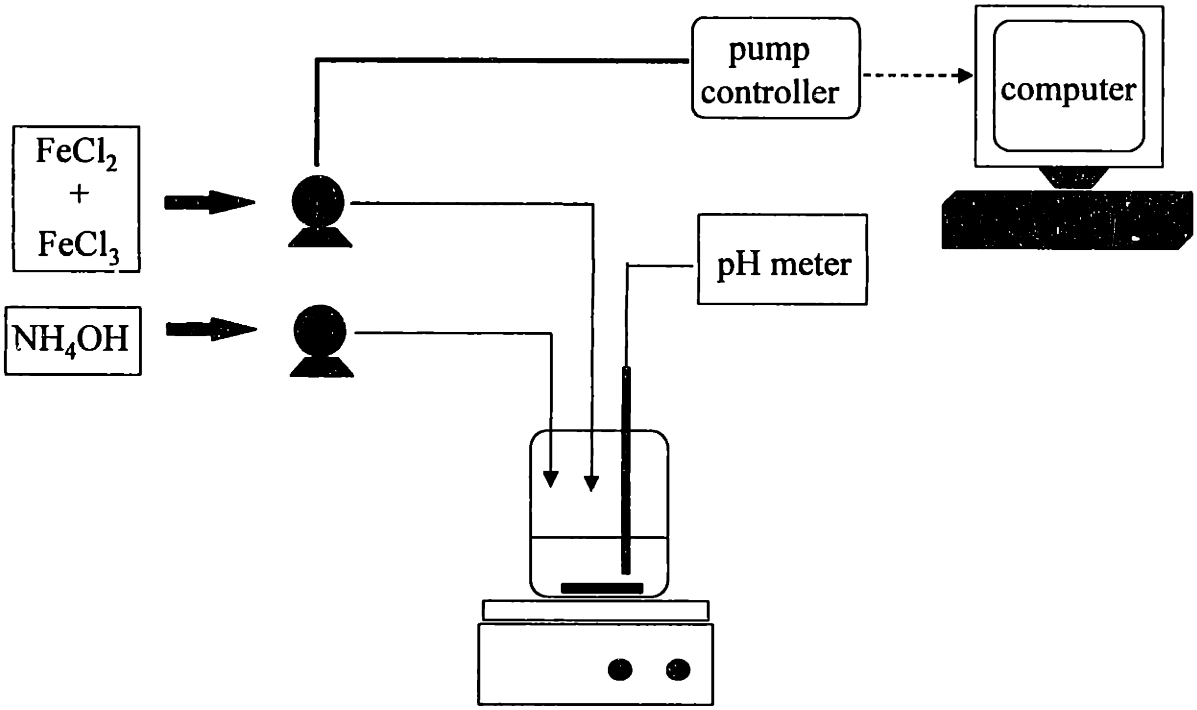

Figure 3.1. Schematic of the computer-controlled constant-pH precipitation apparatus.

In a typical synthesis, a mixture of the iron salt solutions was gradually introduced into 400 ml of an aqueous 0.6 M NH_4OH solution at room temperature. The reacting solution was kept at a constant pH of 10.5 throughout the course of precipitation with the addition of 3 M NH_4OH. A typical pH profile with time is shown in Figure 3.2. The resulting particles were washed with ethanol and separated by sedimentation. This washing process was repeated three times. To prevent the formation of agglomerates, an inert SiO_2 coating was applied onto the surface of the precipitated particles. Typically, 0.2 mol of tetraethoxysilane (United Chemical) in 50 ml ethanol was added to a suspension of precipitated iron oxide and stirred for 24 hours at 50 °C. The final SiO_2-coated iron oxide particles were washed with ethanol and deionized water in a centrifuge, and the process was repeated until the pH became neutral. The final material was recovered by decanting and was subsequently dried in air for a week.

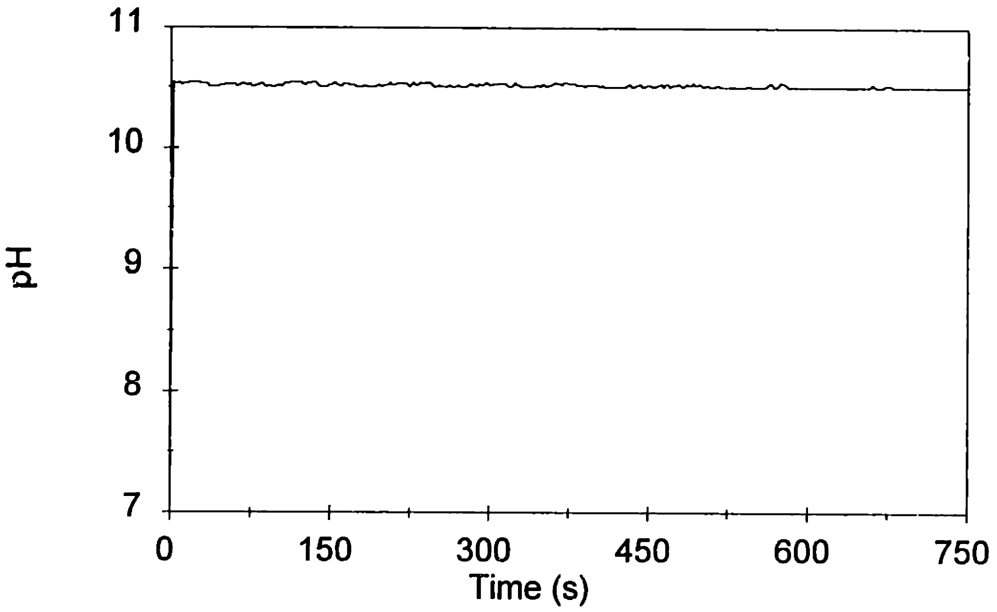

Figure 3.2. The precipitation bath pH as a function of reaction time.

3.3 Microstructure and Morphology of γ-Fe_2O_3/SiO_2-Coated Nanocomposites

The molecular structure of the nanocomposites was characterized by photoacoustic Fourier-transform infrared (PA-FTIR) spectroscopy. Spectra were collected in a 2.5 kHz rapid-scan mode at 4 cm^{-1} resolution in a Bio-Rad FTS-60A spectrometer using a MTEC Model 200 photoacoustic cell. The chemical composition of the Fe_2O_3/SiO_2 nanocomposites was analyzed by X-ray fluorescence spectroscopy (Oneida Research Services, Inc.). The morphology of the magnetic Fe_2O_3 clusters was studied with transmission electron microscopy (TEM) (Akashi 002B, 200 kV). The thermal evolution of nanoclusters was investigated by powder X-ray diffractometry (XRD) (Siemens D5000 θ-θ diffractometer operated at 45 kV and 40 mA using CuK_α radiation).

Fe_2O_3/SiO_2-coated nanocomposites were obtained as a reddish-brown powder. PA-FTIR provides information on the molecular structure of the material. The PA-FTIR spectrum of the nanocomposite (Figure. 3.3) illustrates the characteristic asymmetric Si-O-Si backbone phonon vibration bands at 960-1280 cm^{-1} of the SiO_2 coating.[5] Elemental analysis of the Fe_2O_3/SiO_2-coated nanocomposite showed that this material contained 32.8 wt% Fe. A large quantity of Fe_2O_3 nuclei may be directly created during the coprecipitation of the mixed iron salts to provide a wide range of possible Fe loadings. The BET surface area from N_2 adsorption analysis was ~ 400 m^2/g, indicating the presence of ultrafine particles.

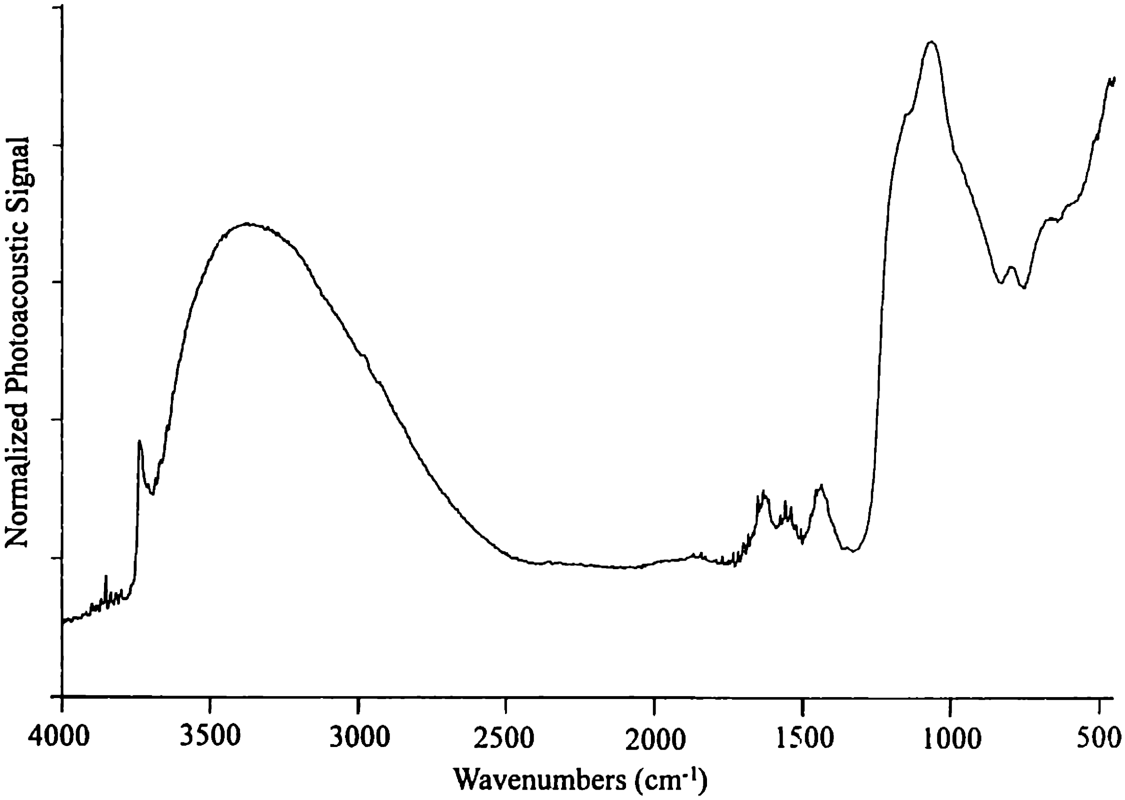

Figure 3.3. PA-FTIR spectrum of as-prepared Fe_2O_3/SiO_2-coated nanocomposite.

The powder XRD patterns of the as-prepared nanocomposites show a broad band centered at $2\theta = 22^\circ$, characteristic of amorphous SiO_2. The absence of well-defined Fe_2O_3 crystalline peaks can be attributed to the ultrafine crystallite size of the iron oxide clusters. The TEM micrograph showed that the spherical clusters of 4-5 nm diameter were isolated by SiO_2 coating (Figure 3.4(a)). No cluster aggregation was noted in the TEM micrograph. After calcination at 250 °C in O_2, the Fe_2O_3 clusters did not show significant grain growth or sintering and remained spherical with diameters of ~ 5 nm (Figure 3.4(b)). The SiO_2 coating provided an effective way to geometrically confine the ultrafine Fe_2O_3 clusters without sintering during the course of the thermal treatment.

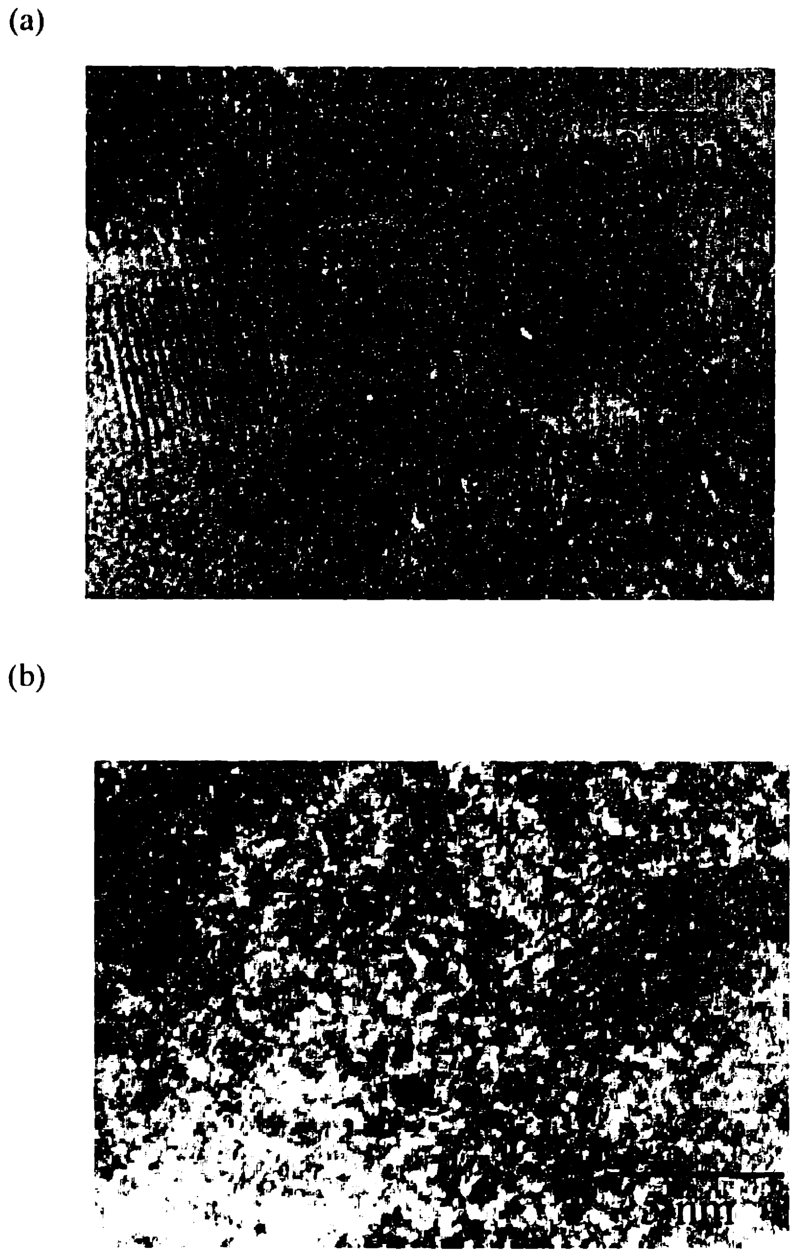

Figure 3.4. TEM micrographs of Fe_2O_3/SiO_2-coated nanocomposite: (a) as-prepared and (b) calcined at 250 °C under O_2.

Tailoring of the sol-gel derived SiO_2 coating can be successfully accomplished through the manipulation of processing variables, such as sol pH, composition, and reaction temperature.[5,6] During precipitation, the surface of the precipitated Fe_2O_3 particles is negatively charged under the basic condition. Alkoxysilane precursor molecules are adsorbed on the surface of the small particles and physically prevent the particles from aggregation by forming a SiO_2 coating on the particle surface via sol-gel reaction. The microstructure of the Fe_2O_3/SiO_2 nanocomposites can be controlled by the sol-gel chemistry as well as the cluster synthesis parameters, such as the iron salt concentration, and the precipitation pH and temperature.

3.4 Magnetic Behavior of the γ-Fe_2O_3/SiO_2-Coated Nanocomposites

Probing the magnetism of small structures presents a special challenge due to superparamagnetic relaxation. The magnetic behavior of the nanocomposite was characterized using SQUID magnetometry and Mössbauer spectroscopy. The magnetization of the samples was measured using a superconducting quantum interference device (SQUID) magnetometer (Quantum Design, MPMS) at temperatures ranging from room temperature to 5 K. The ^{57}Fe Mössbauer spectra were recorded using a conventional constant acceleration transmission spectrometer with a room temperature ^{57}Co radioactive source in a Rh matrix. Mössbauer spectra as a function of temperature were recorded for $4.2\ K < T < 300\ K$ using a Lakeshore temperature controller with a liquid helium cryostat. The Mössbauer experimental spectra were computer-fitted to theoretical spectra using a nonlinear least-square curve fitting procedure. The values of isomer shift (δ), quadrupole splitting (ΔE_o) and magnetic hyperfine field (H_{hf}) were used for the iron oxide phase identification. The transition between superparamagnetism and ferrimagnetism was fully characterized by both SQUID magnetometry and Mössbauer spectroscopy.

3.4.1 Mössbauer Studies

Mössbauer spectra were recorded at selected temperatures for both as-prepared and calcined magnetic Fe_2O_3/SiO_2-coated nanocomposites without an applied field, and are shown in Figures. 3.5 and 3.6, respectively. The Mössbauer parameters derived from the spectra provide information on the oxidation states (isomer shift), coordination symmetry (quadrupole splitting) and local magnetic moment (hyperfine field) (see Table 3.1). At room temperature, both samples exhibited only a central doublet with an isomer shift and quadrupole splitting in agreement with ferric ion (Fe^{3+}) on a paramagnetic or

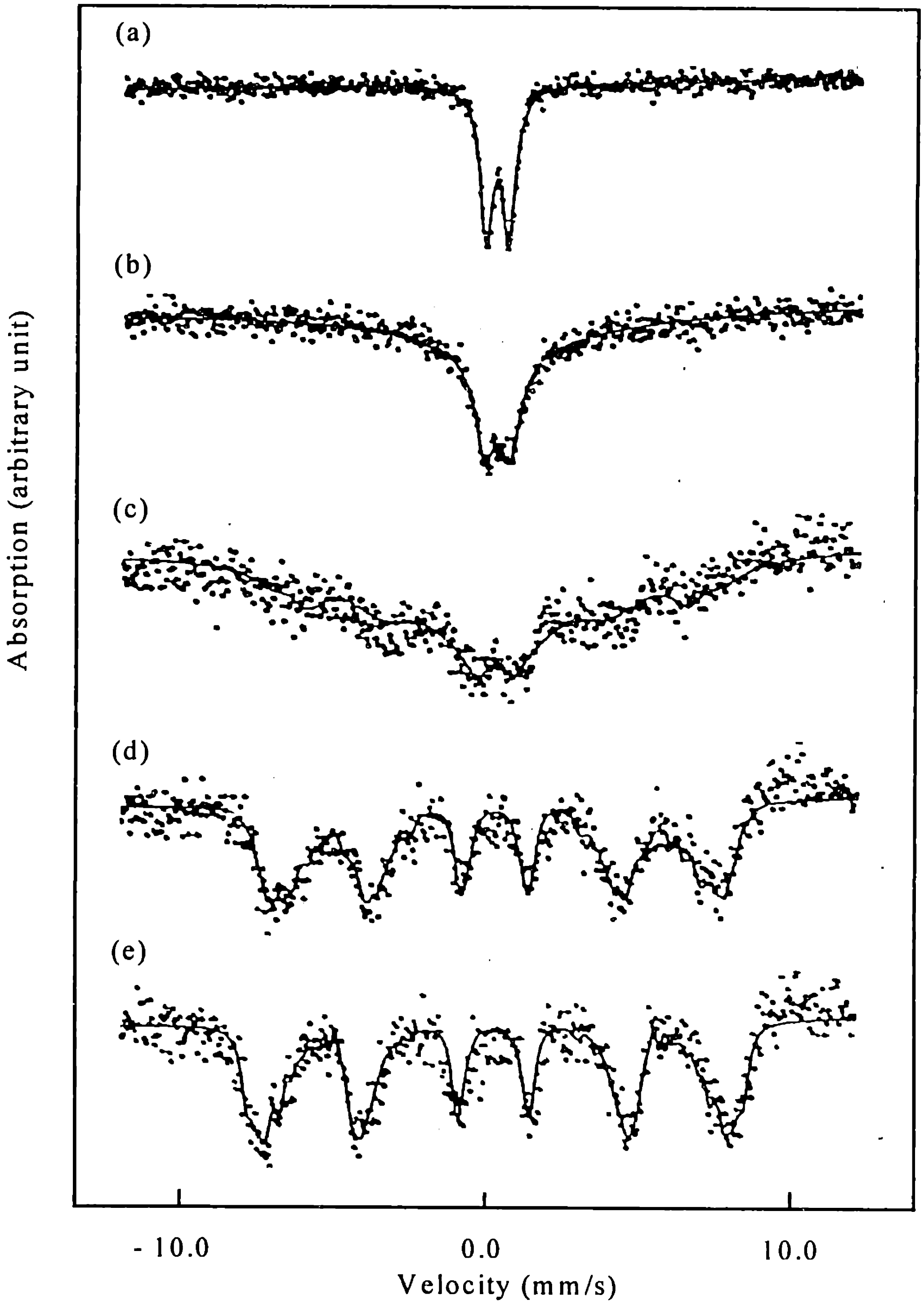

Figure 3.5. Mössbauer spectra of as-prepared Fe_2O_3/SiO_2-coated nanocomposite collected at (a) 150 K, (b) 30 K, (c) 23 K, (d) 15 K and (e) 4.2 K. The solid line is a least-square fit to the experimental data. The magnetic subcomponent was fitted to a distribution of the magnetic hyperfine fields in order to reproduce the observed spectral broadening.

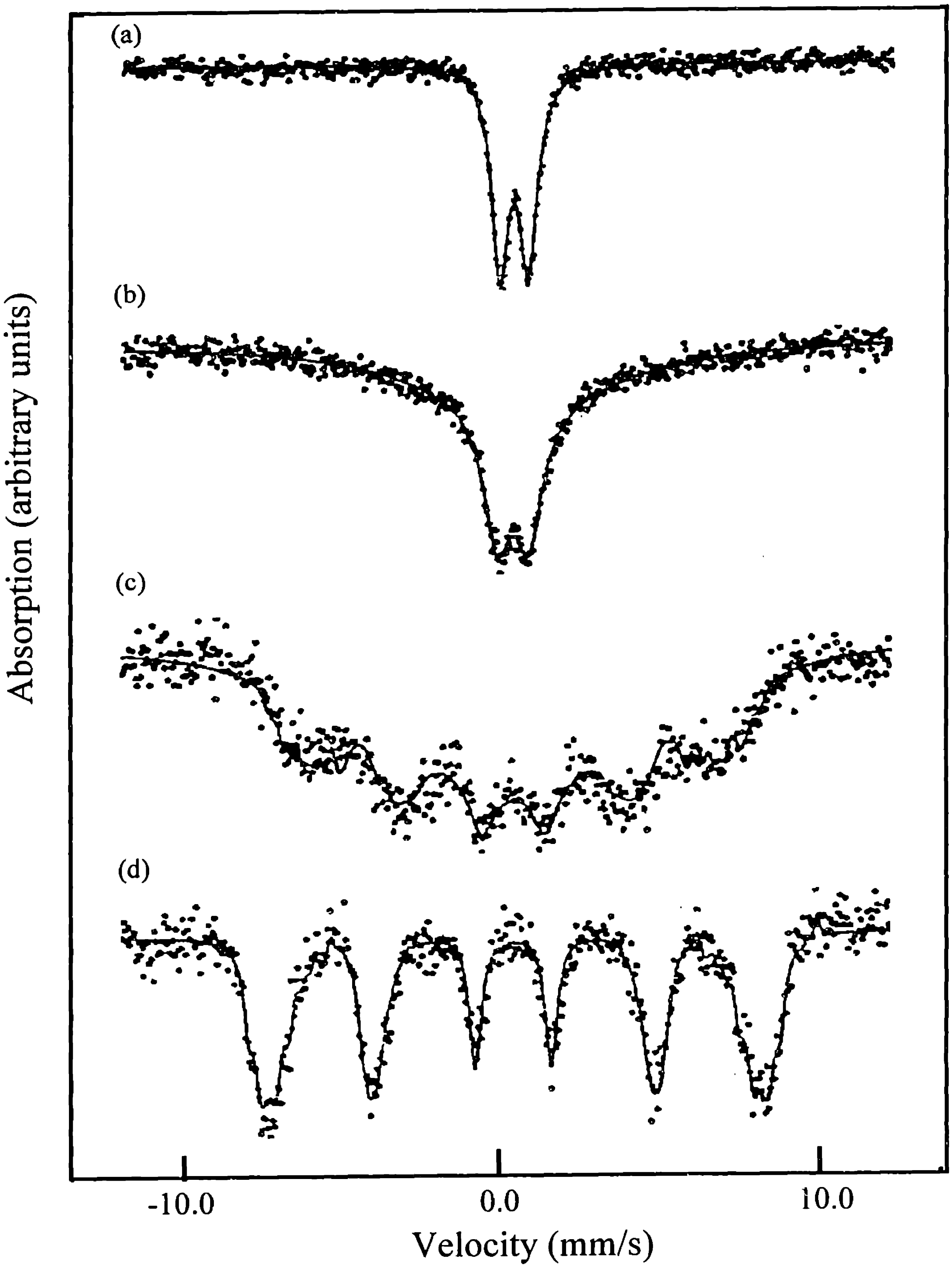

Figure 3.6. Mössbauer spectra of 250 °C O_2-calcined Fe_2O_3/SiO_2-coated nanocomposite collected at (a) 150 K, (b) 40 K, (c) 30 K and (d) 4.2 K. The solid line is a least-square fit to the experimental data. The magnetic subcomponent was fitted to a distribution of the magnetic hyperfine fields in order to reproduce the observed spectral broadening.

superparamagnetic site. Upon cooling, the intensity of the doublet was reduced and a six-line magnetic splitting pattern gradually developed. In Mössbauer spectroscopy, the superparamagnetic blocking temperature (T_b) is defined as the temperature at which the magnetically-split component possesses one-half of the total spectral absorption area. Below the T_b, the relaxation time is long compared to the ^{57}Fe nuclear Larmor precession period and the Mössbauer spectra were magnetically split. The low-temperature magnetic transformation indicated the occurrence of superparamagnetic relaxation. For the as-prepared sample, the blocking temperature was estimated to be ~23 K.

Table 3.1. Mössbauer parameters for the Fe_2O_3/SiO_2-coated samples at selected temperatures

Sample	Temperature T (K)	Isomer Shift[a, b] δ (mm/s)	Quadrupole Splitting[a] ΔE_0 (mm/s)	Hyperfine Field H_{hf} (kOe)
As-prepared Fe_2O_3/SiO_2-coated sample	298	0.35	0.75	---
	150	0.43	0.75	---
	30	0.43	0.83	unresolved background
	23	---	---	relaxation spectrum
	15	0.46	---	H_{max}= 460
	4.2	0.46	---	H_{max}= 480
Fe_2O_3/SiO_2-coated sample calcined at 250 °C	298	0.35	0.90	---
	4.2	0.48	---	H_{max}= 485
Bulk γ-Fe_2O_3 A+B sites averaged	298	0.35 [c]	---	496 [d]

[a] Uncertainties in δ and ΔE_0 are ± 0.03 mm/s and ± 0.05mm/s, respectively.

[b] Isomer shift is relative to metallic iron at room temperature.

[c] Reference 7.

[d] Reference **8.**

For fine particles, line broadening prevents phase identification by XRD. The phase of Fe_2O_3 can be determined from Mössbauer parameters such as isomer shift and magnetic hyperfine field. At room temperature, bulk γ-Fe_2O_3 (maghemite) has an isomer shift of 0.35 mm/s from the averaged values of A and B sites in the spinel structure[7] and

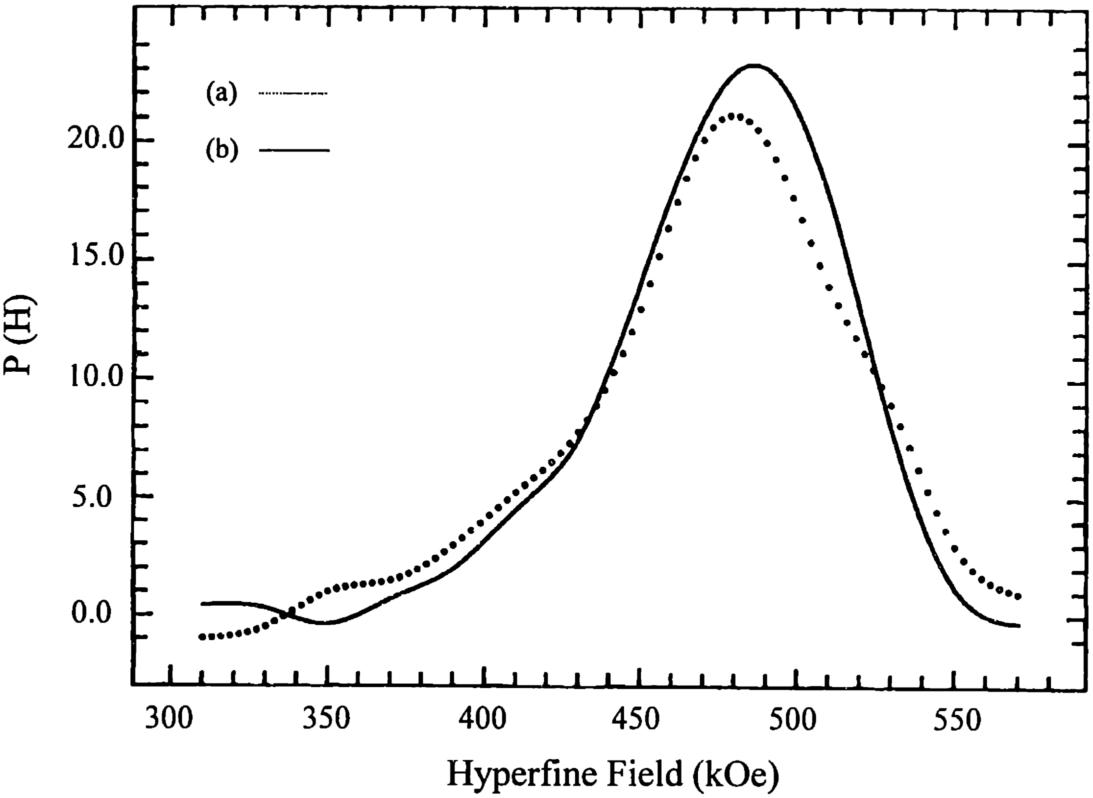

Figure 3.7. The hyperfine field distributions obtained at 4.2 K for Fe_2O_3/SiO_2-coated nanocomposite (a) as-prepared and (b) calcined at 250 °C in O_2.

a hyperfine field of 496 kOe (A + B sites).[8] The observed isomer shift for the nanocomposite is in good agreement with the literature values, confirming the presence of γ-Fe_2O_3 in the SiO_2-coated iron oxide nanocomposite. The value for the magnetic hyperfine field is reduced from that of the bulk material. A number of factors could have contributed to this observed reduction, such as collective magnetic excitations, weaker exchange interactions in the size confined system, and specific particle/matrix interactions.

For ultrafine particles, the Mössbauer spectra are dominated by collective magnetic excitations of the particle moment about the anisotropy axis of the particle at $T < T_b$.[9,10,11] The detailed temperature-dependent studies of the Mössbauer spectra can probe the dynamic magnetism of the particles and spin fluctuations at the particle/support interface.[12] At T = 4.2 K, a broad six-line nuclear Zeeman split spectrum was clearly resolved. Spectral fitting to a discrete distribution of magnetic hyperfine fields gave a field distribution with the maximum value (H_{max}) at 480 kOe, shown in Figure 3.7(a).

The width of the hyperfine field distribution indicated that a distribution of anisotropy energy barriers, $K_{eff}V$, existed in the sample due to a distribution of particle sizes. The overall splitting of the sextet, which would give a measure of the average internal hyperfine field, showed a strong temperature dependence, decreasing with increase in temperature. The presence of the collective magnetic excitations was indicated by the fact that the H_{max} of the magnetic hyperfine field distribution shifted to lower values with increasing temperature. For the as-prepared sample, the spectral fitting gives H_{max} = 460 kOe at 15 K, which is 20 kOe lower than the value at 4.2 K (see Table 3.1).

3.4.2 SQUID Studies

The isothermal magnetization of the as-prepared sample as a function of applied field at 300 K is presented in Fig 3.8(a). With increasing applied magnetic field, the magnetization increased rapidly without saturation up to an applied magnetic field of 30 kG. The lack of magnetic saturation can be attributed to two separate factors: (a) the presence of a distribution of particle sizes and, therefore, persistence of superparamagnetic relaxation of the smaller particles in the size distribution, and (b) the non-collinear spin structure of the small particles.[13,14] The unsaturated magnetization has been reported by de Bakker *et al.*[15] The hysteresis measurement also gave a zero remanence (M_r) and coercivity (H_c). The nanocomposite displayed superparamagnetic behavior at room temperature. As the temperature was reduced, the magnetization of the Fe_2O_3/SiO_2-coated nanocomposite increased and exhibited a symmetric hysteresis loop (relative to the origin) under both zero field cooled and field cooled measurement at $T \leq$ 10 K (Figure 3.8(b)), indicating the transition from superparamagnetic to ferrimagnetic behavior. The lower T_b compared with Mössbauer data could be attributed to the difference in the instrument measurement time, which was of the order of 10-100 sec for SQUID and 10^{-8} sec for ^{57}Fe Mössbauer spectroscopy.

The magnetization M (T = 5 K, Figure 3.8(c)) of 20 emu/g Fe_2O_3 for the nanoclusters under 30 kG applied field is much smaller than that of the bulk γ-Fe_2O_3 (M_s = 76 emu/g) at 298 K. The discontinuity of superexchange bonds between Fe cations near the surface leads to a canted spin structure.[13] The moment of the ultrafine SiO_2-coated particles with a high portion of surface ions has a large average canting angle to the spin direction of the interior of the particle, due to the pinning of the surface spins at the interface between the magnetic particles and the SiO_2 coating, resulting in a significant decrease in the magnetization and lack of saturation for the nanocomposite material. The existence of canted or disordered surface spins as a mechanism for reduction in the magnetic moment of ordered particles has been proven by a number of techniques. Early investigations of chemically precipitated γ-Fe_2O_3 and ball milled $NiFe_2O_4$ by Mössbauer spectroscopy in applied magnetic fields have demonstrated the present of surface spin pinning.[13,16,17] Using spin polarized neutron scattering, recent studies on ball milled $NiFe_2O_4$ were consistent with the presence of a ferrimagnetically aligned core and a spin disordered surface layer.[18] High field magnetization studies of 6.5 nm ball milled $CoFe_2O_4$ particles have been successfully modeled by assuming a spin-glass-like surface layer due to broken superexchange bonds at the surface, in the presence or absence of surfactants.[19]

Typical coercivity of bulk γ-Fe_2O_3 ranges from 250 G to 400 G.[20] At T= 5 K, the hysteresis loop of the nanocomposite (Figure 3.8(c)) corresponded to a remanence of 2.5 emu/g Fe_2O_3 and a coercivity of 635 G. The smaller remanence and larger coercivity of the nanocomposite relative to bulk γ-Fe_2O_3 are due to the single domain size of the clusters in the nanocomposite where the coercivity comes from the coherent rotation of the magnetization of the particle away from its easy axis. This is an energetically more demanding step than the movement of domain walls, which is responsible for the coercivity in the bulk material or the incoherent spin reversal present in larger particles.[21] It is interesting to note that coercivity decreased with an increase in temperature, indicating that a larger fraction of the clusters underwent a superparamagnetic to ferrimagnetic transition at lower temperatures. This effect also resulted from the presence of a distribution of particle sizes in the real system.

When the magnetization was plotted as a function of the reduced parameter H/T (Figure 3.9), the curves at different temperatures above the blocking temperature were

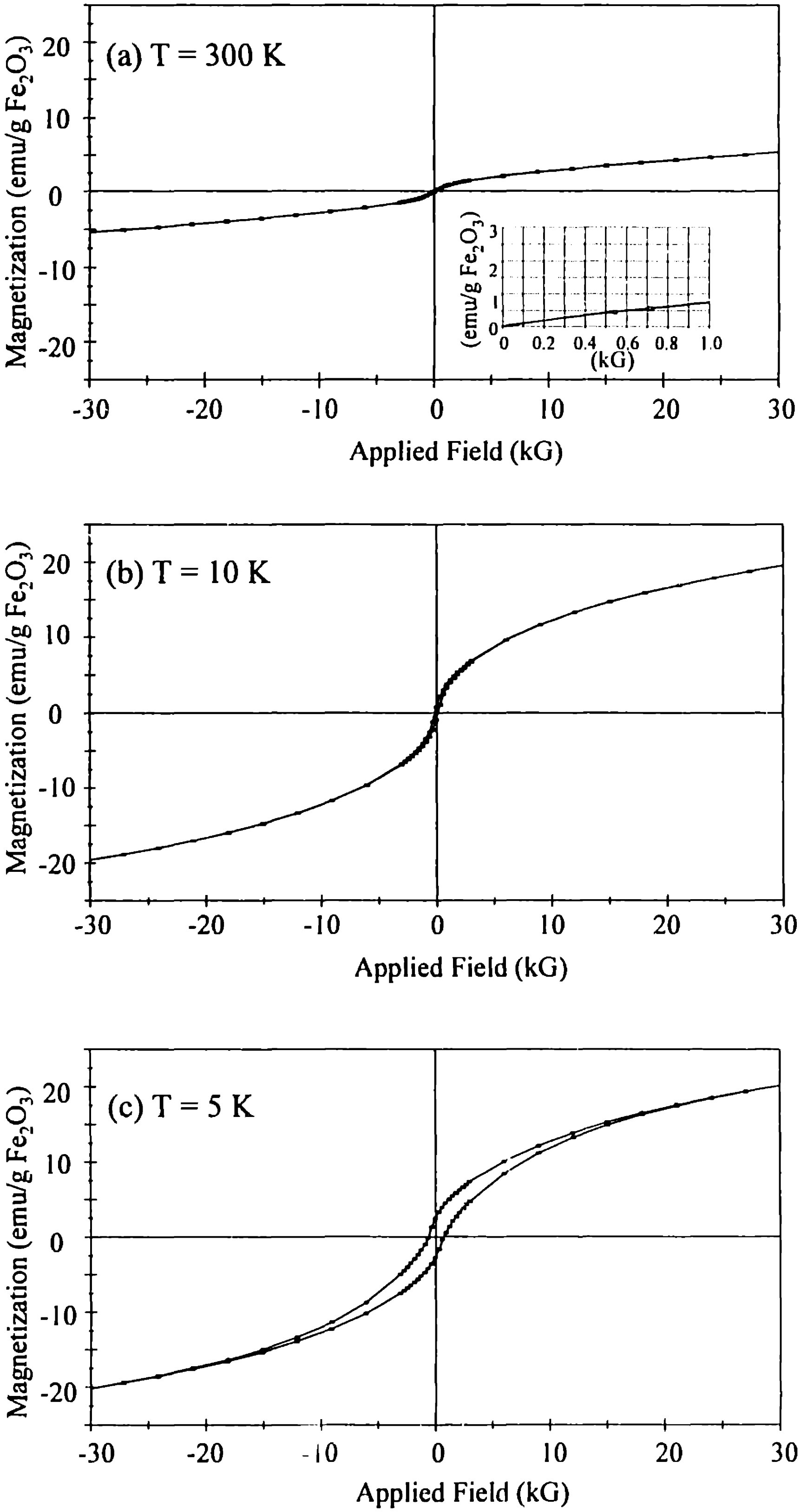

Figure 3.8. Plots of magnetization vs. applied field for as-prepared Fe_2O_3/SiO_2-coated nanocomposite obtained at (a) 300 K, (b) 10 K, and (c) 5 K.

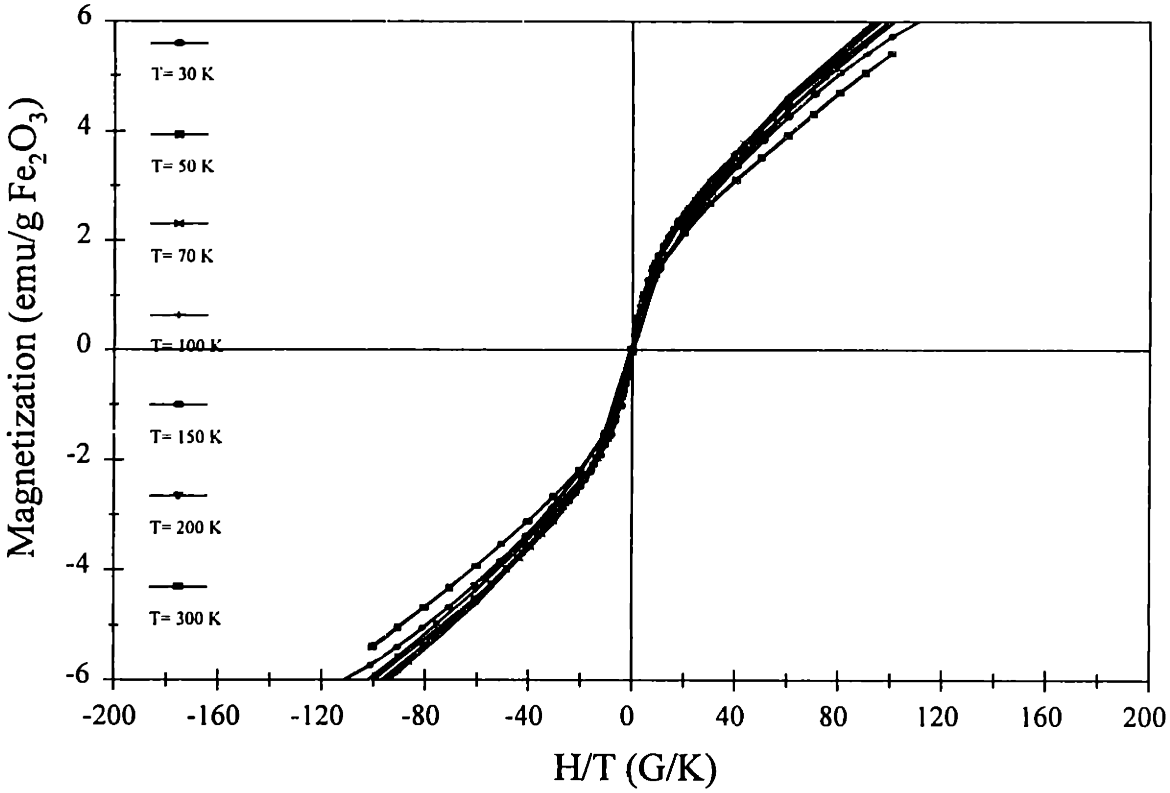

Figure 3.9. Normalized magnetization curves for as-prepared Fe_2O_3/SiO_2-coated nanocomposite obtained at the temperatures noted.

superimposed with a shape consistent with the Langevin function given in Eq. (2.9), confirming the superparamagnetism of the nanocomposite system. The minor deviation between the curves results from the distribution in particle size, and the variation in anisotropy constants arises from the minor differences in particle shape and surface properties.

The temperature dependence of the magnetization investigated under zero field cooling (M_{ZFC}) and field cooling (M_{FC}) gave further confirmation of superparamagnetism in the nanoclusters, as shown in Figure 3.10. The sharp maximum of the M_{ZFC} at T_{max} = 15 K and the splitting between M_{ZFC} and M_{FC} curves just above T_{max} indicate a narrow particle size distribution. The continued increase of the magnetization under field cooling illustrates the presence of ultrafine superparamagnetic particles. T_{max} is related to the superparamagnetic blocking temperature and is somewhat dependent on the strength

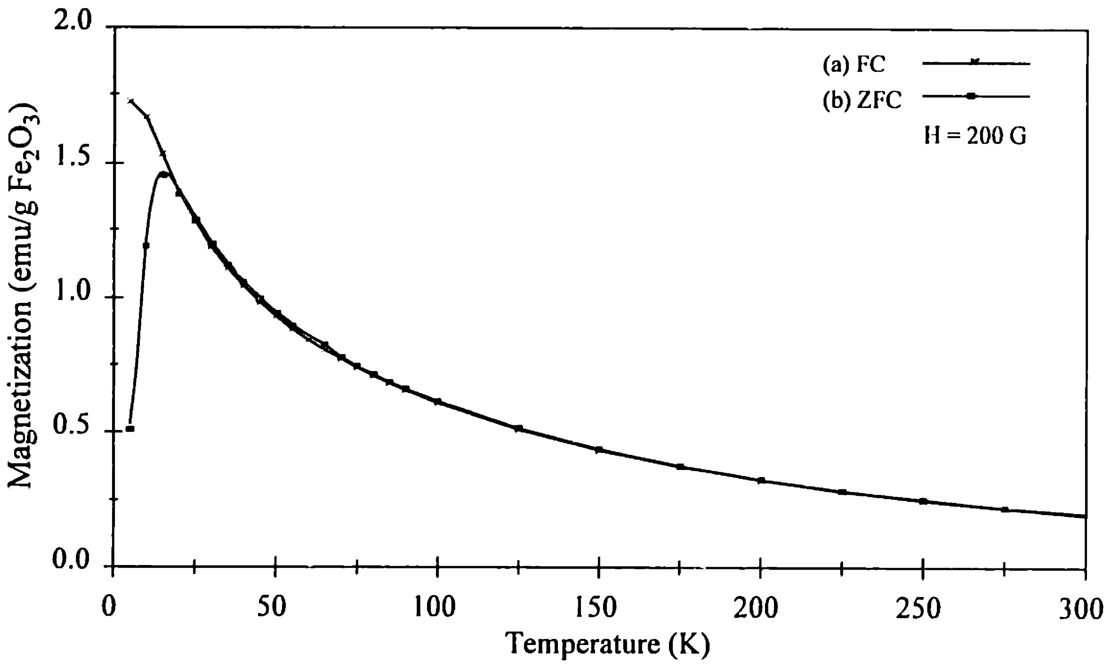

Figure 3.10. Temperature dependence of the magnetization curves under (a) field cooling and (b) zero field cooling for as-prepared Fe_2O_3/SiO_2-coated nanocomposite.

of the external magnetic field. It has been shown that the superparamagnetic blocking temperature decreases with decreasing cluster size. Under the same external field (H = 200 G), the lower T_{max} suggests that the γ-Fe_2O_3 clusters in our SiO_2-coated iron oxide system are smaller compared to the recently reported 83 Å γ-Fe_2O_3 in polymer matrix which has a T_{max} of 40 K.[22,23]

For non-interacting uniformly magnetized particles, the effective anisotropy constant K_{eff} results from the combined effect of magnetocrystalline anisotropy K_V, shape anisotropy K_{sh} and surface anisotropy K_s: $K_{eff} = K_V + K_{sh} + K_s$. For the coated spherical particles, the interface may exert surface strain (compression or tension) on the particles and add another contribution K_σ to the anisotropy constant: $K_{eff} = K_V + K_s + K_\sigma$. The strain effect depends on the magnetostriction constant of the material. These various contributions to the total anisotropy may enhance or oppose each other. Using the average spherical cluster size of 4 nm from TEM imaging, an effective uniaxial anisotropy constant $K_{eff} = 1.57 \times 10^5$ J/m^3 is obtained from Eq. (2.6) with a measuring time τ_m = 100 sec, T_b = 15 K, and a pre-exponential factor $\tau_0 = 10^{-9}$ sec, as usually assumed for these systems. This effective anisotropy constant is of the same order of magnitude as the previously published results for both the 83 Å γ-Fe_2O_3 in polymer matrix (4.4×10^5 J/m^3, magnetic susceptibility data)[23] and the 65 Å γ-Fe_2O_3 particles (1.2×10^5 J/m^3, Mössbauer data);[24] it is two orders of magnitude larger than that of epitaxial single-crystal films and polycrystalline powders of γ-Fe_2O_3 ($K_1 = 4.7 \times 10^3$ J/m^3).[25,26] The large magnetic anisotropy constant suggests that, in our case, the surface and/or strain anisotropy is appreciable and determines the magnetic anisotropy energy, while the magnetocrystalline anisotropy and shape anisotropy are negligible. Since the nanoclusters have a large surface-to-volume ratio and are isolated by the SiO_2 matrix, difficulties exist in separating the surface effects from the strain effect.

The cluster size distribution can also be obtained from the fraction f(T) of the clusters with volume greater than the critical volume (V_c) defined by superparamagnetism.[27] Assuming the Debye-Waller factors are equal, f(T) will be calculated from the ratio of integrated intensity in the magnetic hyperfine spectrum over the total intensity, expressed in Eq. (3.1).

$$f(T) = \frac{\int_{V(T)}^{\infty} n(V')dV'}{\int_0^{\infty} n(V')dV'} = 1 - \frac{1}{N}\int_0^{V(T)} n(V')dV' \qquad (3.1)$$

where n(V') is the particle size distribution, V(T) is the critical volume at a given temperature T, and N is the total number of particles. From equation (3.1), we can see that the particle size distribution n(V') is proportional to -df(T)/dV.

Since V and T are related by Eq. (2.6), we can calculate the fraction of particle volume f(V) from f(T). As shown in Figure 3.11, the solid line is f(T) as a function of temperature. The particle size distribution (Figure 3.11(b)) can be determined from the negative value of the slope of f(T). When the temperature is transformed to diameter (d) on x-axis, we obtained a maximum of the particle size distribution n(d) at 4.2 nm using a

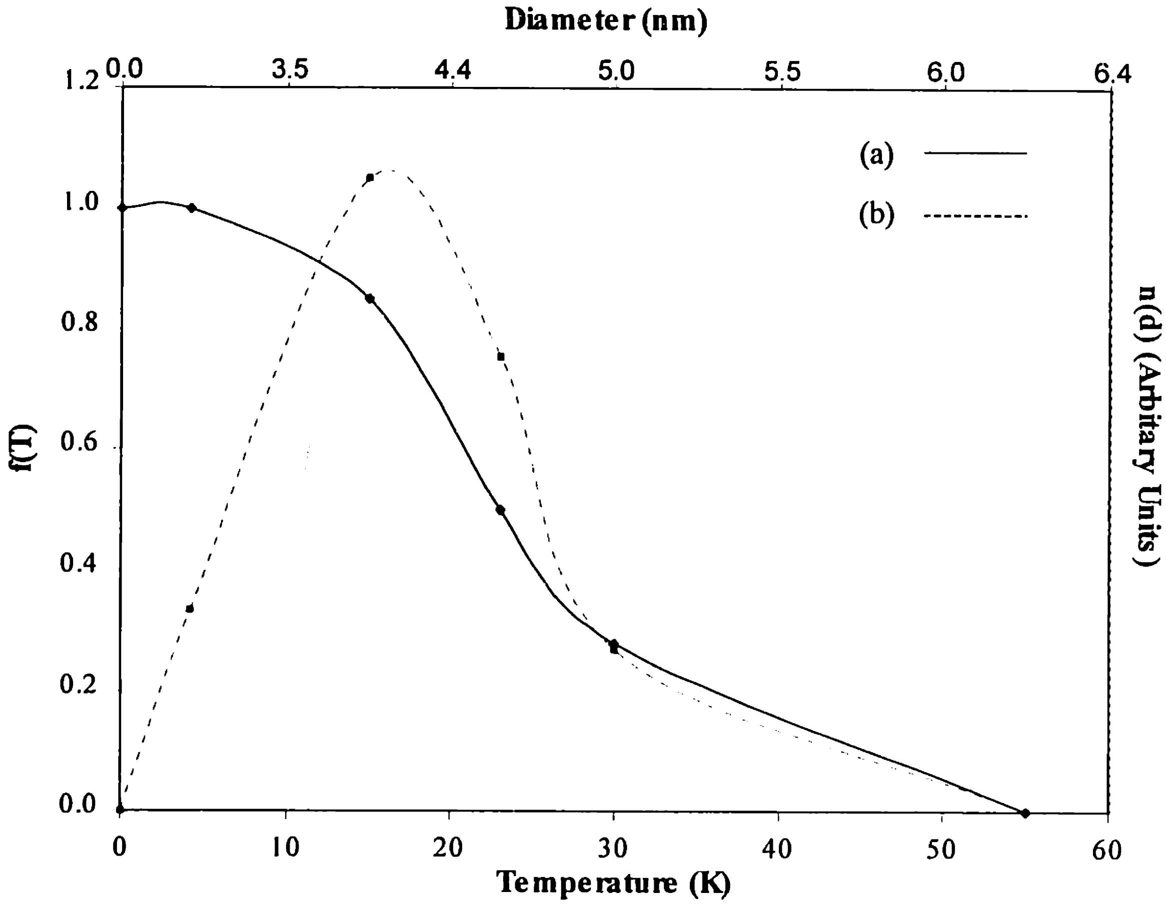

Figure 3.11. (a) The fraction of particles with size larger than the critical volume for superparamagnetic behavior as a function of temperature, and (b) the derived particle size distribution.

constant magnetic anisotropy constant $K_{eff} = 1.57 \times 10^5$ J/m^3. This is in good agreement with the TEM observation of particle size.

Independently, K_{eff} can be calculated from the Mössbauer parameters using the collective magnetic excitation theory[9] and characteristic instrument measurement time of the technique ($\tau_m = 10^{-8}$ sec). Although the probability that the magnetization vector will surmount the energy barrier is negligible at $T < T_b$, the spectra may still be affected by small fluctuations of the magnetization vector about the easy axis. For $kT << K_{eff}V$, the observed magnetic hyperfine field can be approximated with Eq. (3.2):

$$H_{hf} = H_{hf0}(1 - kT/2K_{eff}V) \qquad (3.2)$$

where H_{hf0} is the saturation hyperfine field.[9] Using the volume estimated from the average TEM particle diameter of 4 nm and evaluating Eq. (3.2) at T = 4.2 K and T = 15 K, we can solve for K_{eff} and H_{hf0} expected at 0 K. We obtained $K_{eff} = 0.55 \times 10^5$ J/m^3 and H_{hf0} = 487 kOe. Using the Mössbauer-determined K_{eff} and T_b values with $\tau_m = 10^{-8}$ sec, we arrived at an estimate of $\tau_0 = 3.3 \times 10^{-11}$ sec for the nanocomposite from Eq. (2.6), which is within the accepted range of 10^{-10} - 10^{-13} sec.[28,29] The saturation field for the nanocomposite is smaller than the 528 kOe value calculated for bulk γ-Fe_2O_3.[30] The lower saturation field indicates weaker exchange interactions between iron spins within the clusters and reflects primarily spin exchange at the specific particle/coating interface. However, the distribution of the internal hyperfine fields obtained from fitting the spectra at T = 4.2 K is rather broad and extends to 550 kOe for the larger particles in the distribution. The K_{eff} evaluated from Mössbauer data is of a somewhat smaller value compared with that from SQUID measurements. Since the characteristic measuring times of the instruments are known within a factor of 10 to 100, calculated K_{eff} values may differ by as much as a factor of 2 to 4. However, this difference may also reflect the accuracy to which the first order approximation in Eq. (3.2) describes the dependence on temperature.[9] It is also possible the observed difference in K_{eff}'s indicates the presence of non-uniaxial anisotropy symmetry in our spherical sample with the smaller K_{eff} corresponding to the lower anisotropy energy axis.

3.5 Thermal Stability of γ-Fe_2O_3/SiO_2-Coated Nanocomposites

The excellent thermal stability is an intrinsic advantage with the inorganic matrix of the nanocomposite. The TEM results illustrated that the morphology and particle size remained unchanged in our γ-Fe_2O_3/SiO_2-coated sample calcined at 250 ^{0}C under O_2 (Figure 3.4(b)). The SQUID measurement was also conducted on the calcined sample to explore the magnetic behavior. The isothermal magnetization plots at different temperatures showed the onset of hysteresis at T = 15 K (Figure 3.12). A T_{max} of 23 K was noted in the magnetization measurement under zero field cooling (Figure 3.13).

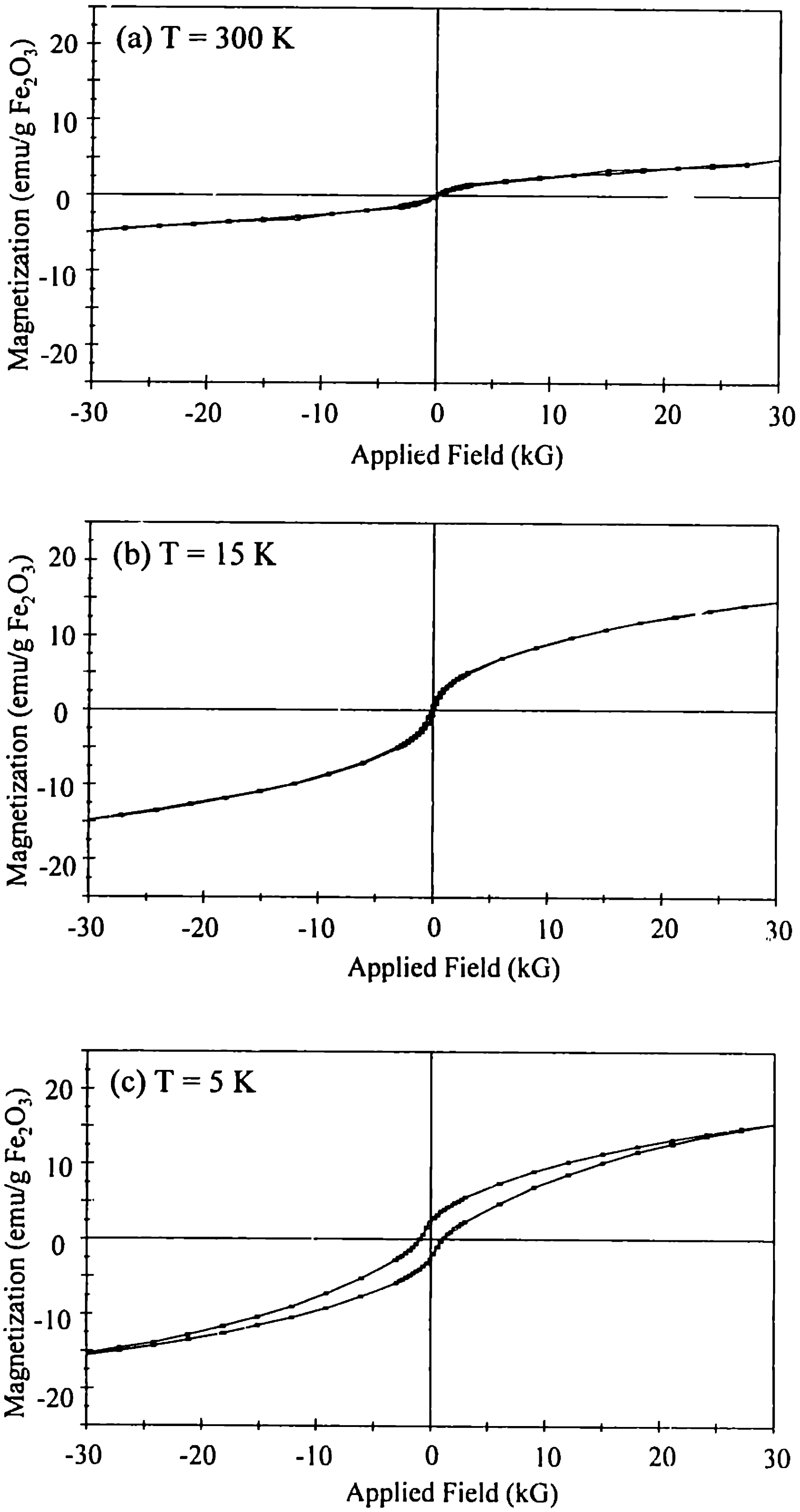

Figure 3.12. Plots of magnetization vs. applied field for 250 °C O_2-calcined Fe_2O_3/SiO_2-coated nanocomposite obtained at (a) 300 K, (b) 15 K, and (c) 5 K.

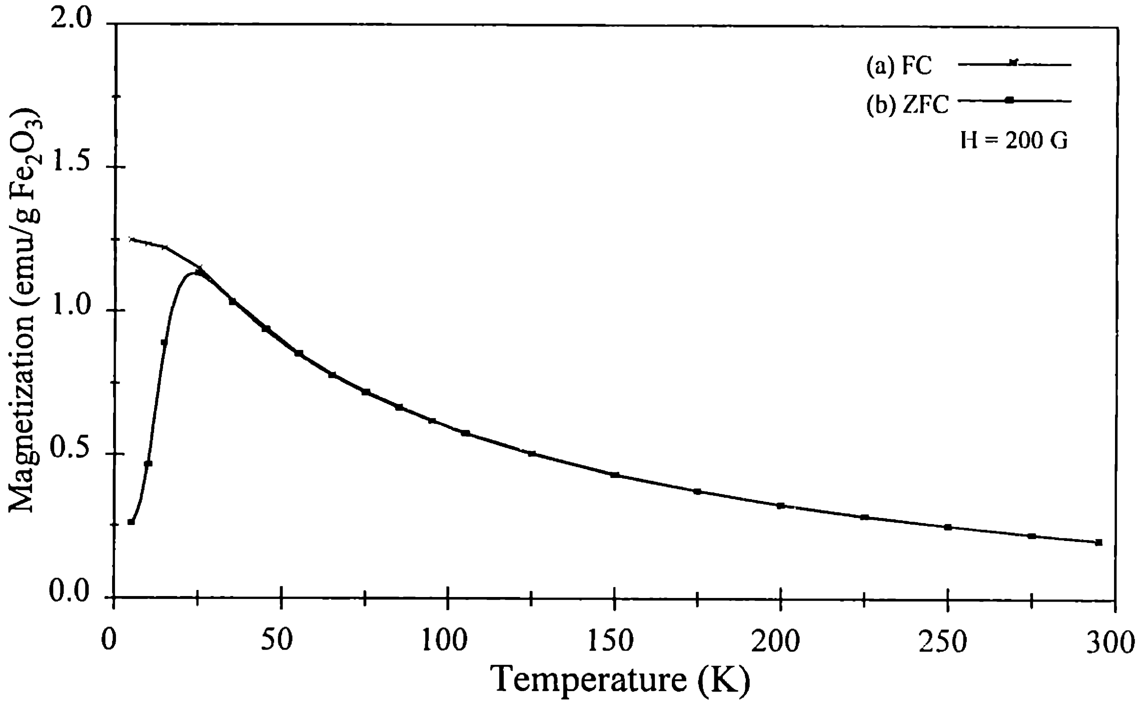

Figure 3.13. Temperature dependence of the magnetization curves under (a) field cooling and (b) zero field cooling for 250 °C O_2-calcined Fe_2O_3/SiO_2-coated nanocomposite.

The Mössbauer studies of the calcined sample showed onset of the magnetic hyperfine splitting at 40 K and a sharper magnetic structure at 4.2 K (Figure. 3.6). Compared to the as-prepared sample, the calcined sample has the same isomer shift and a slightly larger H_{max} of 485 kOe (Table 3.1), with a narrower field distribution (Figure 3.7(b)). The similarity in isomer shift and hyperfine field values suggests no phase change under the heat treatment. The increase in the quadrupole splitting from 0.75 mm/s to 0.90 mm/sec upon calcination probably reflects a change in the particle/coating binding sites. Calcination may have resulted in an increase in Fe_2O_3 crystallinity and the removal of adsorbed water and residual organic substance from the nanocomposite. The similarity in the magnetic behavior of our calcined and as-prepared samples demonstrates the attractive thermal stability of the γ-Fe_2O_3/SiO_2-coated nanocomposites that can present a significant advantage in materials applications.

3.6 Optical Properties of γ-Fe_2O_3/SiO_2-Coated Nanocomposites

To examine the optical properties of the γ-Fe_2O_3/SiO_2-coated nanocomposites, diffuse reflectance spectra were obtained on a Cary 5E UV-VisNir spectrophotometer operating in the UV-Vis range. The sample was ground into a fine powder, and compacted into a pellet with a hydraulic press.

A correlation between the particle size and particle/support interface microstructure with the optical properties of the nanocomposites can provide useful insights into the stress-induced effects on ultrafine nanoclusters. The UV-Vis diffuse reflectance spectrum of the as-prepared sample (Figure 3.14(a)) shows a slight blue shift in the absorption edge compared to the bulk γ-Fe_2O_3 reference. This is consistent with the quantum confinement effect that predicts a widening of the electronic band gap between the valence and conduction bands with decreasing particle size. Considering the

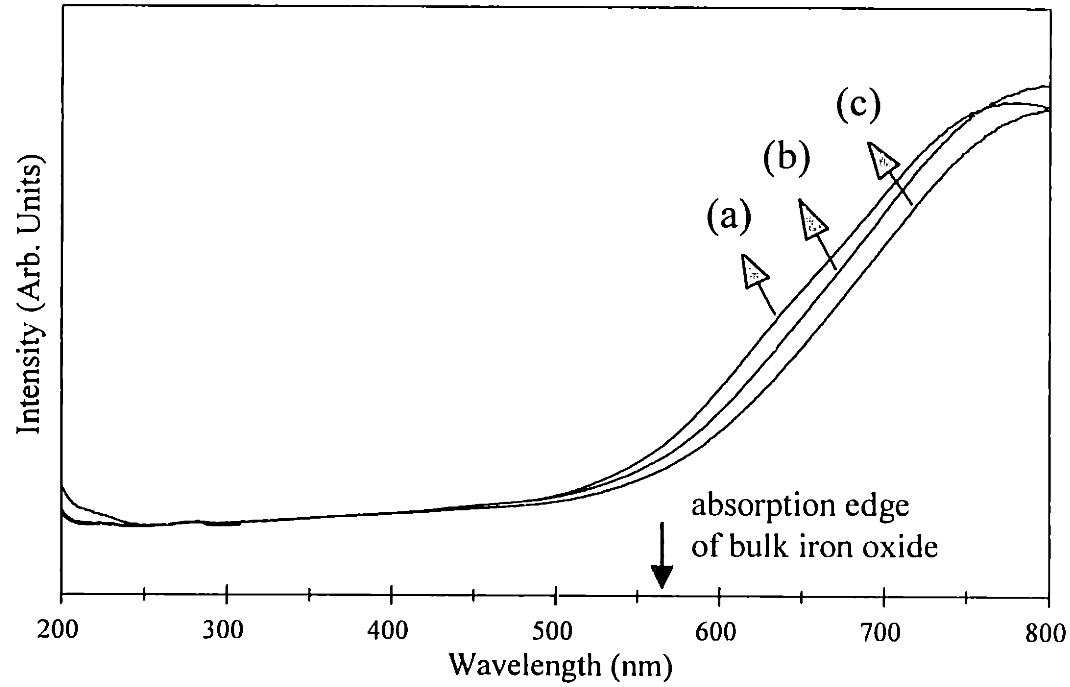

Figure 3.14. UV-Vis diffuse reflectance spectra of Fe_2O_3/SiO_2-coated nanocomposite (a) as-prepared, (b) calcined at 250 °C, and (c) calcined at 350 °C.

size of the nanoclusters, the relatively small shift might be due to the presence of stress exerted by the coating, altering the lattice constant compared to the bulk. Stress has been proposed to produce a red shift of the absorption edge of the polymer-supported γ-Fe_2O_3.[22,23] It is also interesting to note that the absorption edge moves to higher wavelengths with increasing calcination temperatures (Figure 3.14(b) and (c)). This red shift is related to the changes in either the size of the nanoclusters or the stress on the interface during calcination. Since TEM showed that the size change is negligible in this case, it is inferred that the interface plays an important role in determining the optical behavior.

3.7 Summary

Superparamagnetic iron oxide nanoclusters were synthesized via chemical precipitation and isolated with SiO_2 coating. The sol-gel derived inorganic coating enabled iron oxide cluster confinement and manipulation of the interfacial characteristics. The well-dispersed particles derived by this synthetic route displayed a spherical morphology. The magnetic nanocrystallites were identified as γ-Fe_2O_3 by Mössbauer spectroscopy. A lower magnetization was noted in the Fe_2O_3/SiO_2-coated nanocomposites compared to the bulk γ-Fe_2O_3, which might be due to superparamagnetic relaxation, spin canting on the surface of the ultrafine clusters, or a non-collinear spin structure that reduced the total moment of the magnetic clusters. A blue shift was noted in the optical spectra, illustrating the quantum confinement effect in this nanocomposite system. The magnetic and optical studies also indicated that the interface between the iron oxide nanoclusters and the SiO_2 coating is important towards tailoring the overall magnetic and optical properties of the nanocomposites. These new materials are of interest not only to fundamental physics, such as the quantum tunneling effect of magnetization, but also for magneto-optical applications.

3.8 References

[1] L. Zhang, G. C. Papaefthymiou, R. F. Ziolo, and J. Y. Ying, Nanostruct. Mater., **9**, (1997) 185.

[2] L. Zhang, G. C. Papaefthymiou, and J. Y. Ying, J. Appl. Phys., **81**, (1997) 6892.

[3] U. Schwertmann and E. Murad, Clays Clay Miner., **31**, (1983) 277.

[4] E. Tronc and J. P. Jolivet, in *Nanophase Materials: Synthesis-Properties-Applications*, edited by G.C. Hadjipanayis and R.W. Siegel, Kluwer, Boston, (1994) 21.

[5] J. Y. Ying, J. B. Benziger, and A. Navrotsky, J. Am. Ceram. Soc., **76**, (1993) 2571.

[6] C. J. Brinker and G. W. Scherer, *Sol-Gel Science: The Physics and Chemistry of Sol-Gel Processing*, Academic Press, San Diego, CA, (1990).

[7] N. N. Greenwood and T. C. Gibb, *Mössbauer Spectroscopy*, Chapman Hall, London, (1971) 241.

[8] H. V. Kelly, V. J. Folen, M. Hass, W. N. Schreiner, and G. B. Beard, Phys. Rev., **122,** (1961) 1447.

[9] S. Mørup and H. Topsøe, J. Appl. Phys., **11,** (1976) 63.

[10] T. Shinjo, IEEE Trans. Mag., **MAG-12**, (1976) 86.

[11] K. Haneda and A. H. Morrish, Phys. Lett., **64A**, (1977) 259.

[12] A. H. Morrish, in *Magnetic Properties of Fine Particles*, edited by J. L. Dormann and D. Fiorani, Elsevier, North-Holland, (1992) 181.

[13] J. M. D. Coey, Phys. Rev. Lett., **27**, (1971) 1140.

[14] Q. A. Pankhurtst and R. J. Pollard, Phys. Rev. Lett., **67**, (1991) 248.

[15] P. M. A. de Bakker, E. DeGrave, R. E. Vandenberghe, and L. H. Bowen, Hyperfine Int., **54**, (1990) 493.

[16] A. E. Berkowitz, J. A. Bahut, I. S. Jacobs, L. M. Levison, and D. W. Forester, Phys. Rev. Lett., **34**, (1975) 594.

[17] A. E. Berkowitz, J. A. Lahut, and C. E. Vanburen, IEEE Trans. Magn., **MAG-16,** (1980) 184.

[18] D. Lin, A. A. Nunes, C. F. Majkrzak, and A. E. Berkowitz, J. Magn. Magn. Mater., **145**, (1995) 343.

[19] R. H. Kadama, A. E. Berkowitz, E. J. McNiff, Jr., and S. Foner, Phys. Rev. Lett., **77**, (1996) 394.

[20] A. H. Morrish, in *Crystals: Growth, Properties, and Applications*, mgr. edited by H. C. Freyhardt, Springer-Verlag, New York, **2**, (1980) 171.

[21] A. H. Morrish, *The Physical Principles of Magnetism*, Wiley, New York, (1966) Chapter 7.

[22] R. F. Ziolo, E. P. Giannelis, B. A. Weinstein, M. P. O'Horo, B. N. Ganguly, V. Mehrotra, M. W. Russell, and D. R. Huffman, Science, **257**, (1992) 219.

[23] J. K. Vassiliou, V. Mehrotra, M. W. Russell, E. P. Giannelis, R. D. McMichael, R. D. Shull, and R. F. Ziolo, J. Appl. Phys., **73**, (1993) 5109.

[24] J. M. D. Coey and D. Khalafalla, Phys. Stat. Sol. A, **11**, (1972) 229.

[25] H. Takei and S. Chiba, J. Phys. Soc. Jpn., **21**, (1966) 1255.

[26] A. H. Morrish and E. P. Valstyn, J. Phys. Soc. Jpn., **17**, B-1, (1962) 392.

[27] K. S. Kaufman, G. C. Papaefthymiou, R. B. Frankel, A. Rosenthal, Biochim. Biop . Acta., (1980) 522.

[28] D. P. E. Dickson, N. M. K. Reid, C. Hunt, H. D. Williams, M. E. Hilo, and K. O'Grandy, J. Magn. Magn. Mater., **125**, (1993) 345.

[29] C. L. Chien, in *Science and Technology of Nanostructured Magnetic Materials*, NATO ASI Series B, edited by G. C. Hadjipanayis and G. A. Prinz, Plenum Press, New York, **259**, (1991) 477.

[30] E. Murad, in *Magnetic Properties of Fine Particles*, edited by J. L. Dormann and D. Fiorani, Elsevier, North-Holland, (1992) 339.

Chapter 4

SYNTHESIS AND MAGNETIC PROPERTIES OF γ-Fe_2O_3 NANOCLUSTERS IN MESOPOROUS ALUMINOSILCATE MATRICES

4.1 Introduction

Highly-dispersed γ-Fe_2O_3 nanoclusters possess unique magnetic characteristics associated with quantum confinement effects. Mesoporous MCM-41 materials with hexagonally-packed pores of uniform diameters in the 2-10 nm range provide an interesting matrix for hosting magnetic nanoclusters for fundamental studies and potential device applications.[1,2] The one-dimensional cylindrical pore channels of MCM-41 can be ideal for simultaneous control of cluster size and morphology. This chapter describes the synthesis of magnetic γ-Fe_2O_3 nanoclusters within the mesopores of MCM-41 aluminosilicates through an evaporation-condensation approach. A variety of Fe_2O_3 loadings were achieved using highly volatile $Fe(CO)_5$ as a precursor.

4.2 Synthesis of Fe_2O_3 Clusters within Hexagonally-packed Mesoporous Hosts

4.2.1 Synthesis and Characterization of Mesoporous Aluminosilicate

Al-doped mesoporous silica was synthesized from an inorganic siliceous precursor using organic cationic trimethylammonium surfactants ($C_{16}H_{33}(CH_3)_3NBr$ or CTABr) as a supramolecular templating agent. 3.65 g of CTABr surfactant was completely dissolved in H_2O. 22.2 g of 27 % sodium silicate solution dispersed in 50 g of water was slowly added to the surfactant solution at room temperature with vigorous stirring. After stirring for 5 minutes, the pH of the mixture was adjusted to 11.5 with diluted H_2SO_4. A desired amount of aqueous aluminum sulfate solution was then gradually introduced to the loosely-bonded silica gel, and stirred for 3 hours at room temperature before the sample was hydrothermally treated at 100-150 °C for a desired period. The molar composition of the wet gel could be represented as 1 SiO_2 : 0.1 CTABr : 120 H_2O : x Al_2O_3 (where x = 0 to 0.1). The solid powder obtained was washed with ethanol and water, filtered, and then calcined at 540 °C in air for 6 hours to remove the organics. The samples were designated as AlSi-R, where R was given by the precursor molar ratio of Si and Al.

The quality and long-range pore packing order of the mesoporous Al-doped silica were characterized by X-ray diffractometry (XRD) (Siemens D5000 θ-θ diffractometer operated at 45 kV and 40 mA using Ni-filtered CuK_α radiation) and transmission electron microscopy (TEM) (JOEL 200CX, 200 kV). The XRD patterns of calcined AlSi-R shown in Figure 4.1 corresponded to a typical hexagonal P6m space group with the intense (100) peak as well as three well-resolved peaks corresponding to (110), (200) and (210) diffractions. The unit cell parameters of the Al-doped mesoporous silica were found to depend strongly on the aging temperature and the Al dopant concentration. It was shown that the *d*(100) spacing and diffraction peak intensity increased with aging temperature (Figure 4.2). At a given aging temperature, the unit cell parameter calculated from $a_0 = 2d(100)/\sqrt{3}$ was larger for AlSi-R than for mesoporous pure silica, and increased with an increase in the Al-dopant concentration due to the larger ionic radius of Al^{3+} (0.50 Å) and the longer Al-O bond length (1.75 Å) (see Figure 4.1 and Table 4.1).

N_2 adsorption-desorption analysis was performed on a Micromeritics ASAP 2010 gas sorption instrument. The N_2 adsorption-desorption isotherm of the calcined sample showed no hysteresis (Figure 4.3), and corresponded to a narrow Barrett-Joyner-Halenda (BJH) pore size distribution (Figure 4.4). Brunauer-Emmett-Teller (BET) surface areas of the AlSi-R samples were ~1000 m^2/g, and depended on the dopant concentration. The microstructural characteristics of the AlSi-R samples are listed in Table 4.1. The TEM micrographs of Al/Si-35 (Figure 4.5) clearly showed a hexagonally-packed pore array with averaged diameters of 25 Å and 35 Å for samples aged for 2 days at 100 °C and 180 °C, respectively. The AlSi-R molecular sieves could be synthesized with a highly ordered hexagonally-packed pore structure up to a Al:Si molar ratio of 1:5.

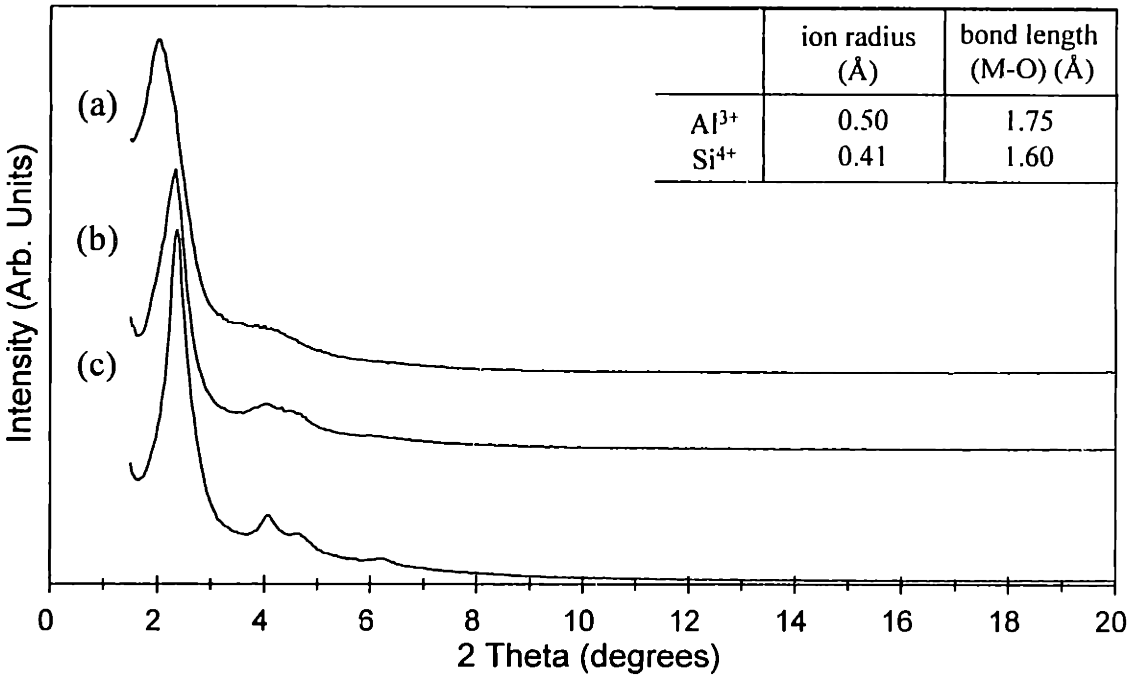

	ion radius (Å)	bond length (M-O) (Å)
Al^{3+}	0.50	1.75
Si^{4+}	0.41	1.60

Figure 4.1. XRD patterns of calcined mesoporous AlSi-R samples of different dopant concentrations aged at 100 °C: (a) R = 5, (b) R = 25, and (c) R = 50.

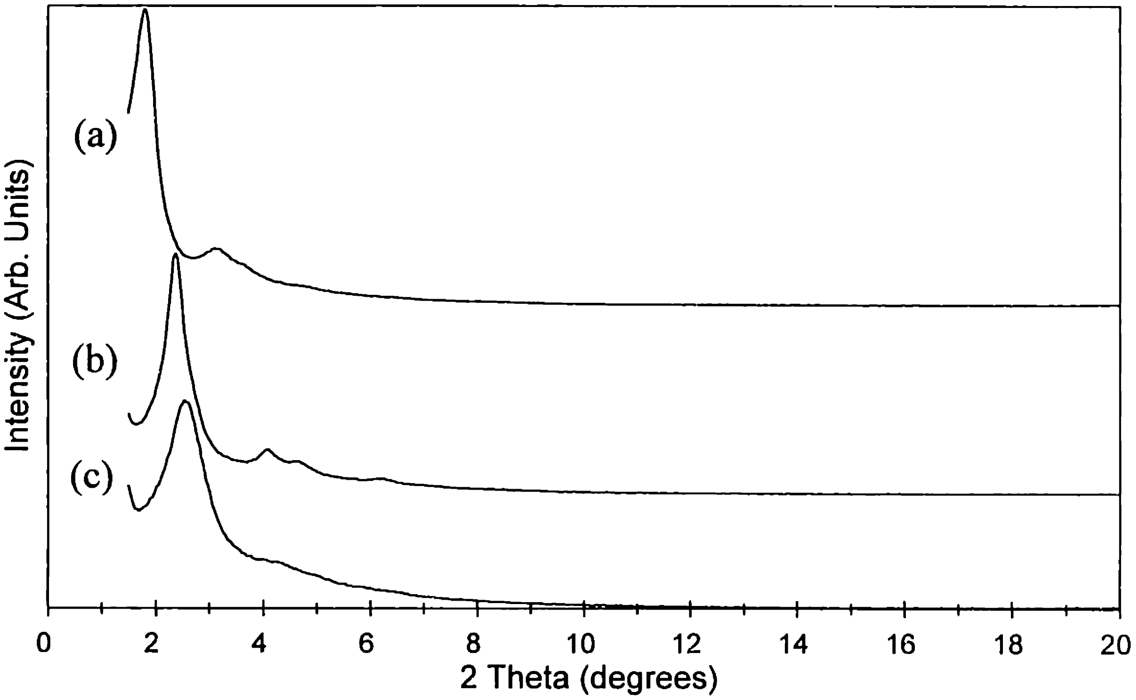

Figure 4.2. XRD patterns of calcined mesoporous AlSi-35 samples aged at (a) 180 °C, (b) 100 °C, and (c) 75 °C.

Table 4.1. Microstructural characteristics of mesoporous AlSi-R samples

R = Si:Al	a_0 (Å)	Pore Size (Å)	Wall Thickness (Å)	Surface Area (m^2/g)
5	50	26	24	1143
25	43	25	18	1217
50	41	23	18	938

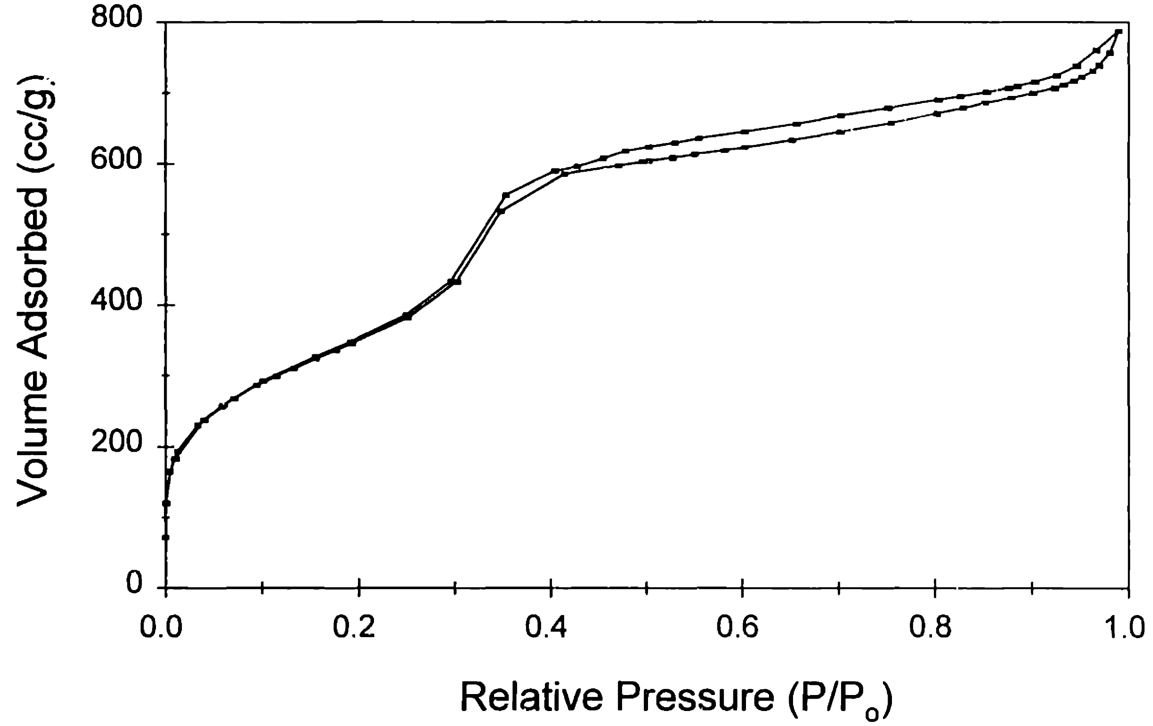

Figure 4.3. N_2 adsorption-desorption isotherm of calcined AlSi-25.

The ^{27}Al magic angle spinning nuclear magnetic resonance (MAS NMR) spectra of AlSi-R samples showed only one peak at ~50 ppm (Figure 4.6), indicating that all Al atoms were tetrahedrally coordinated in the framework of mesoporous silica. The acidity of the mesoporous Al-doped silica was examined with in-situ pyridine adsorption using a Harrick HVC-DRA2 diffuse reflectance infrared Fourier-transform (DRIFT) cell on a Bio-Rad FTS-60A/896 spectrometer. Each mesoporous sample was purged under He at 500 °C,

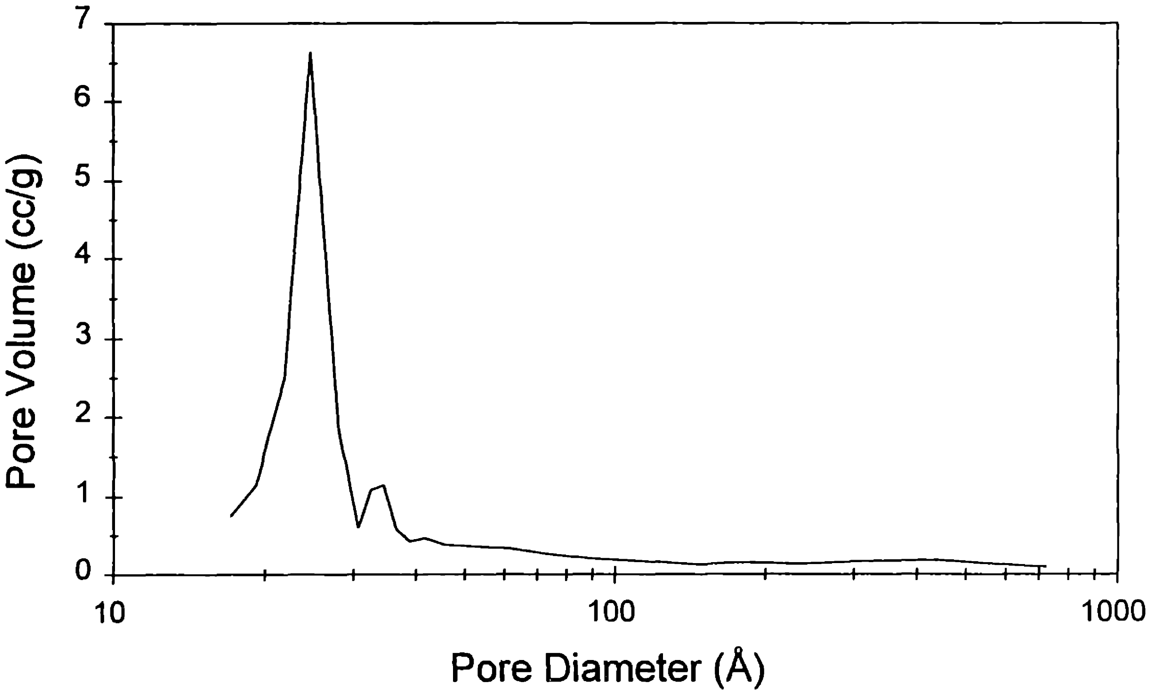

Figure 4.4. BJH pore size distribution of calcined AlSi-25 calculated from the N_2 desorption isotherm.

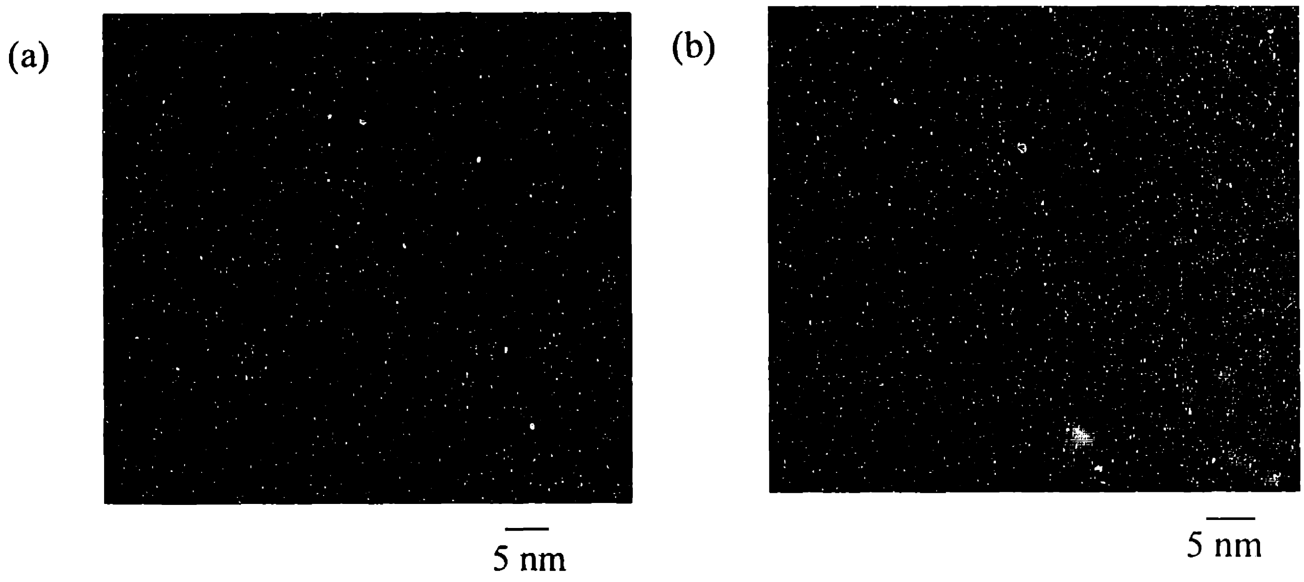

Figure 4.5. TEM images of calcined AlSi-35 aged for 2 days at (a) 100 °C and (b) 180 °C.

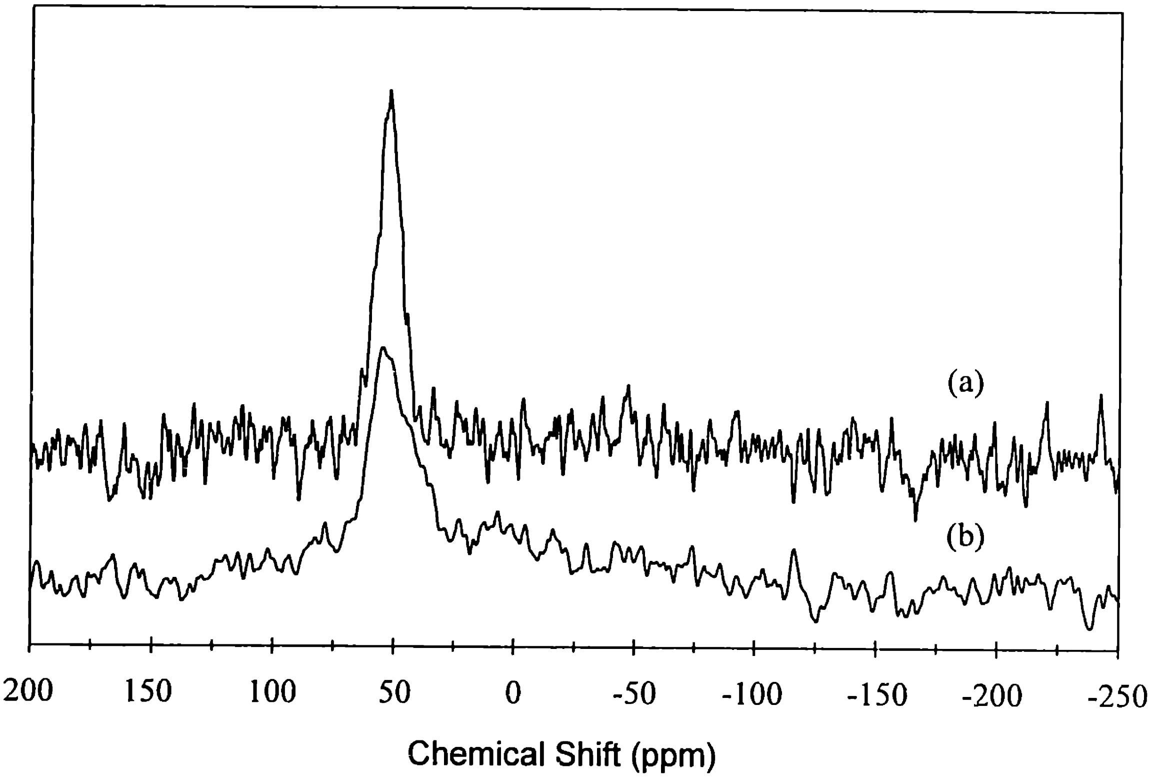

Figure 4.6. ^{27}Al MAS NMR spectra of AlSi-35 samples: (a) as-prepared and (b) calcined at 540 °C.

followed by exposure to pyridine vapor for 1 hour at 150 °C. The spectra of the sample were then collected after 30 min of purging with He at 150-500 °C. The AlSi-R samples possessed both Brönsted and Lewis acid sites (Figure 4.7). The acidity of the mesoporous aluminosilicate materials increased with the Al dopant concentration (Figure 4.8), but was weak compared to zeolitic aluminosilicates.

4.2.2 Introduction of Fe_2O_3 Nanoclusters by Evaporation-Condensation

The microstructural characteristics of porous materials, such as surface area, pore diameter and pore size distribution, would affect the local environment for hosting quantum-sized metal oxide clusters. MCM-41 materials with hexagonally-packed mesopores in the range of 2-10 nm are ideally suited as hosts for the matrix-mediated synthesis of nanoclusters. Both the pore morphology and the dielectric properties of the AlSi-R materials are attractive matrix characteristics. Highly-dispersed iron oxide

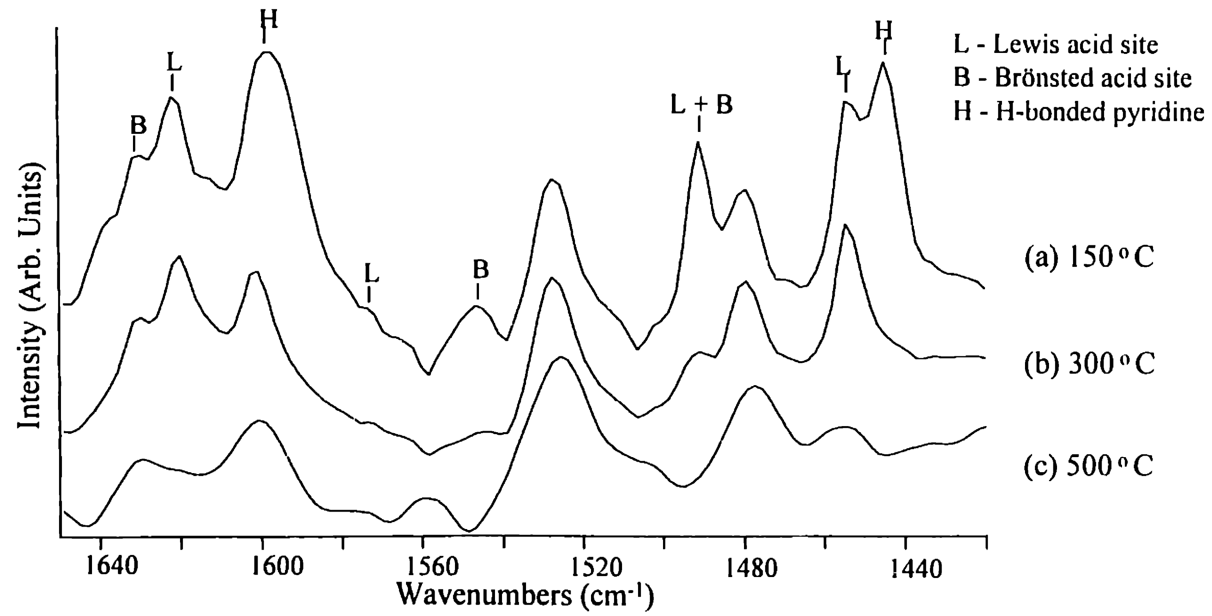

Figure 4.7. In-situ DRIFT spectra of calcined AlSi-5 sample with adsorbed pyridine, taken after 30 min of purging with He at (a) 150 °C, (b) 300 °C, and (c) 500 °C.

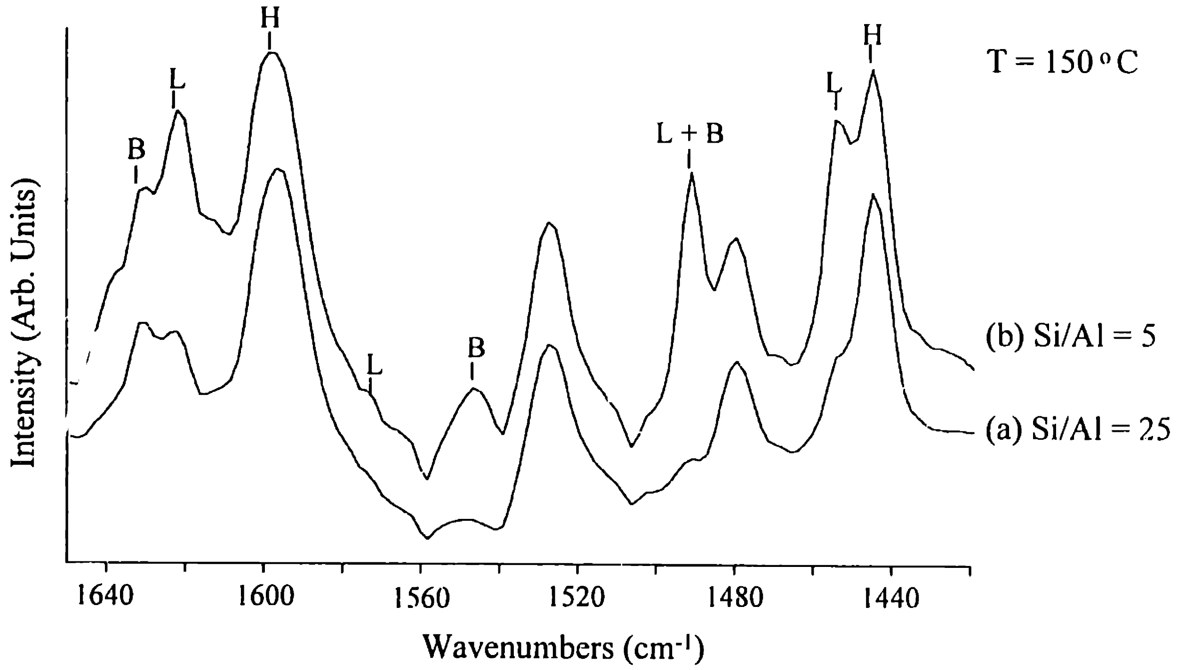

Figure 4.8. In-situ DRIFT spectra of calcined AlSi-R samples with adsorbed pyridine, taken after 30 min of purging with He at 150 °C: (a) R = 25 and (b) R = 5.

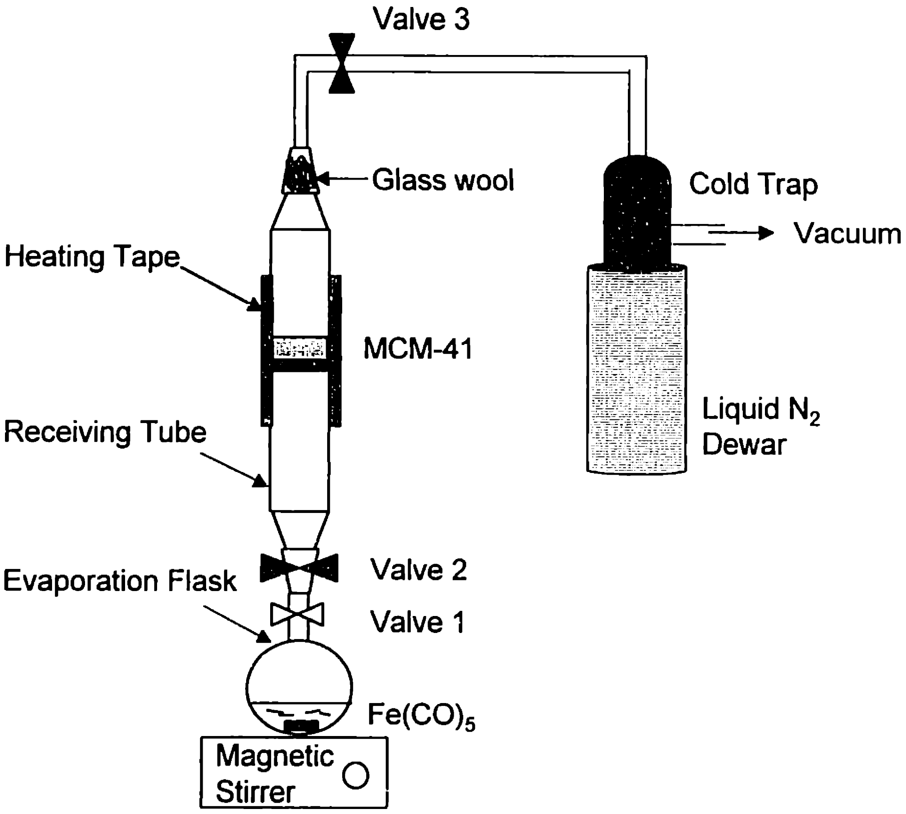

Figure 4.9. A schematic of the evaporation-condensation apparatus.

clusters and/or elongated particles can be formed along the uniform pore channels and be stabilized by the charges of the Al-doped silicate pore walls. The cylindrical channels of AlSi-R may also act as a quantum well and potentially direct the formation of iron oxide wires.

An evaporation-condensation apparatus was used in our synthesis (see Figure 4.9). $Fe(CO)_5$, a highly-volatile precursor, was carefully stored under argon and kept in the dark, while mesoporous aluminosilicate (AlSi-25) was degassed at 350 °C overnight. Typically, 3 ml of $Fe(CO)_5$ and 0.2 g of mesoporous AlSi-25 were introduced to an evaporating flask and a receiving tube, respectively. After assembling the two parts, the mesoporous aluminosilicate was further evacuated for three hours at 250 °C with the heating tape around the receiving tube. The temperature of the receiving tube was then cooled to the desired temperature. Upon opening valves 1 and 2, $Fe(CO)_5$ was evaporated at room temperature and condensed within the mesopores of the aluminosilicate support. Excess $Fe(CO)_5$ was then pumped out of the receiving tube to the cold trap by opening valve 3. The mesoporous silica containing $Fe(CO)_5$ was next subjected to a H_2 stream at 100-200 °C for several hours to decompose and reduce the iron complex. The as-prepared Fe_2O_3/AlSi-25 nanocomposite was further calcined in a tube furnace under O_2 for 3 hours at the desired temperature. The iron loading depended on the synthesis parameters, such as the amount of $Fe(CO)_5$, evaporation rate, saturation time, reaction temperature, and decomposition conditions. The evaporation and condensation procedure could be repeated several times to achieve a high iron loading.

4.2.3 Microstructure of Fe_2O_3/Mesoporous Aluminosilicate Nanocomposites

Three Fe_2O_3/AlSi-25 nanocomposite samples were synthesized with different Fe loadings. Elemental analysis results from direct-current plasma emission spectroscopy (Luvak Inc.) are summarized in Table 4.2.

Table 4.2. Elemental analysis of as-prepared Fe_2O_3/AlSi-25 nanocomposites

Sample	#1	#2	#3
Fe Loading	1.27 wt%	6.82 wt%	57.5 wt%
Receiving Tube Temperature	25 °C	50 °C	80 °C
Reduction Temperature and Time	100 °C, 1 hr, then 150 °C, 5 hr	200 °C, 5 hr	125 °C, 5 hr

The XRD pattern of the as-prepared Fe_2O_3/AlSi-25 nanocomposite #2 showed that the hexagonally-packed mesostructure of AlSi-25 was preserved and no additional peaks associated with Fe_2O_3 crystalline phase was found (Figure 4.10(a)) As the calcination temperature increased, the *d*(100) spacing of the hexagonal phase decreased slightly due to pore shrinkage from condensation. A broad band at $2\theta \sim 22^\circ$ associated with amorphous SiO_2 was noted in all XRD patterns. No crystalline peaks were observed at high 2θ angles (20°-70°), indicating the preservation of ultrafine grain sizes for iron oxide clusters upon calcination.

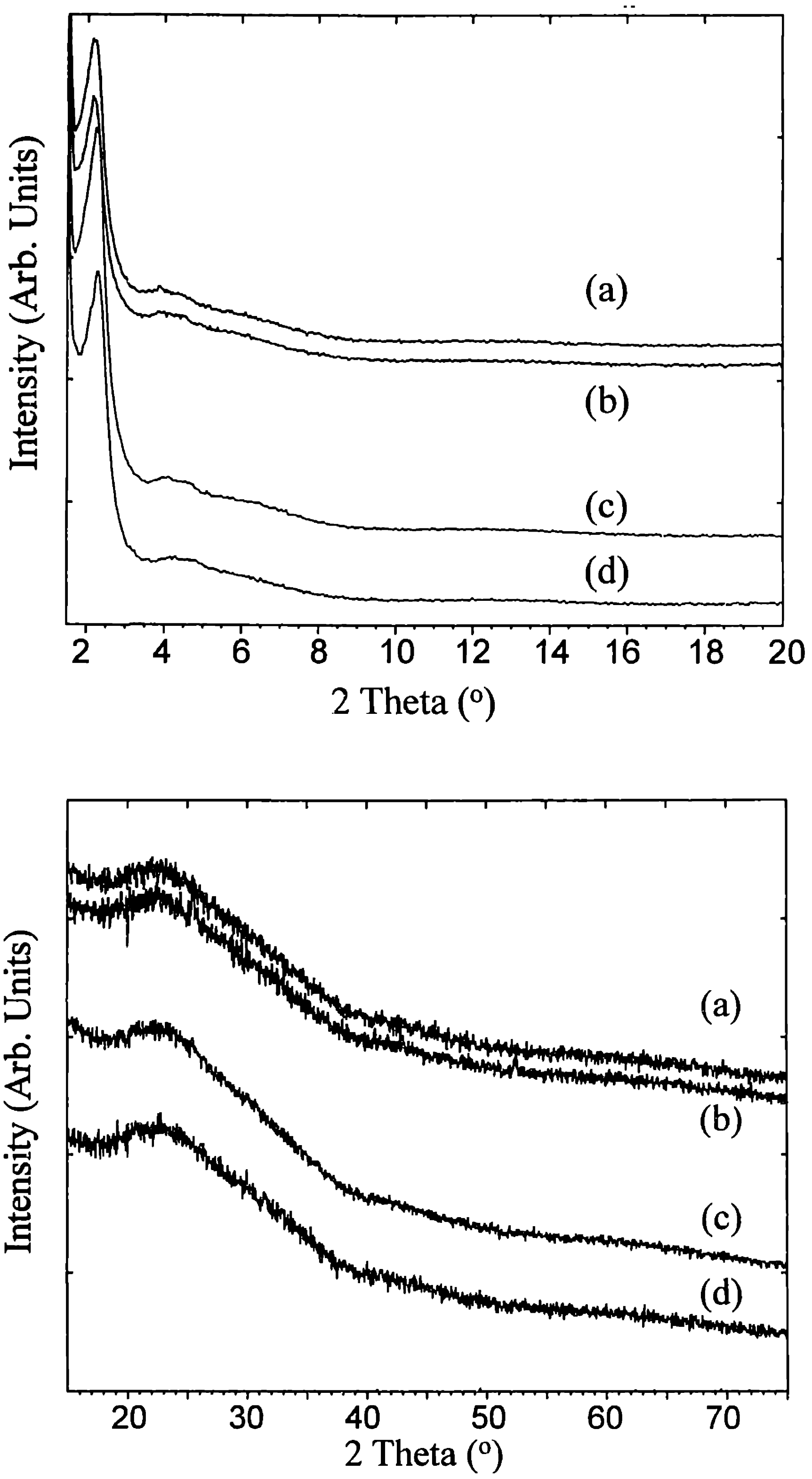

Figure 4.10. XRD patterns of Fe_2O_3/AlSi-25 nanocomposite #2: (a) as-prepared, (b) calcined at 300 °C, (c) calcined at 500 °C, and (d) calcined at 800 °C.

The morphology of the Fe_2O_3 within MCM-41 matrix was studied using both TEM (Akashi 002B, 200 kV), and scanning transmission electron microscopy (STEM) (Vacuum Generators HB603) with elemental mapping. For as-prepared and 500 °C-calcined Fe_2O_3/AlSi-25 nanocomposite #1, TEM bright field images showed a hexagonally-packed array with dark phase contrast inside the pores when viewing normal to the axis of the hexagonally-packed pores (Figure 4.11). The STEM dark field image showed highly-dispersed bright spherical spots of ~2-3 nm in diameter (Figure 4.12). The Fe elemental mapping illustrated that Fe was highly dispersed throughout the selected image area, with higher concentrations indicated by the bright spots. Due to image drifting during scanning, it was very difficult to precisely match the Fe locations on the elemental map with those on the dark field image. Elemental mapping with the point probe (2 nm probe size) was thus employed to verify the Fe locations. When the X-ray probe was pointed at the bright spherical spots shown in the dark field image, strong Fe absorption was detected, indicating the presence of Fe. When the probe was moved to the adjacent dark regions, no Fe was detected. In certain areas, a lamellar structure was noted in the bright field image, corresponding to hexagonal pore arrays oriented perpendicular to the electron beam. This was viewed as elongated bright lines on the dark field image. The point mapping along the bright lines corresponded to a continuous detection of Fe absorption, suggesting the existence of elongated iron oxide particles. For the sample calcined at 500 °C, a homogeneous Fe mapping with dark field image was obtained, reflecting both spherical and elongated morphologies for the iron oxide particles (Figure 4.13). No particle agglomeration or sintering was observed at 500 °C, suggesting a high thermal stability for Fe_2O_3/AlSi-25 nanocomposite #1.

BET surface area and pore volume of the Fe_2O_3/AlSi-25 samples as determined by N_2 adsorption analysis decreased with increasing Fe loading, as shown in Table 4.3. At a high Fe loading, substantial pore plugging by large Fe_2O_3 nanoclusters might have occurred.

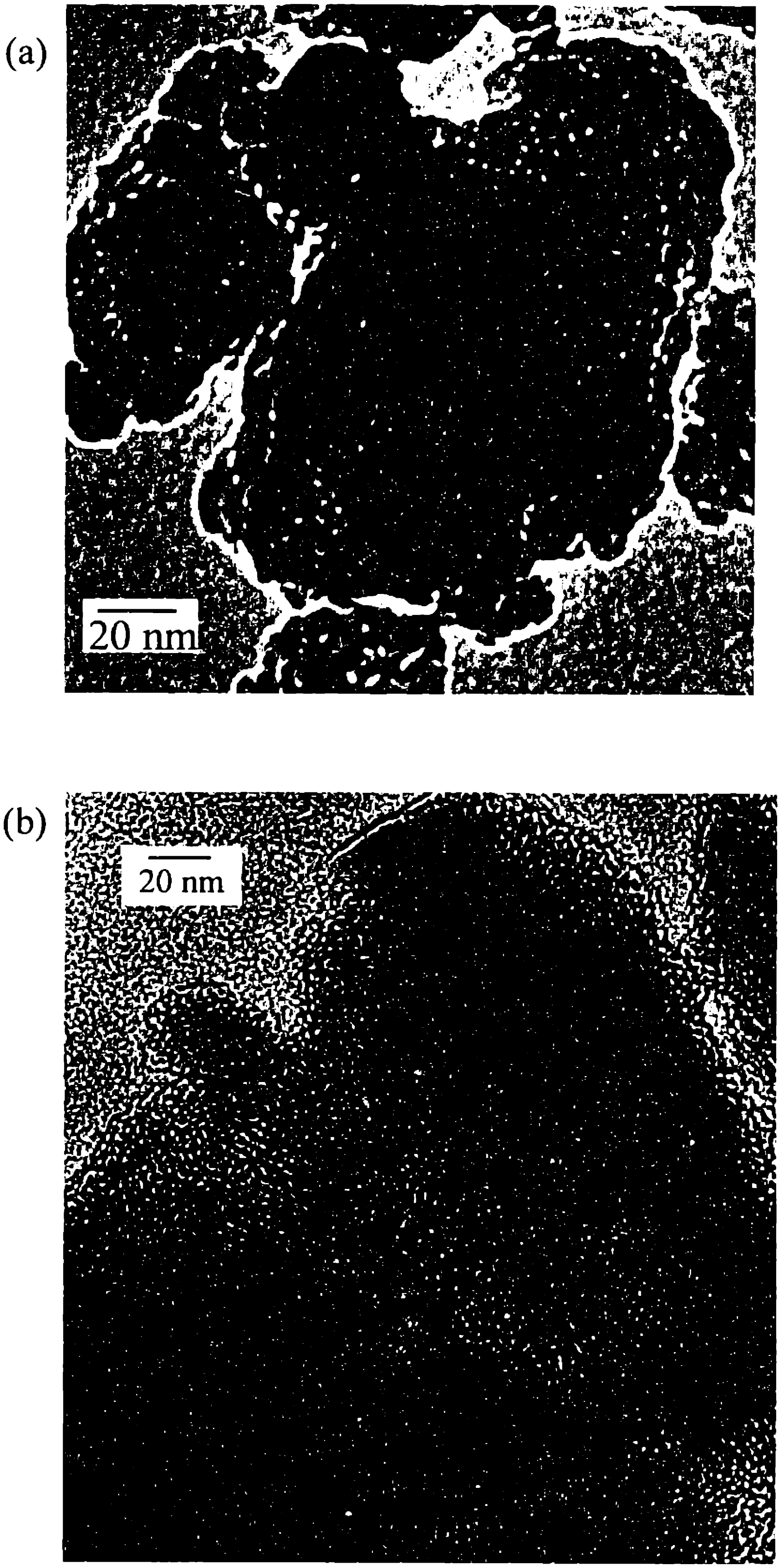

Figure 4.11. TEM micrographs of Fe_2O_3/AlSi-25 nanocomposite #1: (a) as-prepared and (b) calcined at 500 °C.

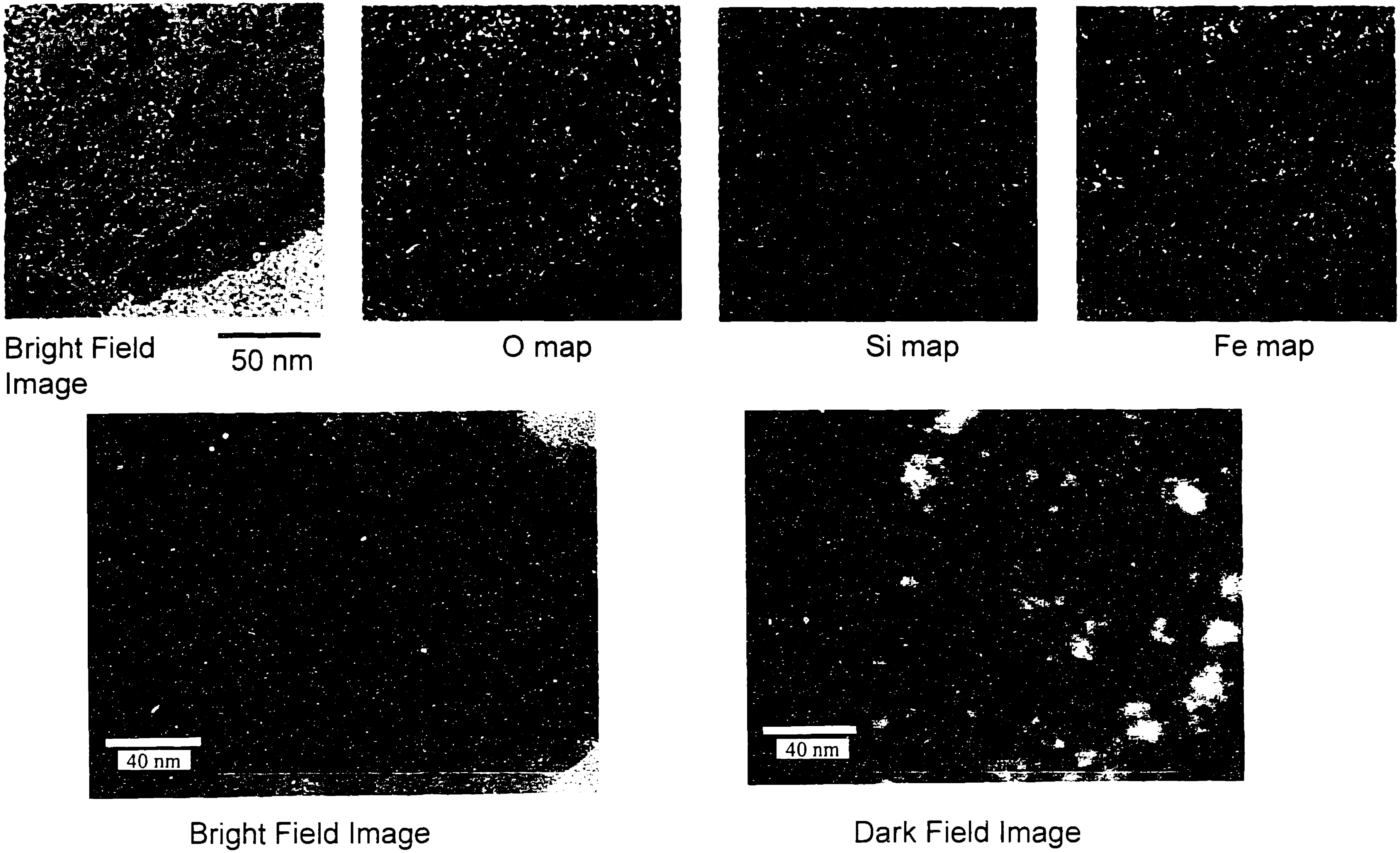

Figure 4.12. Elemental mappings and STEM images of as-prepared Fe_2O_3/AlSi-25 nanocomposite #1.

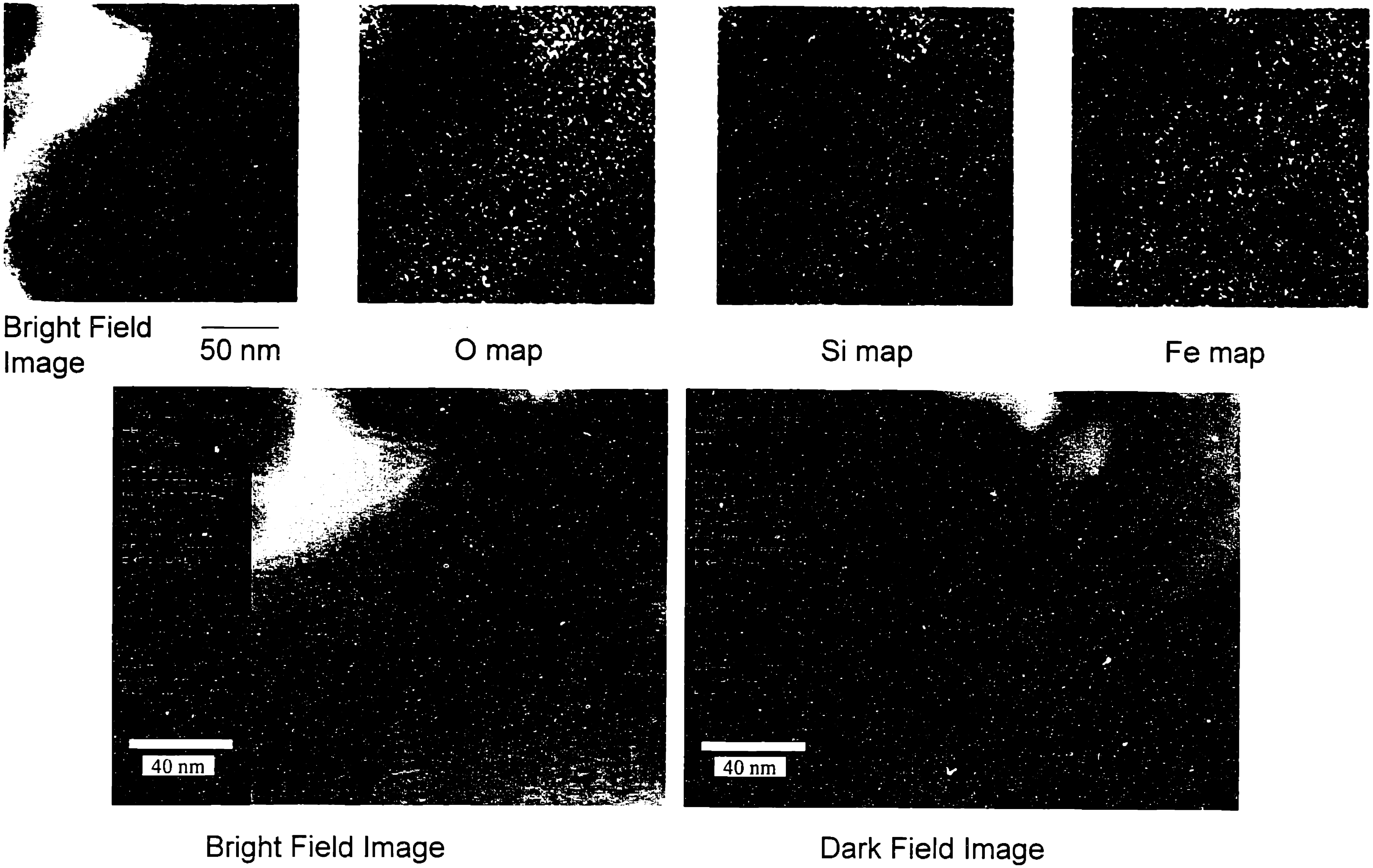

Figure 4.13. Elemental mappings and STEM images of Fe_2O_3/AlSi-25 nanocomposite #1 calcined at 500 °C.

Table 4.3. Surface area and pore volume of calcined mesoporous AlSi-25 and as-prepared Fe_2O_3/AlSi-25 nanocomposites

Sample	AlSi-25	Fe_2O_3/AlSi-25 #1	Fe_2O_3/AlSi-25 #2	Fe_2O_3/AlSi-25 #3
Fe Loading (wt%)	0	1.27	6.82	57.5
Surface Area (m^2/g)	1217	929	763	362
Pore Volume (cm^3/g)	1.10	0.93	0.66	0.29

4.3 Magnetic and Optical Properties of γ-Fe_2O_3/Mesoporous Aluminosilicate Nanocomposites

For superparamagnetic particles, the total magnetic moment displays a paramagnetic behavior obeying a classical Langevin function above the blocking temperature (T_b). The macroscopic magnetic properties of the nanocomposites were investigated by SQUID magnetometry (characteristic measurement time (τ_m) = 10^2 sec) over a wide range of temperatures ($5 < T < 300$ K) and applied magnetic fields ($0 < H < 3$ T). Zero field cooling (ZFC) and field cooling (FC) magnetization curves were recorded, and magnetic hysteresis loops at low temperatures were studied. The internal magnetization and dynamic spin relaxation processes of the nanocomposites were also examined with Mössbauer spectroscopy. The fast 10^{-8} sec characteristic measurement time for Mössbauer spectroscopy yielded information on blocking temperature, below which spin relaxation was slowed down. This enabled the investigation of dynamic and static magnetic properties of the nanocomposites over a convenient temperature range, and provided the capability of zero external field microscopic magnetic study. Mössbauer spectra for the nanocomposites were recorded as a function of temperature for 4.2 K $< T <$ 300 K using a liquid helium cryostat. They were computer-fitted to theoretical curves using a nonlinear least-square curve fitting procedure. The values of isomer shift (δ), quadrupole splitting (ΔE_o) and magnetic hyperfine field (H_{hf}) were used for the iron oxide phase identification.

4.3.1 Mössbauer Studies

In the cluster size range of 2 to 4 nm, a large fraction of the iron oxide lies on the pore surface (assuming a surface layer comprised of two atomic layers), and Mössbauer spectra would reflect the electronic and magnetic properties of surface iron ions to a large extent. Thus, variations in surface and strain anisotropy would be reflected in (i) the value of quadrupole splitting, (ii) the value of hyperfine magnetic field, (iii) the values of magnetic anisotropy energy, blocking temperature and magnetic coercivity of the nanocomposite, and (iv) the collective magnetic excitations detected below the blocking temperature. A simple shell-core model is proposed to analyze the electronic and magnetic contribution from surface and interior iron cations (Figure 4.14). We assume that the highly crystalline core is uniformly magnetized and possibly undergoes a coherent rotation when an external field (H) is applied. However, the surface spins are canted compared to the core spins due to strong pinning forces at the surface, which may induce non-coherent spin rotations.[3]

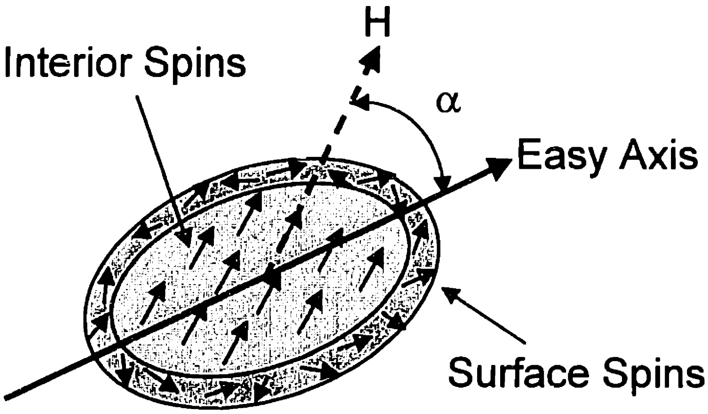

Figure 4.14. A schematic of the shell-core model.

The Mössbauer spectra of the as-prepared Fe_2O_3/AlSi-25 nanocomposite #1 in the absence of an applied field are shown in Figure 4.15. At T = 300 K, a sharp quadrupole doublet was observed with parameters characteristic of superparamagnetic γ-Fe_2O_3 [4] (see Table 4.4). Based on the shell-core model, the spectrum could be fitted as two quadrupole doublets of comparable isomer shifts (0.33 mm/sec) but different quadrupole

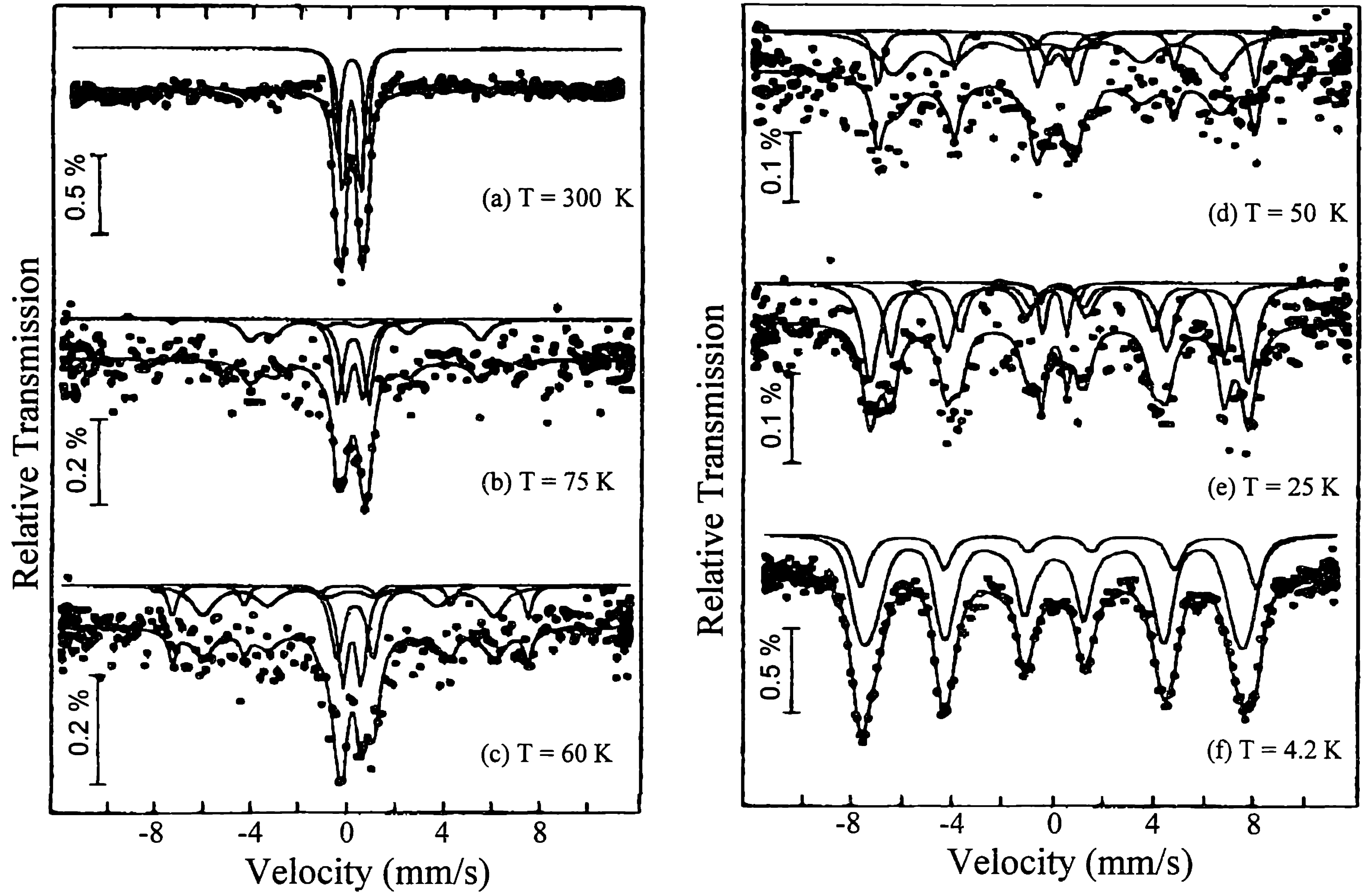

Figure 4.15. Mössbauer spectra of as-prepared Fe_2O_3/AlSi-25 nanocomposite #1 collected at (a) 300 K, (b) 75 K, (c) 60 K, (d) 50 K, (e) 25 K, and (f) 4.2 K. The solid line is a least-square fit to the experimental data. The magnetic subcomponent was fitted to a distribution of magnetic hyperfine fields in order to reproduce the observed spectral broadening.

Table 4.4. Mössbauer parameters for Fe_2O_3/AlSi-25 nanocomposite #1

Fe_2O_3/AlSi-25 Nanocomposite #1	T (K)	Isomer Shift[a, b] δ (mm/sec)		Quadrupole Splitting[a] ΔE_o (mm/sec)		Hyperfine Field H_{hf}(kOe)	
		Surface	Core	Surface	Core	H_1	H_2
As-prepared	300	0.33	0.33	1.25	0.73	---	---
	75	0.41	0.45	1.30	0.77	428.8	296.4
	60	0.54	0.42	1.50	0.77	458.3	375.2
	50	0.35	0.39	1.50	0.78	466.0	402.6
	25	0.46	0.27	1.51	0.94	466.9	411.3
	4.2	---	---	--	-0.026	487.9	458.2
Calcination at 300 °C	300	0.36	0.34	1.24	0.74	---	---
	4.2	---	---	---	-0.056	477.4	447.9
Calcination at 500 °C	300	0.39	0.35	1.10	0.81	---	---
	4.2	---	---	---	-0.132	487.5	442.2
Bulk γ-Fe_2O_3 A+B sites averaged	298	0.35[c]		0		496 [d]	

[a] Uncertainties in δ and ΔE_o are ± 0.03 mm/sec and ± 0.05mm/sec, respectively.

[b] Isomer shift is relative to metallic iron at room temperature.

[c] Reference 5.

[d] Reference 7.

splittings (1.25 mm/sec and 0.73 mm/sec) with an absorption intensity ratio of $A_{surface}:A_{core} = 39:61$. The higher quadrupole splitting of 1.25 mm/sec was attributed to the outer shell spins with distorted coordination symmetry. The superposition of a broadened quadrupole doublet and a small portion of magnetic structure was observed at 75 K, indicating the spin relaxation was of the order of $\tau_m = 10^{-8}$ sec. The complex spectrum at 60 K with 50% area of magnetic structure gave an estimation of the Mössbauer T_b. Below T_b, the area of the broadened magnetic structure continuously increased, and the magnetic spectra were dominated by collective magnetic excitations.[6] The overall splitting of the sextet, which gave a measure of the average internal hyperfine field, showed a strong temperature dependence (See Table 4.4). At 4.2 K, a complete six-line nuclear Zeeman split spectrum was resolved. The negligible quadrupole splitting perturbation value of -0.026 mm/sec from the core magnetic component confirmed the presence of γ-Fe_2O_3. The contribution from surface spins was greatly suppressed at 4.2 K ($A_{surface}:A_{core} = 21:79$) due to the frozen thermal activation. The average hyperfine fields of 487.9 kOe and 458.2 kOe for the two magnetic subcomponents were reduced compared to the corresponding values of bulk γ-Fe_2O_3 (496 kOe at room temperature[7] and 527 kOe saturation field at absolute zero[8]), consistent with the presence of small particles. The observed broad hyperfine field distributions reflected surface effects, such as reduction of the strength of exchange interaction and non-collinear spin structure at the surface of the particle compared to the interior core. The fraction of particles f(T) contributing to the magnetic subspectrum (calculated from Eq. (3.1)) showed a bimodal distribution (Figure 4.16). This suggested that there were two distinct blocking temperatures corresponding to two particle size ranges in as-prepared Fe_2O_3/AlSi-25 nanocomposite #1, in agreement with the TEM and STEM findings.

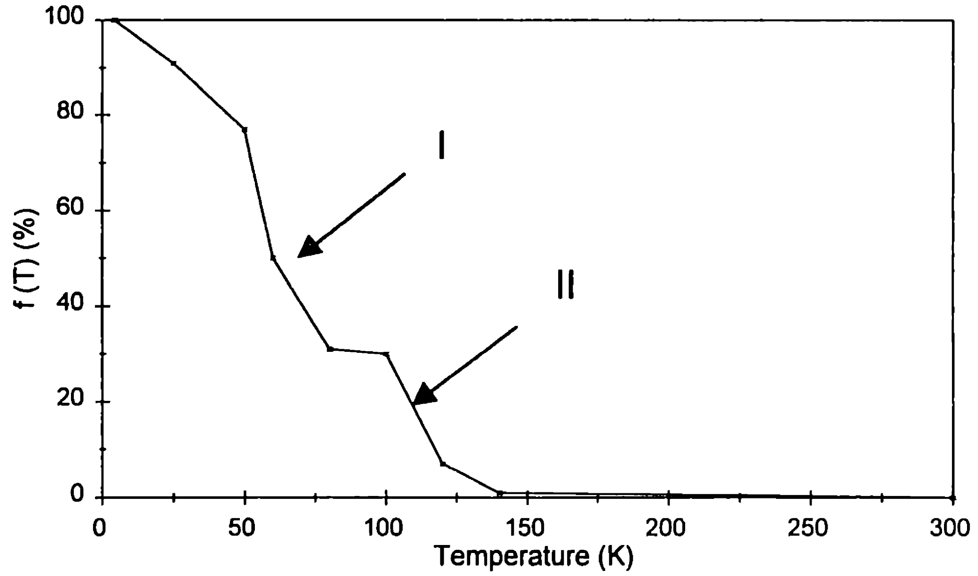

Figure 4.16. The fraction of particles in Fe_2O_3/AlSi-25 nanocomposite #1 contributing to the Mössbauer magnetic subspectrum as a function of temperature. The arrows show the two distinct transition regions.

The geometrical confinement of the Fe_2O_3 clusters by the regular pore structure of the inorganic AlSi-25 matrix could be used towards stabilizing the nanoparticles at high temperatures. The thermal stability of Fe_2O_3/AlSi-25 nanocomposite #1 was examined by Mössbauer spectroscopy. The values of the isomer shift and quadrupole splitting of both the surface and interior components for the Mössbauer spectrum at 300 K remained unchanged for the nanocomposite calcined at 300 °C (Figure 4.17(a), Table 4.4),

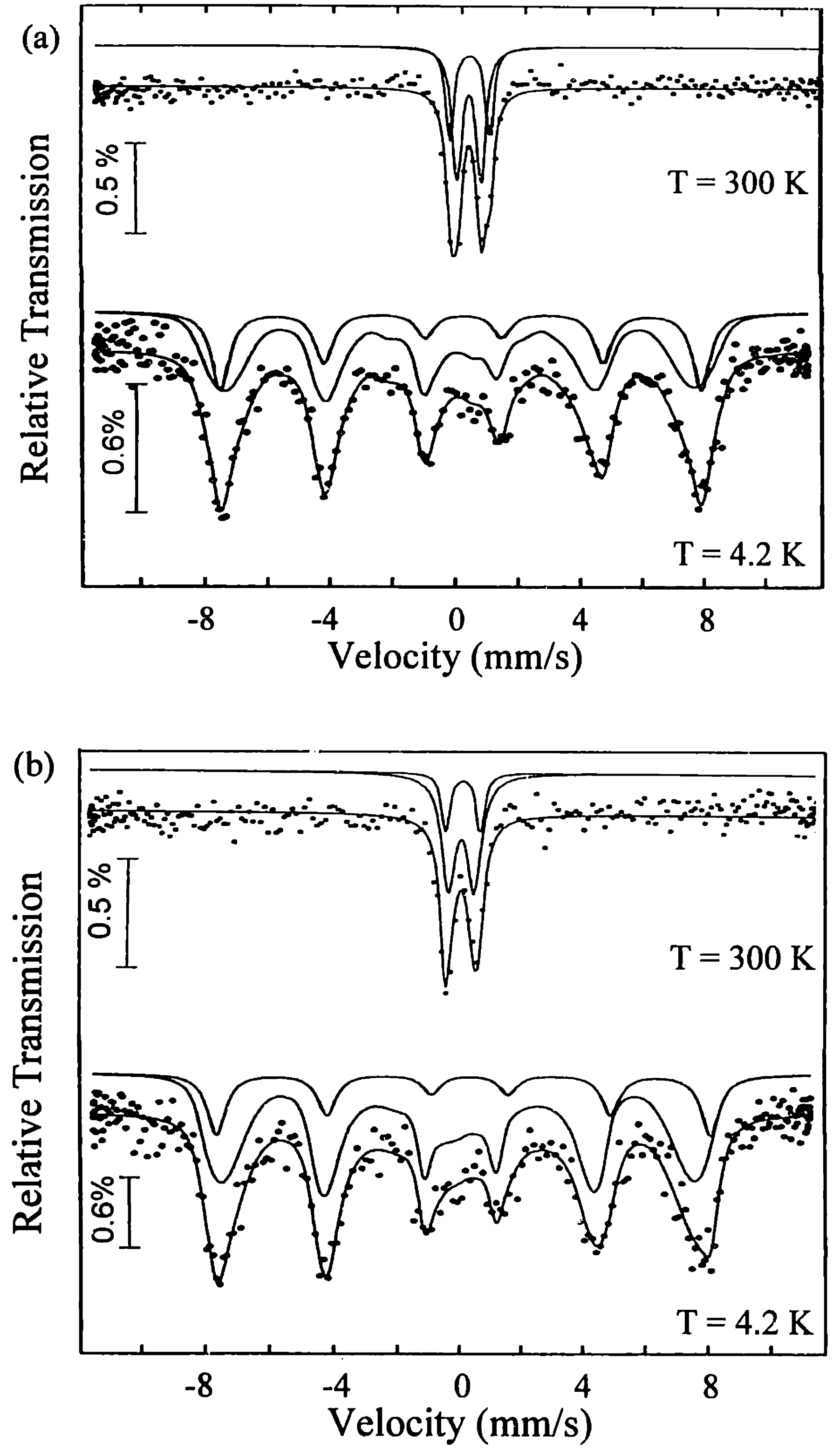

Figure 4.17. Mössbauer spectra of Fe_2O_3/AlSi-25 nanocomposite #1 calcined at (a) 300 °C and (b) 500 °C under O_2. The solid line is a least-square fit to the experimental data. The magnetic subcomponent was fitted to a distribution of magnetic hyperfine fields in order to reproduce the observed spectral broadening.

indicating that no phase transition took place at this calcination temperature. Different quadrupole splitting values were obtained for both components for the sample calcined at 500 °C, suggesting an improved crystallinity or occurrence of phase transition at this calcination temperature (Figure 4.17(b)). The Mössbauer spectrum at 4.2 K gave a small quadrupole splitting perturbation value of -0.056 mm/sec for the sample calcined at 300 °C, supporting the retention of the γ-Fe_2O_3 phase. The 4.2 K spectrum of the sample calcined at 500 °C, however, showed a large quadrupole splitting perturbation value of -0.132 mm/sec, suggesting the presence of a mixture of α-Fe_2O_3 and γ-Fe_2O_3 phases at this temperature (ΔE_o of α-Fe_2O_3 = -0.22 mm/sec at T = 80 K).[5]

4.3.2 SQUID Studies

The isothermal magnetization of as-prepared Fe_2O_3/AlSi-25 nanocomposite #1 was obtained as a function of temperature (Figure 4.18). The hysteresis loop at 300 K gave a zero remanence (M_r) and coercivity (H_c), indicating superparamagnetic behavior.

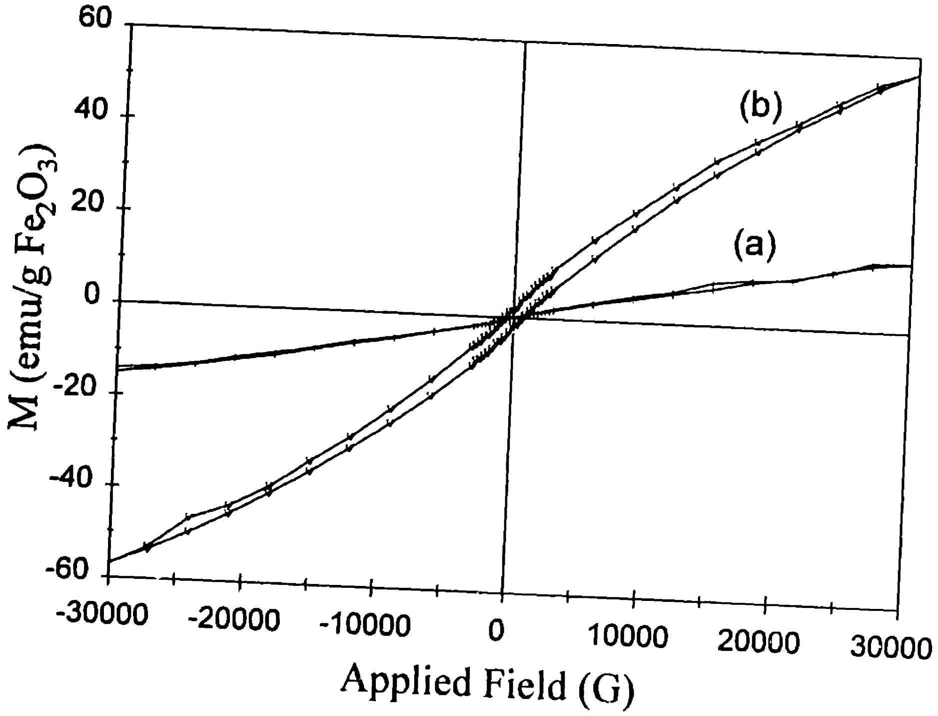

Figure 4.18. Plots of magnetization vs. applied field for as-prepared Fe_2O_3/AlSi-25 nanocomposite #1 obtained at (a) 300 K and (b) 5 K.

With increasing external magnetic field, the magnetization increased rapidly without saturation up to 30 kG due to both spin canting in the ultrafine particle assembly[9] and distribution in particle sizes. The lack of magnetic saturation became more significant at low temperatures. The onset of hysteresis occurred at ~ 50 K. At 5 K, a symmetric hysteresis loop was observed with an unsaturated magnetization of 57 emu/g at 30 kG applied field, a remanence of 1.5 emu/g and a coercivity of 680 G, demonstrating the ferrimagnetic nature of the nanocomposite at low temperature. The spin canting resulting from the discontinuity of the superexchange bonds between Fe cations was responsible for the lower magnetization (compared to bulk γ-Fe_2O_3) and the lack of saturation for the nanocomposite.[10] Compared to bulk γ-Fe_2O_3 that has a remanence of 63 emu/g[11] and a coercivity of 250-400 G,[12] the smaller remanence and larger coercivity of the nanocomposite could be attributed to the single-domain magnetic clusters. For single-domain particles, coercivities are associated with the rotation of the magnetization away from the easy axis; whereas in the bulk system, coercivities reflect magnetic domain wall motion in the presence of a magnetic field.

The temperature-dependent magnetization under H = 200 G was investigated under zero field cooling (ZFC) and field cooling (FC) (Figure 4.19). The ZFC curve exhibited two maxima at 20 K and 50 K. The sharp T_{max} at 20 K could be related to small spherical single-domain magnetic particles. Since the T_{max} is closely related to the blocking temperature and increases with increasing cluster size and magnetic anisotropy constant, the broad T_{max} at 50 K could be attributed to elongated particles with larger average particle volume and shape anisotropy. The existence of two different particle size distributions was also supported by the abnormal isothermal magnetization measurement at 50 K, shown in Figure 4.20. The hysteresis loop of the initial branch was splitted from the final branch at H = -30 kG. This could be related to the superimposition of magnetization from two types of magnetic particles under superparamagnetic relaxation. At temperatures above and below 50 K, the normal superparamagnetic and ferrimagnetic behaviors were observed respectively, as shown in Figure 4.18.

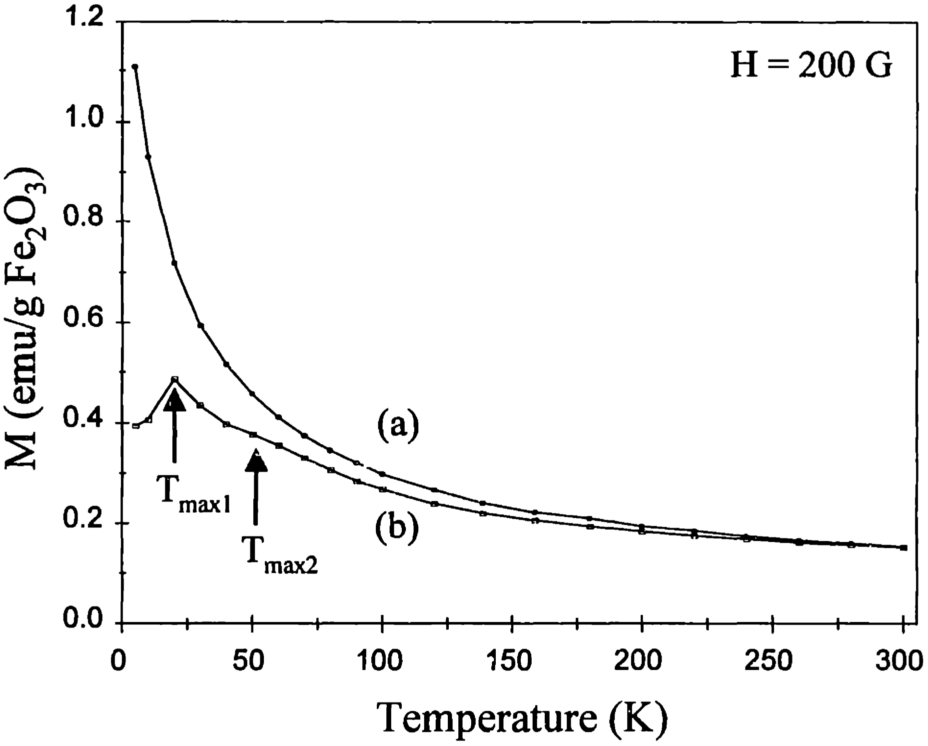

Figure 4.19. Temperature dependence of the magnetization curves under (a) field cooling and (b) zero field cooling for as-prepared Fe_2O_3/AlSi-25 nanocomposite #1.

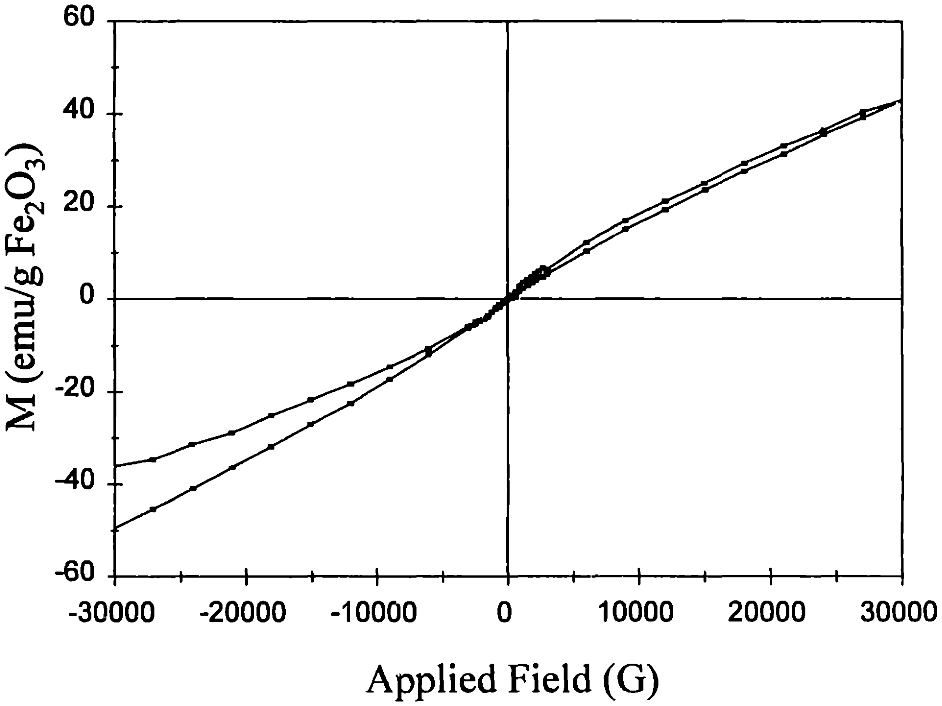

Figure 4.20. Plot of magnetization vs. applied field for as-prepared Fe_2O_3/AlSi-25 nanocomposite #1 obtained at 50 K.

SQUID has also been applied to study the magnetic properties of the calcined samples. The magnetization vs. temperature curves measured under ZFC and FC at 200 G showed that the total magnetization increased with calcination temperature (Figure 4.21). The splitting between FC and ZFC curves occurred at a lower temperature for samples calcined at a higher temperature. The improved crystallinity of Fe_2O_3 core and the reduced contribution from disordered surface spins gave rise to the increase in magnetization. The partial transformation to α-Fe_2O_3, observed in the Mössbauer spectrum of the 500 °C-calcined sample, was not significant enough to lead to a reduction in the overall magnetization. This indicated that Fe_2O_3/AlSi-25 nanocomposite #1 would be an excellent candidate for applications requiring high-temperature stability.

The SQUID results for nanocomposites of different Fe loadings showed that the total magnetization decreased with an increase in Fe content (Figure 4.22). The small magnetization of Fe_2O_3/AlSi-25 nanocomposite #3 (with 57.5 wt% Fe loading) suggested the presence of antiferromagnetically-interacting particles associated with a high degree of agglomeration.

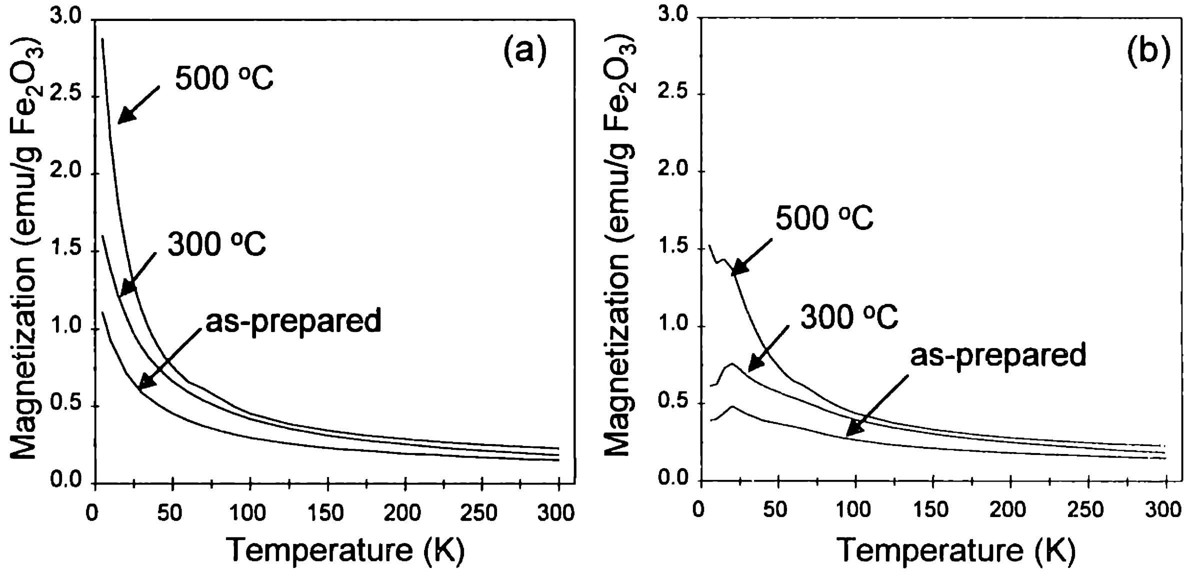

Figure 4.21. Temperature dependence of the magnetization curves under (a) field cooling and (b) zero field cooling for Fe_2O_3/AlSi-25 nanocomposite #1: as-prepared, or calcined to 300 °C and 500 °C.

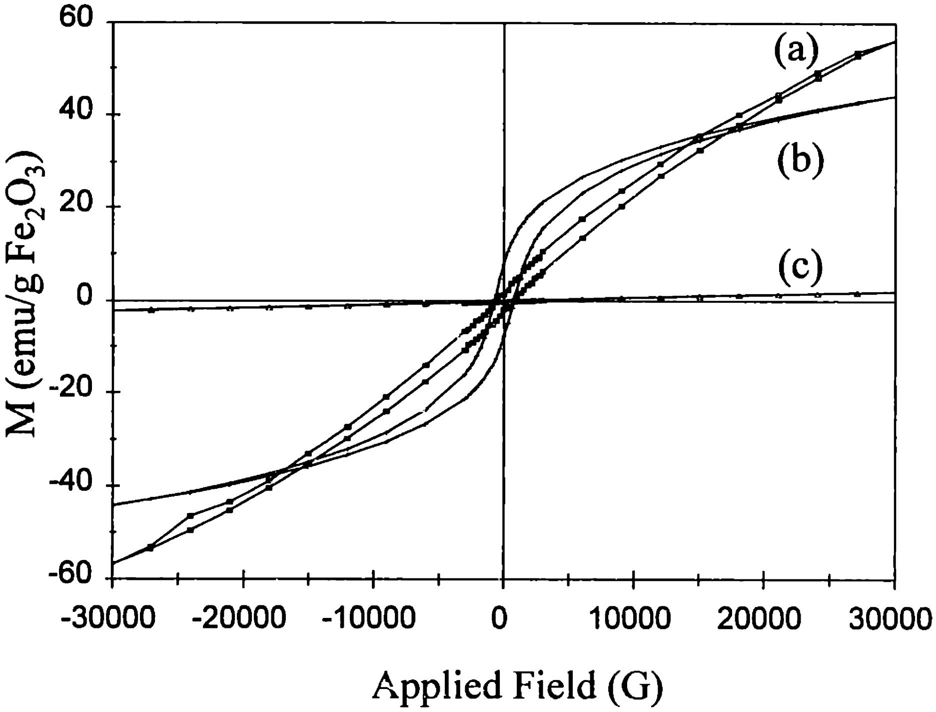

Figure 4.22. Plots of magnetization vs. applied field at 5 K for as-prepared Fe_2O_3/AlSi-25 nanocomposites with Fe loadings of (a) 1.27 wt%, (b) 6.82 wt%, and (c) 57.5 wt%.

The magnetic properties of the three differently prepared Fe_2O_3/SiO_2-based nanocomposites examined in this thesis are summarized in Table 4.5. In comparison to the Fe_2O_3/SiO_2-based nanocomposites discussed in Chapters 2[13] and 3,[4] a complex magnetic system was obtained within cylindrical mesoporous matrix using the evaporation-condensation approach described in this chapter. Large magnetization and coercivity values were obtained using the AlSi-25 supports (bulk γ-Fe_2O_3: 76 emu/g, polymer supported γ-Fe_2O_3 nanoclusters: 46 emu/g[14]). This could be explained by the combination of magnetic contributions from particles of different morphologies. For single-domain magnetic particles, the magnetization is significantly reduced due to the quantum-size effect. The magnetic dipole moment is proportional to the particle volume. The combined effective volume of spherical and elongated Fe_2O_3 nanoclusters in the cylindrical pores of AlSi-25 could be larger than that of the spherical Fe_2O_3/SiO_2-coated particles with diameters of ~4 nm. Therefore, a larger magnetization was obtained with the Fe_2O_3/AlSi-25 nanocomposite. The coercivity of spinel-structured nanocrystals greatly depends on morphology and surface anisotropy. Compared to spherical particles, shape anisotropy of acicular particles can produce a higher coercive field, assuming an ellipsoid model with uniform magnetization. The higher coercivity of Fe_2O_3/AlSi-25 nanocomposite #1 compared with that of Fe_2O_3/SiO_2-coated nanocomposite could be attributed to the presence of elongated particles in the former. On the other hand, the low value of coercivity in the Fe_2O_3/sulfonated-SiO_2 nanocomposite implied that (i) the internal spin structure of the particles in this system significantly deviated from that of uniform magnetization assumed in the Stoner and Wohlfarth model,[15] and/or (ii) the anisotropy was dominated by strain exerted by the sulfonated-silica matrix on the nanoclusters. We noted that a superior thermal stability was achieved with the Fe_2O_3/AlSi-25 nanocomposite system.

Table 4.5. Summary of magnetic properties of the Fe_2O_3/SiO_2-based nanocomposites

As-prepared Sample	M (emu/g Fe_2O_3) (at 3 T, 5 K)	H_c (G) (at 5 K)	T_B (K) (SQUID)	T_B (K) (Mössbauer)
Fe_2O_3/Sulfonated-SiO_2 Nanocomposite	30	270	10	25
Fe_2O_3/SiO_2-coated Nanocomposite	20	635	15	23
Fe_2O_3/AlSi-25 Nanocomposite #1	57	680	20, 50	60

4.3.3 Optical Properties

The optical property of the Fe_2O_3/AlSi-25 nanocomposites was studied using a Cary II UV-Vis spectrometer. The spectrum of as-prepared Fe_2O_3/AlSi-25 nanocomposite #1 exhibited a blue shift of 70 nm relative to bulk γ-Fe_2O_3 (Figure 4.23(a)). The widening of the bandgap was consistent with quantum confinement. Upon calcination, the absorption edge shifted to a slightly higher wavelength, corresponding to changes in (i) the core structure of the Fe_2O_3 nanoclusters, and (ii) the interfacial effects from the particle/support interaction (Figures 4.23(b) and (c)). In comparison, the matrix-mediated synthesis of Fe_2O_3 nanoclusters within sulfonated-SiO_2 gel involved an interconnected porous host with a broad pore size distribution. This might have resulted in relatively less stress effects, and thus a larger blue shift (110 nm) was obtained with the Fe_2O_3/sulfonated-SiO_2 nanocomposite (Figure 4.24 (a)). In the case of Fe_2O_3/SiO_2-coated sample, the presence of high stress exerted by the silica coating might have substantially counteracted the quantum confinement effects, resulting in a relatively small blue shift of 20 nm (Figure 4.24(b)). The strain induced by particle/support interactions could be so significant as to produce red-shifted optical absorption as reported for a γ-Fe_2O_3/polymer nanocomposite system.[14] The hexagonally-packed cylindrical array of uniformly small mesopores (2.5 nm pore diameter) of the AlSi-25 support could induce more stress on the surface of Fe_2O_3 clusters than the irregular pore structure of the sulfonated-SiO_2 gel (4 nm average pore size), but less stress than that imposed by the tightly-bonded silica coating. The combined quantum confinement and stress effects led to the intermediate level of optical blue shift (70 nm) in Fe_2O_3/AlSi-25 nanocomposite #1 (Figure 4.24 (c)).

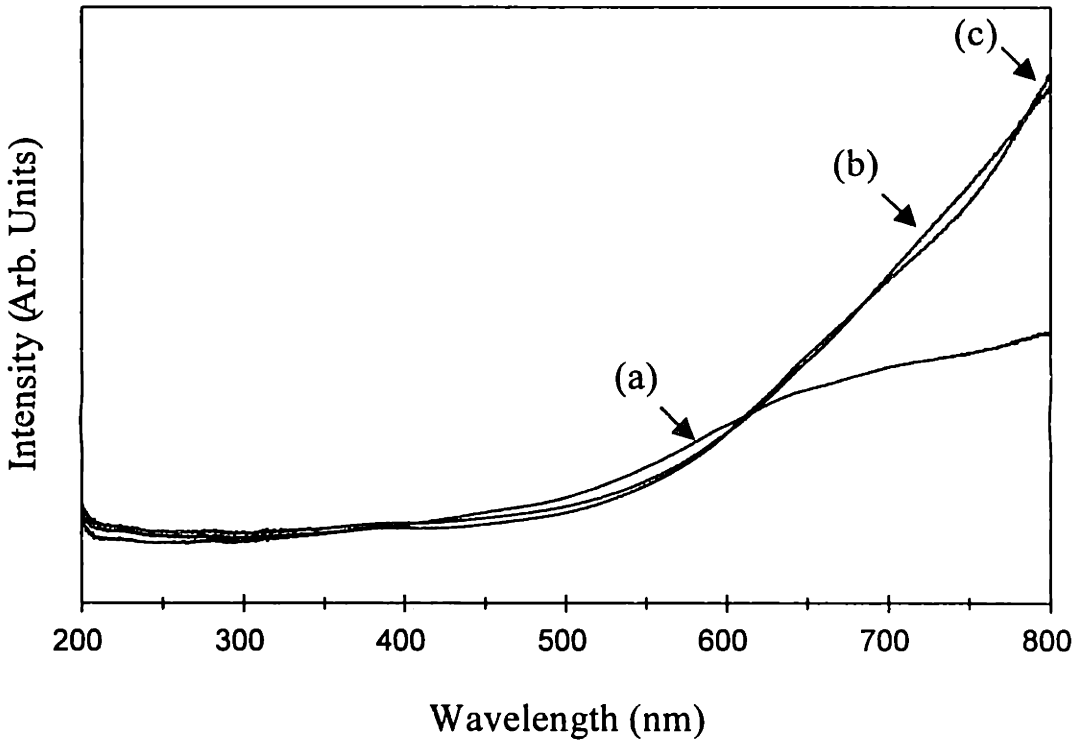

Figure 4.23. UV-Vis diffuse reflectance spectra of Fe_2O_3/AlSi-25 nanocomposite #1: (a) as-prepared, (b) calcined at 300 °C, and (c) calcined at 500 °C.

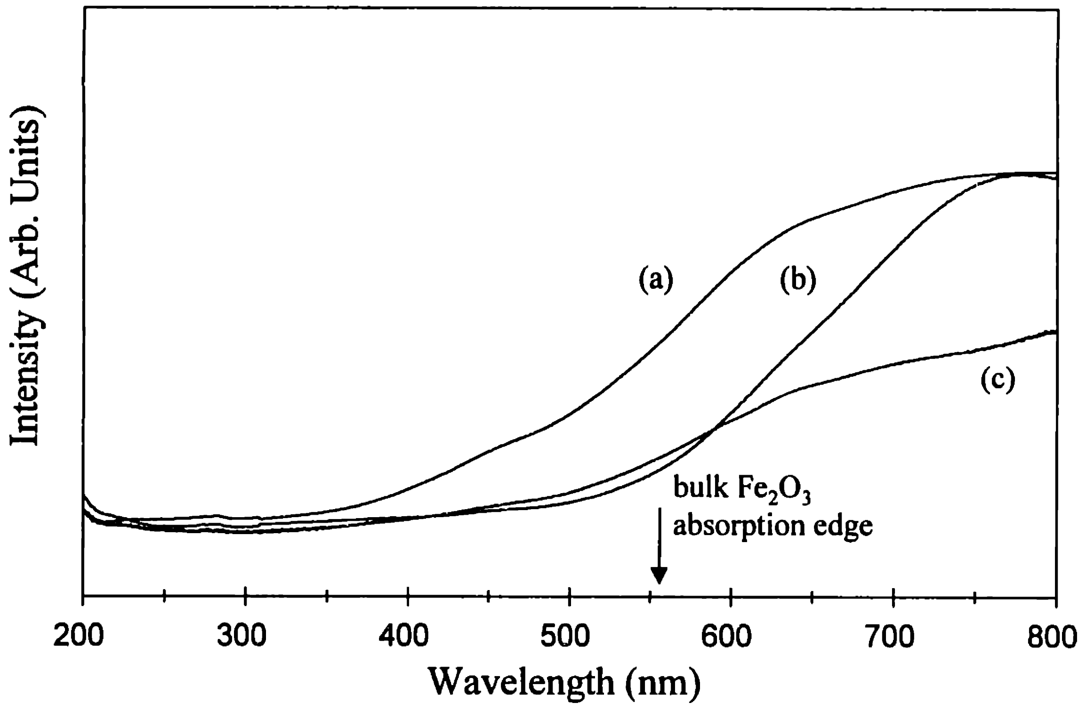

Figure 4.24. UV-Vis diffuse reflectance spectra of (a) Fe_2O_3/sulfonated-SiO_2 nanocomposite, (b) Fe_2O_3/SiO_2-coated nanocomposite, and (c) Fe_2O_3/AlSi-25 nanocomposite #1.

4.4 Summary

Evaporation-condensation of volatile $Fe(CO)_5$ was used to produce Fe_2O_3 nanoclusters within hexagonally-packed mesoporous aluminosilicate matrix. Various Fe loadings could be obtained through control of cluster synthesis parameters, such as precursor amount, evaporation rate, reaction temperature and decomposition conditions. Superparamagnetism was demonstrated by Fe_2O_3/AlSi-25 nanocomposite at low Fe loadings. TEM and STEM with Fe elemental mapping indicated the co-existence of spherical and elongated iron oxide particles within the cylindrical pores of AlSi-25 supports. The magnetic particles were confirmed to be γ-Fe_2O_3 by Mössbauer spectroscopy. Two distinct relaxation phenomena were observed in both SQUID and Mössbauer measurements, associated with the presence of two sets of particle size distributions. The large magnetization and coercivity of Fe_2O_3/AlSi-25 nanocomposite might be attributed to the presence of spherical and elongated magnetic particles. The iron oxide nanoclusters in this nanocomposite exhibited high stability against $\gamma \rightarrow \alpha$

phase transition. Only partial phase transition to α-Fe_2O_3 was detected for the sample calcined at 500 °C. The high thermal stability and increased magnetization from calcination made the material an excellent candidate for high-temperature applications. A blue shift in the absorption edge was noted in the optical spectrum of this nanocomposite system.

4.5 References

[1] C-G. Wu and T. Bein, Chem. Mater., **6**, (1994) 1109.

[2] R. Leon, D. Margolese, G. Stucky, and P. M. Petroff, Phys. Rev. B, **52**, (1995) 2285.

[3] Q. A Pankhurst and R. J. Pollard, Phys. Rev. Lett., **67**, (1991) 248.

[4] L. Zhang, G. C. Papaefthymiou, and J. Y. Ying, J. Appl. Phys., **81**, (1997) 6892.

[5] N. N. Greenwood and T. C. Gibb, *Mössbauer Spectroscopy*, Chapman Hall, London, (1971) 241.

[6] S. Mørup and H. Topsøe, J. Appl. Phys., **11**, (1976) 63.

[7] H. V. Kelly, V. J. Folen, M. Hass, W. N. Schreiner, and G. B. Beard, Phys. Rev., **122**, (1961) 1447.

[8] E. Murad, in *Magnetic Properties of Fine Particles*, edited by J. L. Dormann and D. Fiorani, Elsevier, North-Holland, (1992) 339.

[9] J. M. D. Coey, Phys. Rev. Lett., **27**, (1971) 1140.

[10] J. Teillet, F. Bouree, and R. Krishnan, J. Magn. Magn. Mater., **123**, (1993) 93.

[11] Y. Imaoka, J. Electrochem. Japn, **36**, (1968) 15.

[12] H. Morrish, in *Crystals: Growth, Properties, and Applications*, mgr. edited by H. C. Freyhardt, Springer-Verlag, New York, **Vol. 2**, (1980) 171.

[13] L. Zhang, G. C. Papaefthymiou, R. F. Ziolo, and J. Y. Ying, Nanostruct. Mater., **9**, (1997) 185.

[14] R. F. Ziolo, E. P. Giannelis, B. A. Weinstein, M. P. O'Horo, B. N. Ganguly, V. Mehrotra, M. W. Russell, and D. R. Huffman, Science, **257**, (1992) 219.

[15] E. C. Stoner and E. P. Wohlfarth, Phil. Trans. Roy. Soc. A, **240**, (1948) 599.

Chapter 5

SYNTHESIS AND CHARACTERIZATION OF MESOPROUS Nb-DOPED SILICA MOLECULAR SEIEVES

5.1 Introduction

Mesoporous materials with a well-defined pore structure have recently attracted a great deal of research attention due to their potential in separations and catalytic applications.[1,2,3,4,5] Compared to microporous molecular sieves that have pore sizes less than 2 nm, mesoporous materials have larger pore dimensions in the range of 2-10 nm, which greatly facilitate the diffusion of bulky organic molecules. Currently, the most widely studied mesoporous system is MCM-41, which is an (alumino)silicate material with hexagonally packed cylindrical pores of uniform diameter. Significant benefits can be obtained by increasing the compositional flexibility of this mesoporous material.

Isomorphous substitution of silica with a transition metal is an important strategy in (i) creating catalytically active sites and (ii) anchoring sites for catalytically active molecules in the design of new heterogeneous catalysts. Doping molecular sieves with metals can significantly affect the catalytic behavior and lead to new catalysts with improved properties. For example, Ti-doped MCM-41 has been shown to be very selective for the hydroxylation of aromatics.[6] In addition, the high surface area mesoporous materials can be used as a support for catalytically active molecules. An interaction between the support and the catalytic species can be established based on either ion-exchange or ligand coordination on the internal surface of the mesoporous material. For example, aluminosilicate MCM-41 has been used to host iron (II) phenanthroline for the hydroxylation of phenol. This supported catalyst was prepared by an impregnation method and showed a higher catalytic activity than its homogeneous counterpart.[7] In order to strengthen the catalyst-support interaction, the creation of covalent bonds between the catalyst and the support would be highly desirable. This could be achieved through the manipulation of the surface coordination chemistry of the mesoporous silicates with transition metal dopants. To optimize the catalytic performance of the heterogeneous catalyst and to study the structure-property relationship, it is important to control the microstructure of the metal-doped mesoporous materials and to examine the nature of the metal dopant in the mesoporous silicate framework.

This chapter describes the synthesis of a series of mesoporous Nb-doped silicate materials under systematically varied conditions.[8] Characterization of the nature of the Nb dopant in the mesoporous silica was accomplished through various spectroscopic techniques. The results indicated that the Nb^{5+} species were highly dispersed in the framework of the mesoporous silica. The surface-exposed Nb dopants were easily accessible for coordination with guest molecules such as iron(III) meso-(tetra-aminophenyl)-porphyrin bromide, making this material an excellent catalyst support for use in epoxidation and hydroxylation reactions (see Chapter 6).

5.2 Synthesis of Hexagonally-packed Nb-doped Silica Mesostructure

The Nb-doped mesoporous silica was synthesized under both basic and acidic conditions, based on the interaction between an inorganic siliceous precursor and a cationic alkyltrimethylammonium surfactant ($C_nH_{2n+1}(CH_3)_3NBr$). The siliceous sources used in the synthesis were (i) a 10 wt% aqueous tetramethylammonium silicate (TMAS) solution (Sachem), (ii) a 27 wt% sodium silicate solution (Aldrich), and (iii) tetraethoxysilane (TEOS) (Alfa Aesar). In the first case, 1.82 g of cetyltrimethylammonium bromide (CTABr) (Alfa) dissolved in 21.6 g of water was mixed with 22.4 g of TMAS solution at room temperature and stirred for 30 min. In the second case, 3.65 g of CTMABr was completely dissolved in 166 g of water. To this solution, 22.2 g of sodium silicate solution diluted in 50 g of water was slowly added at room temperature with vigorous stirring for 30 min. In both cases, a gel-like precipitate was obtained. A desired amount of the Nb-dopant precursor, niobium ethoxide ($Nb(OEt)_5$) (Aldrich), was gradually introduced into the loosely-bonded silica gel. The pH of the mixture was adjusted to 11.5 by the addition of dilute H_2SO_4. The resulting gel mixture was stirred continuously for 3 hours at ambient conditions before subjected to a hydrothermal treatment within a temperature range of 75-150 °C for a desired period of time.

The third route of doped MCM-41 preparation involves a low pH synthesis. Acidic conditions were applied when TEOS was used as a siliceous source to promote the formation of mono-silicic acid by rapid hydrolysis of TEOS.[9,10] The cationic silicate species could interact with cationic surfactants via a charge tri-layer ($S^+X^-I^+$) with a halide X^- as a mediating ion, forming SBA-3.[11,12] For this synthesis route, 37.3 g of 48 wt% HBr was diluted in 32.5 g of water, and 1.391 g of CTMABr was dissolved in this acidic media with vigorous stirring. 5 g of TEOS was then slowly introduced with stirring to form a yellowish sol. An amount of $Nb(OEt)_5$required to obtain the desired Si/Nb ratio was then added to the silica sol and stirred at room temperature for 24 hours.

In all three cases, the molar composition of the wet gel was represented as 1 SiO_2 : x CTMABr : 120 H_2O : y Nb_2O_5 (where $x = 0.1\text{-}2$, and $y = 0\text{-}0.25$). The crystallized solid was washed with ethanol and water, filtered, and then calcined at 540 °C in air for 6 hours to remove the organic surfactants. In some cases, mesitylene was used as a swelling agent to enlarge the pores of Nb-doped silica. The Nb-doped mesoporous silicate samples obtained from the TMAS, sodium silicate and TEOS precursors described above are designated as NbSi1-R, NbSi2-R and NbSi3-R, respectively, where R is given by the precursor atomic ratio of Si and Nb. Except where otherwise specified, the NbSi1-R, NbSi2-R, and NbSi3-R samples were synthesized with a surfactant-to-Si ratio of 0.5, 0.1, and 0.24, respectively. A series of samples were prepared by systematically varying the synthesis temperature, solution pH, dopant concentration and surfactant-to-silica molar ratio.

5.3 Characterization Techniques

The pore structure regularity of the Nb-doped mesoporous silica was characterized by powder X-ray diffraction (XRD) (Siemens D5000 θ-θ diffractometer), operated at 45 kV and 40 mA using Ni-filtered CuK$_\alpha$ radiation. The chemical composition of the Nb-doped mesoporous silica was determined by direct current plasma emission spectroscopy (Luvak Inc.). The mesoporous structure was examined with transmission electron microscopy (TEM) using a lanthanum hexaboride (LaB_6) filament (JOEL 200CX, 200 kV). The N_2 adsorption analysis was performed on an ASAP 2010 gas sorption instrument (Micromeritics). The BET (Brunauer-Emmett-Teller) and BJH (Barrett-Joyner-Halenda) methods were used to calculate the samples' surface area and pore size distribution, respectively. Thermal evolution of the materials was investigated by thermal gravimetric analysis (TGA) (Perkin Elmer TGA7). Chemical bonding in the mesoporous materials was studied by photoacoustic Fourier-transform infrared (PA-FTIR) spectroscopy. Spectra were collected in a 2.5 kHz rapid scan mode at 2 cm^{-1} resolution in a Bio-Rad FTS-60A/896 spectrometer using a MTEC Model 200 photoacoustic cell. In order to evaluate the acidity of the mesoporous materials, the adsorption of pyridine was studied in-situ using a Harrick HVC-DRA2 diffuse-reflectance infrared Fourier-transform (DRIFT) cell on the Bio-Rad FTS-60A/896 spectrometer. The mesoporous material was purged under He at 500 $^{\circ}$C followed by exposure to pyridine vapor for 1 hour at 150 $^{\circ}$C. The spectra were then collected after 30 min of sample purging with He in a temperature range of 150–300 $^{\circ}$C. Diffuse-reflectance UV-Vis spectra were obtained on a Cary 5E spectrometer using polytetrafluoroethylene plate as a reference. The sample was ground into a fine powder and compressed into a 1/2"-diameter pellet using a hydraulic press at 15000 pounds. Solid state ^{29}Si magic angle spinning nuclear magnetic resonance (MAS NMR) spectra were acquired on a 270-MHz spectrometer (^{29}Si resonance 53.762 MHz) with tetramethylsilane as the reference (Spectral Data Service, Inc.). Ambient electron spin resonance (ESR) spectra were recorded at X-band (frequency 9.34 GHz) on a Bruker ESP 300 spectrometer. X-ray photoelectron (XPS) spectra were collected on a SSX-100 XPS spectrometer (Surface Science Laboratory) oratory with an AlK$_\alpha$ X-ray source. The powder sample was lightly dusted onto a sample holder with a polymer film-based double-sided adhesive tape. A small metallic mesh was applied onto the sample to minimize disturbance of the powder surface during the evacuation of the analysis chamber.

5.4. Microstructure of Nb-doped Mesoporous Silica

5.4.1 Comparison of Different Synthesis Routes

The Nb-doped mesoporous material prepared through the different methods showed different textural and structural characteristics. The calcined NbSi1-20 and NbSi2-20 samples that have been aged at 100 °C for 4 days gave well-defined hexagonal XRD patterns (Figures 5.1(a) and (b)) associated with highly-ordered pore packing. The NbSi3-20 sample showed only a broad (100) diffraction (Figure 5.1(c)). The absence of diffraction peaks at higher 2θ values may be due to a poorly-defined pore packing in this material. The TEM micrographs, shown in Figure 5.2, clearly display a hexagonally-packed porous array with approximate average diameters of 27 Å and 26 Å for the NbSi1-20 and NbSi2-20 samples, respectively. The surface areas and average pore sizes obtained from N_2 adsorption are summarized in Table 5.1. The N_2 adsorption-desorption analysis for NbSi1-20 and NbSi2-20 showed Type IV isotherms with little hysteresis

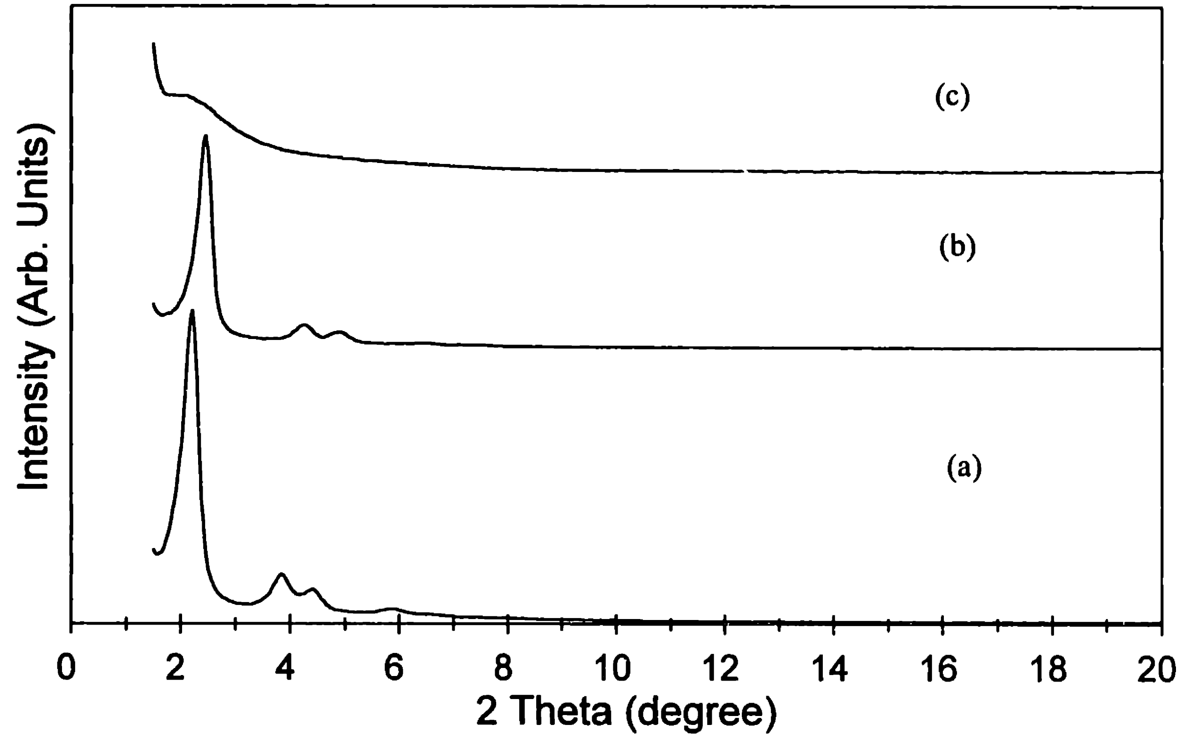

Figure 5.1. XRD patterns of (a) NbSi1-20, (b) NbSi2-20, and (c) NbSi3-20.

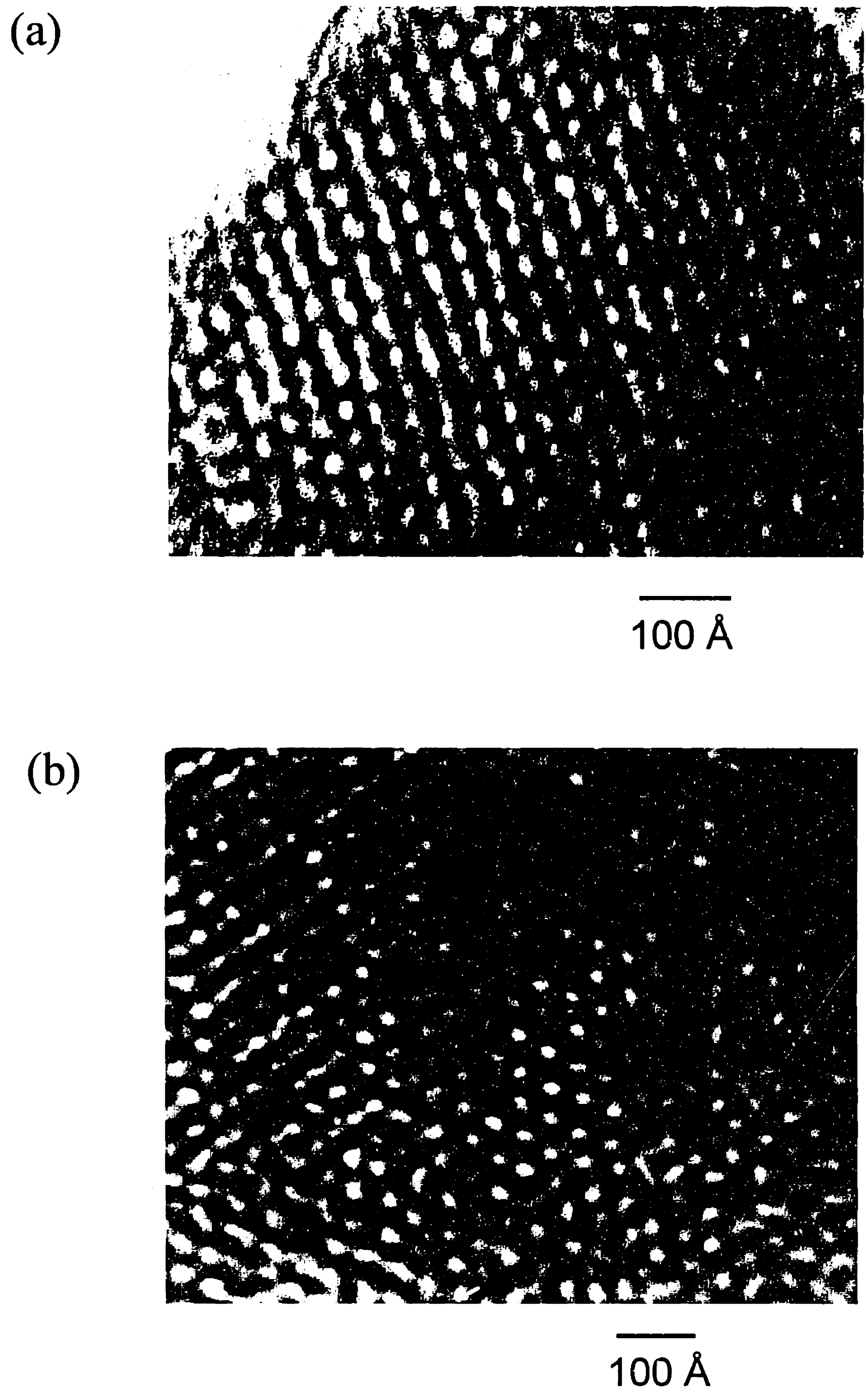

Figure 5.2. TEM images of (a) NbSi1-20 and (b) NbSi2-20.

(Figure 5.3) typical of mesoporous MCM-41, and narrow pore size distributions (Figure 5.4) centered at 28 Å and 23 Å, respectively. We note that the surface areas of the mesoporous materials differ greatly depending on their synthesis routes.

Table 5.1. Microstructure of the mesoporous Nb-doped silicates

Sample	Surface Area (m^2/g)*	Pore Volume (cc/g)*	Average Pore Diameter (Å)*	Unit Cell (a_o) (Å)†	Wall Thickness (Å)
NbSi1-20	1122	1.1	28	46.2	18.2
NbSi2-20	822	0.7	23	41.6	18.6
NbSi3-20	694	0.5	< 17	49.9	-

* From N_2 adsorption analysis

† From XRD analysis

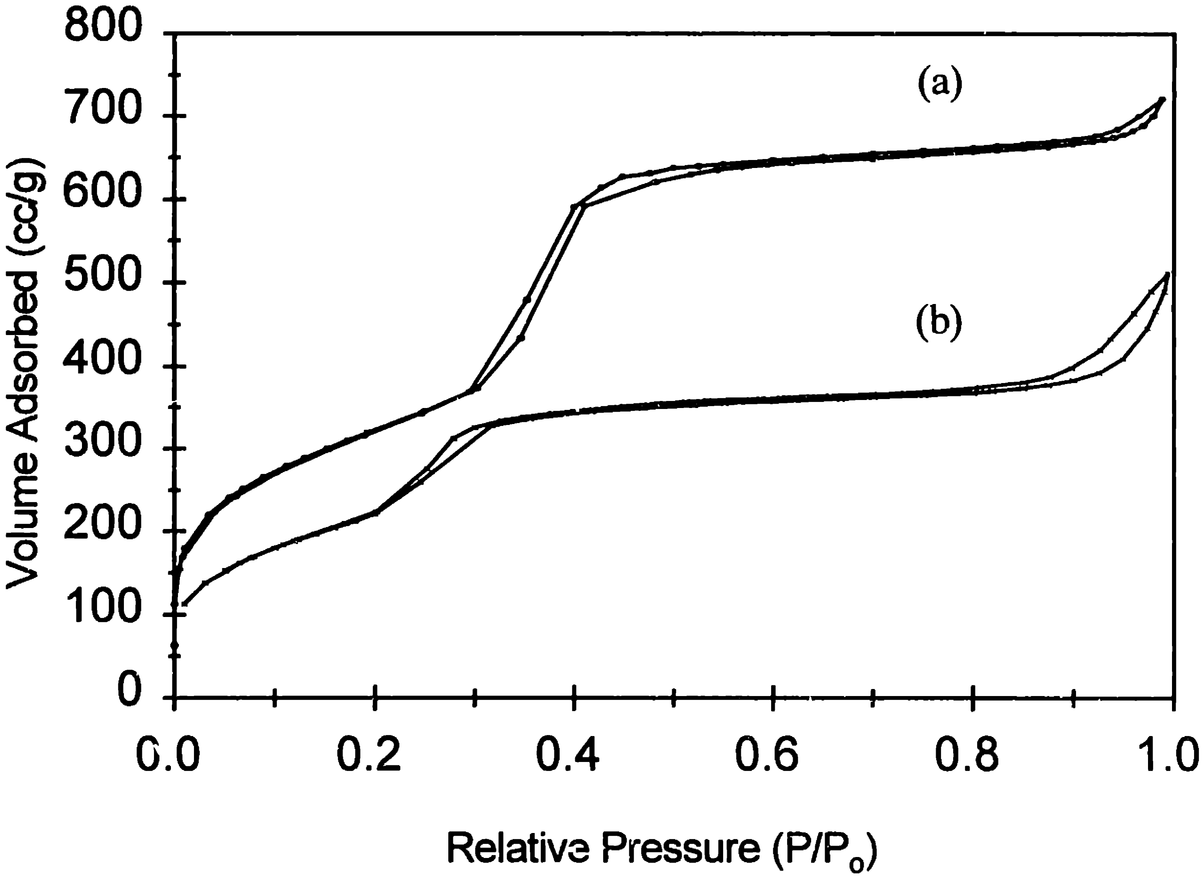

Figure 5.3. N_2 adsorption-desorption isotherms of (a) NbSi1-20 and (b) NbSi2-20.

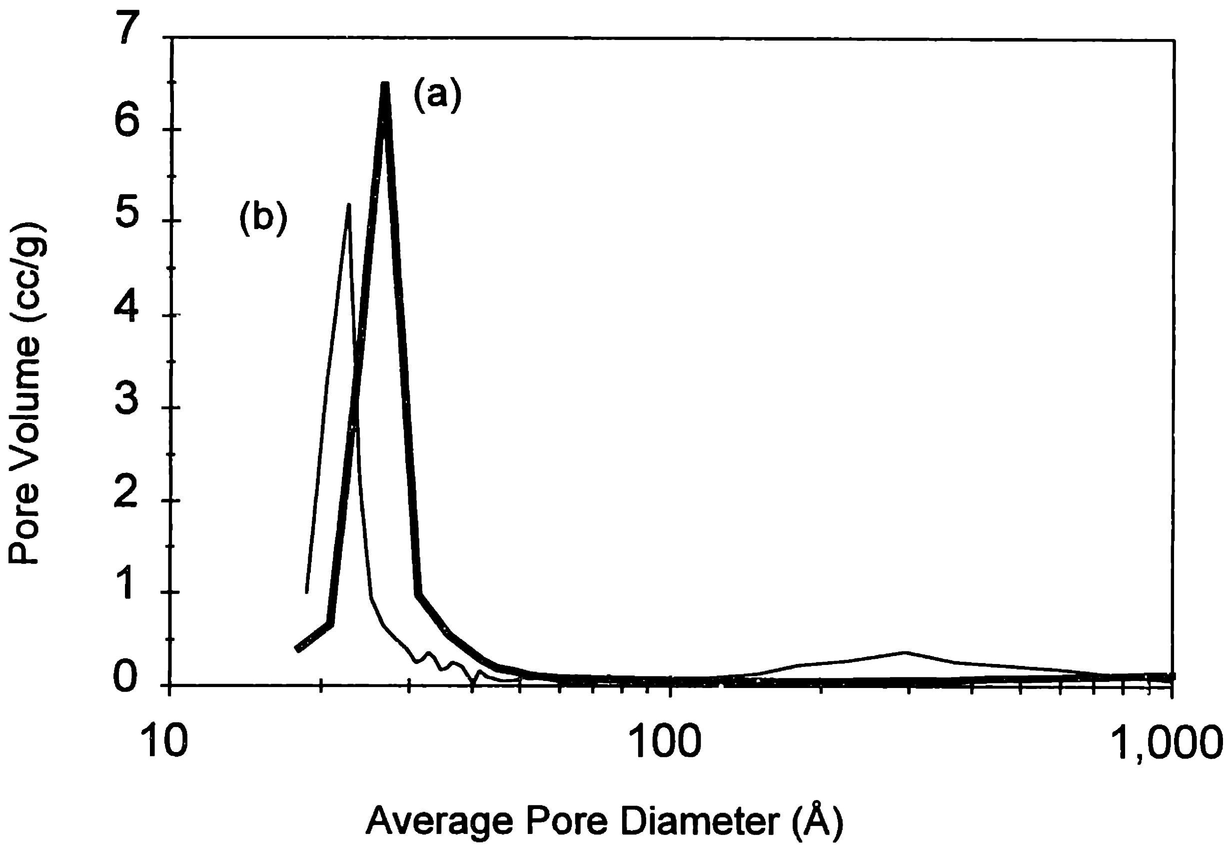

Figure 5.4. BJH pore size distributions of (a) NbSi1-20 and (b) NbSi2-20 obtained from the adsorption branch of their nitrogen isotherms.

In the self-assembly mechanism of MCM-41,[3,11,13] the inorganic molecules are involved in a charge matching interaction with the surfactant templating molecules and their counterions. At the surfactant-to-Si ratios (<1) used for the high pH routes, the hexagonal MCM-41 phase was formed, consistent with Beck *et al.*'s observation.[13] The differences in the microstructure of these materials can be attributed to the nature of the silica source, which plays an important role in the mesostructure formation. At a given sol pH, different siliceous species in the reaction medium have a different relative reactivity with the dopant precursors and a different effect on the ordering of the surfactant molecules to the desired mesostructure. In zeolite synthesis, different crystalline structures could be obtained by varying silica sources due to the size and structure of the silicate species in the reaction media. The chemistry of the organic-based silicate, TMAS, differs from that of the sodium silicate solution in that the former contains more colloidal silica in solution stabilized by an adsorbed monolayer of

$(CH_3)_4N^+$.[14] This monolayer interferes with the condensation of the silica and slows down the precipitation/gelation and particle growth.[15] The $(CH_3)_4N^+$-surrounded silica species further interacts with long-chain cationic surfactants as the $CTMA^+$ can ion-exchange with the surface $(CH_3)_4N^+$ cations, facilitating the organic-inorganic interaction. We could consider the geometry of the surfactant adjacent to $(CH_3)_4N^+$ to be similar to a divalent ammonium surfactant with a $C_{16\text{-}2\text{-}1}$ molecular shape.[16] The effective head group area of the surfactant would be doubled with the $(CH_3)_4N^+$ cations incorporated, increasing the total micellar volume. As a result, the pore diameter of the mesoporous NbSi1-R materials is larger than the other samples (see Table 5.1). In the sodium silicate case, Na^+ cations are too small to significantly affect the micellar volume during the mesostructure formation.

Acidic synthesis route involving low surfactant concentration and low aging temperature has been developed for producing mesoporous silica particles and supported mesoporous silica thin films.[17,18] It provides a convenient process to derive high quality mesoporous materials. When TEOS is used as the siliceous source, its neutral pH and immisciblity in water would only give rise to a weak interaction with the cationic surfactants. This silicate precursor tends to form a bulk amorphous gel without distinct mesostructure at a pH of 10-12. In contrast, a strongly acidic condition leads to rapid hydrolysis of the TEOS to silicic acid and relatively slow condensation, which is favorable towards mesostructure development. When $Nb(OEt)_5$ is introduced, its alkoxy groups undergo rapid hydrolysis in the presence of water. A freshly-precipitated niobium oxyhydroxide gel then results from partial condensation via an olation/oxolation between Nb species.[19,20] In the binary system, it is not favorable to have one alkoxide reacting much faster than another alkoxide precursor when molecular homogeneity is desired. The rapid precipitation of niobium oxyhydroxide interferes with the self-assembly of inorganic species under the acidic conditions examined, and did not allow well-defined mesostructure to be developed. It is also expected that the bridging Si-O-Nb bonds are not likely to be derived in this case for a uniformly doped sample.

5.4.2. Effect of Dopant Concentration

In the synthesis of Nb-doped mesoporous silica, the microstructure of the materials was greatly affected by the dopant concentration. At a given aging temperature, the unit cell parameter[21] calculated by $a_o = 2d_{100}/\sqrt{3}$ is larger for Nb-doped silica ($R \geq 20$) (Figures. 5.5(b) and 5.5(c)) than for the mesoporous pure SiO_2 (Figure 5.5(d)), and increases with an increase in the Nb dopant concentration, due to the larger ionic radius of Nb^{5+} (0.64 Å) and longer Nb-O bond length (1.69 Å). However, a decrease in the d(100) spacing was observed at high Nb-dopant concentrations ($R < 20$) (Figure 5.5(a)). This may indicate a strong interaction of the Nb precursor with the inner silica walls, providing a high surface Nb concentration. Similar results have been reported for V-MCM-48 and Ti-modified MCM-41 systems.[22,23] This suggests that the mechanism of Nb incorporation involves two stages. In the initial stage, the condensation of silicate species is slow at low temperatures.[24] Previous studies showed that mesoporous silica obtained at this early stage has the characteristic of a salt that could redissolve in the aqueous solution.[11] Therefore, the framework of such loosely-bonded silica gel has the flexibility to incorporate hetero-atoms. The partially reacted Nb precursor at room temperature can be incorporated into the silica framework at this stage. That the sample obtained after aging for 3 hours showed a hexagonally-packed XRD pattern with broader peaks and a smaller d(100) spacing than that aged for 4 days confirms the gradual evolution of the mesostructure. During the second stage of synthesis, the Nb polyanions become fully condensed into the lattice of the strengthened silica framework under the high-temperature hydrothermal conditions.

Elemental analysis of the samples (Table 5.2) showed that more of the Nb precursor was incorporated into the framework when sodium silicate was used as the siliceous source instead of TMAS. This can be explained by the faster hydrolysis and polycondensation rates of sodium silicate compared to that of TMAS. Since the reactivity of $Nb(OEt)_5$ is higher than that of the silica precursors, a better match of the reaction rates is helpful towards Nb incorporation into the silica framework. The long-range order and regularity of the pore packing were found to decrease with increasing

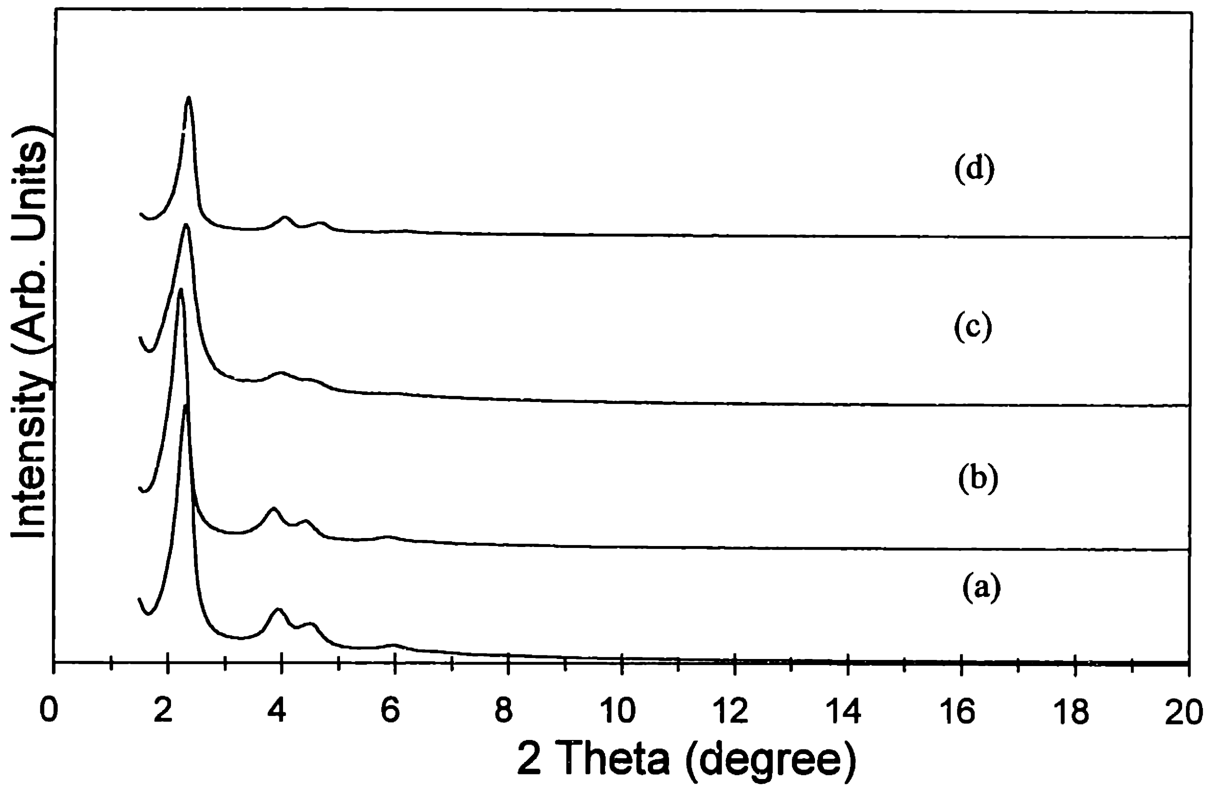

Figure 5.5. XRD patterns of NbSi1-R samples at different dopant concentrations: (a) R = 10, (b) R = 20, (c) R = 100, and (d) R = ∞ (pure mesoporous silica).

Table 5.2. Elemental analysis of the mesoporous Nb-doped silicates

R = Si/Nb (Precursor Atomic Ratio)	NbSi1-R			NbSi2-R		
	Nb(wt%)	Si (wt%)	Si/Nb*	Nb (wt%)	Si (wt%)	Si/Nb*
100	1.44	43.2	100	2.07	43.3	69
20	2.28	42.4	62	3.21	43.6	45
10	3.85	41.5	36	9.36	38.9	14

* atomic ratio from elemental analysis

dopant concentration. In order to maintain the well-defined long-range ordering of the mesostructure during the polymerization of the inorganic species, the hetero-atoms must be able to organize on the same kinetic time scale as the siliceous species. This was facilitated by introducing the $Nb(OEt)_5$ to a pre-hydrolyzed, loosely-bonded silica gel, and then further stirring and aging the mixture at room temperature to maximize the homogeneity of the mixture. We further note that the specific surface area decreased with increased Nb concentration, which could be attributed to the larger Nb atomic weight and the reduced regularity of the pore packing.

5.4.3. Effect of Sol pH and Surfactant Concentration

Self-assembly of the inorganic and organic species in the gel solution into a well-ordered mesostructure only occurs by proper charge matching, which can be tuned by the pH of the reaction medium. Using TMAS as a siliceous source, the mesostructure can be obtained at a pH range of 7-12 (Figure 5.6), however, the intensity of XRD pattern decreased with pH decrease. At around neutral pH, the charges on the oligomeric silica species were substantially lowered, weakening the driving force for self-assembly. pH $\leq$ 5 led to amorphous oxide gels due to rapid reaction of $Nb(OEt)_5$ and silicate precursors.

The surfactant chemistry is critical to the formation of mesostructure. Previous work in silica-based M41S materials showed that hexagonal, cubic and lamellar structures could be formed by increasing the surfactant-to-Si ratio in the precursor sol of pH = 10 at 150 °C.[13,25,26] In our study, the surfactant/Si ratio was varied between 0.1 and 2 in the synthesis of NbSi1-20, and the resulting XRD patterns of all calcined samples exhibited a hexagonal structure (Figure 5.7). The presence of the Nb precursors in the reaction medium under these conditions appeared to favor the hexagonal phase despite the significant variation in surfactant/Si ratio. The incorporation of Nb dopants might have interfered with the interaction between inorganic and organic species. We noted a decrease of the d-spacing at a surfactant-to-Si ratio of 1, which may imply that structural rearrangements occur at different surfactant concentrations. The detail mechanism is unclear at this stage.

The TGA analysis of the Nb-doped samples showed two stages of weight loss in air, resulting from the removal of water at lower temperatures ($T < 150$ °C) and the decomposition of the surfactants at 250-300 °C. A greater weight loss was found in the

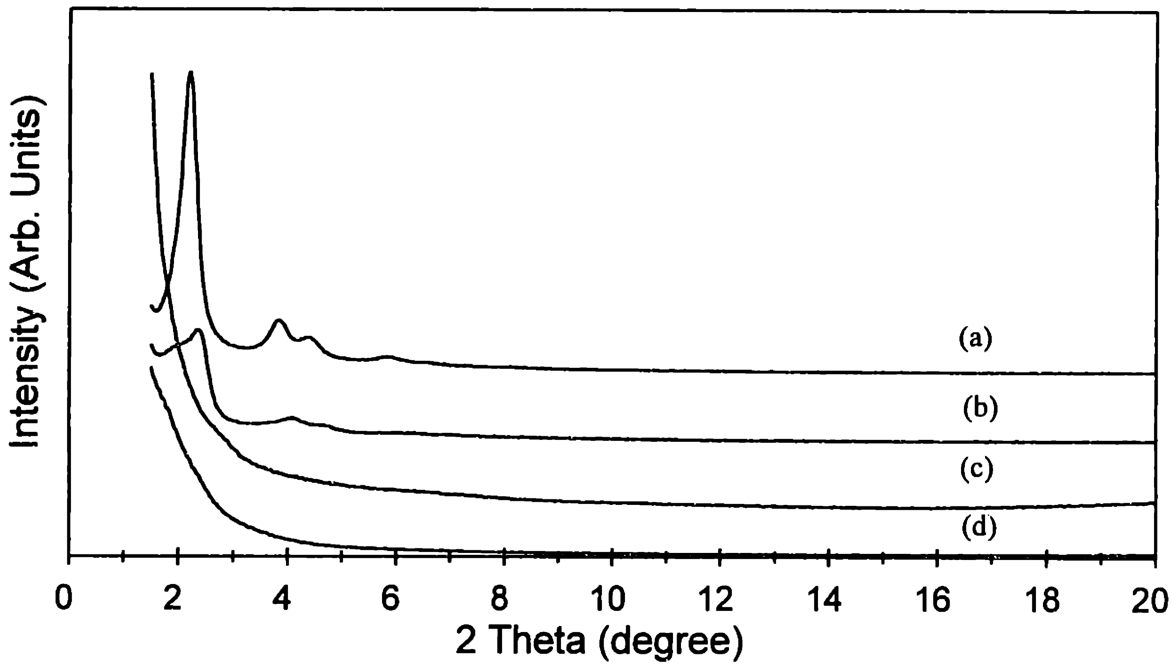

Figure 5.6. XRD patterns of NbSi1-20 samples obtained at a pH of (a) 11.5, (b) 7, (c) 5, and (d) 1.

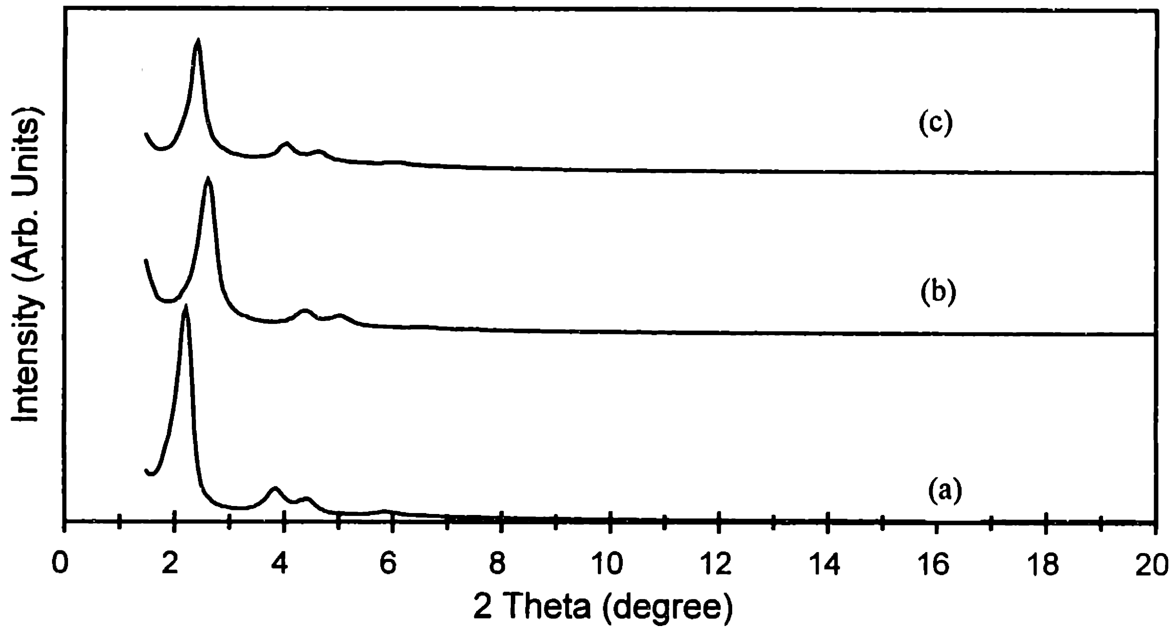

Figure 5.7. XRD patterns of NbSi1-20 samples synthesized with a surfactant-to-Si ratio of (a) 0.5, (b) 1, and (c) 2.

samples prepared with higher surfactant-to-Si ratios.

5.4.4. Effect of Aging Temperature and Addition of a Swelling Agent

Analysis of the thermal evolution of the mesoporous structure indicated that the mesophases could undergo a restructuring process, with stability and pore characteristic being controlled by kinetic parameters such as aging temperature. The structural transformation was affected by entropic changes in the organic array and the rearrangement of the inorganic species.[27] Under basic conditions, partial dissolution and reprecipitation of the silica framework can occur at high temperatures over an extended reaction period. The solubilized silica species are transported to and redeposited at regions of high curvature, further expanding the pore size.[28] Increasing the synthesis temperature can accelerate the condensation of the inorganic precursor and rearrange the mesostructure. In our study, it was found that the pore packing and structure of the Nb-doped mesoporous silica could be controlled by varying the aging temperature (see Figure 5.8). The d(100) spacing increased with an increase in the aging temperature. The higher order peaks became better resolved and increased in intensity with increasing aging temperature, showing an improvement in the long-range pore packing of the materials. The average BJH pore sizes of the resulting materials were observed to increase from 17 Å to 23 Å as the reaction temperature was elevated from 25 °C to 150 °C.

To obtain even larger pore diameters, organic swelling agents can be introduced during synthesis. When the hydrophobic molecules such as mesitylene are added, they are incorporated into the hydrophobic micellar cores to produce MCM-41 with pores > 40 Å.[13] In our study, an as-prepared sample made with 2 equivalents of mesitylene gave a large d(100) spacing of 52.5 Å, but the pore packing in the mesostructure was less well-defined and the pore size distribution was broadened. It was found that the pore size could not be increased beyond 50 Å with mesitylene addition for the Nb-doped silicates.

In general, the microstructure of mesoporous Nb-doped silica is strongly dependent on the siliceous source, Nb dopant concentration, pH of the medium, and aging temperature. The synthesis conditions can be controlled to tailor the microstructure of the materials towards the desired application.

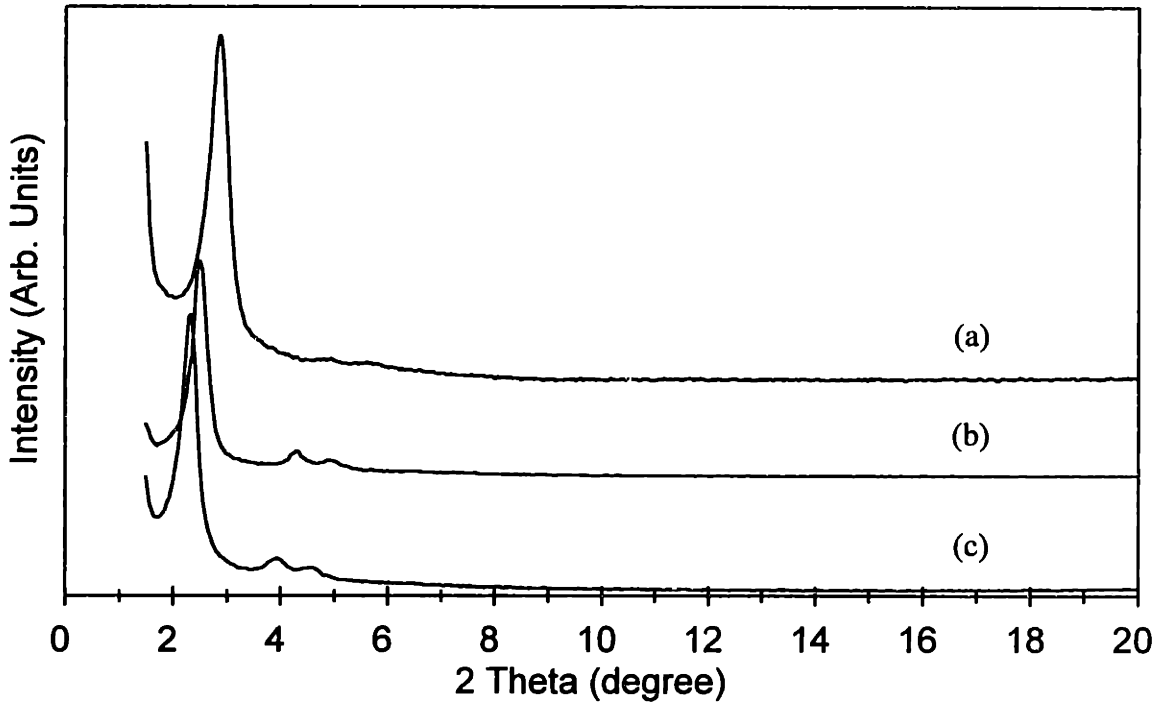

Figure 5.8. XRD patterns of the NbSi2-20 samples aged for 36 hours at (a) 25 °C, (b) 100 °C, and (c) 150 °C.

5.5 Nature of the Nb-dopants in the Mesostructure

Knowledge of the location and coordination of the transition metal cations in the framework of the mesostructure is of practical importance and could lead to a better understanding of the synthesis process and the mechanism of catalytic reactions. Various spectroscopic techniques were employed to characterize the nature of the Nb dopants in the silicate-base mesostructure.

5.5.1 XPS and EPR Studies

XPS provides a surface compositional analysis of the samples. XPS spectra of the calcined Nb-doped mesoporous silica primarily showed the energy absorption from Si, Nb and O elements (Figure 5.9(a)). Some O Auger electrons were noted at the high binding energy. The binding energy of Nb(3d) was obtained from the deconvolution of the Nb($3d_{3/2}$) and Nb($3d_{5/2}$) photoelectron peaks (Figure 5.9(b)). The results (Table 5.3) agreed with previously reported binding energy data for Nb_2O_5 [29,30,31] and SiO_2 supported Nb_2O_5 catalyst.[32] The difference between the binding energy of Nb($3d_{3/2}$) and Nb($3d_{5/2}$) of our Nb-doped silica samples was about 2.6 eV, comparable with that of Nb_2O_5.[33] These results indicated the presence of Nb^{5+} sites in the mesoporous Nb-doped silica materials. The asymmetry of the O(1s) photoelectron peak suggested the presence of Nb-O-Si linkage. The Nb oxidation state was also confirmed by the EPR study. The absence of an EPR signal related to Nb^{5+} species could be explained by the diamagnetic property of Nb^{5+} sites.[34]

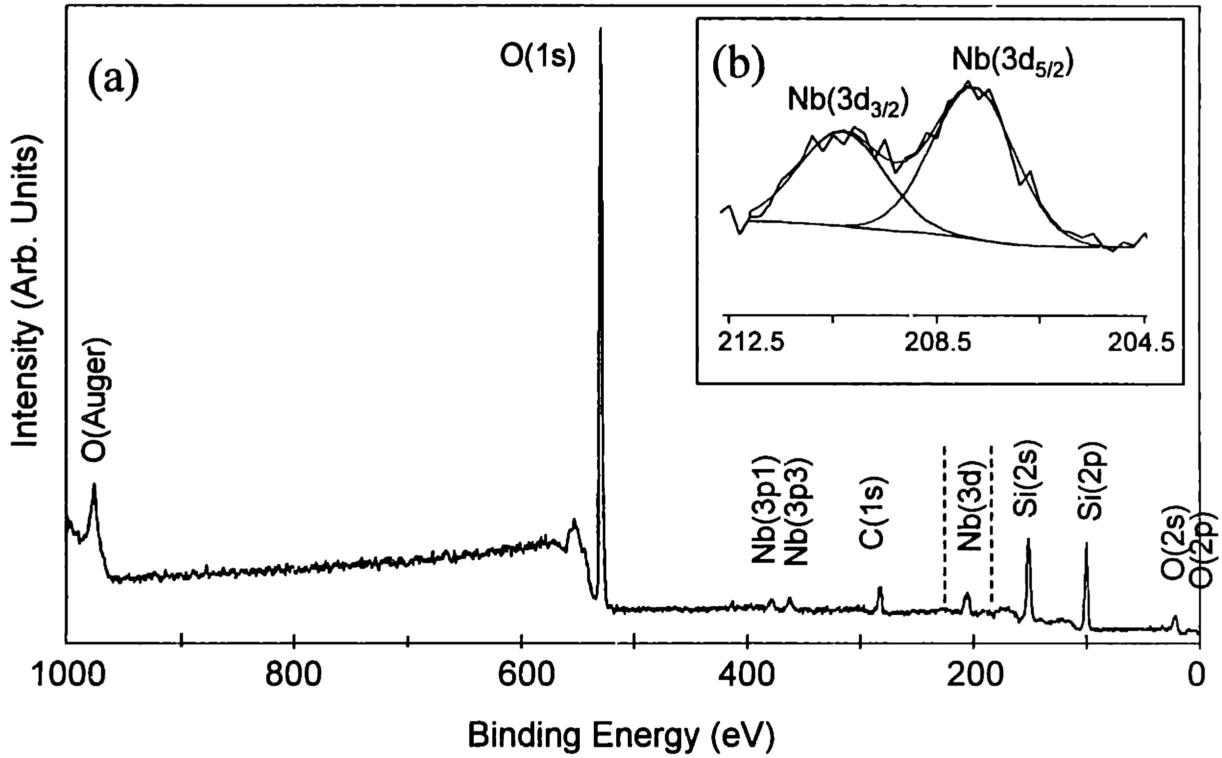

Figure 5.9. XPS spectrum of NbSi1-10: (a) the full spectrum and (b) the section of the spectrum showing the Nb(3d) peaks, which were fitted with a Gaussian distribution.

Table 5.3. Binding energy of the Nb atom in Nb-doped mesoporous silicates

Sample	$Nb(3d_{5/2})$ Binding Energy (eV)	$Nb(3d_{3/2})$ Binding Energy (eV)	Energy Difference (eV) $Nb(3d_{3/2})$ - $Nb(3d_{5/2})$
NbSi1-10	207.8	210.4	2.6
NbSi2-10	207.9	210.6	2.7
NbSi3-10	207.5	210.1	2.6

5.5.2 FTIR and UV-Vis Studies

PA-FTIR spectroscopy provides information on the molecular bonding of the materials. The spectra of the mesoporous materials (Figure 5.10) illustrate the characteristic asymmetric Si-O-Si backbone phonon vibration bands at 960-1280 cm^{-1}, and the symmetric SiO_2 stretchings at 760-880 cm^{-1}.[10] Compared to a pure mesoporous silica, the slight shift of both the symmetric and asymmetric bands might be an indication of Nb incorporation into the silica framework. The Si-OH feature at 978 cm^{-1} was broadened and increased in intensity with increasing Nb dopant concentration. This may be related to the vibrational bands of the dopant component, since the PA-FTIR spectrum of pure Nb_2O_5 shows a broad band starting at 960 cm^{-1}. Similar results were also reported for the Ti-MCM-41 and V-MCM-41 systems.[35,36] Although the origin and assignment of the band are still in debate, the peak broadening may be attributed to the distorted local Nb characteristics in the Si-O-Nb bond.

Pyridine bonds with Lewis acid sites, giving IR characteristic bands at ~1610 cm^{-1} and 1450 cm^{-1}. Brønsted acid sites are represented by a band near 1550 cm^{-1} and two weak bands at 1620-1640 cm^{-1}. In-situ DRIFT studies with pyridine adsorption on NbSi1-20 sample indicated the presence of weak Lewis acid sites and negligible Brønsted acid sites (Figure 5.11). By 300 °C, desorption of pyridine was complete, illustrating the weakness of the acid sites in these materials. The Lewis acidity is attributed to the surface-exposed coordinatively-unsaturated Nb^{5+} sites or extra-framework Nb species. It was reported that the introduction of a high Nb dopant concentration improved the Brønsted acidity of the H^+-form of Nb-MCM-41 materials.[37] Such weak acidity may be useful in catalytic applications, such as synthesis of methanethiol from CH_3OH and H_2S.[37]

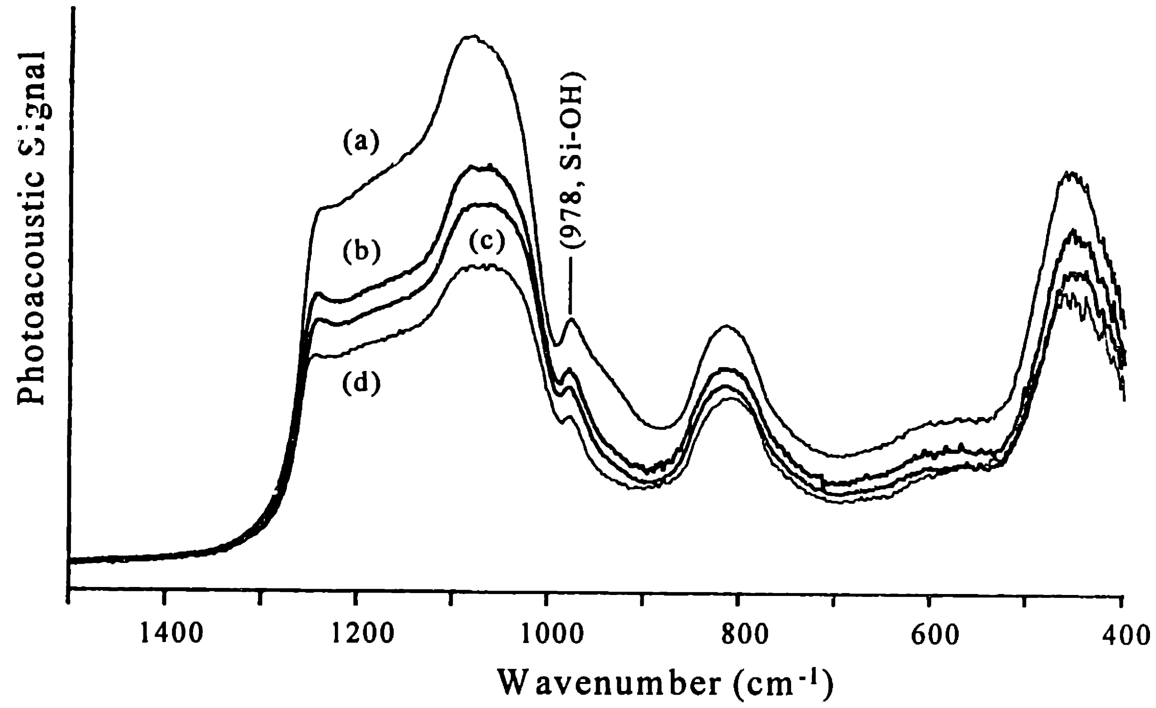

Figure 5.10. PA-FTIR spectra of (a) NbSi1-10, (b) NbSi1-20, (c) NbSi1-100, and (d) pure mesoporous silica.

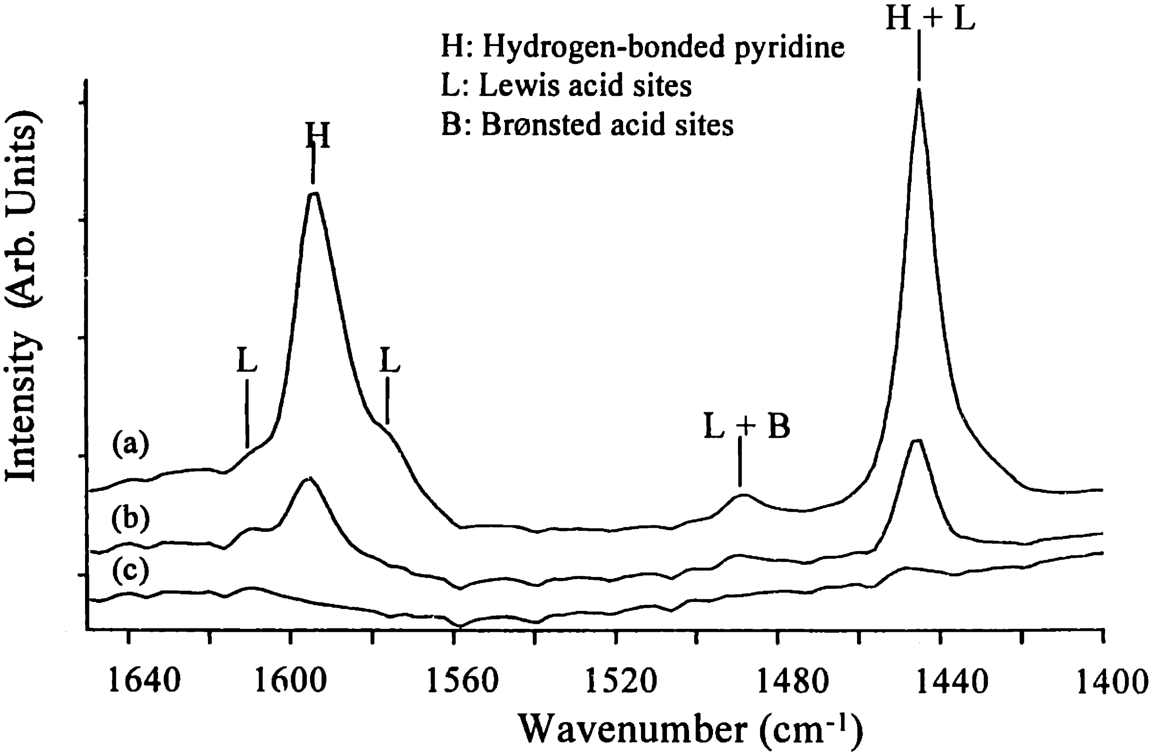

Figure 5.11. In-situ DRIFT spectra of NbSi1-20 sample at (a) 150 °C saturated with pyridine, (b) 150 °C after 30 min of purging with He, and (c) 300 °C after 30 min of purging with He.

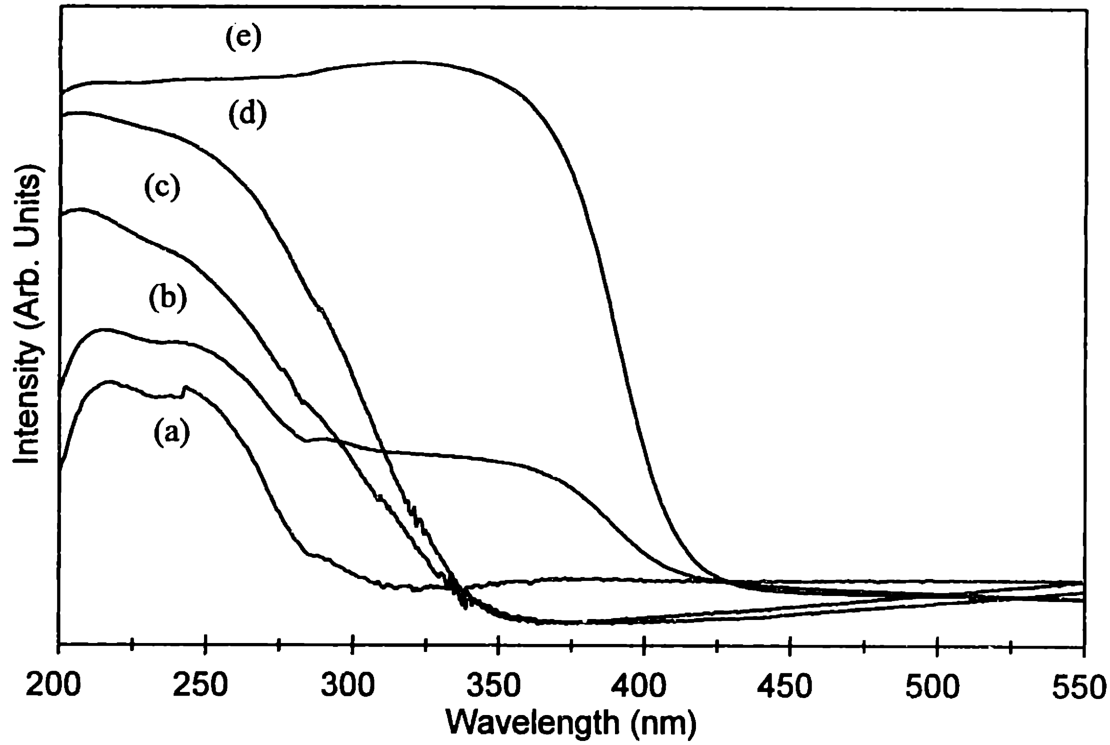

Figure 5.12. Diffuse reflectance UV-Vis spectra of (a) pure mesoporous silica, (b) a physical mixture of mesoporous silica and Nb_2O_5, (c) NbSi1-100, (d) NbSi1-10, and (e) Nb_2O_5.

Compared to the UV-Vis spectrum of mesoporous pure silica with an absorption edge at 270 nm (Figure 5.12(a)), the significant red shift noted with the introduction of Nb dopants could be related to the mixed valence states of Nb and Si, affecting the band energy of the mesoporous materials. This shift to higher wavelength increased with increasing Nb dopant concentration. The absorption edge of pure Nb_2O_5 is near 410 nm (Figure 5.12(e)). The UV-Vis spectra have two small absorption peaks at 210 nm and 245 nm for materials with low Nb-dopant concentration (Figure 5.12(c)). These peaks were greatly broadened at higher dopant levels presumably due to a ligand-to-metal charge transfer (Figure 5.12(d)). In these mesoporous Nb-doped silica materials, the Nb cations are coordinated to four oxygen atoms, but because of their large covalent radius, they can interact with one or two H_2O molecules, thereby creating a distorted tetrahedral environment. In a SiO_2 supported Nb_2O_5 catalyst, the charge transfer band of tetrahedral Nb(V)=O was observed at 235 nm.[38] The spectra of V-MCM-41 exhibited similar bands near this wavelength, which were attributed to the charge transfer bands of V(V) in the tetrahedral coordination.[22,39] The spectrum of a physical mixture of mesoporous pure silica and pure Nb_2O_5 (50:50 wt. ratio) showed two distinct absorption edges corresponding to silica (270 nm) and niobium oxide (410 nm), respectively (Figure 5.12(b)). In contrast, the UV-Vis spectra of the Nb-doped mesoporous silica showed a single, smooth absorption edge, suggesting a homogeneous dispersion of Nb dopants throughout the silica framework.

5.5.3 ^{29}Si MAS NMR Studies

The NMR technique is highly sensitive to the local coordination of detectable species. There is great difficulty in studying our materials with ^{93}Nb NMR, however, due to the large chemical shift and quadrupole interaction of the Nb nuclei.[40] We have consequently utilized ^{29}Si MAS NMR since the possible coupling of Nb to Si can be detected in the molecular structure of silica. The spectrum of a NbSi1-1.33 sample (Figure 5.13 (b)) closely resembles that of the mesoporous pure silica sample (Figure 5.13 (a)). In

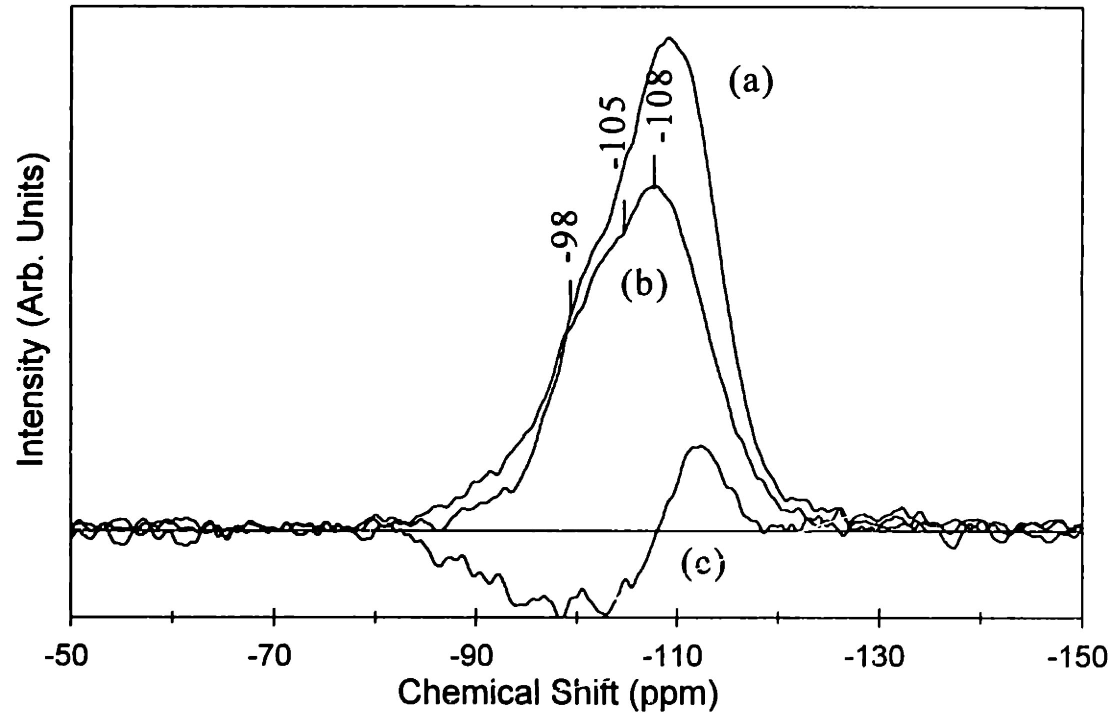

Figure 5.13. ^{29}Si MAS NMR spectra of (a) pure mesoporous silica, (b) NbSi1-1.33, and (c) difference spectrum of (a) and (b).

addition to the Q^4 peak (SiO_4 unit) at ca. -108 ppm and a minor Q^3 peak ($SiO_3(OH)$ unit) at ca. -98 ppm, the spectrum of NbSi-1.33 sample also showed a very broad component at ca. -105 ppm. This may be attributed to the effect of Si interacting with Nb, and therefore can be evidence for Si-O-Nb bonding in the structure. This component can be seen more clearly as the negative peak in the difference spectrum (Figure 5.13(c)). The spectra of NbSi1-10 and NbSi1-20 both presented a weak broad peak in the range of -103 to -105 ppm. A similar broad peak at -106 ppm was observed in previous studies of mesoporous metal-doped silicate materials, and was attributed to framework M-O-Si bonding.[39,41]

5.6 Summary

Mesoporous Nb-doped silicate materials have been successfully synthesized through a micellar templating route. The microstructure of this system can be tailored by controlling various synthesis parameters. The quality and characteristics of the materials depend on the siliceous precursor, dopant concentration, sol pH and aging temperature. It was shown that Nb species were incorporated into the framework of hexagonally-packed mesoporous silica at concentrations as high as ~10 wt%. XPS studies indicated the presence of Nb^{5+} sites in the mesoporous doped silica. The ^{29}Si MAS NMR spectrum of the silica-based material showed a new broad peak at -105 ppm, suggesting the presence of Nb-O-Si bonding in the mesostructure.

5.7 References

[1] C. T. Kresge, M. E. Leonowicz, W. J. Roth, J. C. Vartuli, and J. S. Beck, Nature, **359**, (1992) 710.

[2] C.-Y. Chen, S. L. Burkett, H.-X. Li, and M. E. Davis, Microporous Mater., **2**, (1993) 27.

[3] Q. Huo, D. I. Margolese, U. Ciesla, P. Feng, T. E. Gier, P. Sieger, R. Leon, P. M. Petroff, F. Schüth, and G. D. Stucky, Nature, **368**, (1994) 317.

[4] P. T. Tanev and T. J. Pinnavaia, Science, **267**, (1995) 865.

[5] D. M. Antonelli and J. Y. Ying, Curr. Op. Coll. Interf. Sci., **1**, (1996) 523.

[6] P. T. Tanev, M. Chibwe, and T. J. Pinnavaia, Nature, **368**, (1994) 321.

[7] C-C. Liu, X-K. Ye, and Y. Wu, Catal. Lett., **36**, (1996) 263.

[8] L. Zhang and J. Y. Ying, AIChE J., **43**, (1997) 2793.

[9] C. J. Brinker and G. W. Scherer, *Sol-Gel Science: The Physics and Chemistry of Sol-Gel Processing*, Academic Press, Boston, (1990).

[10] J. Y. Ying, J. B. Benziger, and A. Navrotsky, J. Am. Ceram. Soc., **76**, (1993) 2571.

[11] Q. Huo, D. I. Margolese, U. Ciesla, D. G. Demuth, P. Feng, T. E. Gier, P. Sieger, A. Firouzi, B. F. Chmelka, F. Schüth, and G. D. Stucky, Chem. Mater., **6**, (1994) 1176.

[12] A. Firouzi, D. Kumar, L. M. Bull, T. Besier, P. Sieger, Q. Huo, S. A. Walker, J. A. Zasadzinski, C. Glinka, J. Nicol, D. Margolese, G. D. Stucky, and B. F. Chmelka, Science, **267**, (1995) 1138.

[13] J. S. Beck, J. C. Vartuli, W. J. Roth, M. E. Leonowicz, C. T. Kresge, K. D. Schmitt, C. T.-W. Chu, D. H. Olsen, E. W. Sheppard, S. B. McCullen, J. B. Higgins, and J. L. Schlenker, J. Am. Chem. Soc., **114**, (1992) 10834.

[14] W. C. Beard, in *Molecular Sieves*, edited by R. F. Gould, American Chemical Society, Washington, D. C., (1973) 162.

[15] R. K. Iler, *The Chemistry of Silica*, Wiley, New York, (1979) 150.

[16] Q. Huo, D. I. Margolese, and G. D. Stucky, Chem. Mater., **8**, (1996) 1147.

[17] S. Schacht, Q. Huo, I. G. Voigt-Martin, G. D. Stucky, and F. Schüth, Science, **273**, (1996) 768.

[18] H. Yang, A. Kuperman, N. Coombs, S. Mamiche-Afara, and G. A. Ozin, Science, **379**, (1996) 703.

[19] F. Faiberother, *The Chemistry of Niobium and Tantalum*, Elsevier, Amsterdam, (1967).

[20] C. Alquier, M. T. Vandenborre, and M. Henry, J. Non-Cryst. Solids, **79**, (1986) 383.

[21] G. Oster and D. P. Riley, Acta Cryst., **5**, (1952) 272.

[22] M. Morey, A. Davidson, H. Eckert, and G. D. Stucky, Chem. Mater., **8**, (1996) 486.

[23] S. Schwarz, D. R. Corbin, and A. J. Vega, Mater. Res. Soc. Symp. Proc., **431**, (1996) 137.

[24] D. W. Brack and E. M. Flanigan, *Molecular Sieves*, Society of Chemical Industry, London, (1968) 47.

[25] J. S. Beck, J. C. Vartuli, G. J. Kennedy, C. T. Kresge, W. J. Roth, and S. E. Schramm, Chem. Mater., **6**, (1994) 1816.

[26] J. C. Vartuli, K. D. Schmitt, C. T. Kresge, W. J. Roth, M. E. Leonowicz, S. B. McCullen, S. D. Hellring, J. S. Beck, J. L. Schlenker, D. H. Olsen, and E. W. Sheppard, Chem. Mater., **6**, (1994) 2317.

[27] G. D. Stucky, Q. Huo, A. Firouzi, B. F. Chmelka, S. Schacht, I. G. Voigt-Martin, and F. Schüth, Stud. Surf. Sci. Catal., **105**, (1996) 3.

[28] D. Khushalani, A. Kuperman, G. A. Ozin, K. Tanaka, J. Garces, M. M. Olken, and N. Coombs, Adv. Mater., **7**, (1995) 842.

[29] G. E. McGuire, G. K. Schweitzer, and T. A. Carlson, Inorg. Chem., **12**, (1973) 2451.

[30] D. Simon, C. Perrin, and P. Baillif, C. R. Acad. Sci. Paris, **283C**, (1976) 241.

[31] R. Fontaine, R. Callat, L. Feve, and M. J. Guittet, J. Elect. Spectros., **10**, (1977) 349.

[32] J. G. Weissman, E. I. Ko, and P. Wynblatt, J. Catal., **108**, (1987) 383.

[33] C. D. Wagner, W. M. Riggs, L. E. Davis, J. F. Moulder, and G. E. Muilenberg, *Handbook of X-ray Photoelectron Spectroscopy*, Physical Electronics Division, Perkin-Elmer Corporation, Minnesota, (1992).

[34] F. E. Mabbs and D. Collison, Stud. Inorg. Chem., **16**, (1992) 466.

[35] G. Bellussi and M. S. Rigutto, Stud. Surf. Sci. Catal., **85**, (1994) 177.

[36] P. R. Hari Prasad Rao, R. Kumar, A. V. Ramaswamy, and P. Ratnasamy, Zeolites, **13**, (1993) 663.

[37] M. Ziolek, I. Nowak, and J. C. Lavalley, Catal. Lett., **45**, (1997) 259.

[38] M. Nishimura, K. Asakura, and P. Iwasawa, J. Chem. Soc., Chem. Commun., (1986) 1660.

[39] W. A. Carvalho, P. B. Varaldo, M. Wallu, and U. Schuchardt, Zeolites, **18**, (1997) 408.

[40] D. Redder, Stud. Inorg. Chem., **13**, (1991) 45.

[41] C. F. Cheng, H. He, W. Zhou, J. Klinowski, J. A. Sousa Gonçalves, and L. F. Gladden, J. Phys. Chem., **100**, (1996) 390.

Chapter 6

CATALYTIC ALKENE EPOXIDATION AND ALKANE HYDROXYLATION BY IRON PORPHYRINS ENCAPSULATED IN METAL-DOPED MESOPOROUS SILICA

6.1 Introduction

Metalloporphyrins play an important role in the catalytic oxidation of both saturated and unsaturated hydrocarbons.[1,2] These systems mimic cytochrome P-450 mono-oxygenases, providing excellent chemoselectivity and catalytic activity under mild reaction conditions. Oxidation reaction in mono-oxygenases has been found to occur on the metalloporphyrin surrounded by a globin. Isolated active high-valent oxo-metal sites on the metalloporphyrin are generated by an oxygen transfer from the oxidants.[3] Since synthetic metalloporphyrins lack globin protection, they cannot maintain the physical separation of the active sites. During the catalytic reaction, monomeric oxo-metal adducts tend to convert to a μ-oxo dimer by auto-oxidation and hence lose catalytic activity. Another difficulty encountered in using metalloporphyrins as a homogeneous catalyst is that recovery of the catalyst is prohibitively expensive. We are interested in developing a supported metalloporphyrin heterogeneous catalyst that allows for both site isolation and easy recovery. Since the activity of metalloporphyrins strongly depends on steric and electronic effects, a modification of the chemoselectivity, regioselectivity and shape-selectivity of the metalloporphyrin may be achieved with different catalyst supports. Substantial efforts have been devoted to the development of an effective heterogenized metalloporphyrin catalyst system using amorphous silica, polymer, layered double hydroxides or zeolites as supports.[4,5,6,7,8] Steric hindrance due to the pore geometry of solid matrices and leaching of the porphyrins from conventional supports represent major impediments to the development of effective heterogeneous systems for metalloporphyrin catalysts. To prevent distortion of the porphyrin macrocycles and to facilitate the diffusion of reactants and products in the catalytic reaction, it would be ideal to employ an inorganic support with a well-defined pore structure having pore openings >

2 nm. The hexagonally-packed mesoporous MCM-41 presents an attractive structure for hosting the large metalloporphyrin molecules.

This chapter describes the use of well-define mesoporous doped silicates as an effective support for the large metalloporphyrin molecules.[9,10] To ensure proper encapsulation of metalloporphyrins within the hexagonally-packed cylindrical mesopores of MCM-41, doping of the silica framework with Al was examined to increase surface hydroxyl groups for bonding with the Fe center of porphyrins such as phthalocyanine. We have also devised a novel fixation design that involves ligand interaction between ancillary groups of the metalloporphyrins and the inner surface of the porous structure. Recently, Nb-TMS1 and Ta-TMS1 (the niobium oxide and tantalum oxide analogues of MCM-41) were successfully synthesized via a ligand-assisted templating mechanism. A strong interaction between the amine surfactant molecules and the transition metal precursors was used for structure-directing purposes during surfactant self-assembly.[11,12,13] Using a similar concept, our strategy called for the establishment of a covalent bond between the guest molecule and the host matrix, such that a strong N-Nb interaction is created. This was achieved by using porphyrins with amine terminal groups (e.g. iron(III) meso-(tetra-aminophenyl)-porphyrin bromide ($\mathrm{FeT_{NH2}PPBr}$)), and by introducing Nb dopants into the MCM-41 structure. The resulting heterogeneous catalysts retained the native characteristics of the metalloporphyrins in effective oxidation catalysis, while ensuring that the active sites could not undergo self-oxidation. Besides preventing the leaching of active complexes, these systems enabled easy catalyst recovery and reuse. Specifically, iron porphyrins supported on Al- and Nb-doped MCM-41 were examined for the epoxidation and hydroxylation of large cyclic molecules under ambient conditions.

6.2 Synthesis of Supported Iron Porphyrin Catalysts

6.2.1 Iron Phthalocyanine Encapsulated in Mesoporous Al-doped Silica

The mesoporous aluminosilicates were synthesized using surfactant templating route. 3.65 g of $C_{16}H_{33}(CH_3)_3NBr$ (CTABr) surfactant was completely dissolved in 80 g of H_2O. 22.2 g of 27% sodium silicate solution was slowly added to the surfactant solution at room temperature with vigorous stirring for 5 minutes. The pH of the mixture was then adjusted to 11.5 with diluted H_2SO_4. After stirring for 15 min, 0.682 g of aluminum sulfate dissolved in 20 g of water was then gradually introduced to the loosely-bonded silica gel, and continuously stirred for 3 hours at room temperature before the sample was hydrothermally treated at 100 °C for 4 days. The molar composition of the wet gel could be represented as 1 SiO_2 : 0.1 CTABr : 120 H_2O : 0.02 Al_2O_3. The solid powder obtained was washed with ethanol and water, filtered, and then calcined at 540 °C in air for 6 hours to remove the organics. The samples were designated as AlSi-R, where R = 25 was given by the precursor molar ratio of Si and Al. 1 g of calcined AlSi-25 was first degassed at 350 °C overnight, and then mixed with 0.1 g of iron phthalocyanine (FePc) (90%) (Aldrich) in 100 ml of acetone or dichloromethane (CH_2Cl_2) with stirring for 24 hours at ambient conditions. The catalyst-loaded mesoporous material was next washed thoroughly with acetone and CH_2Cl_2 by Soxhlet extraction. The FePc on the external surface was removed by extended Soxhlet extraction with pyridine for 24 hr. The sample was then dried in vacuum oven at 120 °C. A schematic of the heterogeneous catalyst obtained is shown in Figure 6.1.

Chemical bonding in the mesoporous materials was studied by photoacoustic Fourier-transform infrared (PA-FTIR) spectroscopy. Spectra were collected in a 2.5 kHz rapid scan mode at 2 cm^{-1} resolution in a Bio-Rad FTS-60A/896 spectrometer using a MTEC Model 200 photoacoustic cell. Compared to the PA-FTIR spectrum of the unloaded AlSi-25 matrix, the spectrum of FePc-loaded material exhibited a group of additional peaks in the range of 1400-1500 cm^{-1} and 2840-2980 cm^{-1}, which corresponded to the C-H vibrations of the encapsulated porphyrins (Figure 6.2). These peaks were slightly shifted in position from those of free porphyrins in solution, indicating the confinement of the porphyrin molecules in the pore structure of AlSi-25 (see insert in Figure 6.2). A significant decrease in the intensity of the free M-OH peak (~3745 cm^{-1}) after the loading of FePc into the mesoporous aluminosilicate suggested

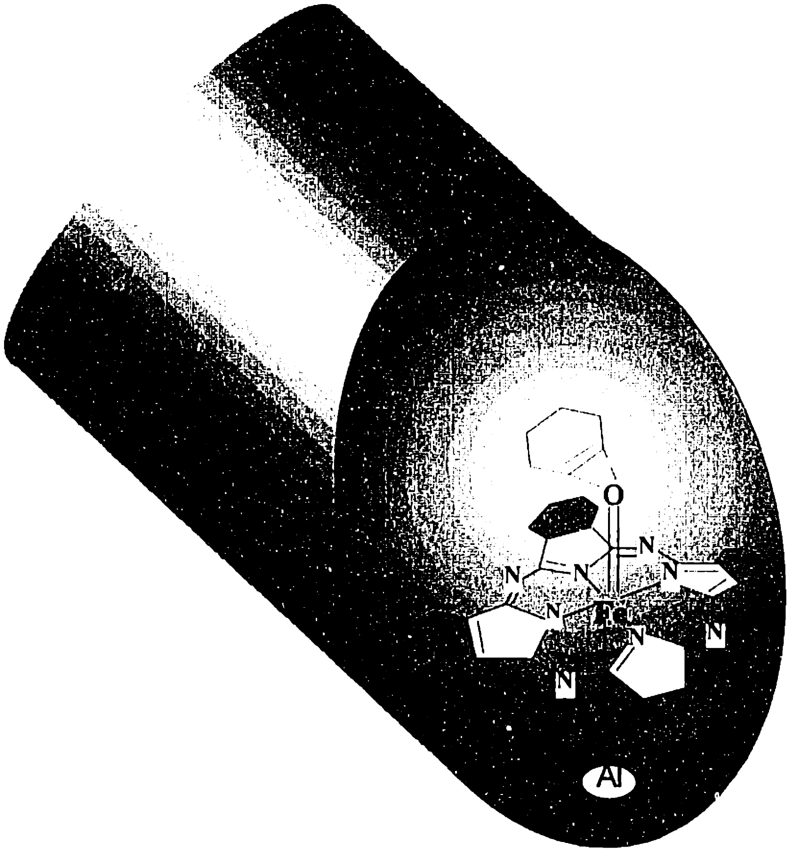

Figure 6.1. Schematic illustrating the iron phthalocyanine encapsulated in the pore channel of mesoporous Al-doped silica, interacting with cyclohexene.

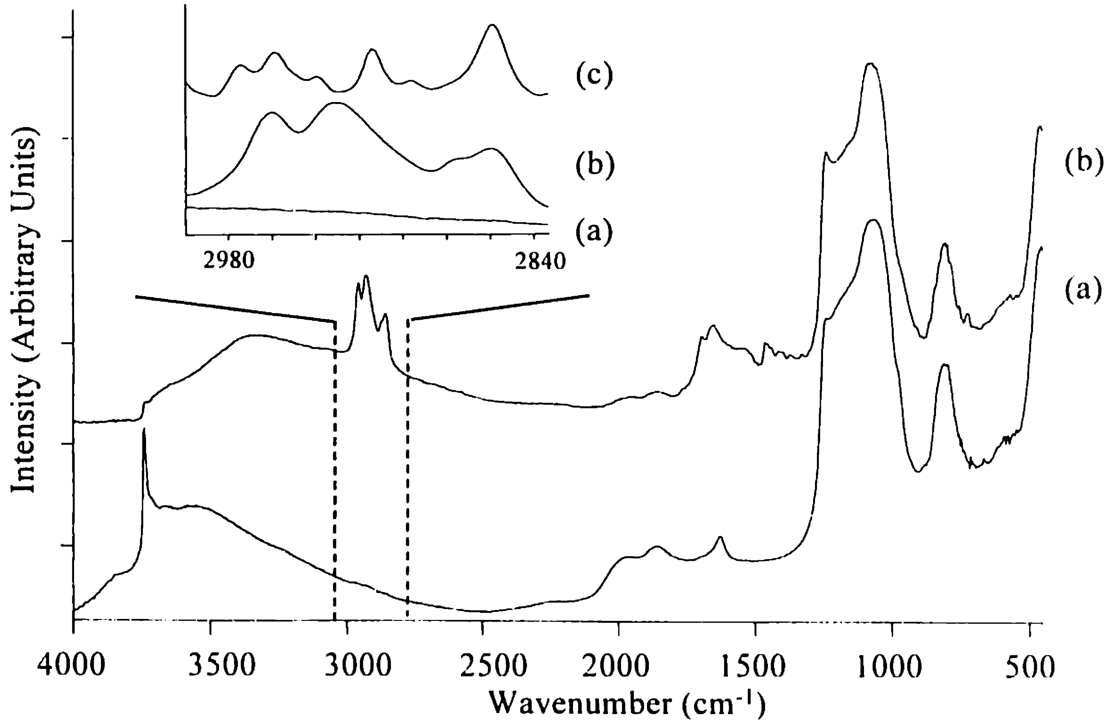

Figure 6.2. PA-FTIR spectra of (a) mesoporous AlSi-25, (b) FePc/AlSi-25, and (c) unsupported FePc. The insert is an enlargement of the spectral region of 2830-3000 cm^{-1}.

that a strong interaction was present between the Fe center and the surface free -OH groups of the AlSi-25 matrix. The regularity of the pore structure of the catalyst support was characterized by powder X-ray diffraction (XRD) (Siemens D5000 θ-θ diffractometer, operated at 45 kV and 40 mA using Ni-filtered CuK_α radiation). XRD pattern illustrated that the FePc-loaded AlSi-25 retained the hexagonal pore packing of the mesoporous support. No crystalline peaks associated with FePc were detected by X-ray diffraction, confirming a high dispersion of the FePc complexes.

6.2.2 Amine-substituted Iron Porphyrin Encapsulated in Mesoporous Nb-doped Silica

The siliceous sources used in the synthesis of NbSi1 and NbSi2 were a 10 wt% aqueous tetramethylammonium silicate (TMAS) solution (Sachem) and a 27 wt% sodium silicate solution (Aldrich), respectively.[14] Specifically, in the synthesis of NbSi1-5.4, 50 g of TMAS was stirred for 10 min after the addition of 0.5 g of sulfuric acid (H_2SO_4). 6.8 g of cetyltrimethyl ammonium bromide (CTABr) (Alfa) dissolved in 20.3 g of water was then mixed with TMAS solution and stirred for 30 min. 1.32 g of niobium ethoxide ($Nb(OEt)_5$) (Aldrich), was gradually introduced into the loosely bounded silica gel and stirred for 30 min. 10 g of water was then added to the gel, which was then aged at 100 °C for 7 days. In the synthesis of NbSi2-20, 3.65 g of CTABr was completely dissolved in 166 g of water. 22.2 g of sodium silicate solution diluted in 50 g of water was slowly added to this surfactant solution at room temperature with vigorous stirring for 30 min. 1.585 g of $Nb(OEt)_5$ was gradually introduced into the loosely-bonded silica gel. The pH of the mixture was adjusted to 11.5 by the addition of dilute H_2SO_4. The resulting gel mixture was stirred continuously for 3 hours at ambient conditions before subjected to a hydrothermal treatment at 100 °C for 5 days. The molar compositions of the wet gels of NbSil-5.4 and NbSi2-20 were represented as 1 SiO_2 : 0.5 CTABr : 120 H_2O : 0.093 Nb_2O_5 and 1 SiO_2 : 0.1 CTMABr : 120 H_2O : 0.02 5 Nb_2O_5, respectively. The hydrothermally treated materials were washed with ethanol and water, filtered, and then calcined at 540 °C in air for 6 hours to remove the organic surfactants.

To increase the pore size of Nb-doped mesoporous silica, a mixture of cationic surfactants and neutral surfactants was used as templating agents in the modified synthesis described below. 1.82 g (5 mmol) of CTABr and 0.534 g (2.5 mmol) of tetradecylamine (C14-NH_2) (Acros) were dissolved in 108 g of water. 11.4 g of tetraethoxysilane (United Chemical) was gradually added to the surfactant solution at room temperature and stirred for 30 min. A desired amount of the $Nb(OEt)_5$ was then introduced dropwise into the loosely-bonded silica gel. The pH of the mixture was adjusted to 11 by the addition of tetraethylammonium hydroxide. The resulting gel mixture was stirred continuously for 3 hours at ambient conditions before subjected to a hydrothermal treatment at 120 °C for 4 days. The molar composition of the wet gel was represented as $1\ SiO_2 : 0.1\ CTABr : 2x\ C14\text{-}NH_2 : 120\ H_2O : x\ Nb_2O_5$ (where $x = 0\text{-}0.05$). The hydrothermally treated material was washed with ethanol and water, filtered, and then calcined at 540 °C in air for 6 hours to remove the organic surfactants. The calcined mesoporous material was designated NbSi4-R, where R is given by the precursor atomic ratio of Si to Nb. The XRD pattern of calcined NbSi4-20 showed a large d(100) spacing of 50 Å (Figure 6.3).

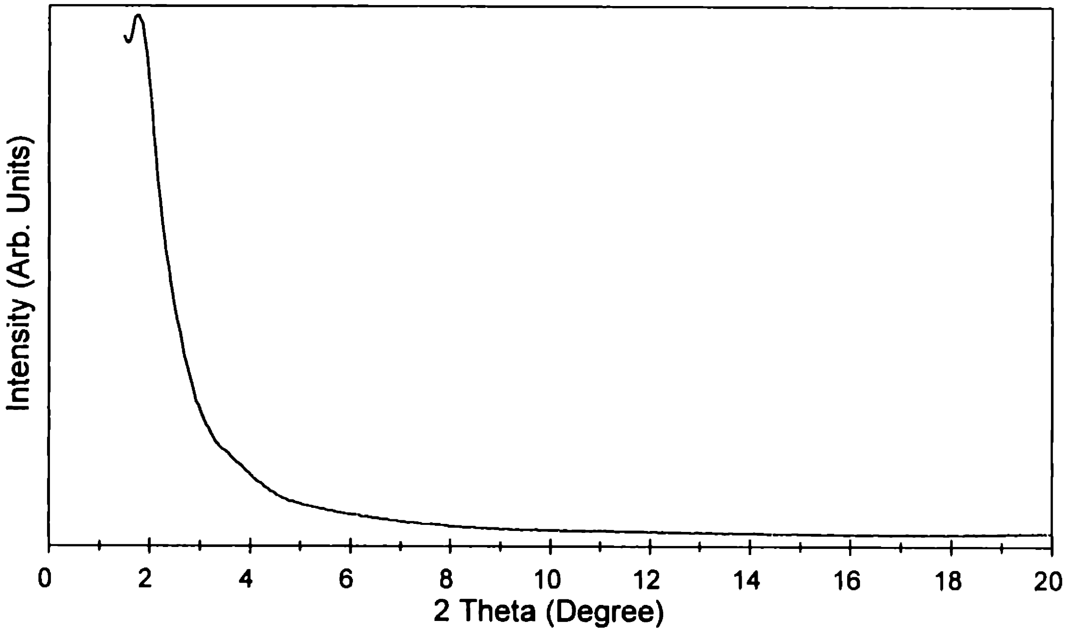

Figure 6.3. XRD pattern of calcined mesoporous NbSi4-20.

In order to examine the effect of support microstructure on catalytic activity, an amorphous Nb-doped silica gel was synthesized by sol-gel processing under acidic conditions without the presence of surfactant templating agents. 10.4 g (0.05 mol) of tetraethoxysilane was dissolved in a mixture of 2.3 g (0.05 mol) of ethanol and 14.4 g (0.8 mol) of water. The pH of the solution was adjust to ~2 by adding 0.05 g of 37% HCl, and the resulting sol was vigorously stirred at room temperature for 26 hours. 1.59 g (0.005 mol) of $Nb(OEt)_5$ was then slowly introduced dropwise to the silica sol. The Nb-doped silica gel was aged at room temperature for 3 days. The molar composition of the wet gel was represented as 1 SiO_2 : 0.05 Nb_2O_5 : 1 C_2H_5OH : 16 H_2O : 0.01 HCl. After drying at ambient conditions for 2 weeks, the dried gel was calcined at 540 °C in air for 6 hours.. It was subjected to N_2 adsorption analysis with an ASAP 2010 gas sorption instrument (Micromeritics). The BET (Brunauer-Emmett-Teller) and BJH (Barrett-Joyner-Halenda) methods were used to calculate the sample's surface area and pore size distribution, respectively. The amorphous Nb-doped SiO_2 has a N_2 adsorption/desorption isotherm (Figure 6.4) characteristic of microporous materials (pore size < 20 Å) and a BET surface area of 557 m^2/g.

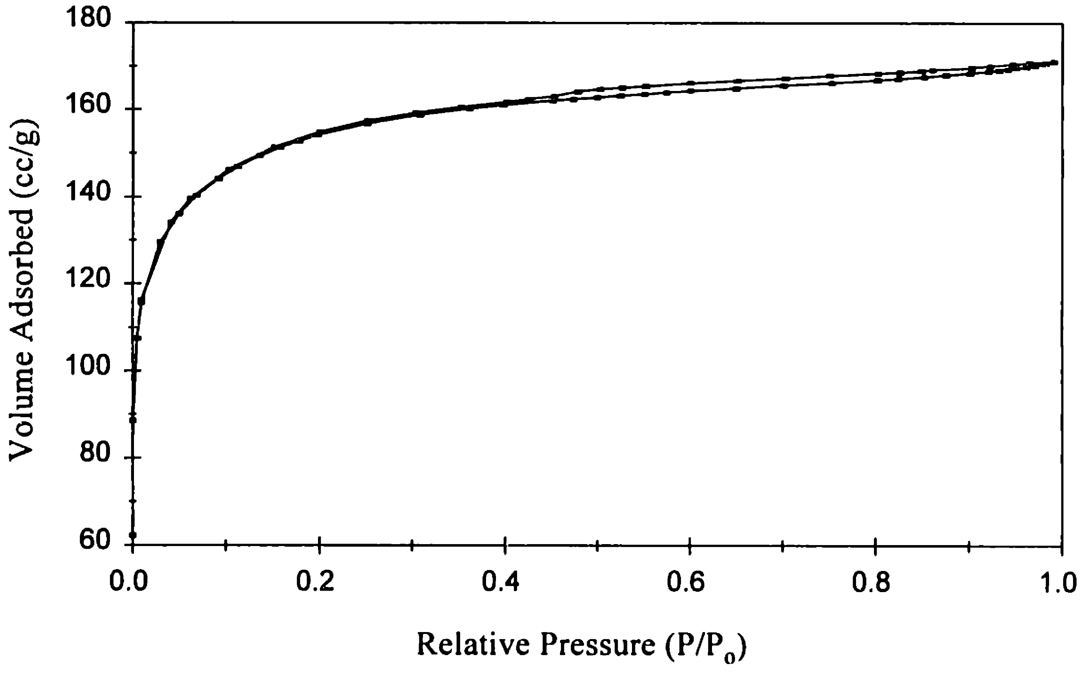

Figure 6.4. N_2 adsorption/desorption isotherm of the amorphous sol-gel derived Nb-doped silica

The amine-substituted iron porphyrin was synthesized following the published procedure[15] (Figure 6.5). In the first step, meso-tetra(nitrophenyl)porphyrin ($H_2T_{NO2}PP$) was derived by dissolving 27.5 g of p-nitrobenzaldehyde (98%) (Strem) in 250 ml of refluxing glacial acetic acid, followed by dropwise addition of 11.6 ml of pyrrole (98%) (Alfa) with further reflux for 20 min. The resulting dark purple solution was cooled with an ice bath to 35 °C after addition of 67.5 ml of chloroform ($CHCl_3$). The crystalline purple solid was collected by filtration and washed with $CHCl_3$. The free porphyrin was vacuum dried at 100 °C overnight.

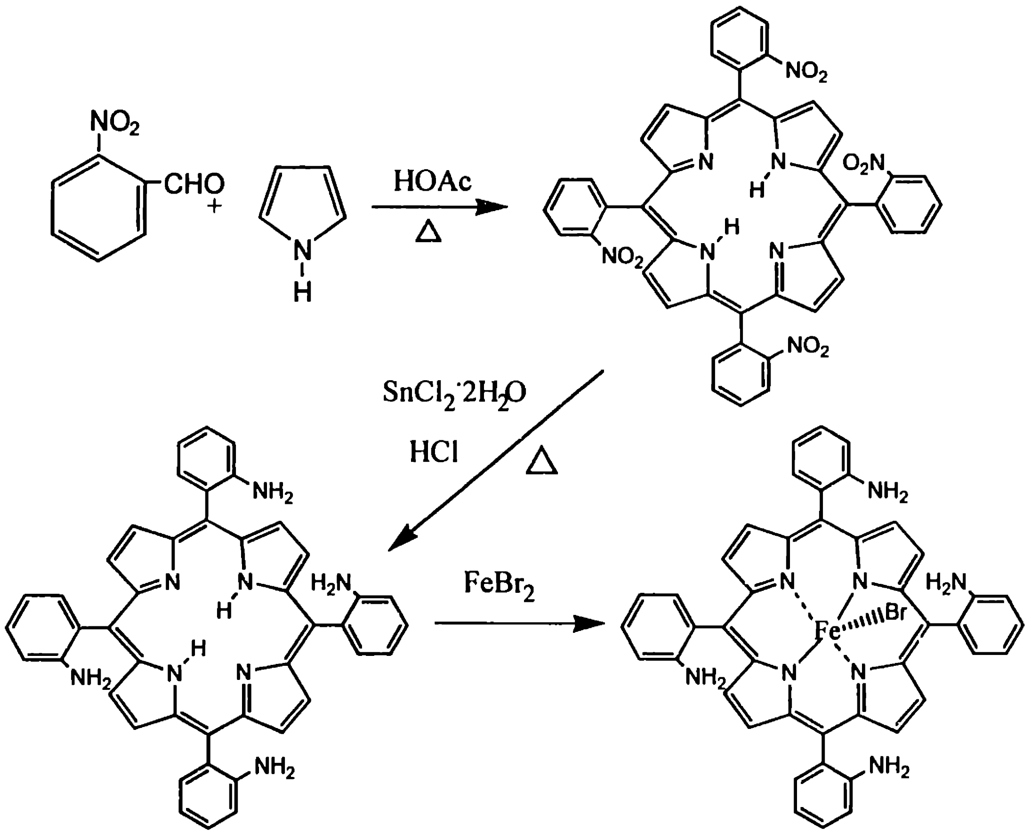

Figure 6.5. Schematic illustrating the synthesis route of $FeT_{NH2}PPBr$.

The meso-tetra(nitrophenyl)porphyrin ($H_2T_{NO2}PP$) obtained was used in the second step of the reaction scheme to synthesize meso-tetra(*o*-aminophenyl)porphyrin ($H_2T_{NH2}PP$) by reduction of the NO_2 groups to NH_2 groups. Generally, 4 g of $H_2T_{NO2}PP$ was dissolved in 200 ml hydrochloric acid at room temperature. 16.7 g of the reducing agent, tin chloride dihydrate ($SnCl_2{\bullet}2H_2O$) (Aldrich), was next added to the porphyrin solution, which was then quickly heated to 65-70 °C for 25 min. The resulting green solution was neutralized by slow addition of concentrated ammonium hydroxide. 300 ml of $CHCl_3$ was then added to the solution. The mixture was stirred for 1 hour before extraction of the $CHCl_3$ layer. The $CHCl_3$ phase was reduced to 200 ml by rotary evaporation, washed with aqueous ammonia and water, and dried over anhydrous sodium sulfate (Na_2SO_4). A further purification was conducted with the addition of 100 ml of ethanol and 50 ml of heptane. A purple crystalline powder was obtained after solvent evaporation and methanol washing. The elemental analysis of the amine-substituted porphyrins (74.26:5.21:15.73) was in good agreement with the expected C:H:N weight ratios (78.5:5.05:16.6). The ultraviolet-visible (UV-Vis) spectrum was collected using a Cary II UV-Vis spectrometer. The UV-Vis transmission spectrum of the sample consisted of absorption peaks at 421 nm, 514 nm, 589 nm, and 650 nm, which are characteristic of $H_2T_{NH_2}PP$ (Figure 6.6).

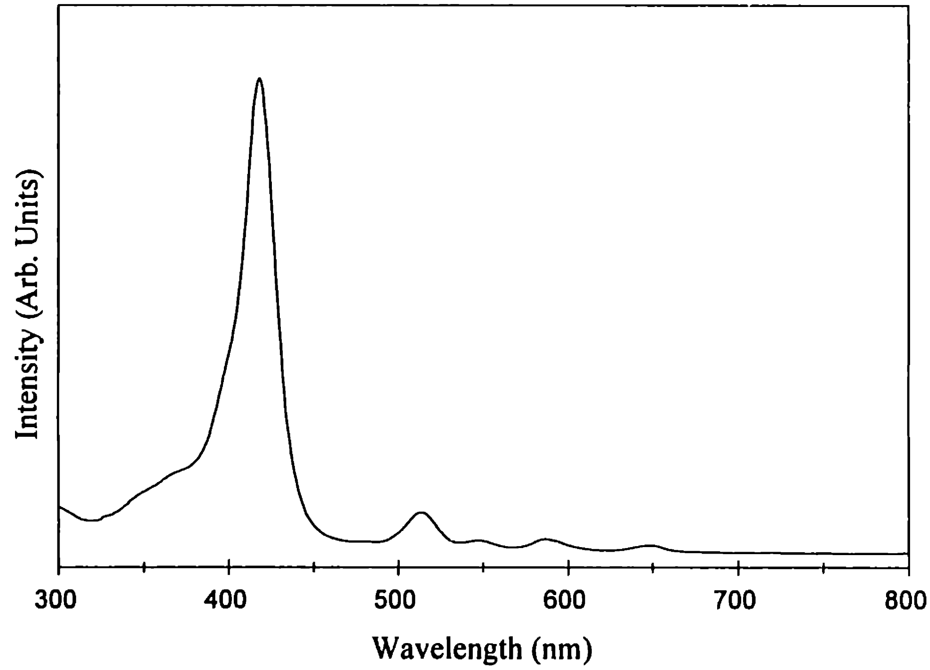

Figure 6.6. UV-Vis transmission spectrum of $H_2T_{NH_2}PP$ porphyrin synthesized.

The iron metallation of $H_2T_{NH_2}PP$ (1 g) was achieved with anhydrous $FeBr_2$ (1 g) (99.9 %) (Aldrich). The reactants were refluxed in 200 ml of dry tetrahydrofuran under nitrogen for 3 hours. The solvent was removed by rotary evaporation and extracted by

$CHCl_3$. The separated $CHCl_3$ layer was treated with 2 ml KOH and dried over anhydrous Na_2SO_4. The anhydrated solution was then reduced to 20 ml, and 10 ml of methanol and 3-4 drops of hydrobromic acid were added to it. The fine blackish-purple amine-substituted iron porphyrin (Fe(III)T_{NH_2}PPBr) was finally recovered by evaporation of the solvents at room temperature. The UV-Vis transmission spectrum of this material showed broader bands at 420 nm, 510 nm, 600 nm, and 660 nm (Figure 6.7).

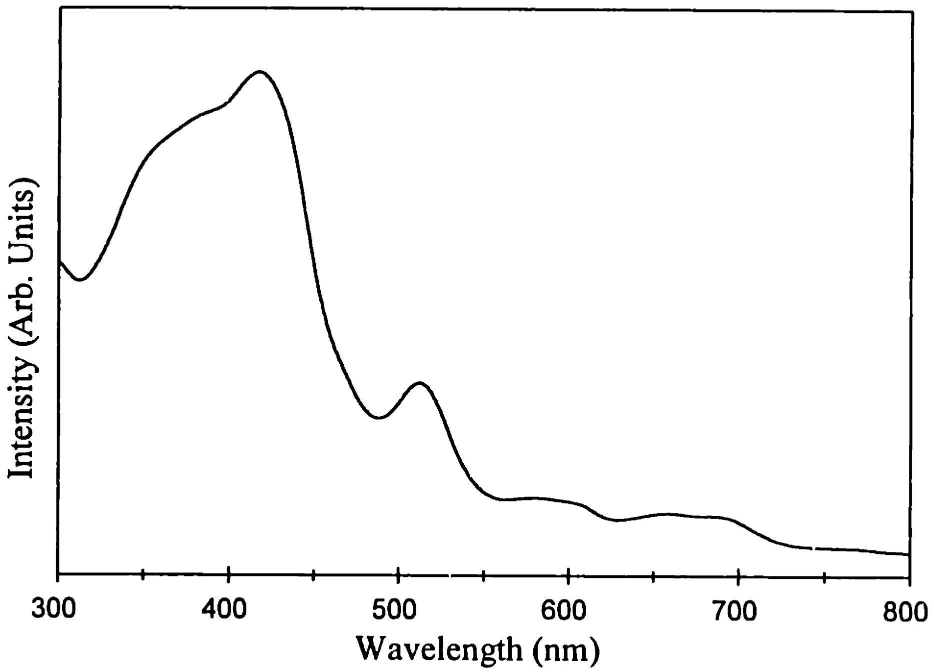

Figure 6.7. UV-Vis transmission spectrum of FeT_{NH_2}PPBr synthesized.

The three series of calcined Nb-doped mesoporous silica samples (NbSi1, NbSi2, and NbSi4) and the amorphous sol-gel derived Nb-doped silica were individually mixed with the desired amount of Fe(III)T_{NH_2}PPBr in 100 ml of chloroform and stirred for 24 hours at room temperature. The catalyst-loaded mesoporous support was washed thoroughly with $CHCl_3$ and CH_2Cl_2 until the solution appeared colorless. The sample was then vacuum dried at 100 °C for 12 hours. A schematic of the supported catalyst is shown in Figure 6.8. The fixation mechanism was designed to be different from the Coulombic or hydrogen-bonding interaction involved in conventional supported systems. The Nb dopants in MCM-41 could form a strong covalent bonding with the terminal NH_2 groups of the metalloporphyrins.[16] The formation of such Nb-N covalent bonds might be crucial for the immobilization of the iron complexes within the mesoporous matrix. This design strategy could provide for an effective fixation of the porphyrin molecules without engaging their metal centers. This would then allow the Fe centers to be freely accessible as active sites for catalytic oxidation.

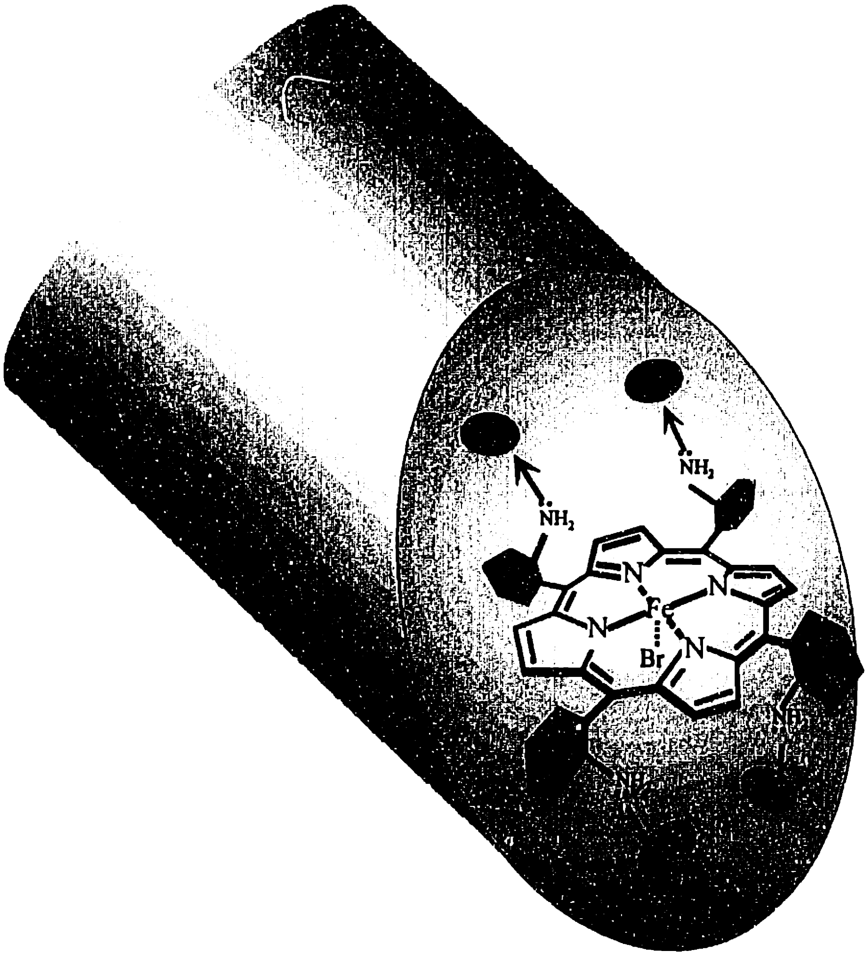

Figure 6.8. Schematic illustrating the encapsulation of NH_2-functionalized iron porphyrin in the pore channel of mesoporous Nb-doped silica.

The diffuse reflectance UV-Vis spectrum of the supported $FeT_{NH2}PPBr$ showed a broad Soret absorption band at 420 nm, indicating the presence of iron porphyrins in the mesoporous matrix (Figure 6.9). The appearance of the Q band implied that there was no distortion of the conjugated porphyrin plane[17] in the large pore opening of our mesoporous matrix.

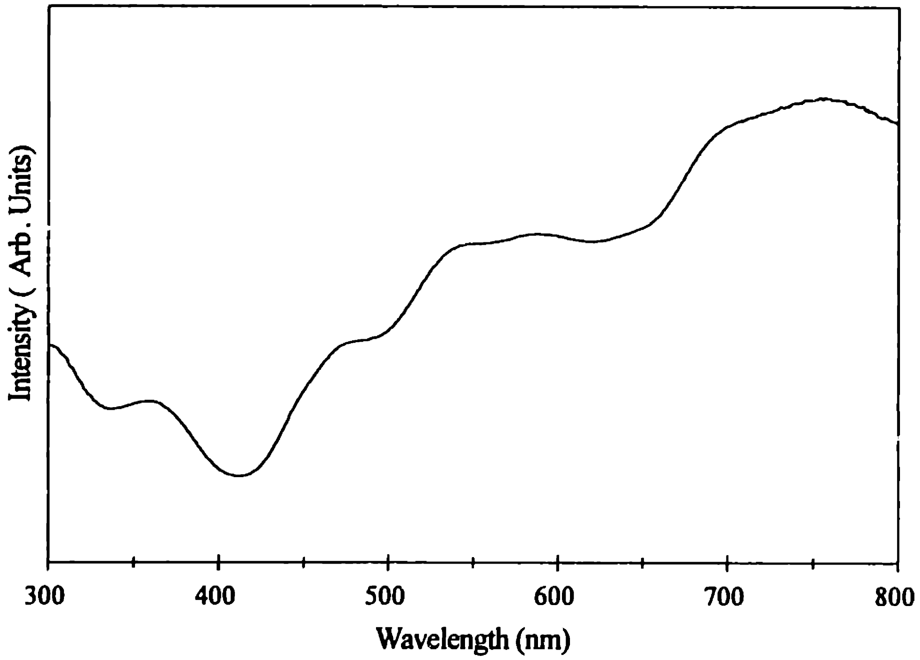

Figure 6.9. UV-Vis diffuse reflectance spectrum of $FeT_{NH_2}PPBr$/NbSi2-20.

Compared to the PA-FTIR spectrum of the unloaded NbSi1-10 matrix, the spectrum of encapsulated $FeT_{NH_2}PPBr$ exhibited two groups of additional peaks in the ranges of 1400-1500 cm^{-1} and 2820-3020 cm^{-1} (Figure 6.10), corresponding to the C-H vibrations of the encapsulated porphyrins. These peaks were slightly shifted in position from those of homogeneous iron porphyrin solution, indicating the presence of a strong interaction between the porphyrin molecules and the NbSi1-10 matrix. Elemental analysis data of the catalysts are presented in Table 6.1. For NbSi1 samples, our studies showed that the saturated iron porphyrin loading was greater in the mesoporous matrix containing the higher Nb dopant concentration. XRD patterns showed a preservation of the support's mesostructure with no additional peaks associated with iron porphyrin crystallites, confirming that the porphyrins were highly dispersed in the mesoporous matrix. The heterogenized $FeT_{NH_2}PPBr$/NbSi2-20 catalyst has a lower BET surface area of 629 m^2/g compared to 822 m^2/g for the unloaded NbSi2-20 matrix. With iron porphyrin loading, the peak of the BJH pore size distribution of NbSi2-20 was shifted from 23 Å to 21 Å (Figure 6.11), and the pore volume was decreased from 0.74 cm^3/g to 0.52 cm^3/g, indicating that iron porphyrins were located inside the mesopores of the support. Using NbSi4-20 as a catalyst support, $FeT_{NH_2}PPBr$/NbSi4-20-1 catalyst showed

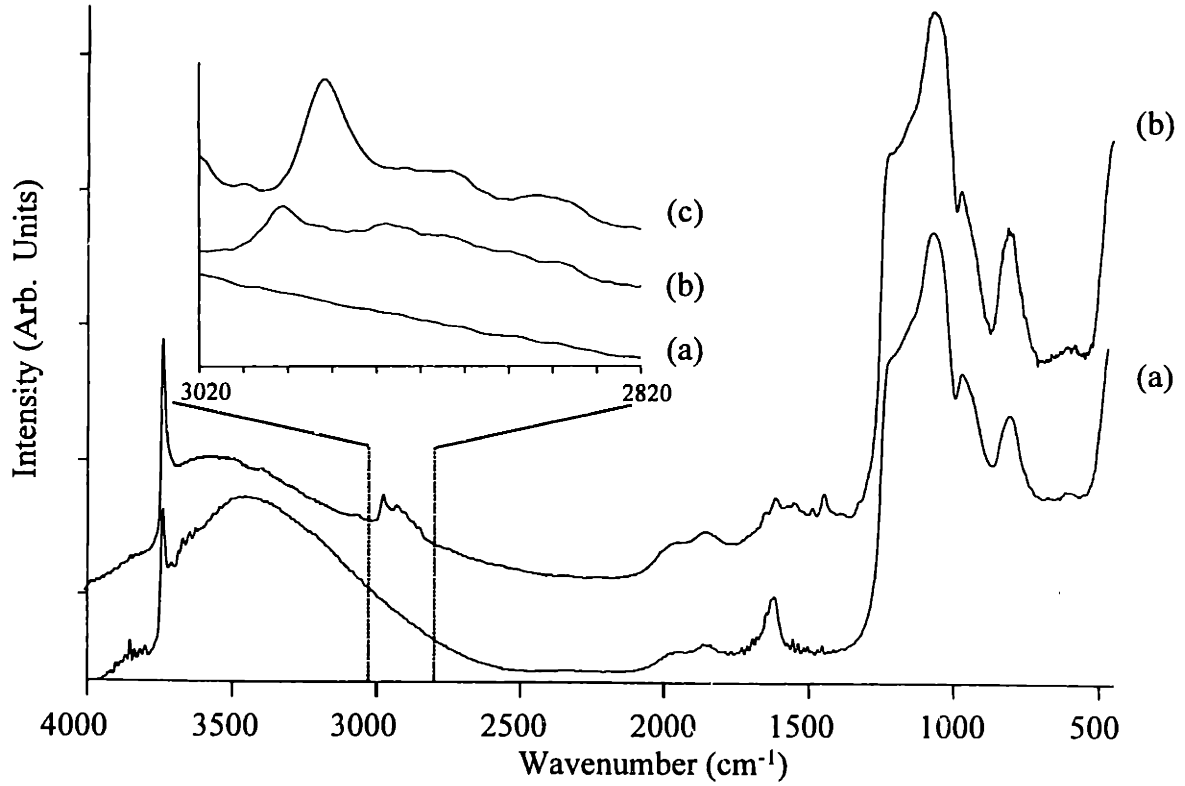

Figure 6.10. PA-FTIR spectra of (a) mesoporous NbSi1-5.4, (b) Fe(III)T$_{NH2}$PPBr/NbSi1-5.4, and (c) unsupported Fe(III)T$_{NH2}$PPBr. The insert is an enlargement of the spectral region of 2820-3020 cm^{-1}.

a lower BET surface area (666 m^2/g) than the unloaded NbSi4-20 support (865 m^2/g) (Figure 6.12). A pore volume reduction from 1.14 cm^3/g to 0.89 cm^3/g was also observed upon porphyrin loading. The average pore size of the FeT$_{NH2}$PPBr-loaded NbSi4-20-1 (32 Å) was slightly reduced compared to that of the unloaded NbSi4-20 (33 Å).

Table 6.1. Elemental analysis of FeT$_{NH_2}$PPBr/NbSi-R catalysts

Catalyst Support	Si (wt%)	Nb (wt%)	Fe (wt%)
NbSi1-5.4	42.8	7.72	0.75
NbSi1-11.4	43.1	3.64	0.36
NbSi2-20	43.6	3.21	0.25
NbSi4-20-1	25.9	6.00	0.14
NbSi4-20-2	25.9	6.00	0.37
Nb-doped Sol-Gel Derived Silica	32.9	8.60	0.36

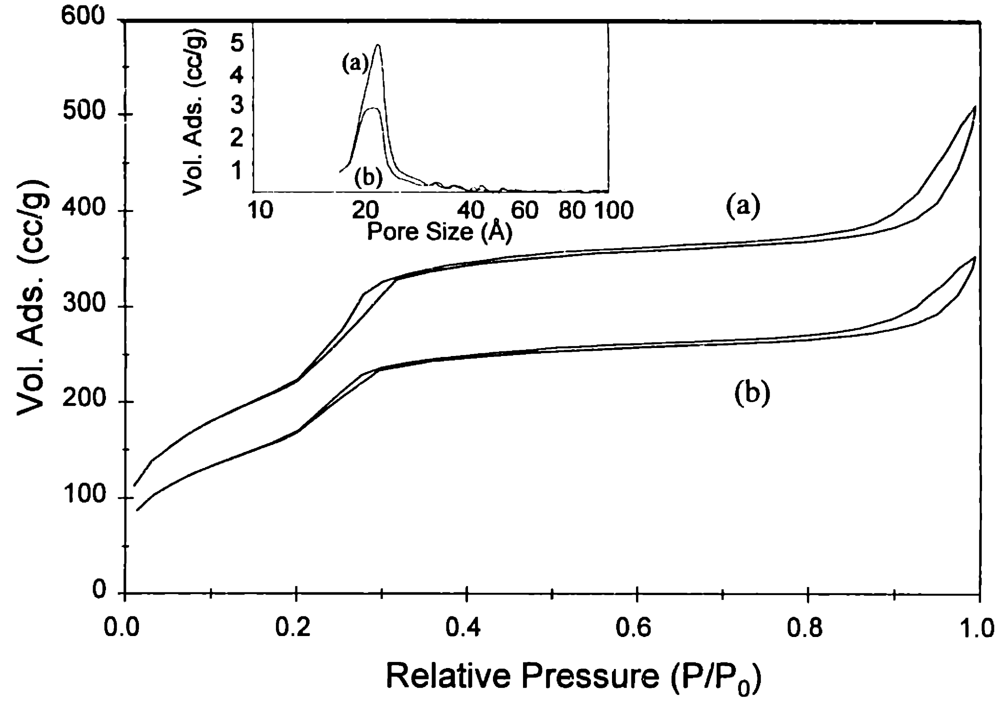

Figure 6.11. N_2 adsorption/desorption isotherms of (a) NbSi2-20 matrix and (b) heterogeneous Fe(III)T_{NH2}PPBr/NbSi2-20 catalyst. The insert is the BJH pore size distribution calculated from the desorption isotherm.

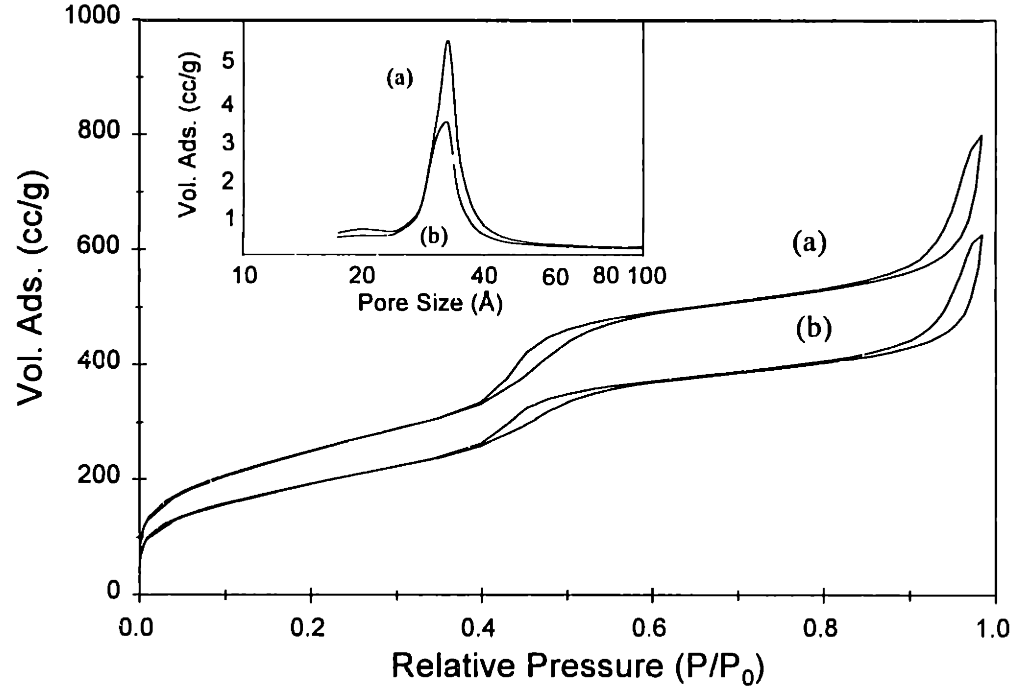

Figure 6.12. N_2 adsorption/desorption isotherms of (a) NbSi4-20 matrix and (b) heterogeneous Fe(III)T_{NH2}PPBr/NbSi4-20-1 catalyst. The insert is the BJH pore size distribution calculated from the desorption isotherm.

6.2.3 Experimental Set-up for Catalytic Studies

The vacuum dried heterogeneous metalloporphyrin catalysts were examined for alkene epoxidation and alkane hydroxylation at ambient conditions in a 25 ml batch micro-reactor. In both oxidation reactions, the conversion was monitored at regular time intervals by gas chromatography (HP 5880), using a HP-Wax capillary column (0.32 mm x 0.5 μm) and FID detector. The experimental set-up is shown in Figure 6.13. A blank run without the addition of catalyst, and a homogeneous reaction with unsupported metalloporphyrin catalyst were also examined.

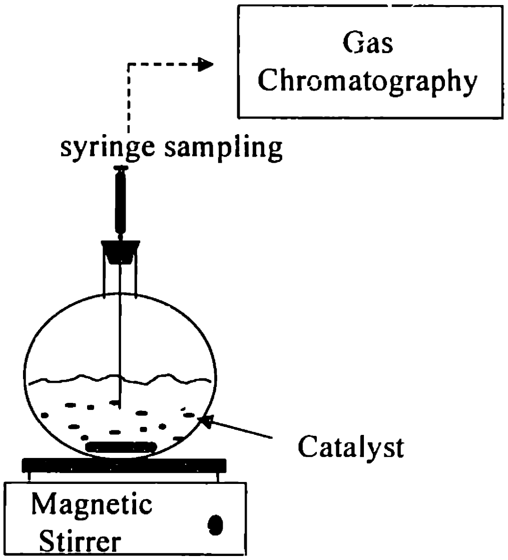

Figure 6.13. Schematic of the catalytic reactor set-up.

6.3 Hydroxylation of Cyclohexane over Supported Iron Porphyrin Catalysts

In hydroxylation of saturated hydrocarbons by metalloporphyrins, primary alcohol is formed via hydrogen atom abstraction, followed by rapid recombination of a metal bound OH. Here, hydroxylation of cyclohexane to cyclohexanol, an important precursor for the production of adipic acid, was examined using iron porphyrins supported on mesoporous metal-doped silica materials with iodosobenzene (PhIO) as the oxidant. PhIO was prepared from the hydrolysis of iodosobenzene diacetate with aqueous sodium hydroxide.[18] The cyclohexane hydroxylation reaction is illustrated as follows,

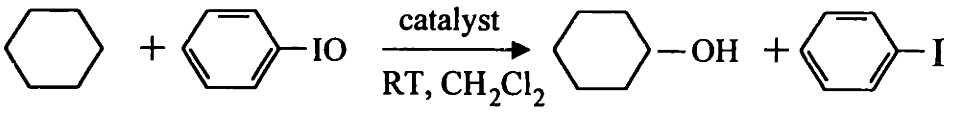

(6.1)

6.3.1 FePc/Al-doped Silica Catalysts

The heterogeneous reaction was conducted in a septum-sealed 25 ml mini-flask at ambient conditions. Typically, 3 ml of cyclohexane was mixed with 7 ml CH_2Cl_2, with 30 µl of chlorobenzene as the internal standard. 100 mg of heterogeneous catalyst and 110 mg (0.5 mmol) of iodosobenzene were then added to the reaction vial and stirred. The reaction progress was monitored with GC through hourly sampling. A blank run of the reaction without catalyst addition was examined. The catalytic results were calculated based on the iodosobenzene charged, the full conversion of which was analyzed by introducing 2 ml of 10% sodium bisulfite ($NaHSO_3$) or sodium sulfite (Na_2SO_3) solution to the blank run. The corresponding homogeneous reaction was performed at an identical condition with an equivalent molar amount of the Fe porphyrin catalyst used in the heterogeneous reaction. Turnover number (TON) was calculated from the mmoles of product obtained per mmole of Fe porphyrin catalyst empolyed.

No activity for cyclohexane hydroxylation was observed in the absence of catalyst or with unloaded mesoporous support. A conversion of 74% was obtained after 6 hours for cyclohexane hydroxylation over FePc/AlSi-25 (Fe loading: 0.53 wt%, FePc: 5.4 mg) (Figure 6.14). The selectivity to cyclohexanol was 100% throughout the reaction. The turnover number of 43 with the heterogeneous system after 6 hours was similar to that achieved by the homogeneous catalyst (FePc: 5.4 mg, TON = 42). The total conversion was higher than that reported for the zeolite-encapsulated iron phthalocyanine (Fe loading: 2.4 wt%, FePc: 24.5 mg, steady state conversion: 14%, TON = 1.5).[19] This might be attributed to the much larger pore opening of the mesoporous support, which provided ample room for hosting the porphyrin catalysts without distortion of their macrocycle plane, and which facilitated diffusion of the reactants and products. In addition, an enhanced nucleophilic characteristic could be expected for the active center of the confined iron complex due to electron donation from AlSi-25.

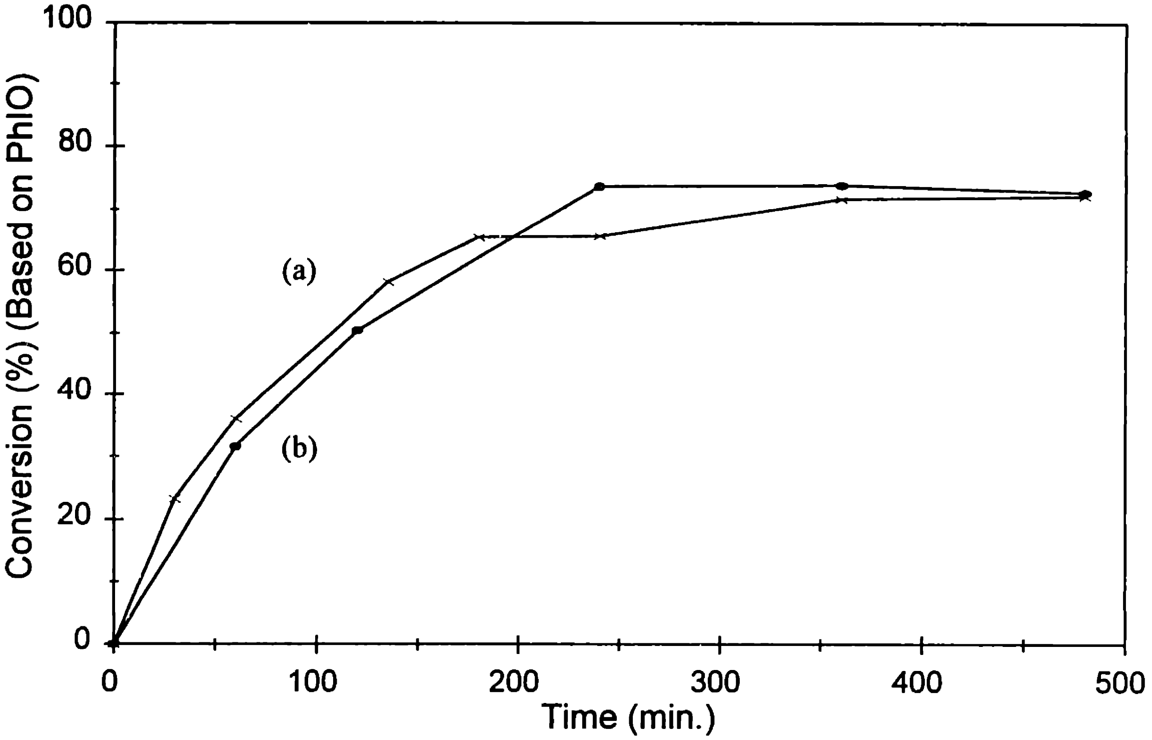

Figure 6.14. Conversion of cyclohexane hydroxylation over (a) unsupported FePc (5.4 mg), and (b) supported FePc/AlSi-25 catalyst (containing 5.4 mg FePc).

6.3.2 Fe(III)T_{NH2}PPBr/Nb-doped Silica Catalysts

The exclusive formation of cyclohexanol was achieved with a conversion of 49% in 6 hours over Fe(III)T_{NH2}PPBr/NbSi1-5.4 (Fe loading: 0.75 wt%, FeT_{NH2}PPBr: 10.8 mg, TON = 19). The heterogeneous reaction initially took place at a slower rate than the homogeneous reaction (Figure 6.15). This might be due to steric and electronic effect in the immobilized catalyst. After 6 hours of reaction, the conversion of our heterogeneous catalyst was slightly lower than that obtained with the homogeneous catalyst (10 mg) (59%, TON = 24), and was greater than that reported for a zeolite-supported iron phthalocyanine catalyst (Fe loading: 2.4 wt%, FePc: 24.5 mg, steady state conversion: 14%, TON = 1.5).[19] Compared to the zeolitic supports, the larger pore diameter and pore volume of the mesoporous matrix provided sufficient space for hosting the porphyrins without distorting their macrocycles and facilitated diffusion of the reactants and products. The advantage of the mesoporous support was further evident in the finding that activity for cyclohexane hydroxylation was negligible over metalloporphyrins supported on acid-catalyzed sol-gel derived amorphous 8.6 wt% Nb-doped silica (Fe loading: 0.36 wt%). No cyclohexanol was produced over this system after 6 hours of reaction. The microporous support could provide porphyrin immobilization via Nb-N bonding as in NbSi1-5.4, but its small pore diameters would have severely restricted the diffusion of the reactant and product molecules.

During the course of the reaction, no catalyst leaching was detected in our Fe(III)T_{NH2}PPBr/NbSi1-5.4 system, as indicated by the lack of the characteristic Soret band associated with free Fe(III)T_{NH2}PPBr in the UV-Vis spectrum of the reaction solution (Figure 6.16). This confirmed that catalyst fixation was successfully achieved with the unique Nb-N ligand interaction we devised.

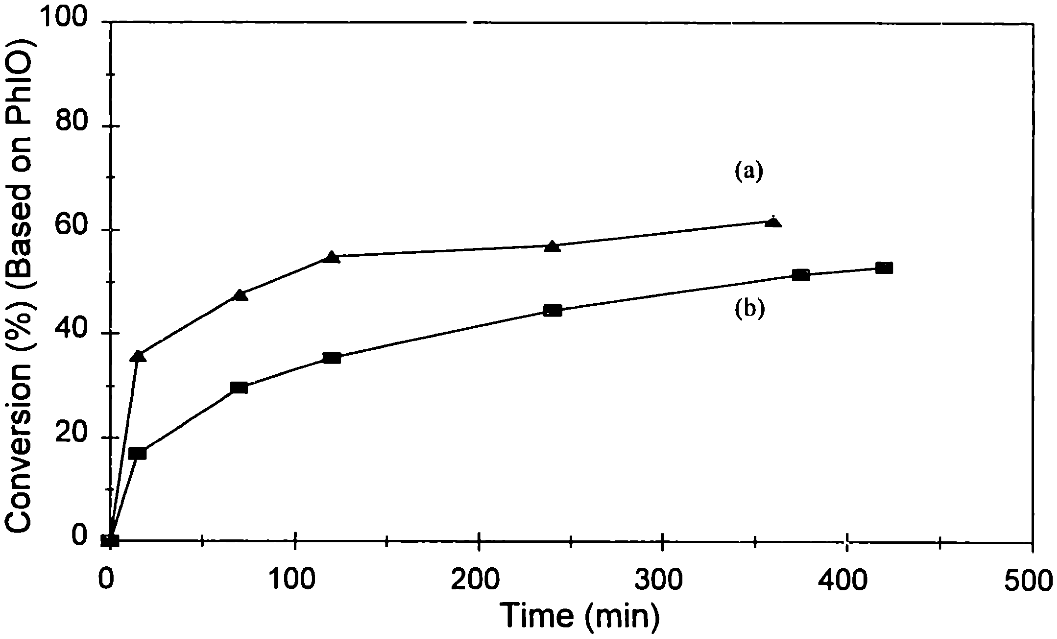

Figure 6.15. Conversion of cyclohexane hydroxylation over (a) unsupported $FeT_{NH2}PPBr$ (10 mg) and (b) supported $FeT_{NH2}PPBr$/NbSi1-5.4 catalyst (containing 10.8 mg $FeT_{NH2}PPBr$).

6.4 Epoxidation of Alkenes over Supported Iron Porphyrin Catalysts

Epoxidation of olefins is an important partial oxidation reaction in organic

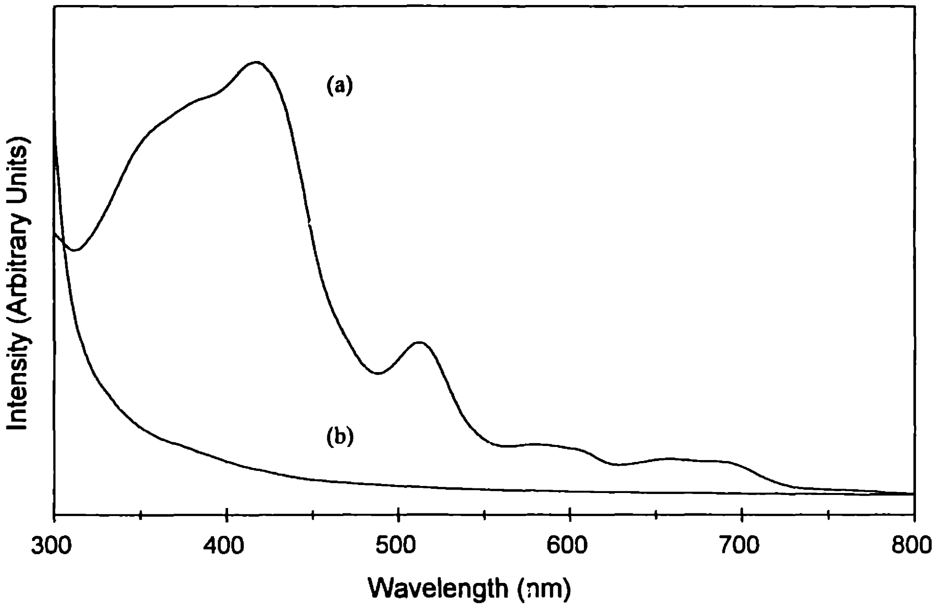

Figure 6.16. UV-Vis transmission spectra of (a) $FeT_{NH2}PPBr$ solution and (b) the reaction solution after 7 hours of cyclohexane hydroxylation over $FeT_{NH2}PPBr$/NbSi1-5.4 catalyst.

synthesis. Using metalloporphyrins as catalysts, epoxidation can be performed under mild conditions with a large variety of oxidants, such as iodosobenzene, hypochlorite, organic peroxide, oxygen and electron source. The stability of the metalloporphyrins can be greatly enhanced through a catalyst support.

6.4.1 FePc/Al-doped Silica Catalysts

The epoxidation of cyclohexene (Eq. 6.2) was used as a model reaction to test our heterogeneous catalyst.

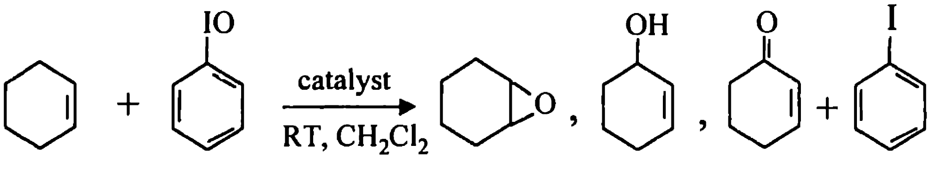

(6.2)

Typically, 1 ml of alkene was mixed with 4 ml CH_2Cl_2, with 20 μl of chlorobenzene as the internal standard. 100 mg of heterogeneous catalyst and 110 mg

(0.5 mmol) of iodosobenzene were then added to the reaction vial and stirred. The reaction progress was monitored with GC at regular intervals. The catalytic results were calculated based on the iodosobenzene charged, the full conversion of which was analyzed by introducing 2 ml of 10 wt% Na_2SO_3 to an identical blank run without catalyst addition. The corresponding homogeneous reaction was performed at identical conditions with equivalent mole of iron porphyrin catalyst as the heterogeneous reaction.

In the epoxidation of cyclohexene over FePc/AlSi-25 (Fe loading: 0.53 wt%, FePc: 5.4 mg) with PhIO, 64% and 98% conversion were obtained after 2 hours and 6 hours, respectively, with cyclohexene oxide as the major product (Figure 6.17). In addition to cyclohexene oxide, 2-cyclohexen-1-ol and 2-cyclohexen-1-one were produced via allylic oxidation. A mechanism for allylic oxidation proposed by Groves *et al.* suggests that auto-oxidation is initiated by dioxygen, resulting in cyclohexenyl peroxyl radicals.[20] A similar allylic oxidation also occurred over polymer-supported iron porphyrin catalyst, with 2- cyclohexen-1-one as the main product.[21] In our case, however, the formation of cyclohexene oxide dominated the reaction. This might be

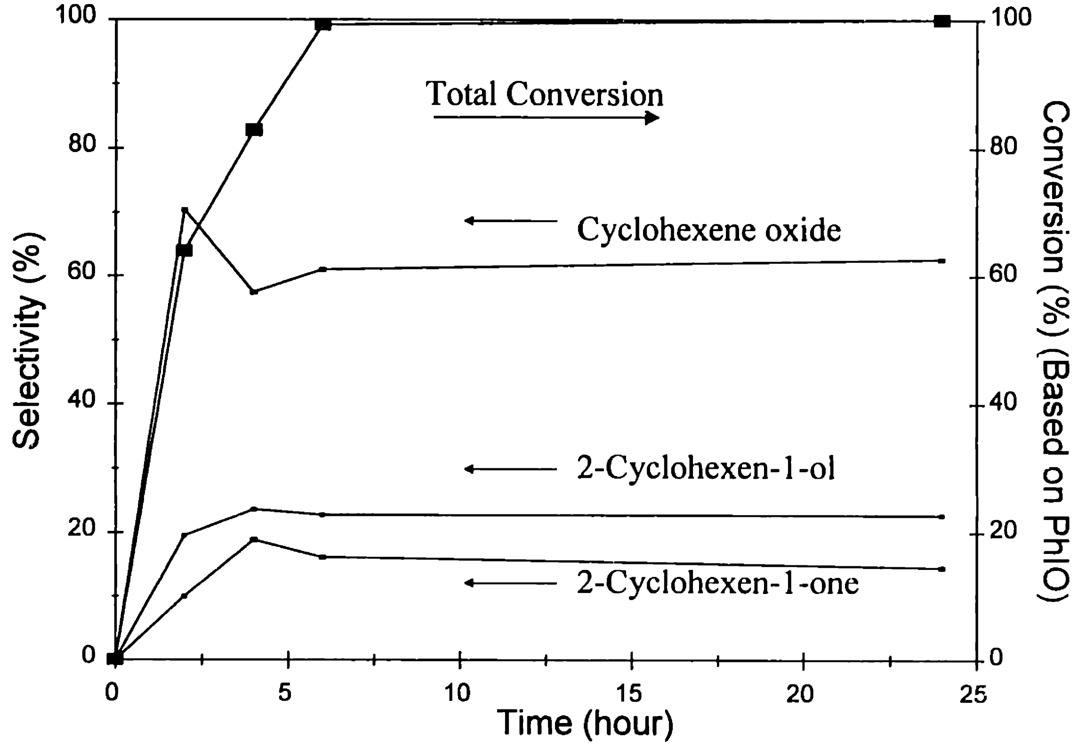

Figure 6.17. Conversion and product selectivity of cyclohexene epoxidation with iodosobenzene over supported FePc/AlSi-25 catalyst (containing 5.4 mg FePc) under air.

attributed to the uniform, large pore diameter of the mesoporous matrix, which facilitated the formation and diffusion of cyclohexene oxide products without substantial further oxidation.

6.4.2 Fe(III)T$_{NH2}$PPBr/Nb-doped Silica Catalysts

6.4.2.1 Epoxidation of Cyclohexene

Epoxidation of cyclohexene over encapsulated FeT$_{NH2}$PPBr/NbSi1-5.4 catalysts gave a total conversion of 86% after only 2 hours (Figure 6.18(b)). In addition to the formation of cyclohexene oxide, allylic oxidation was also observed, yielding 2-cyclohexen-1-ol and 2-cyclohexen-1-one as by-products (Figure 6.19). As with FePc/AlSi-25 catalyst, high selectivity to cyclohexene oxide was achieved with FeT$_{NH2}$PPBr/NbSi1-5.4 catalyst. This could be attributed to the ease of diffusion of most

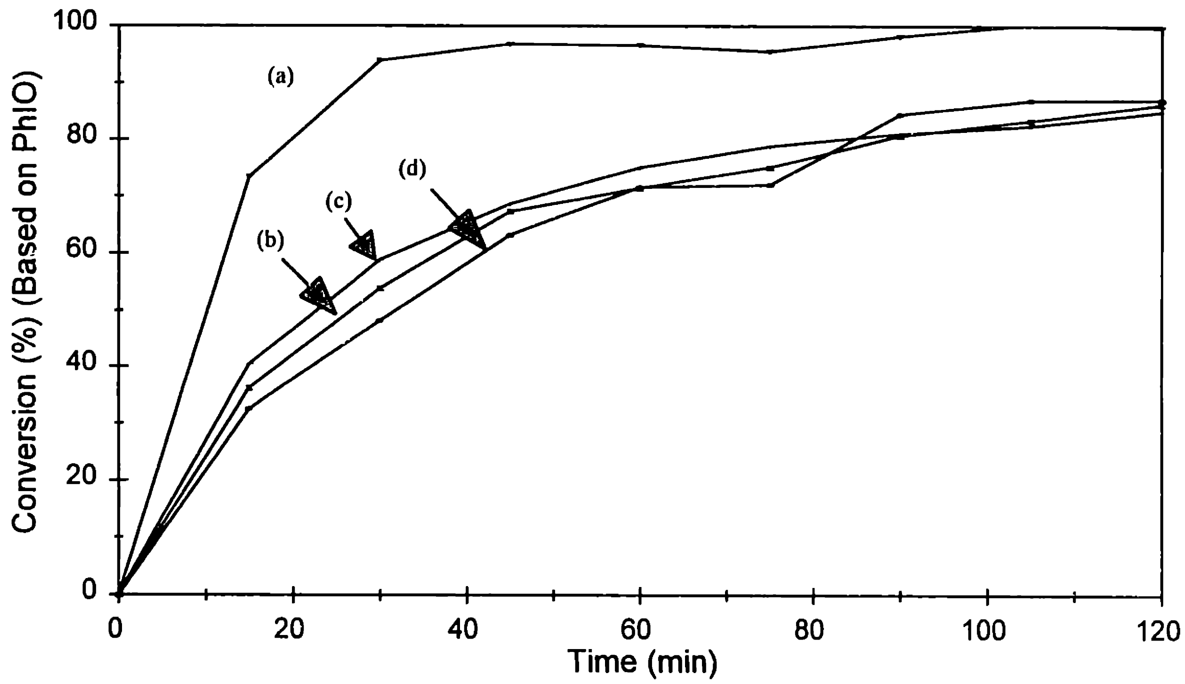

Figure 6.18. Conversion of cyclohexene epoxidation with iodosobezene over (a) unsupported FeT$_{NH2}$PPBr (10 mg) under air, (b) supported FeT$_{NH2}$PPBr/NbSi1-5.4 catalyst (containing 10.8 mg FeT$_{NH2}$PPBr) under air, (c) supported FeT$_{NH2}$PPBr/NbSi4-20-2 catalyst (containing 2.2 mg FeT$_{NH2}$PPBr) under air, and (d) supported FeT$_{NH2}$PPBr/NbSi4-20-2 catalyst (containing 2.2 mg FeT$_{NH2}$PPBr) under N_2.

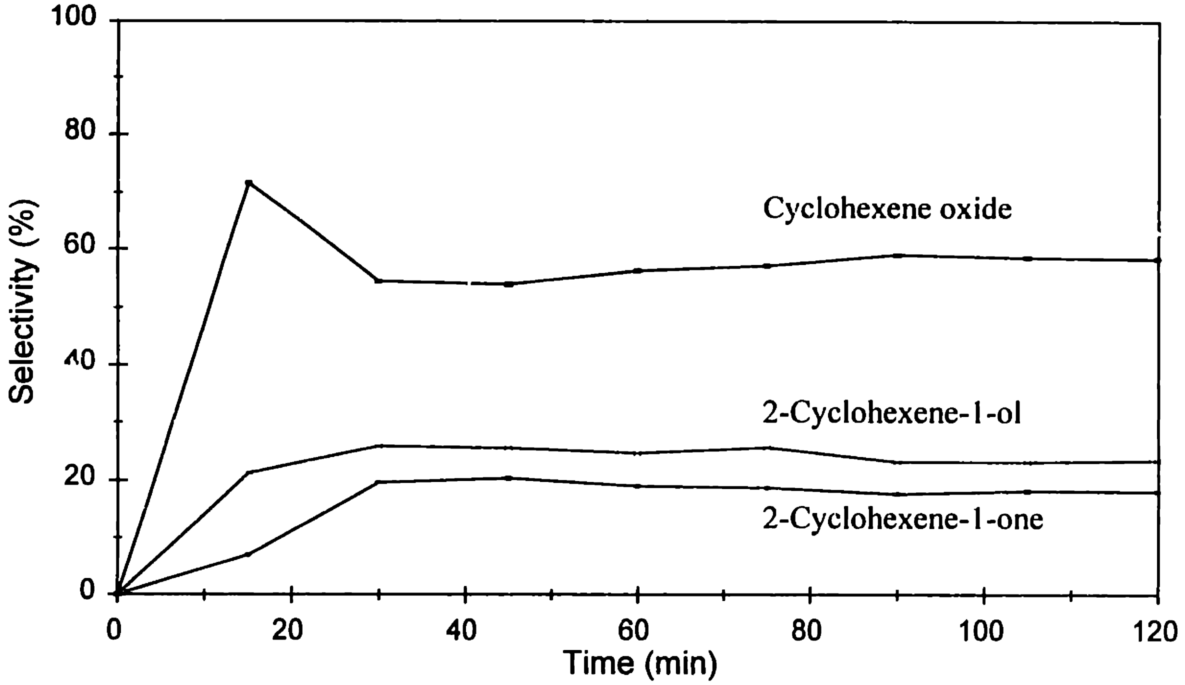

Figure 6.19. Product selectivity of cyclohexene epoxidation with iodosobenzene over supported $FeT_{NH2}PPBr$/NbSi1-5.4 catalyst (containing 10.8 mg $FeT_{NH2}PPBr$) under air.

of the cyclohexene oxide products out of the mesoporous structure without further oxidation. However, since there were no steric hindrance effects and more diluted substrate concentration near the active sites in the homogeneous system, a better epoxide selectivity was achieved with the unsupported metalloporphyrin catalysts (see Table 6.2). Diffusion was facilitated with NbSi4-20-2 support, which has a larger pore of 33 Å than NbSi1-5.4 (24 Å). The conversions of these two supported $FeT_{NH2}PPBr$ catalysts were similar (Figures 6.18 (b) and (c)), although less ctalyst loading was used in $FeT_{NH2}PPBr$/NbSi4-20-2. The selectivity to cyclohexene oxide of $FeT_{NH2}PPBr$/NbSi4-20-2 (Figure 6.20) was higher than that of $FeT_{NH2}PPBr$/NbSi1-5.4 catalyst and comparable to that of homogeneous catalyst (Table 6.2). It was known that the allylic reaction could be greatly suppressed in an inert atmosphere. We have found that reaction over $FeT_{NH2}PPBr$/NbSi4-20-2 in N_2 led to an overall conversion of 87% after 2 hours, (Figure 6.18(d)), with increased selectivity to epoxide (87.1%). Only 9.9% of 2-cyclohexen-1-ol and 3.0% of 2-cyclohexen-1-one were found after 2 hours of reaction under N_2 (Figure 6.21). We also examined the epoxidation of cyclohexene using tert-butyl hydroperoxide (TBHP) as an oxidant. A total conversion of 73% was obtained

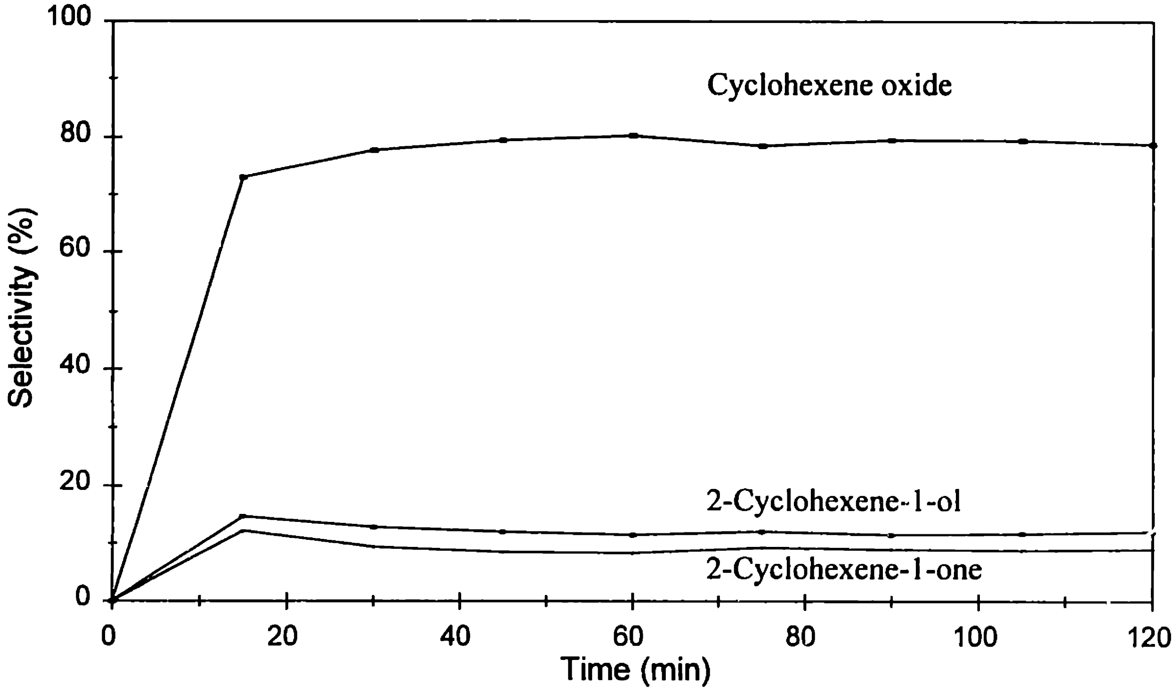

Figure 6.20. Product selectivity of cyclohexene epoxidation with iodosobenzene over supported FeT$_{NH2}$PPBr/NbSi4-20-2 catalyst (containing 2.2 mg FeT$_{NH2}$PPBr) under air.

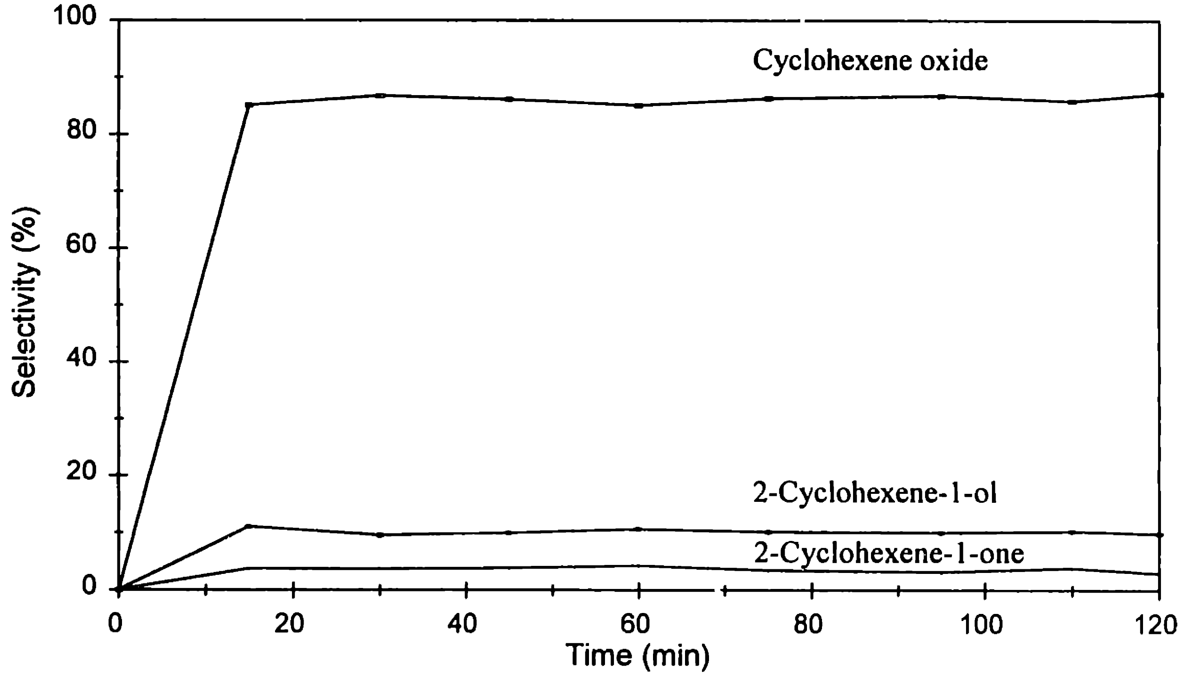

Figure 6.21. Product selectivity of cyclohexene epoxidation with iodosobenzene over supported FeT$_{NH2}$PPBr/NbSi4-20-2 catalyst (containing 2.2 mg FeT$_{NH2}$PPBr) under N$_2$.

after 2 hours with an epoxide selectivity of 43.6% over $FeT_{NH2}PPBr/NbSi4-20$ (Fe loading: 0.58 wt%) (Figures 6.22 and 6.23). The catalyst showed trace epoxide formation using H_2O_2 as oxidant. This might be due to the dismutation of H_2O_2 by the inorganic support.[5]

Table 6.2. Comparison of unsupported and supported $FeT_{NH2}PPBr$ catalysts in the epoxidation of cyclohexene after 2 hours of reaction

Support	$FeT_{NH2}PPBr$	Atmosphere	Oxidant	Conv. (%)[c]	Selectivity (%)			TON (mmol/ mmol Fe)
					Oxide	1-ol	1-one	
--	10	Air	PhIO[a]	100	79.4	13.3	7.3	40
NbSi1-5.4	10.8	Air	PhIO[a]	86	58.2	25.1	17.7	32
NbSi4-20-2	2.2	Air	PhIO[a]	85	78.9	12.1	9.0	170
NbSi4-20-2	2.2	N_2	PhIO[a]	87	87.1	9.9	3.0	174
--	4.2	Air	TBHP[b]	99	14.6	34.1	51.3	189
NbSi4-20	4.2	Air	TBHP[b]	73	43.6	33.2	23.2	141

[a] Reaction mixtures: 1 ml (10 mmol) of cyclohexene, 4 ml of CH_2Cl_2, 110 mg (0.5 mmol) of iodosobenzene, and 10 mg of homogeneous catalyst or 100 mg of heterogeneous catalyst.

[b] Reaction mixtures: 0.5 ml (5 mmol) of cyclohexene, 5 ml of CH_2Cl_2, 1 mmol of TBHP, and 4.2 mg of homogeneous catalyst or 50 mg of heterogeneous catalyst.

[c] Conversion was determined by GC and based on moles of iodobenzene formed or moles of THBP consumed during the reaction.

6.4.2.2 Epoxidation of (Z)-Cyclooctene

To better understand the epoxidation characteristics, we have also examined (Z)-cyclooctene as a substrate that is less prone to allylic oxidation than cyclohexene. Although the overall conversion of (Z)-cyclooctene was lower than that for cyclohexene, the selectivity to epoxide was 100% (see Eq. (6.3)).

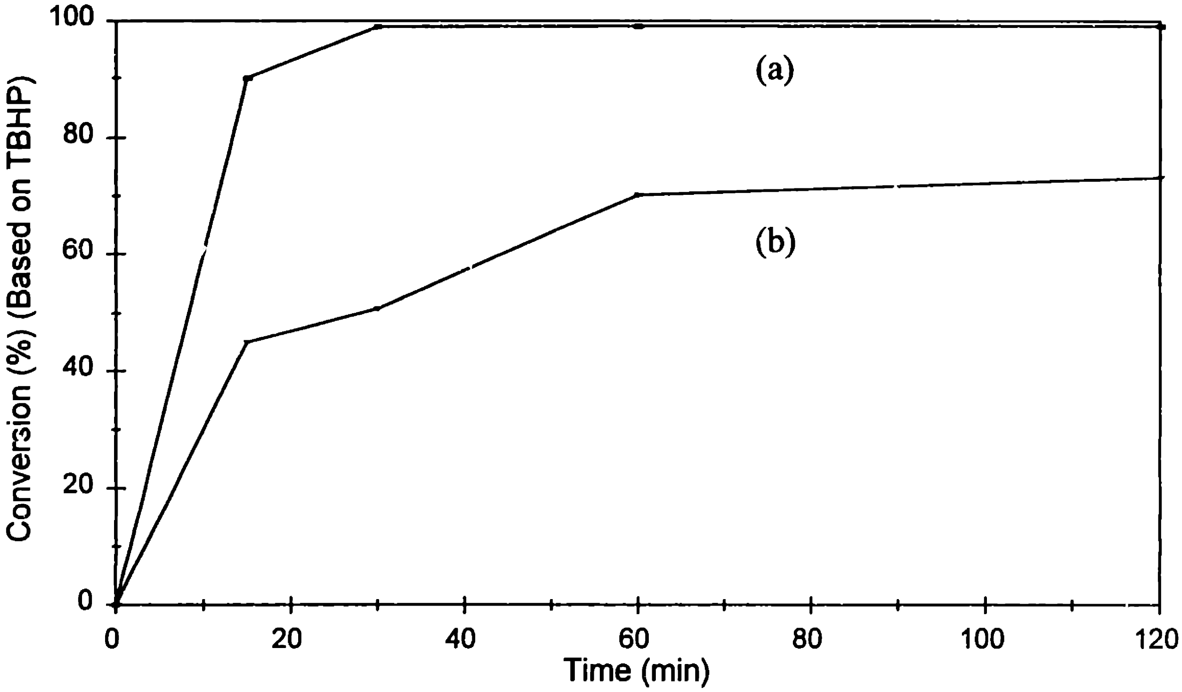

Figure 6.22. Conversion of cyclohexene epoxidation with TBHP over (a) unsupported $\mathrm{FeT_{NH2}PPBr}$ (4.2 mg) and (b) supported $\mathrm{FeT_{NH2}PPBr}$/NbSi4-20 catalyst (containing 4.2 mg $\mathrm{FeT_{NH2}PPBr}$).

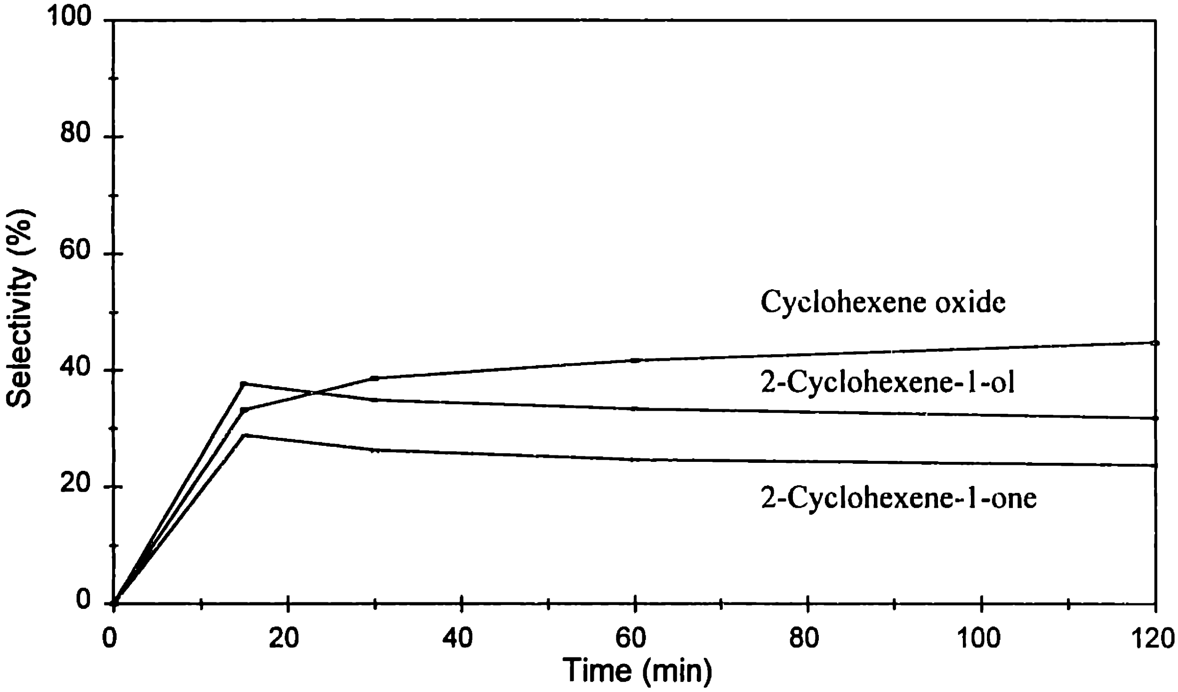

Figure 6.23. Product selectivity of cyclohexene epoxidation with TBHP over supported $\mathrm{FeT_{NH2}PPBr}$/NbSi4-20 catalyst (containing 4.2 mg $\mathrm{FeT_{NH2}PPBr}$).

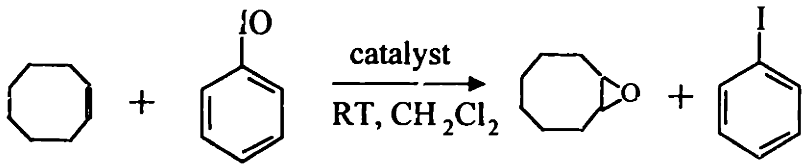 (6.3)

The effects of the catalyst loading and the support microstructure on the catalytic conversion of this reaction were investigated in detail. The conversion after 5 hours of reaction was increased using a mesoporous NbSi1 support with a higher Nb dopant concentration, which allowed for a higher metalloporphyrin loading (Table 6.3, Figures 6.24(b) and (c)). However, the TON decreased with higher metalloporphyrin loading, suggesting that not all the metalloporphyrin sites were accessible for epoxidation, possibly due to the constraint of the pore size of NbSi1. For (Z)-cyclooctene epoxidation, compared to poly(4-vinylpyridine)-supported iron(III) 5,10,15,20-tetra(2,6-dichlorophenyl)porphyrin in methanol (40% conversion after 24 hours, TON = 55),[22] excellent stability was achieved with our supported catalyst.

Table 6.3. Cyclooctene epoxidation over supported $FeT_{NH2}PPBr$/NbSi-R catalysts after 5 hours of reaction[a]

Support	Nb (wt%)	Fe (mg)[b]	Surface Area (m^2/g)	Pore Size (Å)	Conversion (%)[c]	TON (mmol/ mmol Fe)
NbSi1-5.4	7.72	0.75	1140	24	57	21
NbSi1-11.4	3.64	0.36	1477	23	42	33
NbSi1-20	2.00	0.17	1282	27	45	74
NbSi2-20	3.21	0.25	822	23	38	43
NbSi4-20-1	6.00	0.37	864	33	98	74
NbSi4-20-2	6.00	0.14	864	33	98	196
Nb-doped Silica Gel	8.60	0.36	557	< 20	14	11
Unsupported-1	--	0.75	--	--	89	33
Unsupported-2	--	0.36	--	--	90	73
Unsupported-3	--	0.14	--	--	85	170

[a] Reaction mixture: 1 ml of (Z)-cyclooctene, 4 ml of CH_2Cl_2, and 0.5 mmol of iodosobenzene.

[b] Total Fe content from unsupported porphyrin catalysts, or from 100 mg of supported porphyrin catalysts.

[c] Conversion was determined by GC and based on moles of iodobenzene formed during the reaction in air.

Catalytic epoxidation results over porphyrins supported on differently derived mesoporous Nb-doped silica matrices were compared. $FeT_{NH2}PPBr$ supported on NbSi1-20 gave a higher cyclooctene conversion than that supported on NbSi2-20, although the iron porphyrin catalyst loading was higher in the latter (Table 6.3). The differences in catalytic conversion and TON might be attributed to the differences in the supports' microstructure. NbSi1-20 and NbSi2-20 were both synthesized from a precursor Si/Nb atomic ratio of 20. However, NbSi1-20 derived from TMAS precursor has a higher surface area and a larger average pore size than NbSi2-20 derived from sodium silicate, possibly providing slightly greater accessibility for the active sites and faster diffusion for the reactants and products. This result further suggested that pore size was a very critical parameter in the control of catalytic performance. The dynamic diameter of the iron porphyrin molecules was ~ 20 Å. Upon porphyrin loading, the reduction in pore volume (from 0.74 cm^3/g to 0.52 cm^3/g for 0.25 wt% Fe loading) of NbSi2-20 (23 Å pore diameter) suggested that some pore blockage might have occurred in this support material (Figure 6.11). Supports with different pore sizes were therefore examined further to investigate the diffusional effects in our heterogeneous systems.

The pore size distributions of different Nb-doped silicates and the corresponding conversion of cyclooctene are presented in Figures 6.24 and 6.25, and Table 6.3. The $FeT_{NH2}PPBr$ supported on sol-gel derived amorphous Nb-doped silica showed the lowest activity (14% conversion after 5 hours, TON = 11) (Figure 6.24(a)), which could be attributed to steric constraints within this microporous support (Figure 6.4). The use of tetraethoxysilane as silica precursor and mixed surfactants as templating agents resulted in a mesoporous support (NbSi4-20) with comparable surface area as NbSi2-20, but much larger pore size (33 Å). The epoxidation conversion over NbSi2-20 and NbSi4-20-2 were 38% and 98%, respectively. An excellent TON of 196 was achieved over $FeT_{NH2}PPBr$/NbSi4-20-2, which had 0.14 mg Fe loading. After 5 hours of reaction, the conversion and TON attained with $FeT_{NH2}PPBr$/NbSi4-20-2 were more than two times that of $FeT_{NH2}PPBr$/NbSi1-20, which has a similar Fe loading but a smaller pore size (27 Å). This could be attributed to the facilitated diffusion of both reactants and products within the larger pores of the NbSi4-20-2 support. With the $FeT_{NH2}PPBr$/NbSi4-20-1 catalyst (which contained 0.37 mg Fe loading) (Figure 6.24(e)), a faster initial reaction rate was achieved in the first 2 hours of reaction compared to FeT$_{NH2}$PPBr/NbSi4-20-2 (which contained 0.14 mg Fe loading) (Figure 6.24(d)). Essentially complete conversion (98%) was attained by both FeT$_{NH2}$PPBr/NbSi4-20-1 and FeT$_{NH2}$PPBr/NbSi4-20-2 within 5 hours of reaction. It was further noteworthy that FeT$_{NH2}$PPBr/NbSi4-20-2 achieved a higher TON of 196 than the FeT$_{NH2}$PPBr unsupported-3 catalyst (TON = 170) of the same Fe loading (0.14 mg) (Table 6.3). This suggested that isolated and highly dispersed iron porphyrins achieved with the appropriate support system would lead to the optimized oxidation catalyst. Our study clearly showed that iron porphyrin loading, and support pore size and surface area were important factors governing the catalytic performance. Highly-dispersed iron porphyrin loading, large pore size and high surface area were highly desirable features for catalytic oxidation reaction involving large molecules.

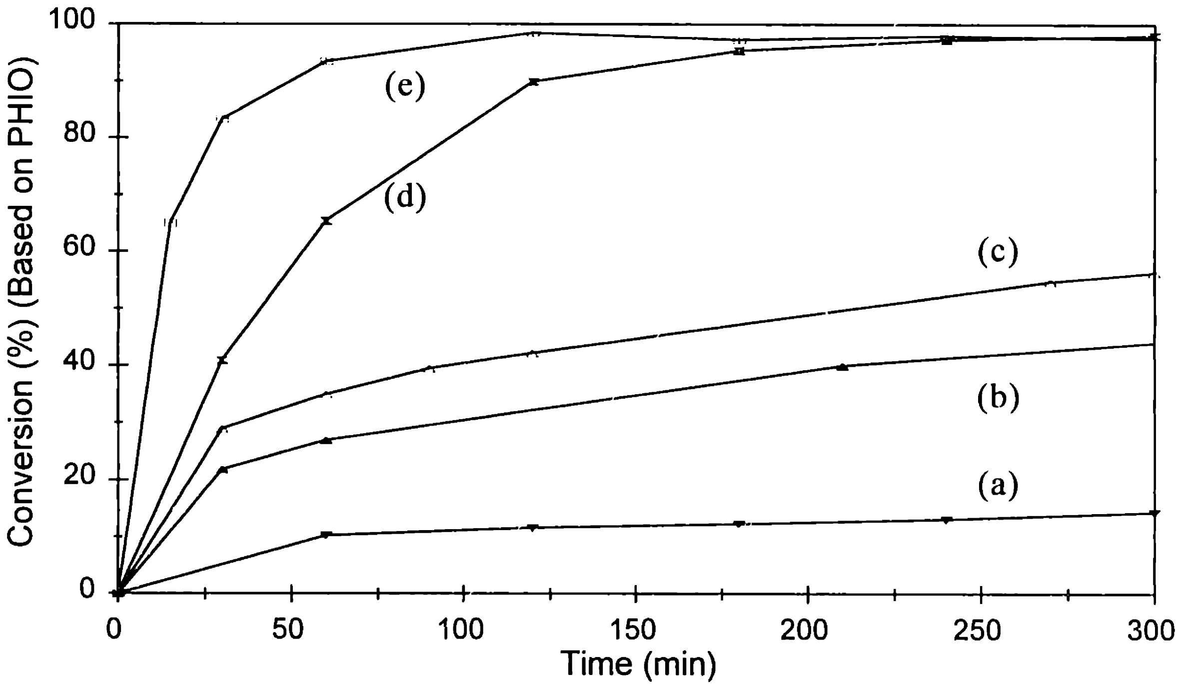

Figure 6.24. Conversion of cyclooctene epoxidation with iodosobenzene over (a) FeT$_{NH2}$PPBr/Nb-doped silica gel, (b) FeT$_{NH2}$PPBr/NbSi1-11.4, (c) FeT$_{NH2}$PPBr/NbSi1-5.4, (d) FeT$_{NH2}$PPBr/NbSi4-20-2, and (e) FeT$_{NH2}$PPBr/NbSi4-20-1.

Lastly, to illustrate the stability and reusability of our heterogeneous catalyst systems, the catalytic behavior in multiple oxidation cycles was examined for epoxidation of (Z)-cyclooctene with $FeT_{NH2}PPBr$/NbSi1-5.4. No degradation in conversion was detected over our supported catalyst for at least three oxidation cycles, indicating that the fixation scheme we devised effectively isolated the metalloporphyrin complexes from self-oxidation and leaching problems commonly encountered in conventional homogeneous and heterogeneous systems.

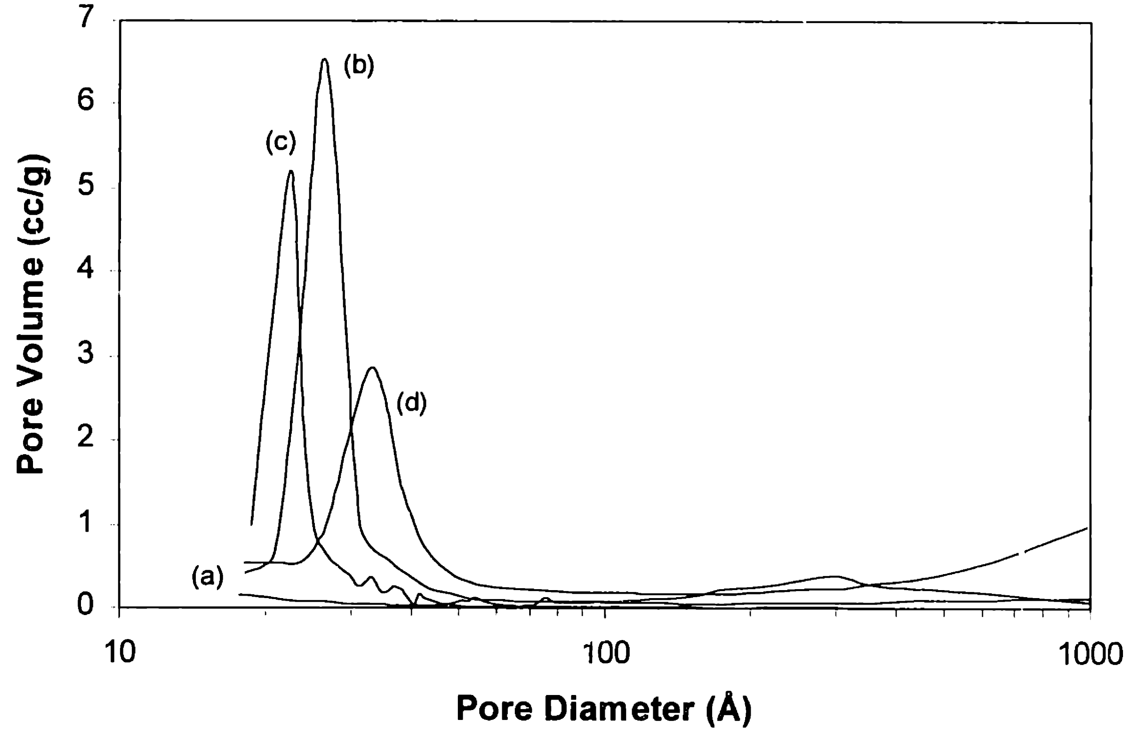

Figure 6.25. BJH pore size distributions from adsorption isotherms of calcined (a) 8.6 wt% Nb-doped silica gel, (b) NbSi1-20, (c) NbSi2-20, and (d) NbSi4-20.

6.5 Summary

The design strategy presented in this chapter provided an effective fixation mechanism for metalloporphyrin catalysts. The large pore openings of the mesoporous supports used provided sufficient space for hosting the large catalytic complexes and allowed for facile diffusion of the reactants and products. In the case of FePc encapsulated in mesoporous Al-doped silica, the porphyrin molecules interacted with the surface free Al-OH groups through their Fe centers. The amine-substituted iron porphyrins were successfully immobilized within mesoporous Nb-doped silica via N-Nb linkages. Compared to conventional heterogeneous systems, our supported catalysts demonstrated high oxidation activity and selectivity, with ease of diffusion of reactants and products in the large pore channels of the well-defined mesoporous supports. The immobilized catalysts successfully overcame the leaching and self-oxidation problems associated with conventional systems. By manipulating the structural characteristics of the support material, such as surface area, pore size, nature of dopant and dopant concentration, the catalytic performance of the heterogeneous systems was optimized for oxidation reactions.

6.6 References

[1] B. Meunier, Chem. Rev., **92**, (1992) 1411.

[2] D. Ostovic, G. S. He, and T. C. Bruce, *Metalloporphyrins in Catalytic Oxidations*, edited by R. A. Sheldon, Marcel Dekker, New York, (1994) Chapter 2.

[3] J. Groves and T. E. Nemo, J. Am. Chem. Soc., **105**, (1983) 5786.

[4] T. Tatsumi, M. Nakamura, and H. Tominaga, Chem. Soc. Japn., Chem. Lett., (1989) 419.

[5] M. A. Maritinez-Lorente, P. Battioni, W. Kleemiss, J. F. Bartoli, and D. Mansuy, J. Molec. Catal. A, **113**, (1996) 343.

[6] M. Chibwe, L. Ukrainczyk, S. A. Body, and T. J. Pinnavaia, J. Molec. Catal. A, **113**, (1996) 249.

[7] S. Campestrini and B. Meunier, Inorg. Chem., **31**, (1992) 1999.

[8] N. Herron, G. D. Stucky, and C. A. Tolman, J. Chem. Soc., Chem. Commun., (1986) 1521.

[9] L. Zhang, T. Sun, and J. Y. Ying, to be submitted to Chem. Commun.

[10] L. Zhang and J. Y. Ying to be submitted to J. Catal.

[11] D. M. Antonelli and J. Y. Ying, Angew. Chem. Int. Ed. Engl., **35**, (1996) 426.

[12] D. M. Antonelli and J. Y. Ying, Chem. Mater., **8**, (1996) 874.

[13] D. M. Antonelli, A. Nakahira, and J. Y. Ying, Inorg. Chem., **35**, (1996) 3126.

[14] L. Zhang and J. Y. Ying, AIChE J., **43**, (1997) 2793.

[15] J. Collman, R. R. Gagne, C. A. Reed, T. R. Halbert, G. Lang, and W. T. Robinson, J. Am. Chem. Soc., **97**, (1975) 1427.

[16] R. C. Mehrotra, A. K. Rai, P. N. Kapoor, and R. Bohra, Inorg. Chimi. Acta, **16**, (1976) 237.

[17] P. Rothemund, J. Am. Chem. Soc., (1939) 2012.

[18] H. Saltzmann and J. G. Sharefkin, Org. Synth., **43**, (1963) 60.

[19] N. Herron, J. Coord. Chem., **19**, (1988) 25.

[20] J. T. Groves and D. V. Subramanian, J. Am. Chem. Soc., **106**, (1984) 2177.

[21] D. R. Leanord and J. R. Lindsay Smith, J. Chem. Soc., Perkin Trans., **2**, (1990) 1917.

[22] P. R. Cooke and J. R. Lindsay Smith, J. Chem. Soc., Perkin Trans., **1**, (1994) 1913.

Chapter 7

CONCLUSIONS AND FUTURE RESEARCH DIRECTIONS

7.1 Thesis Conclusions

This thesis describes the effective synthesis of superparamagnetic iron oxide nanoclusters and supported iron porphyrin oxidation catalysts via matrix-mediated route. The research has focused on tailoring the properties of magnetic nanoclusters and catalysts through the manipulation of the matrix microstructure and the guest-host interaction.

Single-domain magnetic clusters are of interest for fundamental understanding of micromagnetism, and for potential applications in information storage and magnetic refrigeration. The main challenge in the synthesis of nanoclusters lies in the precise control of cluster size, morphology, and surface/interfacial characteristics. Iron-oxide/silica nanocomposites have been prepared to examine the magnetic and quantum confinement behavior associated with nanostructures. We have developed synthetic approaches that isolated single-domain Fe_2O_3 clusters within three different matrices: (1) a sol-gel derived silica matrix modified with SO_3^- functional groups, (2) an inert silica coating, and (3) a hexagonally-packed mesoporous aluminosilicate matrix. The microstructure and surface chemistry of the host matrices were designed to offered excellent control of the cluster size and morphology. In the first approach, iron cations, attracted to the inorganic sulfonated silica gel with ion-exchange capability, were oxidized to form elongated Fe_2O_3 nanoclusters (4 nm x 20 nm) that were highly dispersed within the matrix. In the second route, the precipitated Fe_2O_3 clusters were encapsulated with a silica coating to give individual spherical magnetic particles of ~4 nm diameters. Thirdly, Fe_2O_3 nanoclusters were synthesized within the mesoporous aluminosilicate support via an evaporation-condensation approach. The well-defined hexagonally-packed cylindrical pore structure of MCM-41 led to the derivation of guest particles with spherical and elongated morphologies.

With the three different host matrices, nanometer-sized γ-Fe_2O_3 particles with unique size, morphology, and surface strain effects were obtained and systematically investigated for magnetic and optical characteristics. SQUID and Mössbauer characterizations, in combination with TEM studies, enabled the determination of not only the macroscopic magnetic properties (M and H_c), but also the microscopic magnetic parameters (K_{eff}, H_{max} and τ_0) from which the superparamagnetic and coercive properties of these systems were obtained. Furthermore, structure-property relationship was established for the nanometer-sized clusters as so to gain a better understanding of nanoscale magnetism. Magnetization studies and Mössbauer spectroscopy indicated that the γ-Fe_2O_3/SiO_2 nanocomposites were superparamagnetic. The coercivities and superparamagnetic barrier energies could be manipulated through modification of the microstructure and the cluster/support interface. The surface and strain effects were shown to play a critical role in the overall magnetic and optical behavior of the nanocomposites. Tailoring of the magnetic properties of these novel systems was possible through the control of the matrix structure and the cluster synthesis conditions.

Metalloporphyrins provide a high chemoselectivity and catalytic activity for oxidation of both saturated and unsaturated hydrocarbons under mild reaction conditions. Isolation of active sites and facile recovery of catalysts are the major challenges in the utilization of metalloporphyrin systems. MCM-41 with its well-defined large pore openings is very suitable for supporting the sizable metalloporphyrin complexes. To achieve metalloporphyrin fixation within the matrix pore structure, MCM-41 silicates were doped with Al or Nb. The significant amount of surface hydroxyl groups in mesoporous aluminosilicate was used to provide interaction with the Fe centers of phthalocyanine. Amine-substituted iron porphyrin ($FeT_{NH2}PPBr$) was immobilized onto the pore walls of Nb-doped silica through N-Nb covalent bonding. High catalyst stability was achieved through this designed interaction, effectively preventing auto-oxidation and leaching of the metalloporphyrins. The resulting heterogeneous catalysts demonstrated high oxidation activity and improved selectivity in both alkane hydroxylation and alkene epoxidation due to the facilitated diffusion of reactants and products in the large pore channels of the support materials. By controlling the structural characteristics of the mesoporous supports, such as the nature of dopant, dopant concentration, pore size and surface area, the catalytic activity and selectivity were successfully optimized.

7.2 Future Research Directions

It would be of interest to conduct further research to better understand the micromagnetism of nanostructures. Mössbauer spectra collected in this study could be dependent on an interplay between the anisotropy energies and the applied field spin polarization effects. The application of a moderate magnetic field in Mössbauer studies will enable us to determine whether each cluster behaves as a large, spin-coupled molecule or a magnetically-ordered particle above its blocking temperature. In general, for a spin-coupled molecule, the induced hyperfine fields are collinear with the applied field and smaller than those associated with full, saturated moments. In a magnetically-ordered particle, a large magnetic hyperfine field close to saturation will be induced non-collinearly with the applied field. Low-temperature Mössbauer spectra with applied field can yield information about the spin canting at the particle/support interface, and the internal spin structure of the nanoclusters. Investigations over a wide range of applied magnetic fields below, above and at the blocking temperature can reveal detailed information about the nature and magnitude of the magnetic interactions present and the spin structure at the particle/support interface. Information obtained from combined temperature-dependent ferromagnetic resonance (FMR) and Mössbauer investigations can probe the internal spin structure of the clusters, the possible spin coupling schemes among iron ions, and the onset of collective magnetic correlation leading to intra-cluster short-range order and overall magnetic behavior of the cluster. It would further be of interest to develop the nanocomposites derived in this study in the form of thin films for magnetic device fabrication. Understanding and precise control of the materials synthesis and processing parameters are key to achieving this goal.

A detailed understanding of the catalytic oxidation mechanism of supported iron porphyrins can be obtained by in-situ monitoring the Fe oxidation state with Mössbauer spectroscopy and UV-Vis spectroscopy. Further confirmation of the formation of Nb-N bonding in the porphyrin fixation scheme in mesoporous Nb-doped silicate can be achieved by synthesizing $^{15}NH_2$-containing iron porphyrins and studying the chemical interaction between NH_2 and surface Nb sites with ^{15}N nuclear magnetic resonance spectroscopy. Our study has illustrated the effectiveness of catalyst design through combined tailoring of the microstructure and composition of the porous support, and of the matrix interaction with the functionalized catalytic species. A similar approach could be applied towards fixating a variety of active homogeneous catalysts within inorganic large-pore supports. This will offer exciting new possibilities for introducing chirality and excellent activity associated with enzymes and special organometallic complexes into heterogeneous asymmetric catalysis of fine chemicals and pharmaceuticals.

Appendix I

NOMENCLATURE

A_{core}	magnetic contribution from the core of magnetic particle
$A_{surface}$	magnetic contribution from the surface of magnetic particle
a_o	unit cell parameter
d	spacing of crystal plane
δ	isomer shift
E	superparamagnetic energy barrier
ΔE_o	quadrupole splitting
f(V)	fraction of particle volume
γ_0	gyromagnetic ratio
H	applied field
H_c	coercivity
H_{hf}	hyperfine field
H_{hf0}	saturation hyperfine field at $T = 0$ K
H_{max}	maximum hyperfine field
K	Boltzmann's constant
K_1	crystalline anisotropy
K_{eff}	effective magnetic anisotropy constant
K_s	surface anisotropy
K_{sh}	shape anisotropy
K_σ	surface strain anisotropy
K_V	magnetocrystalline anisotropy
M	magnetization
M_{FC}	magnetization under field cooling
M_r	magnetic remanence
M_s	saturation magnetization
M_{ZFC}	magnetization under zero field cooling
μ	magnetic moment
N	total number of particles

n(V')	particle size distribution
θ	angle between magnetization direction and easy axis of magnetic particle
T	measurement temperature
T_b	critical magnetic blocking temperature
T_{max}	temperature at which a maximum magnetization is obtained under zero field cooling
τ	relaxation time
τ_0	simplified time constant in Equation (2.6)
τ_m	measurement time
V	volume of magnetic particle